Université de Strasbourg

Université de Strasbourg

École doctorale | ED 182
Physique et Chimie Physique
Université de Strasbourg

École doctorale de Physique et Chimie Physique

Institut Pluridisciplinaire Hubert Curien
CNRS/Université de Strasbourg, UMR7178

Thèse présentée par

Jonathan Collin

soutenue le : 12 novembre 2025

pour obtenir le grade de : Docteur de l'Université de Strasbourg
Discipline/Spécialité : Physique des constituants élémentaires

Estimation de l'activité induite par des neutrons et de l'inventaire radiologique auprès d'accélérateurs de haute puissance

Thèse dirigée par :

Abdel-Mjid Nourreddine — Professeur, Université de Strasbourg

Rapporteurs :

Claire Michelet — Professeure, LP2I Bordeaux
Abdallah Lyoussi — Directeur de Recherche, CEA Cadarache

Autres Membres du Jury :

Maëlle Kerveno — Directrice de Recherche, IPHC
Jean-Emmanuel Groetz — Professeur, Université Marie et Louis Pasteur
Guilhem Lacaze — Docteur, Transmutex SA

Université de Strasbourg

University of Strasbourg

École doctorale | ED 182
Physique et Chimie Physique
Université de Strasbourg

Doctoral College of Physics and Chemistry-Physics

Institut Pluridisciplinaire Hubert Curien
CNRS/Université de Strasbourg, UMR7178

Thesis presented by

Jonathan Collin

defended on: 12 November 2025

to obtain the degree of: Doctor of the University of Strasbourg
Discipline/Speciality: Elementary Constituents Physics

Estimation of neutron-induced activity and radiological inventory around high-power accelerators

Thesis supervised by:

Abdel-Mjid Nourreddine — Professor, Université de Strasbourg

Reviewers:

Claire Michelet — Professor, LP2I Bordeaux
Abdallah Lyoussi — Research Director, CEA Cadarache

Other Examiners:

Maëlle Kerveno — Research Director, IPHC
Jean-Emmanuel Groetz — Professor, Université Marie et Louis Pasteur
Guilhem Lacaze — Doctor, Transmutex SA

Because this fish cares. And this fish and this fish...

(The story of the Boy and the Fishes on the Beach, Mistakenly Saving the Villain, Feng Yu Nie)

Acknowledgements

These words closes this chapter of my life, and ends my university years, but also starts I hope my scholar years. I will surely forget to mention people, but if you read this words, even if not mentioned, there are also directed to you (especially if you ever offered me food).

First and foremost, I would like to thank the jury, who accepted to be maybe the only persons in the world to ever read this document in its entierety, Jean-Emmanuel Groetz, Maëlle Kerveno, Abdallah Lyoussi and Claire Michelet.

I cannot forget to thank deeply my PhD supervisor Abdel-Mjid Nourreddine, who was not only the best PhD advisor I could have asked for, never forgot to bring sweets from his trips ! I did enjoy our conversations, and that he introduced me to this great detectors that are the SSNTDs, I will quote him and say indeed "Physics is still in the plastics".

I must thank also Transmutex which not only financed my thesis, but allowed to take part of their adventure and contribute, even if modically, to their world changing ADS project. I should thank first the ones who gave me the opportunity to start this PhD, Franklin Servan-Schreiber and Federico Carminati, who hired me. I wish to thank also Yves Schutz, who not only introduced this collaboration, but also allowed to transform my "sparadrap" code into an optimised implementation for database access in `TMX_Bateman`, and introducing neutron interactions enabling easy benchmarks and giving more depth to this code.

I thank the entire Transmutex team, especially the one that supervised me, during my experimental shennanigans: Massimo Barbagallo, Lucas J. Tagliapietra; and for the second part of my PhD, Patricia Mendez and Guilhem Lacaze; and consistently, Donovan Maire. I cannot forget Ieva Kasuza, who helped me organise my different stays at Transmutex headquarters. But also all the colleagues: Giacomo, Judit, Franz, Sevda, Nataliia, Thomas, Cliff, Laryssa, Jean-Pierre, Guido and Giuliana.

This PhD could not have happened without the discussions with the developers of all these tools granting access to state-of-the-art knowledges, especially BetaShape's main developer Xavier Mougeot, as well as its counterpart for the GEF code, Karl-Heinz Schmidt.

I thank the CYRCé team, who granted me access to the facilities especially Michel Pellicioli and Jacky Schüler, as well as Thierry Foehrenbacher who did the gamma spectroscopy for the need of this PhD.

This latter work around CYRCé could only happens thanks to Jean-Michel Horodynski who allowed me to take part in its experimental campaign, which I thank as it enabled me to push the tools in actual context.

The picture could not be complete without mentionning the dream team, the DeSIs team. I wish to thank Nicolas, who was my first mentor in the group during my internship, but also always an help when guidance was needed (or Shokobons). I thank also Marie for her guidance, and the chocolates she offered me (even if you were a bit to keen in your attacks towards the "Terre Sainte"). I thank also our happy manager, Christian, from which I will remember the great motto "What separates Bretagne and Elsaß is only France". I cannot forget Lévana, who canonized me during my PhD, do not fear world-domination is still planned. I also thank Séverine, for her help in my attempts in chemical shenanigans. I thank also Lucia, for making me discovery spanish food specialities. Shout-out to Djokhar, even if I fear he will suffer "indigestion" after attempting to read this manuscript. I extend my thanks to Mehdi, Sylvia, Antoine, Addil, Florent and Eric.

I was mentioned in their acknowledgments, so I will not forget to thanks my TPS friends, or rather my restaurants companions, by order of preference (maybe or by alphabetical order who knows): Quentin, Raphaël, Emma, Xavier, and Ronan.

Enfin, je souhaite remercier ma famille, ma soeur et mon frère, et mes parents. J'ai pu atteindre ce degré d'éducation, seulement grâce à leur soutien indéfectible. Je vous remercie pour les valeurs que vous m'avez transmises, et si peu souvent dit, mais souvent pensé, je profite de cette page, pour vous remercier du fond du coeur.

Contents

List of Figures . . . . . **ix**

List of Tables . . . . . **xiii**

List of Listings . . . . . **xv**

Introduction **1**

1. General Considerations **9**
1.1. Nuclear taxonomy 9
1.2. Radionuclides 12
1.2.1. Stability valley 13
1.2.2. Radioactive decay 14
1.2.3. Activity and radioactive filiation 21
1.3. Characterisation of Ionising radiations 27
1.3.1. Charged particles: Stopping Power 28
1.3.2. Neutrons and Photons: Absorption law 28
1.4. Photon-matter interaction 31
1.4.1. Photoelectric effect 31
1.4.2. Compton effect 32
1.4.3. Pair production 33
1.5. Neutrons-matter interaction 33
1.5.1. Classification 34
1.5.2. Scattering 36
1.5.3. Capture 37
1.5.4. Resonance 38
1.5.5. Sources of neutrons 41
1.6. Conclusion 42

2. Assessment of induced activation around particle accelerators **43**
2.1. Generalities on Monte Carlo Methods 44
2.1.1. Principle 45
2.1.2. Codes of interest 48
2.2. Experimental methods 56
2.2.1. Gamma spectroscopy 57
2.2.2. Solid State Nuclear Track Detector 64
2.3. Assessment of induced activation 69
2.3.1. Around medical LINAC 69

2.3.2. Around an AmBe source . . . 77
2.3.3. Model assumptions . . . 79
2.3.4. Around CYRCé . . . 84
2.3.5. Conclusions and perspectives . . . 91

3. Tracking radionuclide vector through time: Bateman equations . . . 95
3.1. The interest of developing a new Bateman solver . . . 96
3.2. Bateman equations resolution . . . 97
3.2.1. Livermore Solver for Ordinary Differential Equations . . . 98
3.2.2. Chebyshev Rational Approximation Method . . . 99
3.2.3. Transmutation Trajectory Analysis . . . 100
3.3. TMX_Bateman . . . 100
3.3.1. Implementation of the decay and transmutation equation . . . 103
3.3.2. Inputs . . . 105
3.3.3. Evaluated databases . . . 106
3.3.4. Outputs . . . 108
3.3.5. Isotopic composition . . . 108
3.3.6. Activity . . . 108
3.3.7. Heat load . . . 111
3.3.8. Committed dose . . . 116
3.3.9. Decay spectra . . . 116
3.4. Benchmark of `TMX_Bateman` against `FISPACT-II` and `DCHAIN-PHITS` . . . 117
3.4.1. Universe material check . . . 117
3.4.2. Decay only . . . 120
3.4.3. Transmutation/depletion considerations . . . 124
3.5. Application . . . 127
3.5.1. Extracting the γ spectra. . . . 127
3.5.2. Extracting the alpha spectrum . . . 129
3.5.3. Identifying β pure emitters. . . . 129
3.6. Conclusion . . . 133

4. A strategy to choose the cross-sections . . . 135
4.1. Systematic access tool for evaluations : eval_explorer . . . 140
4.2. Applications . . . 141
4.2.1. Comparison of (n, γ) cross-sections . . . 141
4.3. Impact of evaluated library on models . . . 142
4.3.1. Comparison of cross-sections models . . . 143
4.3.2. Simplified case . . . 143
4.3.3. Complex case . . . 145
4.4. Conclusion . . . 148

5. Global Evaluated Nuclear File, GENF/D . . . 149
5.1. Overview of decay databases . . . 151
5.1.1. ENSDF . . . 152

5.1.2. ENDF6 Decay Sub-libraries . . . 152
5.1.3. NUBASE . . . 154
5.1.4. RIPL . . . 156
5.2. Generation of the decay database . . . 157
5.2.1. Procedure Summary and Tools . . . 157
5.2.2. Step 1: Generation of basic ENDF6 database. . . . 161
5.2.3. Step 2: Insertion of decay spectra. . . . 168
5.2.4. Step 3: Addition of spontaneous fission properties . . . 172
5.2.5. Average energy estimations . . . 173
5.3. Comparison to evaluated databases . . . 175
5.3.1. Extensiveness considerations . . . 175
5.3.2. Energetics considerations . . . 176
5.4. Validation against integral measurements . . . 183
5.4.1. Fission fragments difficulties . . . 184

Conclusions . . . 187

A. `TMX_Bateman`: advanced uses . . . 193
A.1. Input . . . 193
A.1.1. Irradiation . . . 193
A.1.2. External yield . . . 194
A.1.3. Secondary spectra . . . 194
A.1.4. Threshold for outputs . . . 195
A.2. Supported decays and reactions . . . 195
A.3. Committed dose . . . 195
A.4. Inputs for examples . . . 195

B. GENF/D: list of faulty isotopes . . . 203

C. Inventory of ADS decay data needs . . . 205
C.1. ADS test libraries . . . 206
C.2. Status on decay data . . . 207
C.2.1. Short Lived Isotopes . . . 208
C.2.2. Delayed neutron emitters . . . 211
C.3. Status on Fission Fragments . . . 215
C.3.1. Spontaneous fission . . . 215
C.3.2. Neutron-induced fission . . . 219
C.4. Conclusion . . . 221

Synthesis of PhD (french) . . . 226

Acronyms . . . 257

References . . . 261

List of Figures

1. Number of particle therapy centers in operation, under construction and in planning stage, according to PTCOG data. . . . 2
2. Range of beam maximum energies of cyclotrons listed by Radioisotope Products and Radiation Technology Section, Division of Physical and Chemical Sciences, IAEA (2024 dataset). . . . 2
3. Radiotoxicity reduction considering a Partitioning and Transmutation strategy . . . 4
4. Roadmap for the decommissioning of a particle accelerator in the light of a PhD. . . . 7

1.1. ENDF/B-VIII.0 distribution of stable nuclides and radionuclides as function of atomic number and number of neutrons . . . 10
1.2. Atomic model, with SIEGBAHN representation of electron shells . . . 11
1.3. Neutron and proton shell structure in the potential wells . . . 11
1.4. Level scheme of ^{99m}Tc . . . 12
1.5. Mass excess as a function of mass number . . . 13
1.6. Level scheme of ^{24}Na . . . 15
1.7. Level scheme of ^{22}Na . . . 16
1.8. Level scheme of ^{232}Th . . . 18
1.9. Normalised Ground to Ground Beta Transition of ^{22}Na and ^{24}Na, calculated with BetaShape . . . 20
1.10. Continuous Beta radiation of ^{22}Na and ^{24}Na, calculated with BetaShape . 20
1.11. Internal Bremsstrahlung of ^{24}Na β^- decay, calculated with RADLST . . . 21
1.12. Level scheme of ^{203}Hg . . . 22
1.13. Decay path of ^{232}Th, according to ENDF/B-VIII.0 decay data . . . 24
1.14. General form of irradiation-cooling according to Bateman equations . . . 26
1.15. Stopping power and range in polycarbonate of proton and alpha . . . 30
1.16. Partial and total attenuation coefficients for γ on Germanium (Z=32), according to XMuDat . . . 32
1.17. Classification of main neutron cross-sections . . . 35
1.18. Main neutron interaction on ^{232}Th, based on ENDF/B-VIII.1 . . . 35
1.19. Comparison between ENDF/B-VIII.1 ^{1}H(n,n) and Gammel semi-empirical model . . . 37
1.20. Relative radioactivity from fission products as a function of decay time . . 39
1.21. (n,γ) cross-sections for several odd/odd atoms, according to ENDF/B-VIII.1 . . . 40

2.1. Basic structure of Monte Carlo transport simulation . . . 45
2.2. Cartography of physics model of PHITS . . . 54
2.3. Example spectra illustrating the various spectral features expected . . . 58
2.4. Reaction of interest for gamma spectroscopy . . . 59
2.5. Schematics of the electronic band structures in insulators, semiconductors and metals . . . 60
2.6. Efficiency calibration example . . . 63
2.7. General classification of SSNTD materials, per track formation and etching properties . . . 66
2.8. Geometry of the track development. The incident angle is normal with respect to the detector surface, and V_T is constant . . . 67
2.9. Schematic of the Wide Range Neutronpit (left) and the TechnoTrack2 detector (right) . . . 68
2.10. Cross-sectional view with radiator material irradiated by incident neutrons (left) and image of pits due to recoil protons in a CR-39 track detector (right) . . . 69
2.11. Simplified head of radiotherapy accelerator . . . 70
2.12. Benchmark geometry . . . 71
2.13. Schematic representation of the total photonuclear cross section per nucleon as a function of photon energy E_γ . . . 73
2.14. Neutron spectrum in the copper target simulated by MCNP, PHITS and FLUktuierende KAskade (FLUKA) . . . 76
2.15. Measured and simulated activities in 18 MeV flattening filter LINAC . . . 78
2.16. Barrel geometry and source characteristics . . . 80
2.17. Au-198 activated gamma spectra . . . 81
2.18. V52 acquired gamma spectrum . . . 81
2.19. Track-length estimation of the neutron fluence inside the vanadium sample irradiated by the direct neutron field . . . 82
2.20. Compilation of measured vs estimated activities for the direct field experiment with the vanadium sample . . . 82
2.21. CYRCé and its target selector for radioisotope production . . . 85
2.22. Locations for the irradiated samples. In red, the room walls. In purple the cyclotron, in blue the biological shield, and in pink the target selector. Red dots correspond to sample positions . . . 86
2.23. Comparison of simulated neutron lethargy spectra inside the biological shielding using ENDF library . . . 87
2.24. The ratio of estimated over measured activity for FLUKA, Particle and Heavy Ion Transport code System (PHITS) and GEometry ANd Tracking (Geant4) using the ENDF library . . . 88
2.25. Location for the SSNTD with estimated neutron fluence from FlukaCERN 89
2.26. Typical SSNTD image acquisition, with splitting between Fast (HDPE) and Thermal area (BN) . . . 90
2.27. Stacked histogram of measured average track densities and ratio between fast and thermal area of TechnoTrak2 . . . 90

2.28. Expected neutron spectrum at Location 3 and Location 5 91

3.1. Principle of TTA 102
3.2. Check for main observables correct parsing 119
3.3. Decay path of ^{48}V based on ENDF/B-VIII.0, produced with JANIS-4.0 . 120
3.4. Comparison for the decay of ^{48}V $\rightarrow$ ^{48}Ti. Relative difference of FISPACT-II and DCHAIN-PHITS with respect to TMX_Bateman 121
3.5. Decay path of ^{211}Tl based on ENDF/B-VIII.0, produced with JANIS-4.0 122
3.6. Comparison for the decay of ^{211}Tl. Relative difference of FISPACT-II and DCHAIN-PHITS with respect to TMX_Bateman 122
3.7. Comparison for the decay of uranium oxyde fuel, with trace of nuclides up to Californium. Relative difference of FISPACT-II and DCHAIN-PHITS with respect to TMX_Bateman 123
3.8. Comparison of ^{52}V build-up from ^{51}V irradiation between FISPACT-II, DCHAIN-PHITS and TMX_Bateman 125
3.9. Comparison of several 5 minutes irradiation with fast neutron sources, between FISPACT-II and TMX_Bateman 126
3.10. Comparison of ^{52}V build-up from ^{51}V irradiation between FISPACT-II, DCHAIN-PHITS and TMX_Bateman 128
3.11. Comparison of expected gamma-rate (energy-weighted) spectra for FISPACT-II and DCHAIN-PHITS with respect to TMX_Bateman 130
3.12. Comparison of experimental Tantalum spectra, against estimation from TMX_Bateman (with and without efficiency considerations) 131
3.13. Estimated alpha spectrum for Universe material according to TMX_Bateman and ENDF/B-VIII.1 database 131
3.14. Map of β-pure emitters, identifiable through TMX_Bateman, considering ENDF/B-VIII.1 database 132

4.1. Comparison of distributed and pre-processed partial cross-section of Au-197 142
4.2. Comparison of ^{45}Sc (a) and ^{197}Au (b) cross-sections (evaluation and experiment) 144
4.3. Ratio of estimated activity varying evaluated library using FISPACT-II, with ENDF/B as ratio reference 146
4.4. Comparison of expected activity inside the samples using PHITS with ENDF/B library as reference 147

5.1. Flowchart of data source for GENF/D generation 158
5.2. Segrè diagram of available ground states and their main decay mode in the GENF decay sub-library 166
5.3. Log-scaled relative difference between ENDF/B original and recomputed from Q-value decay heat by atomic number Z. The discrepancies for the total decay heat (blue hexagon), as well as light particle (yellow diamond), electromagnetic (green square) heavy particle (grey bullet) decay heat are represented, with their global average 174

5.4. Relative difference between GENF/D half-lives and JENDL-5 176
5.5. Relative discrepancy between GENF/D and JEFF-4.0 for available decay energy and neutron multiplicity 179
5.6. Comparison of the gamma relaxation spectra of the SF channel of GENF/D and JEFF-3.3. 180
5.7. Log-scaled relative difference between ENDF/B decay heat estimates (considering 10^{23} W total heat of each radionuclides) and the one recomputed based on Table 5.8 convention, considering only the nuclides with spectral information. The discrepancies for the total decay heat (blue hexagon), as well as light particle (yellow diamond), electromagnetic (green square) heavy particle (grey bullet) decay heats are represented, with their global average 181
5.8. Ratio of the average beta energy (from BetaShape) to the NUBASE2020 Q-value. The top panel shows results for β^+ emissions, and the bottom panel for β^- emissions. Data are shown for distinct isomeric states (I=1 corresponds to first isomeric states, in darker tones, and I=0 to ground states, in lighter tones), alongside the global average and a linear fit over atomic number Z 182
5.9. Decay heat benchmark using ENDF/B-VIII.0 neutron cross-section for GENF/D against ENDF/B, JEFF and JENDL decay data (using their associated fission fragments). On the left, a long thermal irradiation on ^{235}U. On the right, a thermal pulse experiment on ^{239}Pu 184
5.10. Decay heat benchmark using TENDL-2017 neutron cross-section, GEFY fission fragments and GENF/D against ENDF/B, JEFF and JENDL decay data. Five minutes irradiation at FNS of ^{nat}Ni, ^{nat}Mn, ^{nat}Fe, ^{nat}Cr . . 185

C.1. Distribution of nuclides present in current ADS libraries 207
C.2. Distribution of missing ground states between evaluated databases and NUBASE20 209
C.3. Discrepancies in short half-lives against NUBASE2020 210
C.4. Distribution of missing delayed neutron channels between evaluated databases and NUBASE20 214
C.5. Nuclides with Fission Fragments lists for spontaneous fission 216
C.6. Distribution of all spontaneous fission yields per evaluated databases . . . 217
C.7. Distribution of spontaneous fission yields for ^{244}Cm per evaluated databases 218
C.8. Mass distribution of spontaneous fission yields for ^{244}Cm and ^{252}Cf 219
C.9. Distribution of nuclides with Neutron Induced Cross-sections 220
C.10. Distribution of nuclides with Neutron Induced Fission Yields 221
C.11. Distribution of all neutron-induced fission yields per evaluated databases . 222

List of Tables

1. Accelerator Driven System Status in the world. 5

1.1. Emissions of ^{232}Th, from DDEP. 19
1.2. Direct and Indirect Ionising radiations 29
1.3. Category of neutrons per velocity and temperature 34
1.4. Main reaction (α, n) available with ^{210}Po (E_α=5.304 MeV) 41

2.1. Properties of semi-conductors materials for γ-ray detectors 60
2.2. Characteristics of different gamma spectrometers 61
2.3. Composition of SS316LN 71
2.4. Composition of polluted Copper, of 8.96 g·cm^{-3} density 72
2.5. Energy threshold and photonuclear cross section for stable isotopes of copper and tungsten 74
2.6. Radionuclides activation products of linear medical accelerator of 25 MeV 75
2.7. Measured activities in the 18 MeV LINAC flattening filter 77
2.8. Comparison of expected yield in the irradiated samples 83
2.9. Characteristics of CYRCé beam for the three targets 84

3.1. Comparison of Bateman solving algorithm. 101
3.2. `RTYP` translation table. 107
3.4. `STYP` translation table. 107
3.6. Correspondance table between `TMX_Bateman`, `FISPACT-II` and `DCHAIN-PHITS`. 118
3.7. Comparison of emission rate of `FISPACT-II` and `DCHAIN-PHITS` with respect to `TMX_Bateman`. 120

4.1. Listing of main files available in ENDF6 format. 136
4.2. Synthesis of number of nuclides for neutron, proton and alpha incident cross-sections of main ENDF6 sub-libraries. 139
4.3. Scoring the available experimental data for neutron capture of several materials 143
4.4. Averaged weighted ratio of cross-sections available over the full energy range, with ENDF/B as reference 145
4.5. Averaged weighted ratio of cross-sections available over the full energy range, with EXFOR as reference 145
4.6. Comparison of expected activity inside the samples considering materials, using PHITS, with ENDF/B library as reference 146

4.7. Comparison of expected activity inside the samples considering materials, using PHITS, with experimental measurements as reference. *In blue, the best of four* 147

5.1. Livechart API summary with cut-off from May 2025. 152
5.2. List of ENDF6 Decay Databases with MF=8, MT=457. 155
5.3. Summary of NUBASE channels. 156
5.4. BrIcc default mixing ratio, when no mixing ratio is given 160
5.5. NUBASE decay mode translation matrix. 164
5.6. Summary of conversion criteria. Actions ordered by the priority of application.. 165
5.7. Delayed decay channels with non-null branching in GENF/D. 173
5.8. Convention for average energy estimation from Q-value, with $\langle E_{LP} \rangle$ the light particle decay heat, $\langle E_{EM} \rangle$ the electromagnetic decay heat and $\langle E_{HP} \rangle$ the heavy particle decay heat 175
5.9. Comparison of GENF/D against JENDL-5, ENDF/B-VIII.0 and JEFF-3.3 over the main observables available. The proportion, expressed in percent, of common nuclides, which have relative difference below 10% are presented. Only nuclides in their ground states and with half-lives greater than one second are considered 177
5.10. Average energy, in MeV, of gamma $\langle E_\gamma \rangle$, neutron $\langle E_n \rangle$, fission fragments $\langle E_{FF} \rangle$ as well as available energy Q_{SF}, and neutron-multiplicity $\langle xn \rangle$ for the spontaneous fission of ^{238}U and ^{232}Th 178

A.1. List of supported reactions. 196
A.2. List of supported decays. 197

C.1. Average and median half-lives of isotopes with ambiguous half-lives, with respect to NUBASE. 210
C.2. Average and median half-lives of isotopes with ambiguous half-lives, with respect to JENDL. 211
C.3. Comprehensive list of isotopes with mean-lives discrepancies higher than 100 % (w.r.t. NUBASE), but half-lives greater than 1 s. 212
C.4. Comprehensive list of isotopes with mean-lives discrepancies higher than 100 % (w.r.t. NUBASE), but half-lives greater than 1 s and present in ADS libraries. 213

List of Listings

3.1. Simple input file for `TMX_Bateman` 105

5.1. Excerpt of Cr-51 beta decay spectrum 154
5.2. Excerpt of NUBASE2020 162

A.1. Complete input file for `TMX_Bateman` 193
A.2. Irradiation section of input file for `TMX_Bateman` 193
A.3. Yield section of input file for `TMX_Bateman` 194
A.4. Secondary spectra section of input file for `TMX_Bateman` 194
A.5. Polynomial efficiency functions for `TMX_Bateman` 194
A.6. Threshold section of input file for `TMX_Bateman` 195
A.7. UOx fuel input example for `TMX_Bateman` 195

Chapter

Introduction

J'adore l'eau ... dans 20/30 ans, il n'y en aura plus.

(Jean-Claude Van damme*)*

Since the pioneering work of G. Ising in 1924 [1][1] and the cyclotron patent of E. Lawrence in 1934 [2][2], particle accelerators have become a cornerstone of modern science. This breakthrough enabled major discoveries and the consequent development of a diverse family of accelerators (from LINear ACcelerator (LINAC) to synchrotron). Over the decades, their use has expanded far beyond fundamental research into critical fields such as medicine (radiotherapy, medical isotope production), industry (material processing, sterilization), environmental science (pollutant analysis), and even art (dating and restoration of heritage works [3][3]).

This evolution has led to a vast and growing fleet of accelerators around the world. The European Coordination for Accelerator Research and Development (EuCARD)-2 report estimates that there are over 30 000 accelerators in operation today in the world, with only about 1% used for "pure" research [4][4]. The expansion of clinical facilities, as shown in Figure 1, and the broad energy range of cyclotrons in use (Figure 2), are an illustration of the dynamic growth of the world fleet. This expanding fleet introduces a pressing end-of-life consideration: the systematic decommissioning and radioactive waste management of these facilities.

A few words on Accelerator Driven Systems

This landscape is expected for a significant evolution with the emergence of Accelerator Driven System (ADS), an advanced nuclear technology designed to address the dual challenges of energy production and long-lived radioactive waste management.

An ADS comprises three key components: a high-power particle accelerator, a spallation target, and a subcritical nuclear reactor, such design gained momentum after

[1] G Ising. 'Prinzip einer Methode zur Herstellung von Kanalstrahlen hoher Voltzahl'. In: *Ark. Mat. Astron. Fys.* 18.30 (1924), pp. 1–4.

[2] Ernest O. Lawrence. 'Method and apparatus for the acceleration of ions'. US1948384A. Feb. 1934.

[3] M. Menu et al. 'The dedicated accelerator-based IBA facility AGLAE at the Louvre'. In: *Nuclear Instruments and Methods in Physics Research Section B: Beam Interactions with Materials and Atoms* 45.1 (Jan. 1990), pp. 610–614. ISSN: 0168-583X. DOI: 10.1016/0168-583X(90)90910-M.

[4] The EuCARD-2 Collaboration. *Applications of Particle Accelerators in Europe*. en. 2020. DOI: 10.17181/CERN.HA4I.UT3N.

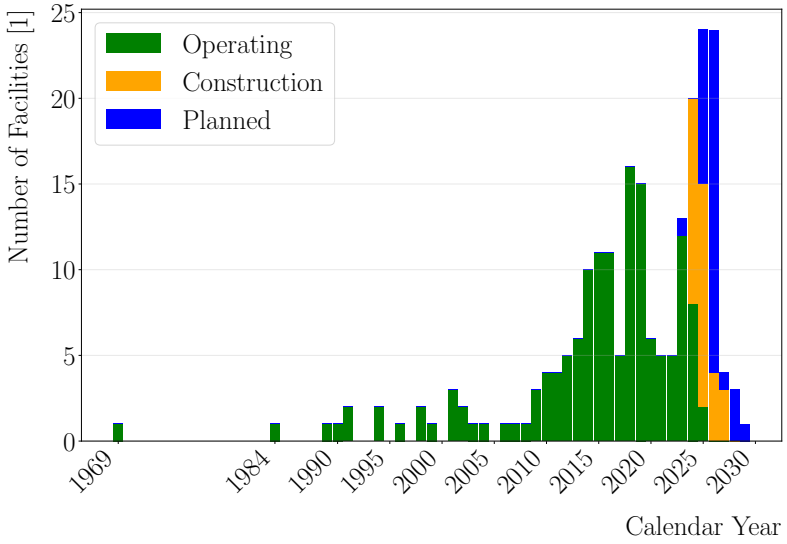

Figure 1.: Number of particle therapy centers in operation, under construction and in planning stage, according to Particle Therapy Co-Operative Group (PTCOG) data (April 2025 dataset).

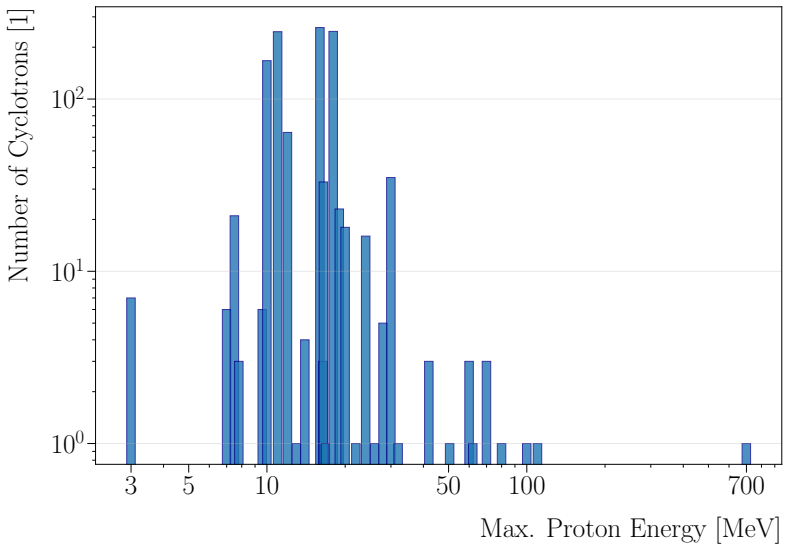

Figure 2.: Range of beam maximum energies of cyclotrons listed by Radioisotope Products and Radiation Technology Section, Division of Physical and Chemical Sciences, IAEA (2024 dataset).

the proposal of Carlo Rubbia in 1995 [5][1]. The system operates by directing a high-intensity proton beam (typically in the mA range) from the accelerator onto a heavy metal spallation target (e.g., Lead-Bismuth Eutectic (LBE)).

The reactor core is maintained in a subcritical state (i.e. an effective neutron multiplication factor $k_{eff} < 1$), meaning it cannot sustain a chain reaction on its own. It relies entirely on the external neutron source provided by the accelerator (and its spallation target), inherently enhancing operational safety: as the fission process terminates immediately if the accelerator beam is stopped [6][2].

The primary motivation for ADS development is to implement the Partitioning and Transmutation (P&T) strategy for nuclear waste. This strategy, illustrated in Figure 3, involves:

- *Partitioning*: the chemical separation of long-lived radioactive isotopes, particularly minor actinides like Neptunium, Americium, or Curium, from spent nuclear fuel.
- *Transmutation*: the subsequent irradiation of these separated actinides in the ADS reactor. The intense neutron flux converts them into shorter-lived or stable isotopes through fission.

The result is a dramatic reduction in the radiotoxicity and required isolation time of the final waste, from hundreds of thousands of years to a more manageable scale of several centuries, with reduced volumes, thereby alleviating the burden on deep geological storage facilities [7, 8][3].

As summarized in Table 1, there are numerous ADS project started worldwide. The Genevan company Transmutex also proposes its own design, with its prototype called Subcritical Transmutation Accelerated Reactor Technology (START). This reactor would allow the transmutation of current and future nuclear waste by using Thorium based nuclear fuel while safely producing decarbonised energy. Transmutex aims at building a pre-industrial prototype by 2032.

While most designs, like Multi-purpose hYbrid Research Reactor for High-tech Applications (MYRRHA) and Japanese Atomic Energy Agency - ADS (JAEA-ADS), utilize superconducting LINACs, some proposals, such as Sungkyunkwan University - ADS (SKKU-ADS) and TRANSMUTEX-START, explore high-power cyclotrons.

However, while ADS offer a transformative solution to one nuclear waste problem, they themselves represent a new, complex class of high-power accelerator facility that will

[1] Carlo Rubbia et al. *Conceptual design of a fast neutron operated high power energy amplifier*. Tech. rep. Geneva: CERN, 1995.

[2] Bruce Yee-Rendón. 'Overview of ADS Projects in the World'. en. In: *Proceedings of the 31st International Linear Accelerator Conference* LINAC2022 (2022). Ed. by McIntosh Peter (Ed.) et al. Artwork Size: 4 pages, 2.664 MB ISBN: 9783954502158 Medium: PDF, 4 pages, 2.664 MB. ISSN: 2226-0366. DOI: 10.18429/JACOW-LINAC2022-TU2AA01.

[3] Xunchao Zhang et al. 'Strategies of eliminating nuclear waste using accelerator-driven system in the transition stage for sustainable and clean nuclear energy in China'. In: *Annals of Nuclear Energy* 185 (June 2023), p. 109713. ISSN: 0306-4549. DOI: 10.1016/j.anucene.2023.109713, Ogugua P. Unokiwedi et al. 'Deep geological repositories — A review of design concepts, near-field evolution, and their implications for nuclear waste containment'. In: *Journal of Environmental Radioactivity* 289 (Oct. 2025), p. 107750. ISSN: 0265-931X. DOI: 10.1016/j.jenvrad.2025.107750.

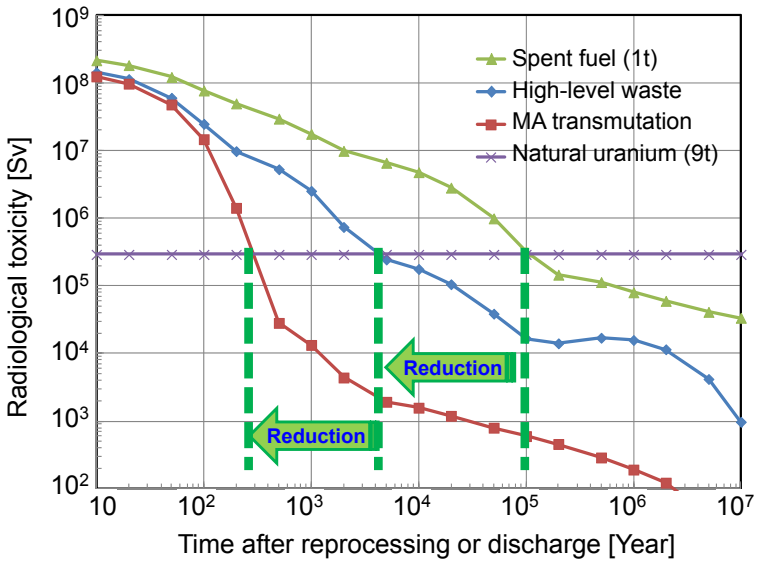

Figure 3.: Radiotoxicity reduction from partitioning and transmutation strategy [9][a]

[a]H. Oigawa. 'JAEA's R&D Activities on Transmutation Technology for Long-lived Nuclear Wastes'. In: *ImPACT International Symposium on New Horizons of Partitioning and Transmutation Technologies with Accelerator System*. Tokyo, Japan, Dec. 2018.

eventually require decommissioning. The high-energy and high-intensity beams involved are expected to generate significant activation products in components like beam dumps, shielding, and magnets —far exceeding the activation levels typically encountered in clinical or industrial accelerators. This makes advanced radiological characterization and decommissioning planning a critical requirement for the sustainability of these projects.

The Decommissioning Challenge: From Characterization to Waste Management

The operation of particle accelerators, above specific energy thresholds, induces radioactivity in their materials and components through nuclear reactions. The activation levels in most medical and industrial accelerators are historically considered low, this relative perception has led to the decommissioning of accelerator facilities being a secondary concern. This was entertained by the fact that the widespread application of these machines is relatively recent, with many early installations managed by research institutes that developed unique, one-off designs, hindering the establishment of standardized decommissioning protocols.

However, given the vast size of the current global fleet, the dismantling of these facilities is now an urgent and growing challenge. This urgency is driven by operators, waste management entities (like Agence Nationale des Dechets Radioactifs (ANDRA) in France), and safety authorities, all faced with a wave of installations reaching their end-

Table 1.: Accelerator Driven System Status in the world [6][1].

Accelerator	Country	Type	Purpose	Status (in 2022)
CiADS	China	2.5 (10)-MW SRF proton LINAC	ADS demo	Commissioning
MYRRHA	Belgium	2.4-MW SRF proton LINAC	ADS demo	Construction
JAEA-ADS	Japan	30-MW SRF proton LINAC	Transmutation of nuclear waste	Design
SKKU-ADS	Korea	5-MW SRF proton cyclotron	ADS Th based nuclear reactor	Design
IFSR	India	1-MW SRF proton LINAC	Energy production	Design
ADS-Troitsk	Russia	0.75 MW proton LINAC	ADS demo	Design
Mu*STAR	USA	2.5-MW proton LINAC	Transmutation of nuclear waste	Design
CYCLADS	EU	5 (10)-MW proton cyclotron	Transmutation of nuclear waste	Design
KIPT	Ukraine	0.1-MW electron LINAC	ADS demo	Scientific Program under development

of-life. The challenge is further amplified by the development of high-power accelerators, such as ADS, where activation levels are expected to be significantly higher.

Recognizing this, the International Atomic Energy Agency (IAEA) recommends establishing decommissioning plans before the commissioning of any new facility [10][2], raising the standard of particle accelerator facility towards the one of nuclear installations. A critical first step, and the central challenge this thesis addresses, is the radiological characterization: the accurate prediction and measurement of the inventory of radionuclides produced during operation. The IAEA emphasizes a "graded approach", where the complexity of planning is directly tied to the accelerator's class, energy, and particle type.

The primary waste from accelerator decommissioning is activated solid material (e.g., magnets, shielding concrete, beam dumps, collimators, cables), with contamination being rare but important to consider. A typical example is the concrete activation, where contaminant induce the presence of Europium [11][3]. Follows a non-exhaustive list of isotopes from most activated materials found around particle accelerator: ^{3}H, ^{7}Be, ^{11}C, ^{22}Na, ^{24}Na, ^{32}P, ^{42}K, ^{45}Ca, ^{44}Sc, ^{44m}Sc, ^{46}Sc, ^{47}Sc, ^{48}Sc, ^{48}V, ^{51}Cr, ^{52}Mn, ^{52m}Mn, ^{54}Mn, ^{55}Fe, ^{56}Mn, ^{57}Co, ^{57}Ni, ^{58}Co , ^{59}Fe, ^{60}Co, ^{61}Cu, ^{63}Ni, ^{63}Zn, ^{64}Cu, ^{65}Ni, ^{65}Zn, ^{152}Eu, ...

The key principles for managing this waste are:

– Waste Minimization: achieved through intelligent design choices (e.g., material

[2]International Atomic Energy Agency. *Decommissioning of Particle Accelerators*. en. Text. International Atomic Energy Agency, 2020, pp. 1–160.

[3]P. Carbonez et al. 'Residual radioactivity at the CERN 600MeV synchro-cyclotron'. en. In: *Nuclear Instruments and Methods in Physics Research Section A: Accelerators, Spectrometers, Detectors and Associated Equipment* 694 (Dec. 2012), pp. 234–245. ISSN: 01689002. DOI: 10.1016/j.nima.2012.08.011.

selection, modular shielding) and operational practices that minimize beam loss.
- Clearance and Recycling: a significant fraction of material may qualify for clearance from regulatory control, allowing for recycling or conventional disposal. However, the absence of clear clearance provisions in some countries complicates this process.
- Accurate Characterization: essential for determining the appropriate disposal pathway, but is notoriously challenging due to the complex mix of radionuclides produced.

The core of the characterization problem lies in the limitations of current measurement methods. Generally, standard practice during dismantling relies on simple on-site controls, sensitive only to gamma radiation. This method fails completely if the dominant radionuclides are *pure beta-emitters* (e.g., ^{3}H, ^{32}P, ^{63}Ni, i.e. nuclides emitting only β without γ relaxation), leading to a severe underestimation of the total activity and potentially misclassifying waste.

Therefore, computational modelling, particularly with Monte Carlo codes (e.g., Monte Carlo N-Particle (MCNP), FLUKA, Geant4) coupled with activation solvers (e.g., `FISPACT-II`), is identified as indispensable for pre-emptive characterization [10][1]. This is especially true for new facilities where no experimental data exists. These tools are the only method capable of providing a complete picture of the radiological vector, including hard-to-detect pure beta-emitters, thus forming a reliable basis for planning waste streams, estimating costs, and ensuring worker safety.

Ultimately, the decommissioning of particle accelerators is a manageable process if planned and executed systematically from the earliest design phases. Success relies on early and continuous planning, a robust radiological characterization strategy that integrates advanced modelling, and the application of a graded regulatory approach proportional to the hazards.

This work aims is to contribute to solving this challenge by developing an approach, and tools, to improve the accuracy of these predictive simulations.

A strategy to tackle this decommissioning challenge

This thesis is part of a collaboration between CNRS/University of Strasbourg and the start-up TRANSMUTEX SA.

It proposes a methodology to tackle the predictive decommissioning planning. This work organizes itself around the roadmap depicted in Figure 4.

While Monte Carlo codes coupled with activation solvers are recognized as essential tools, their predictions can vary significantly. This work propose comparison between such codes, to familiarise better with the challenges of modelling.

This variance stems not only from differences in their physical models, but also the underlying nuclear data libraries they rely upon.

[1] International Atomic Energy Agency. *Decommissioning of Particle Accelerators*. en. Text. International Atomic Energy Agency, 2020, pp. 1–160.

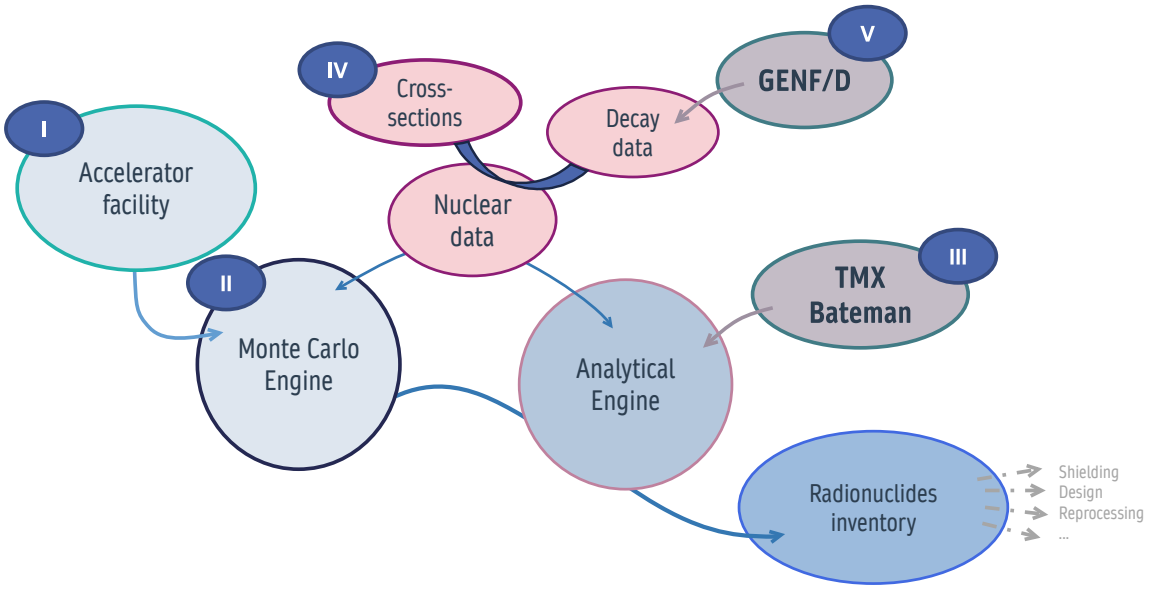

Figure 4.: Roadmap for the decommissioning of a particle accelerator in the light of a PhD.

Nuclear data are fundamental for many applications. Evaluations have been performed on nuclear properties, in order to provide the ability to accurately model the interactions between particles, especially low energy neutrons, and integrates properties of the atomic nuclei, beyond unique models. These databases enable the modelling, design, and optimization of complex systems.

The most commonly used evaluated databases are Evaluated Nuclear Data File B (ENDF/B), Joint Evaluated Fission and Fusion File (JEFF), Japansese Evaluated Nuclear Data Library (JENDL), Chinese Evaluated Nuclear Data Library (TENDL) or Talys Evaluated Nuclear Data Library (TENDL). They provides cross-sections data (from neutrons to alphas), but also decay data and fission data.

This work proposes a comparison of such databases, as they can have a significant impact on particle accelerator facilities. It presents a framework for simulating and analysing radiological inventories at particle accelerators. The framework uses advanced computational tools and enriched nuclear data to inform decommissioning strategies. The manuscript is organised into five interdependent chapters.

Chapter 1 lays the theoretical groundwork essential for understanding the behaviour of ionizing radiation and its interaction with matter. It presents a classification of radionuclides, details the mechanisms of photon and neutron interactions, and introduces the physical principles governing radiation transport. These foundational elements un-

derpin the computational models and experimental protocols developed in the subsequent chapters.

Chapter 2 is devoted to the study of activation phenomena. It describes a series of experimental measurements and Monte Carlo simulation employed to evaluate induced radioactivity in various contexts, including the vicinity of an AmBe neutron source, the activated components of a dismantled medical accelerator, and areas surrounding a cyclotron. The chapter will highlight the intricate nature of activation processes and will underscore the necessity of precise modelling for ensuring operational safety and guiding decommissioning strategies.

Chapter 3 introduces `TMX_Bateman`, a proprietary solver for Bateman equations, designed to simulate the temporal evolution of radionuclide decay chains. The solver is benchmarked against established computational tools such as `FISPACT-II` and `DCHAIN-PHITS`, with comparative analyses demonstrating its accuracy, robustness, and computational efficiency across a range of representative scenarios.

Chapter 4 addresses the critical issue of nuclear data selection by proposing a systematic strategy for choosing evaluated cross sections. This methodology is supported by the development of a python tool, which facilitates the exploration, comparison, and validation of nuclear data libraries. The chapter examines the influence of cross-section selection on simulation fidelity and offers a structured approach to compiling datasets tailored to specific applications.

Chapter 5 presents Global Evaluated Nuclear File, Decay Data (GENF/D), a comprehensive and internally consistent database of compiled evaluated nuclear decay data, which has been generated during this PhD. It details the compilation methodology, validation procedures, and performance benchmarking relative to other reference libraries. The chapter emphasizes the database's relevance for decay heat calculations and radioactive waste characterization, positioning GENF/D as a valuable resource for both research and operational decision-making.

Chapter

1. General Considerations

Les calculs sont pas bons, Kevin !
C'est quand que tu vas mettre des paillettes dans ma vie, Kévin !

(Ines Reg*)*

1.1. Nuclear taxonomy . . . 9
1.2. Radionuclides . . . 12
1.2.1. Stability valley . . . 13
1.2.2. Radioactive decay . . . 14
1.2.3. Activity and radioactive filiation . . . 21
1.3. Characterisation of Ionising radiations . . . 27
1.3.1. Charged particles: Stopping Power . . . 28
1.3.2. Neutrons and Photons: Absorption law . . . 28
1.4. Photon-matter interaction . . . 31
1.4.1. Photoelectric effect . . . 31
1.4.2. Compton effect . . . 32
1.4.3. Pair production . . . 33
1.5. Neutrons-matter interaction . . . 33
1.5.1. Classification . . . 34
1.5.2. Scattering . . . 36
1.5.3. Capture . . . 37
1.5.4. Resonance . . . 38
1.5.5. Sources of neutrons . . . 41
1.6. Conclusion . . . 42

1.1. Nuclear taxonomy

Atoms are constituted from nucleus, composed of protons and neutrons, and of a cloud of electrons, organised in shells.

The number of protons (Z) and the number of neutrons (N) or their total number of nucleus ($A = Z + N$) pertain different behaviour. Nuclides can be classified as isobars, same mass number (^{40}K and ^{40}Ca), or isotones, same number of neutrons (^{11}B and ^{12}C), or when mentioning a single element, isotopes (^{12}C and ^{14}C).

The Figure 1.1 presents the known nuclides. From the 3821 isotopes and isomers on

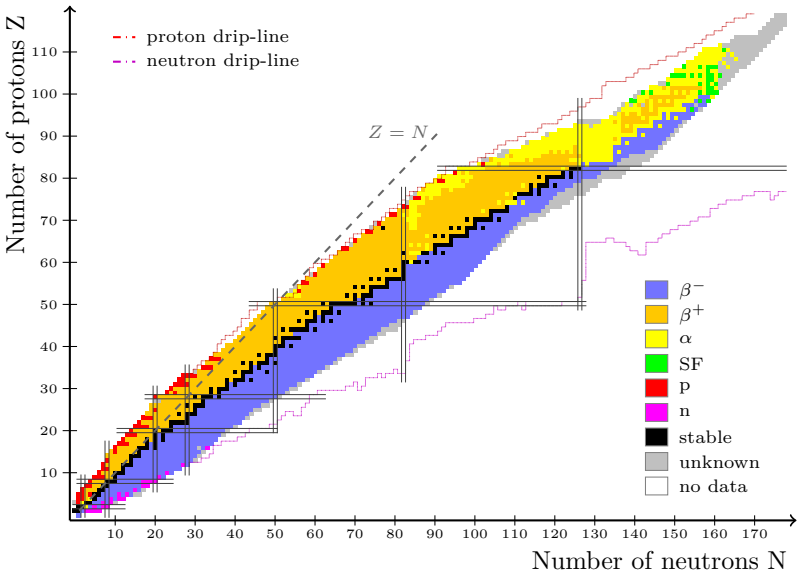

Figure 1.1.: ENDF/B-VIII.0 distribution of stable nuclides and radionuclides as function of atomic number and number of neutrons, adapted from JANIS [12][a]

[a] N. Soppera, M. Bossant, and E. Dupont. 'JANIS 4: An Improved Version of the NEA Java-based Nuclear Data Information System'. In: *Nuclear Data Sheets* 120 (June 2014), pp. 294–296. ISSN: 0090-3752. DOI: 10.1016/j.nds.2014.07.071.

this chart, 289 occur in nature, the other can only be obtained artificially.

This nuclides have intrinsic structures, both in their nucleus and their atom cloud.

Electron orbitals Due to electron vacancies rules, the atom structure is well defined and discrete. The constituent electrons of the electron cloud can be seen as distributed, by energy, into shells. Each shell is characterized by a particular binding energy, and a maximum capacity.

There are several shell convention labelling, but one the most usual one is the SIEGBAHN notation, as represented in Figure 1.2. The shell are associated with specific binding energy (the closer it is from the nucleus the higher it is), with the first three shell named K, L and M. Within this excitation levels, sublevels are present that are identified with a sub-name as α, β and so on.

This configuration has been historically used, to identify atoms. Indeed, when exciting an atom, and its electrons, with the electrons transition back to lower levels, they will emit characteristics photon rays, called X-rays.

Level schemes The nucleus follows similar quantum rules, creating discrete structure inside the nucleus. Nucleus will excite in well defined levels. This regular structure can be described, notably by the shell model, which represents the nucleons in a similar manner to the electron orbitals. This model is based on the determination of a nuclear

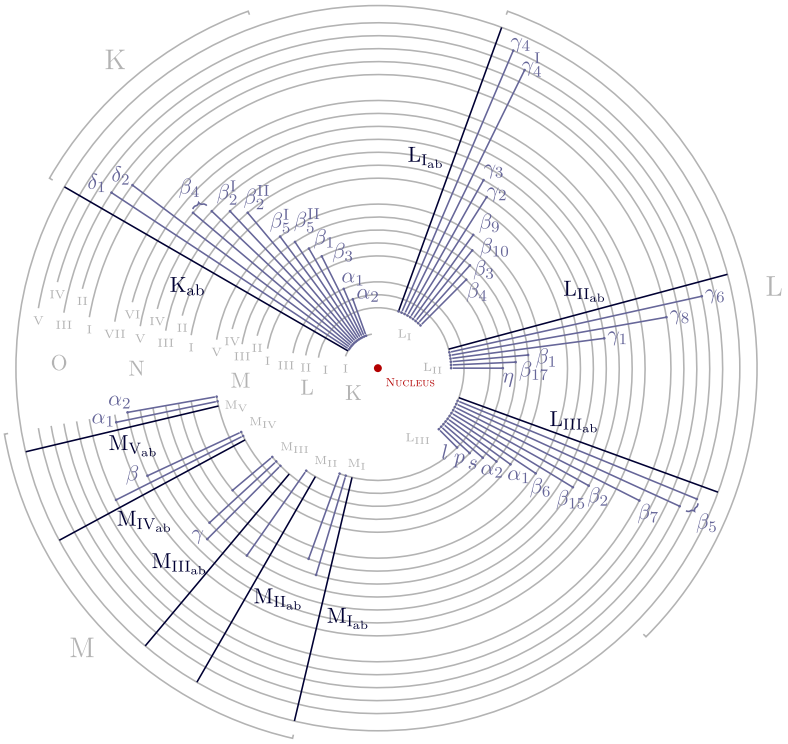

Figure 1.2.: Atomic model, with Siegbahn representation of electron shells [13][a]

[a]Rolf Woldseth. *X-ray energy spectrometry*. en. First. Kevex Corporation, 1973.

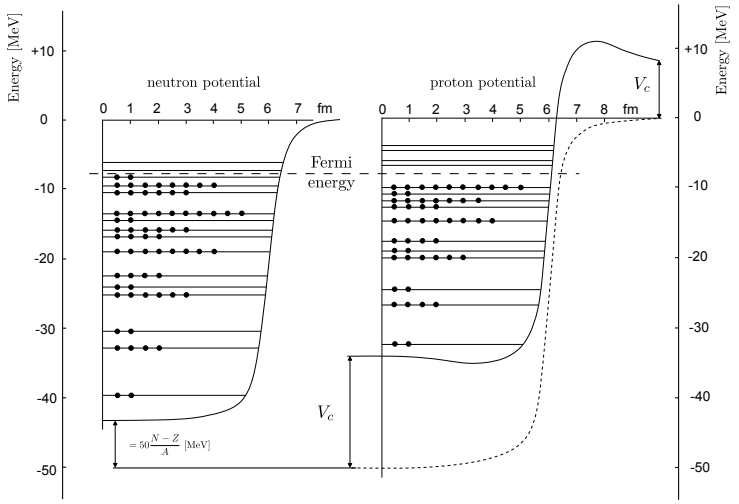

Figure 1.3.: Neutron and proton shell structure in the potential wells, extracted from [14][a]

[a]Walter D. Loveland, David J. Morrissey, and Glenn T. Seaborg. 'Nuclear Structure'. en. In: *Modern Nuclear Chemistry*. John Wiley & Sons, Ltd, 2017, pp. 125–165. ISBN: 978-1-119-34845-0. DOI: 10.1002/9781119348450.ch6.

potential, a representation is shown in Figure 1.3.

When the level can be sustained in a measurable time, we classify them as isomeric states, and simply number them or identify the isomers with an additional letter. For example the first isomeric state of ^{99}Tc is named as ^{99m}Tc, for which the level scheme in given as an example in Figure 1.4. This identification varies, some use in order of energy m, n, p, q, r and x, other will prefer $m1$, $m2$, ... The former classification will be prefered from now on.

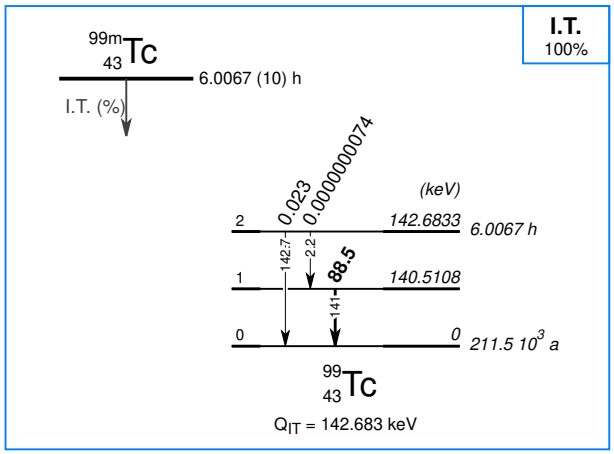

Figure 1.4.: Level scheme of ^{99m}Tc, extracted from [15][a]

[a] Laboratoire National Henri Becquerel. *Nucléide – Lara Application – Laboratoire National Henri Becquerel*. en-GB.

1.2. Radionuclides

Henri Becquerel is credited with the discovery that certain elements spontaneously emit energy through radiation. In 1896, he found that uranium salts could induce the blackening of a photographic plate wrapped in protective paper, without the necessity of prior exposure to light. This pivotal observation demonstrated that Uranium emitted a penetrating, invisible radiation, distinct from the phosphorescence he had initially set out to study.

Marie Curie subsequently characterised and named this phenomenon. It was Curie who first introduced the term ”radioactivity” to describe the spontaneous emission of such rays, which she also observed in Thorium. This finding extended the concept of what were initially termed ”uranic rays” beyond a single element, establishing radioactivity as a property exhibited by other nuclides.

Radioactivity is the ability of certain nuclei to transform, or decay, spontaneously into different nuclei. This process releases energy through the emission of secondary particles, primarily Helium nuclei (α particles), electrons or positrons (β particles), and are often associated with electromagnetic waves (e.g. γ rays).

1.2.1. Stability valley

Nuclei can be categorised into two classes: stable nuclei, which possess infinite (or near-infinite) lifetimes; and unstable nuclei, with lifetimes ranging from yoctoseconds to billions of years.

There are 254 known stable nuclides. This figure includes 69 isotopes that are theoretically unstable according to energy considerations but have not been observed to decay [16][1]. As energy tends to be minimal, stable nuclides typically reside at the minimum of a potential well, which can be defined by the mass excess (the difference between a nucleus's actual mass and its mass number). This configuration gives rise to the concept of the "valley of stability", as illustrated in Figure 1.5.

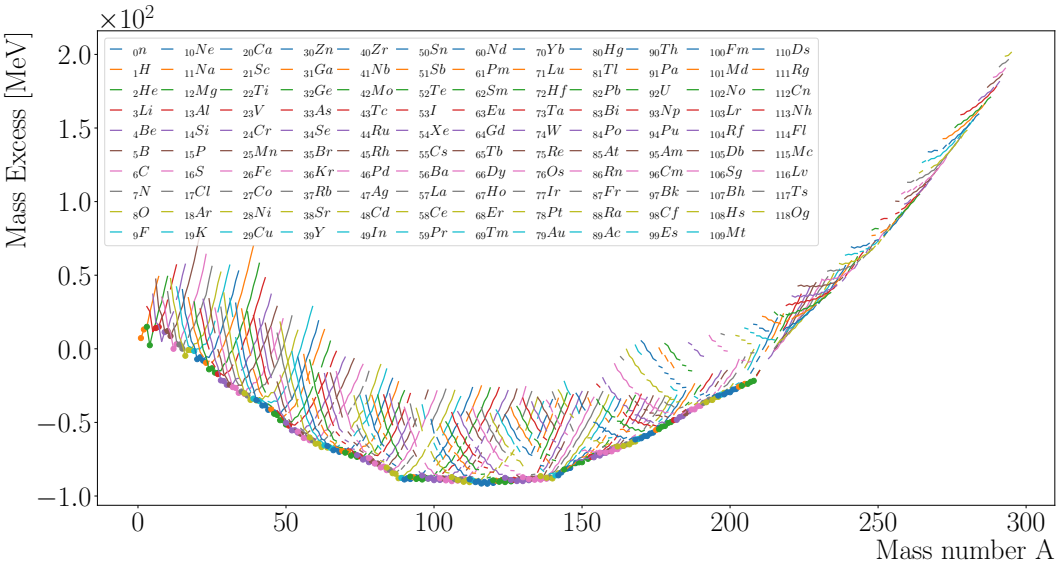

Figure 1.5.: Mass excess as a function of mass number, based on AME2020 [17][a]. Stable elements are identified with bullet markers

[a] W.J. Huang et al. 'The AME 2020 atomic mass evaluation (I). Evaluation of input data, and adjustment procedures*'. en. In: *Chinese Physics C* 45.3 (Mar. 2021), p. 030002. ISSN: 1674-1137, 2058-6132. DOI: 10.1088/1674-1137/abddb0.

Atoms with unstable nuclei are called radioactive, and are referred as radionuclides or radioisotopes. Such species can occur naturally, or be produced artificially through processes such as capture, fission or fusion [18][2].

Not every arbitrary combination of protons and neutrons results in a stable nuclide;

[1] F.G. Kondev et al. 'The NUBASE2020 evaluation of nuclear physics properties *'. en. In: *Chinese Physics C* 45.3 (Mar. 2021), p. 030001. ISSN: 1674-1137, 2058-6132. DOI: 10.1088/1674-1137/abddae.

[2] H. M. Devaraja et al. 'Systematic studies to produce heavy above-target nuclides in multinucleon transfer reactions'. In: *Physics Letters B* 862 (Mar. 2025), p. 139353. ISSN: 0370-2693. DOI: 10.1016/j.physletb.2025.139353.

furthermore, beyond certain limits, a bound nucleus cannot form at all. These limits are defined by the proton and neutron driplines, which correspond to the points where the separation energy for an additional proton or neutron approaches zero.

The precise locations of these driplines, particularly for heavier elements, remain uncertain. Experimentally, the neutron dripline has only been determined with confidence up to Sodium (Z=11) [19][1].

1.2.2. Radioactive decay

The primary modes of radioactive decay are α, β^-, and β^+ decay. These processes are frequently accompanied by the emission of one or several γ-ray photons, which result from the relaxation of the daughter nucleus from an excited state to a lower-energy state. For higher excitation energies and for more proton-rich or neutron-rich isotopes, this de-excitation can also occur through the emission of protons or neutrons, respectively.

Collectively, these decay mechanisms enable an unstable nucleus to transition towards the valley of stability depicted in Figure 1.5.

The existence of a potential decay path can be ascertained by applying the law of energy conservation. The energy available for a decay, denoted as the Q-value, is calculated as the difference between the initial mass-energy of the parent nucleus and the final mass-energy of all decay products:

$$Q = E(X_i) - \sum_f E(Y_f) \tag{1.1}$$

$$= M_{atm}(X_i)c^2 + E^*(X_i) - \sum_f \Big(M_{atm}(Y_f)c^2 + E^*(Y_f)\Big) \tag{1.2}$$

where E^* is the excitation energy, X_i the parent nuclide, Y_f the daughter products, and M_{atm} is the atomic mass.

The atomic mass is defined to include the mass of nucleus (M_{nucl}) as well as the mass of the electrons and their binding energies:

$$M_{atm}({}^A_Z X) = M_{nucl}({}^A_Z X) + Z \times m_e - B_e(Z)/c^2 \tag{1.3}$$

where A is the atomic mass number and Z the atomic number. An empirical formula for the total electron binding energy $B_e(Z)$ in electronvolts is given by [17][2]:

$$B_e(Z) = 14.4381 \times Z^{2.39} + 1.55468 \times 10^{-8} \times Z^{5.35} \tag{1.4}$$

The following subsections will detail the specific characteristics of each decay mode.

[1] H. L. Crawford et al. 'Crossing $N=28$ Toward the Neutron Drip Line: First Measurement of Half-Lives at FRIB'. in: *Physical Review Letters* 129.21 (Nov. 2022), p. 212501. DOI: 10.1103/PhysRevLett.129.212501.

[2] W.J. Huang et al. 'The AME 2020 atomic mass evaluation (I). Evaluation of input data, and adjustment procedures*'. en. In: *Chinese Physics C* 45.3 (Mar. 2021), p. 030002. ISSN: 1674-1137, 2058-6132. DOI: 10.1088/1674-1137/abddb0.

a) β^- decay

This decay is a results of weak interaction, from which neutrons are transformed into protons.

$$ {}^{A}_{Z}X \longrightarrow {}^{A}_{Z+1}Y + {}^{0}_{-1}e^- + {}^{0}_{0}\bar{\nu}_e \tag{1.5} $$

The conservation of nuclear mass-energy during this process gives:

$$ Q_{\beta^-} = M_{nucl}({}^{A}_{Z}X)c^2 - M_{nucl}({}^{A}_{Z+1}Y)c^2 - m_e c^2 - m_{\bar{\nu}_e}c^2 \tag{1.6} $$

Within the standard model, the neutrino mass is negligible[1] (68 % CL) [20][2], and hence can be safely ignored. When the atomic masses are used (electron accounted for), the available energy can be rewritten as:

$$ Q_{\beta^-} = M_{atom}({}^{A}_{Z}X)c^2 - M_{atom}({}^{A}_{Z+1}Y)c^2 - m_{\bar{\nu}_e}c^2 \tag{1.7} $$

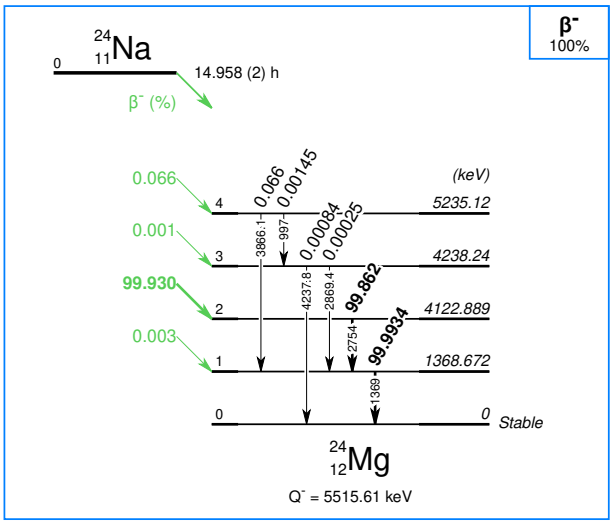

Figure 1.6.: Level scheme of ^{24}Na, extracted from [15][a]

[a] Laboratoire National Henri Becquerel. *Nucléide – Lara Application – Laboratoire National Henri Becquerel*. en-GB.

If we take the example of ^{24}Na, the available energy for this reaction is of 293.4 keV for ground state to ground state. But as depicted in Figure 1.6, and it will have a small chance to also emit a photon.

[1] The electron neutrino mass is below $460\,\mathrm{eV}\cdot\mathrm{c}^{-2}$

[2] S. Navas et al. 'Review of Particle Physics'. In: *Phys. Rev. D* 110.3 (Aug. 2024), p. 030001. DOI: 10.1103/PhysRevD.110.030001.

b) β^+ decay and electron-capture

A similar decay for proton rich atoms happens, where protons are transformed into neutrons.

$$ {}^{A}_{Z}X \longrightarrow {}^{A}_{Z-1}Y + {}^{0}_{1}e^{+} + {}^{0}_{0}\nu_e \tag{1.8} $$

This reaction is only possible if sufficient energy is available. A "partial" reaction can happen, with electron-capture.

$$ {}^{A}_{Z}X + {}^{0}_{-1}e^{-} \longrightarrow {}^{A}_{Z-1}Y + {}^{0}_{0}\nu_e \tag{1.9} $$

For the β^+ emission, the available energy is given by:

$$ Q_{\beta^+} = M_{nucl}({}^{A}_{Z}X)c^2 - M_{nucl}({}^{A}_{Z-1}Y)c^2 + m_e c^2 - m_{\nu_e}c^2 \tag{1.10} $$

If the atomic masses are used (electron accounted for), the available energy can be rewritten as:

$$ Q_{\beta^+} = M_{atom}({}^{A}_{Z}X)c^2 - M_{atom}({}^{A}_{Z-1}Y)c^2 - 2m_e c^2 - m_{\nu_e}c^2 \tag{1.11} $$

Hence, the mass-energy difference between parents and daughters atoms must be greater than $2m_e c^2 = 1.022\,\text{MeV}$, in order to emit a positron during the conversion of a proton into a neutron. One can assume pure electron capture below this threshold, but above it, both capture and positron emission can happen.

For example, the ^{22}Na does both electron-capture and positron emission, as its available energy is 2.843 MeV, see Figure 1.7. In the case of ^{55}Fe, the Q-value is of 231.12 keV, hence only capture is possible.

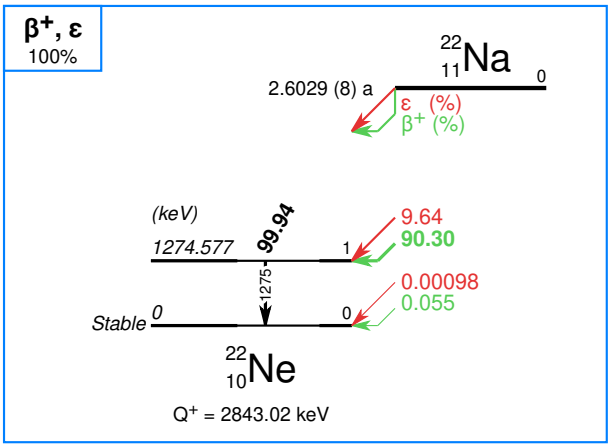

Figure 1.7.: Level scheme of ^{22}Na, extracted from [15][a]

[a] Laboratoire National Henri Becquerel. *Nucléide – Lara Application – Laboratoire National Henri Becquerel.* en-GB.

Auger electron and X-rays The nucleus preferentially captures an electron lying on a so-called core orbit, i.e. an orbit that comes very close to the nucleus. This phenomenon disturbs the strict organization of the electron cloud, which then rearranges itself, to expel, from one orbit to the next, the vacancy thus arising, to the atom's outer reaches. This rearrangement gives rise to the emission of electromagnetic radiation (X-rays), and/or electron emissions, called "Auger electrons".

The energy spectra obtained, for these radiation emissions, are line spectra. The energy values, for such radiation of extra-nuclear origin, are related to the atom's atomic number Z, though they are most generally found to stand lower than 100 keV. The following empirical relation allows an approximate value to be arrived at, for the X-ray emission energy:

$$E(^{A}_{Z}X) = \frac{Z^2}{100} keV \tag{1.12}$$

Annihilation photons In the case of β^+, annihilation of the positron happens with the neighbouring electrons, consequently a pair of photons of 511 keV (mass of electrons) will be emitted.

c) α decay

Nuclides with high atomic number, the starting threshold of Z of 83 is often given, can also emit an alpha ($^{4}_{2}He$), thanks to tunnel effect. Contrary to β-decay, this is a two-body emission:

$$^{A}_{Z}X \rightarrow ^{A-4}_{Z-2}Y + ^{4}_{2}He \tag{1.13}$$

The conservation law gives:

$$Q_\alpha = M_{nucl}(^{A}_{Z}X)c^2 - M_{nucl}(^{A-4}_{Z-2}Y)c^2 - M_{nucl}(^{4}_{2}He)c^2 \tag{1.14}$$

As an example, ^{232}Th follows such a decay, see Figure 1.8.

d) Other decays

As present, in Figure 1.1, there are also isomeric transition (IT), Spontaneous fission (SF), neutron and proton emission.

The $2p$ emission has been observed for 14 isotopes, and $3p$ decay found for ^{41}K [16][1]. The $2n$ decay mode has been accounted for in 6 nuclides, but $3n$ only predicted as of now.

In addition, more seldom cluster decay with emission of Carbon (Z=6), Neon (Z=10), Magnesium (Z=12) or Silicon (Z=14) have been observed.

When considering near-infinite nuclides, the double β^+ decay has been predicted, as is the $2\beta^-$. The latter decay modes has been observed for 10 natural isotopes, which are ^{48}Ca, ^{76}Ge, ^{82}Se, ^{96}Zr, ^{100}Mo, ^{116}Cd, ^{128}Te, ^{130}Te, ^{136}Xe, ^{150}Nd, ^{238}U.

[1] F.G. Kondev et al. 'The NUBASE2020 evaluation of nuclear physics properties *'. en. In: *Chinese Physics C* 45.3 (Mar. 2021), p. 030001. ISSN: 1674-1137, 2058-6132. DOI: 10.1088/1674-1137/abddae.

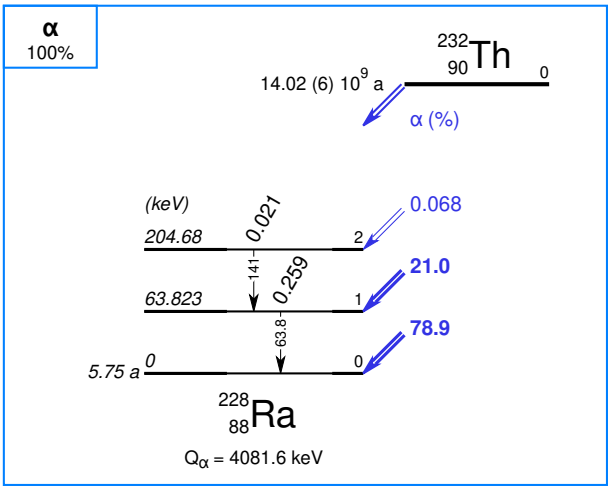

Figure 1.8.: Level scheme of ^{232}Th, extracted from [15][a]

[a] Laboratoire National Henri Becquerel. *Nucléide – Lara Application – Laboratoire National Henri Becquerel*. en-GB.

e) Emission spectra

Emission intensity is defined as the percentage of radiation of a specific type, and energy, that is emitted, over all the decay channels involved. The distribution plotting emission intensity, for a given radiation, as a function of energy, is known as that radiation's "energy spectrum".

Alpha decay As a two body emission, the associated spectrum distribution is discrete. As an example, another representation of the level scheme of Figure 1.8, the decay emissions of ^{232}Th are synthesised Table 1.1. Due to the ionisation from alpha, we expect to have X-rays, and as mentioned decay can go into excited states of the daughter nucleus hence the emission of gammas.

Beta decay As a three body emission, β decay associated spectrum are continuous. To measure them is difficult, as they often interact with the detector material, or the sample itself. As such, destructive measurements are preferred, for example liquid scintillation. Hence spectra are, as such, usually estimated, see Figure 1.10 for an example.

The precise shape of the spectrum curve is heavily dependent on the spin of the parent level and of the daughter nucleus level. Consequently, each gamma transition is associated with a specific continuous spectrum, and the sum will give the total β spectrum expected. From their spins, transition can either be allowed, superallowed, (first, second, ...) forbidden transitions. According to spin rules, such transitions are in competition and some are more favoured.

The maximum energy value is usually the only indication provided by publications measuring out characteristic quantities for radionuclides. As a whole, it may be noted

Table 1.1.: Emissions of ^{232}Th, from DDEP [21][a].

Energy (keV)	Intensity (%)	Type	Origin	Start Level	End Level
14.489 (-)	7.2 (3)	X_L	Ra		
63.811 (10)	0.259 (15)	γ	^{228}Ra	1	0
85.43 (-)	0.0017 (5)	$X_{K_{\alpha_2}}$	Ra		
88.47 (-)	0.0028 (8)	$X_{K_{\alpha_1}}$	Ra		
100.1 (-)	0.00097 (28)	$X_{K_{\beta_1}}$	Ra		
103.3083 (-)	0.00032 (10)	$X_{K_{\beta_2}}$	Ra		
140.88 (1)	0.021 (6)	γ	^{228}Ra	2	1
3810.0 (14)	0.068 (20)	α	^{232}Th	0	2
3948.5 (14)	21.0 (13)	α	^{232}Th	0	1
4011.2 (14)	78.9 (13)	α	^{232}Th	0	0

[a] M.-M. Bé et al. *Table of Radionuclides*. Vol. 1. Monographie BIPM-5. Pavillon de Breteuil, F-92310 Sèvres, France: Bureau International des Poids et Mesures, 2004. ISBN: 92-822-2206-3.

that maximum emission energy values, for $\beta-$radiation yielded by radioactivity, lie in the 10 keV — 3 MeV range.

As a thumb rule, we can estimate that the average energy of β are one third of their maximum energy. Due to the proton repulsion, the average energy of β^+ is higher than the one of β^-. Indeed when comparing, the same transition and normalising the energy per the Q-value, as shown in Figure 1.9, we can see the effect of the nuclei. It should be noted, that with spin effect, and whether the transitions are allowed or forbidden, this statement becomes invalid, see for comparison the β^+ spectra of ^{24}Na in Figure 1.10.

Internal Bremsstrahlung When isotope does β decay, especially with β^- as there average mean path is longer, the displacement of electrons will generate an internal bremsstrahlung (due to the electron-nucleus interaction within the atom). The intensity of such process is inversely proportional to the energy of the electron emitted. This emission is continuous, as an example see the estimated spectrum from ^{24}Na in Figure 1.11

X-ray emission The X-rays emitted correspond to discrete energy transitions, similar to gamma transitions, but related to the electron configuration of the atoms.

Auger electrons In the event of an Auger electron emission, the energy released, as the electron cloud undergoes rearrangement, is transferred to another electron in the cloud, belonging to a less strongly bound shell. The latter, known as an Auger electron, is then ejected with the following energy:

$$E_{Auger} = E_K - E_L - B_e \tag{1.15}$$

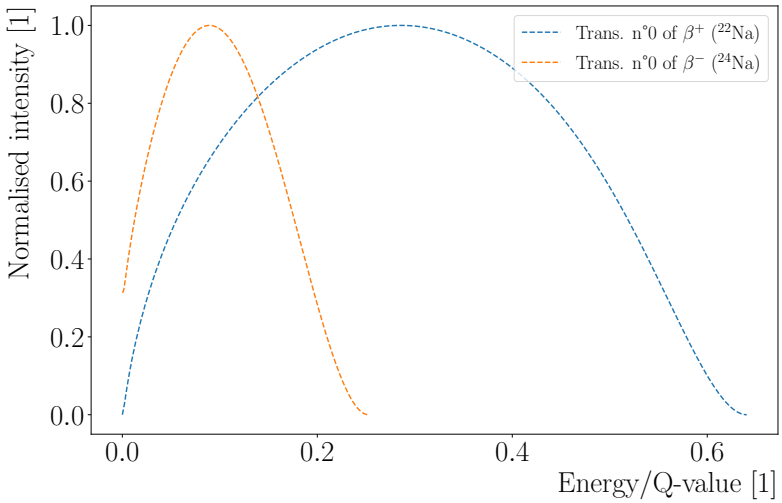

Figure 1.9.: Normalised Ground to Ground Beta Transition of ^{22}Na and ^{24}Na, calculated with BetaShape [22][a]

[a]Xavier Mougeot. 'Atomic exchange correction in forbidden unique beta transitions'. In: *Applied Radiation and Isotopes* 201 (Nov. 2023), p. 111018. ISSN: 0969-8043. DOI: 10.1016/j.apradiso.2023.111018.

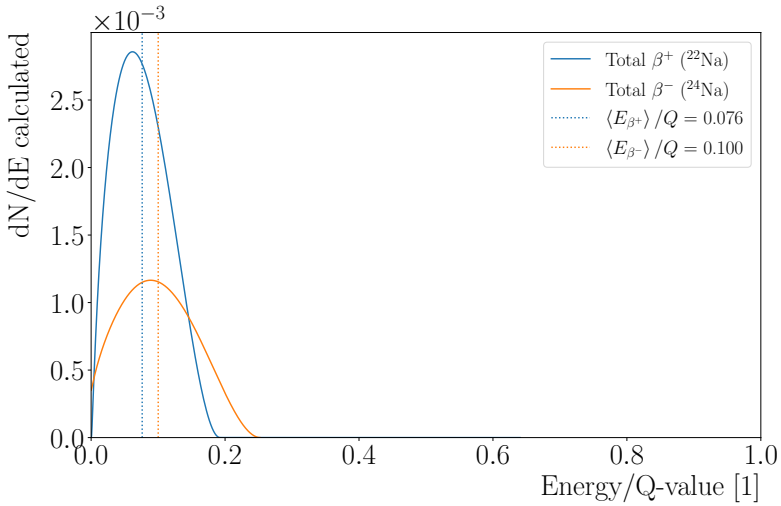

Figure 1.10.: Continuous Beta radiation of ^{22}Na and ^{24}Na, calculated with BetaShape [22][a]

[a]Xavier Mougeot. 'Atomic exchange correction in forbidden unique beta transitions'. In: *Applied Radiation and Isotopes* 201 (Nov. 2023), p. 111018. ISSN: 0969-8043. DOI: 10.1016/j.apradiso.2023.111018.

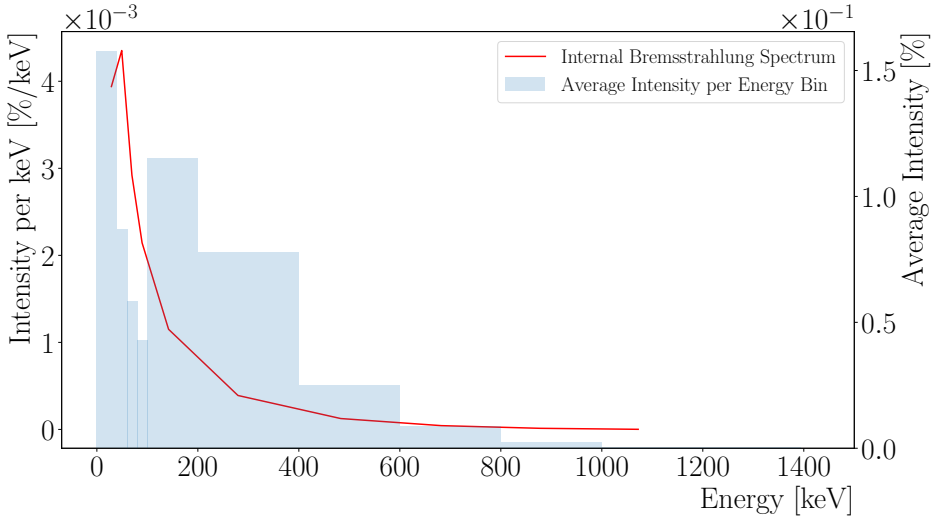

Figure 1.11.: Internal Bremsstrahlung of ^{24}Na β^- decay, calculated with RadiationReport [23][a]

[a] Jun Chen. *IAEA-NSDDNetwork/RadiationReport*. original-date: 2022-08-25T19:42:34Z. Apr. 2025.

where B_e is the binding energy of the electron to which is transferred the energy.

Internal conversion electron A conversion electron is emitted when an excited nuclide transfers its energy directly to one of its own orbital electrons, rather than via gamma relaxation. The energy usually transfers to the electron of lower orbitals (K- or L-shells).

The energy of an internal conversion electron is equal to the energy of corresponding gamma radiation and the energy required to strip the electron from its orbital. For instance, the internal conversion electron originating from the K-shell, if E_γ is the photon energy, and B_e the binding energy, we have:

$$E_{CE_K} = E_\gamma - B_e({}^A_Z X, K) \tag{1.16}$$

In the case of ^{203}Hg, according to its level scheme given in Figure 1.12, for the main photon of 279.2 keV, as the binding energy is equal to circa 85 keV, we get $E_{CE_K} =$ 194.2 keV

1.2.3. Activity and radioactive filiation

Decay is a probabilistic phenomenon, we can ascertain that after a certain time, half the amount of radionuclides initially present (N_0) will have decayed: this duration is called half-life ($T_{1/2}$) of the radionuclide.

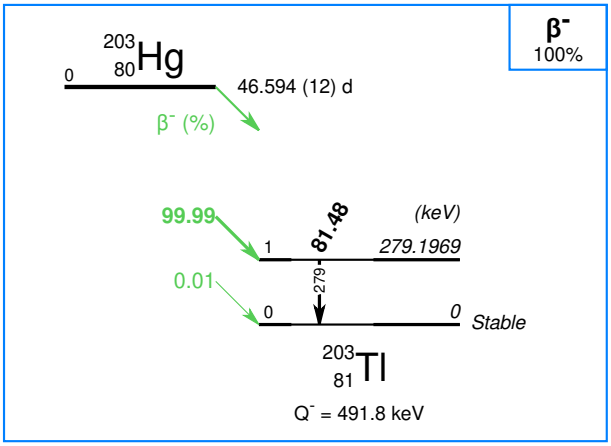

Figure 1.12.: Level scheme of ^{203}Hg, extracted from DDEP [15][a]

[a]Laboratoire National Henri Becquerel. *Nucléide – Lara Application – Laboratoire National Henri Becquerel*. en-GB.

When formulating the radionuclides properties, the decay constant (λ), in s^{-1}, is preferred allowing to express the number of disintegrations per unit of time, i.e. the activity (A), as:

$$A = \lambda N \tag{1.17}$$

In the International System of Units, the activity is described in becquerel, where 1 Bq corresponds to 1 disintegration per second.

This entails that the disintegration of nuclides can be followed with:

$$\frac{dN(t)}{dt} = -\lambda N(t) \tag{1.18}$$

where $N(t)$ is the ammount of the nuclide considered at time t.

One can then derive an average survival time, or mean life time (τ) as:

$$\tau = \frac{\int_0^{+\infty} te^{-\lambda t}dt}{\int_0^{+\infty} e^{-\lambda t}dt} = \frac{1}{\lambda} \tag{1.19}$$

We can express the half-life as function of τ by simply solving $N(T_{1/2}) = {}^{N_0}/_2$, with

$$T_{1/2} = \tau \times \log(2) \tag{1.20}$$

Tracking through time The decay of nuclides can be expressed as Equation 1.18.

By simple integration, one can obtain the activity of the sample after any elapsed time t, defined as:

$$A(t) = A_0 \times e^{-\lambda t} \tag{1.21}$$

where $A_0 = \lambda \times N_0$ is the initial activity of the sample.

Specific activity Usually, we prefer to express it as specific activity:

$$\frac{A_0}{m} = N_A \frac{1}{M} \frac{\log(2)}{T_{1/2}} \tag{1.22}$$

where:

- N_A the Avogadro number, $N_A = 6.022\,140\,761\,0 \times 10^{23}\,\mathrm{mol}^{-1}$
- m the mass in grams
- M the molar mass of the radioisotope

a) Radioactive filiation

When the daughter nuclide is also unstable, then the decay are chained.

Considering two nuclide in serie, i.e.

$$X_1 \xrightarrow{\lambda_1} X_2 \xrightarrow{\lambda_2} X_3 \text{ (stable)}$$

When at initial time, only a nuclide X_1 is present, with an initial activity of A_1^0, the number of nuclei of the three species are then:

$$\begin{aligned}
N_1(t) &= \frac{A_1^0}{\lambda_1} \times e^{-\lambda_1 t} \\
N_2(t) &= A_1^0 \times \frac{1}{\lambda_2 - \lambda_1}(e^{-\lambda_1 t} - e^{-\lambda_2 t}) \\
N_3(t) &= A_1^0 \times \frac{\lambda_2}{\lambda_2 - \lambda_1}\left(\frac{1 - e^{-\lambda_1 t}}{\lambda_1} - \frac{1 - e^{-\lambda_2 t}}{\lambda_2}\right)
\end{aligned}$$

n-length decay chain These formula can then be generalised for any length, with the same initial amount hypothesis:

$$A_n(t) = A_1^0\left(\prod_{i=2}^{n} \frac{\lambda_i}{\lambda_i - \lambda_n} \times e^{-\lambda_1 t} + \prod_{i=1, i\neq 2}^{n} \frac{\lambda_i}{\lambda_i - \lambda_n} \times e^{-\lambda_2 t} + \ldots + \prod_{i=1}^{n-1} \frac{\lambda_i}{\lambda_i - \lambda_n} \times e^{-\lambda_n t}\right) \tag{1.23}$$

where:

$$X_1 \xrightarrow{\lambda_1} X_2 \xrightarrow{\lambda_2} \cdots \xrightarrow{\lambda_n} X_{n+1} \text{ (stable)}$$

This formulation was first introduced by Bateman [24][1].

As an example, the Figure 1.13 gives the entire decay paths of ^{232}Th. The previous formula can be applied to the two sub-path in order to get the total amount of Lead from the decay of a sample of pure ^{232}Th.

[1] G. M. Volkoff. 'The Atomic Nucleus. Robley D. Evans. McGraw-Hill, New York, 1955. xv+ 972 pp. Illus. $14.50.' In: *Science* 123.3197 (Apr. 1956), pp. 592–593. DOI: 10.1126/science.123.3197.592.b.

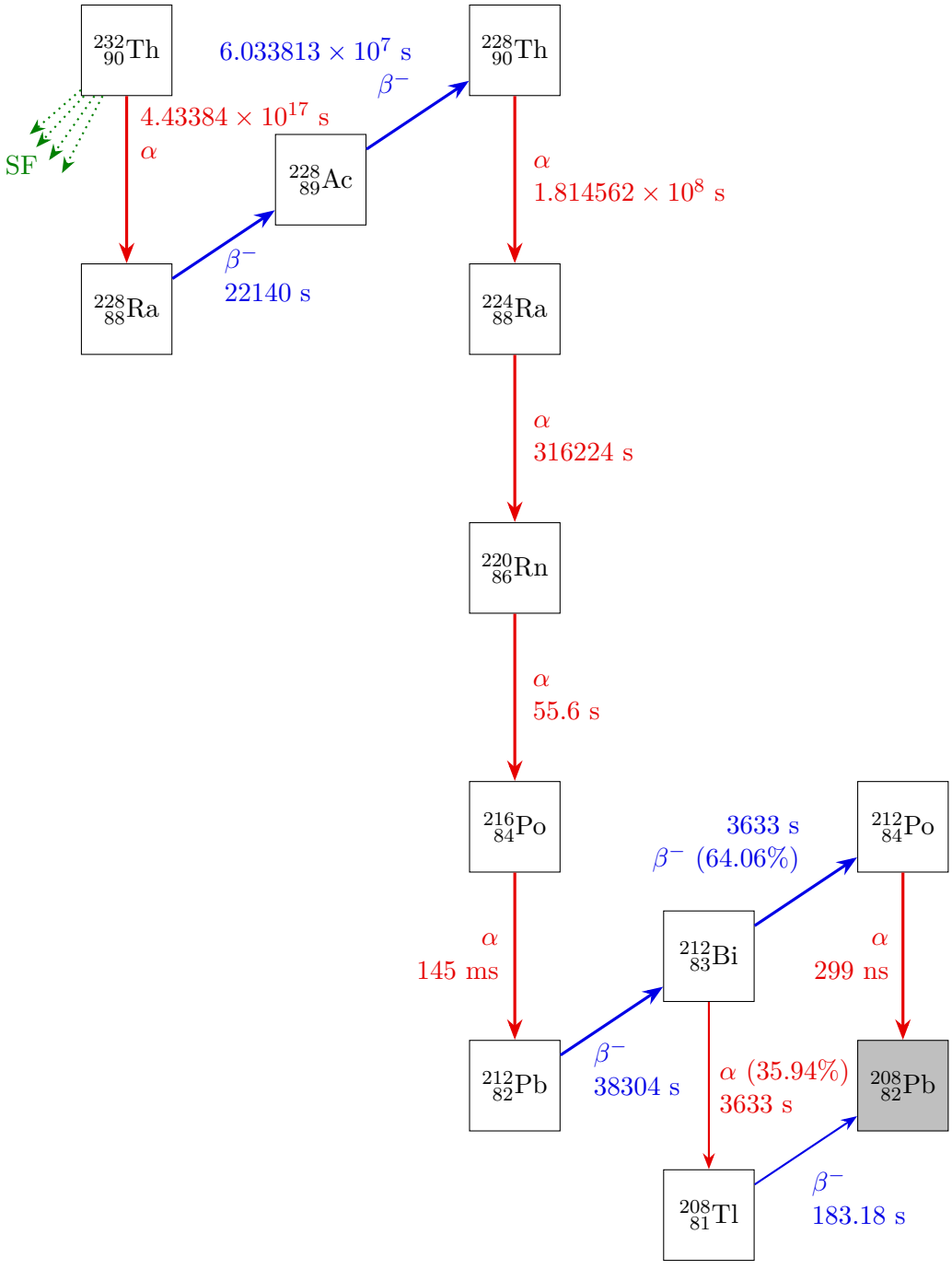

Figure 1.13.: Decay path of ^{232}Th, according to ENDF/B-VIII.0 decay data

b) Production of radionuclides

As mentioned, if more than 3000 nuclides have been discovered, only 289 are naturally present.

The isotopes are produced via nuclear reactions, either within or in the vicinity of nuclear reactors or accelerators. The easiest way involves neutron activation or charge-particle interactions with stable nuclei.

Such reaction are usually represented as $X\,(a,b)\,Y$, where:

- a is the projectile (e.g. a neutron, a proton, a deuteron, an alpha particle or an electron);
- X the target nucleus (in many cases a stable nuclide, more rarely a radioactive nuclide);
- b the product particle;
- Y the product nucleus, which is usually radioactive.

If we consider the situation mentioned before, and considering mono-energetic projectile, the number of nuclides N_Y produced is proportional to the number of atoms in the target (N_X), to the incident projectile flux ϕ (i.e. the number of incoming particle per surface unit, per time unit), and to the probability for the reaction σ (i.e. the cross-section for that reaction, expressed in surface units).

If we consider a small duration dt during which N_X does not vary, the produced number of Y species (N_Y^+) is given by:

$$dN_Y^+ = N_X \phi \sigma dt \tag{1.24}$$

Yet as the product Y is unstable, there is also a loss (N_Y^-):

$$dN_Y^- = -N_Y \lambda_Y dt \tag{1.25}$$

Hence the variation of products if considering both phenomenon:

$$dN_Y = N_X \phi_n \sigma dt - N_Y \lambda_Y dt \tag{1.26}$$

Considering an irradiation of t_{irr}, we get:

$$N_Y(t_{irr}) = \frac{N_X \sigma \phi}{\lambda_Y - \sigma\phi} \left(e^{-\sigma\phi t_{irr}} - e^{-\lambda_Y t_{irr}} \right) \tag{1.27}$$

As for the activity produced, we can establish if $N_X \sigma\phi << \lambda_Y$:

$$A_Y(t_{irr}) \simeq N_X \sigma\phi \left(1 - e^{-\lambda_Y t_{irr}} \right) \tag{1.28}$$

If $t_{irr} > 10\tau$, we get a saturation, $A_Y(t_{sat}) = N_X\sigma\phi = A_{sat}$. If we irradiate for 4τ, we get already 98 % of the saturation.

Usually we consider also a cooling time t_{cool} before measuring an activity, let's call the measurement duration t_{meas}, the expected activity becomes:

$$A_Y(t_{irr} + t_{cool} + t_{meas}) \simeq N_X \sigma\phi \left(1 - e^{-\lambda_Y t_{irr}} \right) e^{-\lambda_Y t_{cool}} \left(1 - e^{-\lambda_Y t_{meas}} \right) \tag{1.29}$$

In Figure 1.14, we represent the time evolution of this unstable Y compound. To give an order of magnitude, irradiating a sample of 5 g of natural Vanadium (99.75 % of ^{51}V), at a thermal flux of $1 \times 10^6\,\mathrm{s}^{-1}\cdot\mathrm{cm}^{-2}$ for thirty minutes, we expect around 28.9 GBq of ^{52}V and about 11.5 GBq after 5 minutes of cooling (as its half-life is 3.75 min)[1].

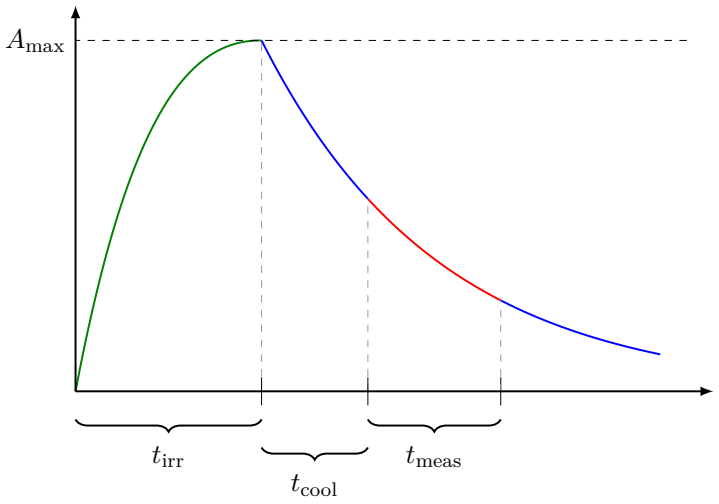

Figure 1.14.: General form of irradiation-cooling according to Bateman equations

General Bateman equations The Bateman equations from Equation 1.18 can be generalised with transmutation in the form:

$$\frac{dN_j(t)}{dt} = -\left[\lambda_j + \xi_j\right] N_j + \sum_{\substack{i=1 \\ i\neq j}}^{J} \left[\lambda_{i\to j} + \xi_{i\to j}\right] N_i \tag{1.30}$$

$$\xi_j = \int_0^{+\infty} \sigma_j(E)\phi_n(E)dE \tag{1.31}$$

$$\xi_{i\to j} = \sum_{q=1}^{M} \int_0^{+\infty} \sigma_{q,i\to j}(E)\phi_n(E)dE \tag{1.32}$$

where:

- $N_j(t)$ is the number of nuclei of isotope j at time t with an initial value $N_{j,0}$;
- J is the total number of isotopes present in the database;
- M is the total number of reactions capable of transmuting an isotope;
- $\sigma_j(E)$ is the microscopic cross-section of isotope j at energy E (in b);
- $\sigma_{q,i\to j}(E)$ is the microscopic cross-section of transmutation reaction q from isotope i to isotope j at energy E (in b);

[1] Using https://www.ncnr.nist.gov/resources/activation/

- $\phi_n(E)$ is the energy spectrum of the neutron flux in the material considered (in $cm^{-2} \cdot MeV^{-1} \cdot s^{-1}$);
- λ_j is the decay constant of isotope j (in s^{-1});
- ξ_j is the total transmutation rate of isotope j under the neutron flux (in s^{-1});
- $\lambda_{i \to j}$ is the decay constant from isotope i to isotope j (in s^{-1}) ;
- $\xi_{i \to j}$ is the production rate of isotope j under the neutron flux from isotope i (in s^{-1});

1.3. Characterisation of Ionising radiations

The term "radiations" covers any processes whereby energy is emitted or transmitted in the form of electromagnetic waves or particles. Radiation is referred to "ionising" radiation when it has the ability to strip electrons.

The interaction of charged particles traversing a medium are governed by their electric charge, which mediates Coulomb interactions with the constituent atoms of the material. These particles are classified as directly ionizing due to their ability to deposit energy through continuous electromagnetic interactions along their trajectory.

The primary energy loss mechanism for charged particles occurs via inelastic collisions with atomic electrons.

Each collision results in a discrete energy transfer, δE, ranging from eV to keV scales. While individually small compared to the particle's total kinetic energy, the collective effect of a vast number of such collisions results in a gradual and continuous dissipation of energy, leading to the particle's eventual stopping provided the medium is of sufficient thickness.

These collisional energy transfers manifest in two principal outcomes: the local absorption of energy by the medium, primarily through the ionization and excitation of atoms, and the consequent reduction in the kinetic energy of the incident particle. Interactions with atomic nuclei, while generally less frequent, become significant for high-energy electrons, giving rise to bremsstrahlung radiation.

The process of ionization entails the transfer of sufficient energy from the incident particle to an atomic electron to overcome its binding energy, resulting in its ejection and the formation of an ion-electron pair. The probability of ionization is shell-dependent, with outer-shell interactions being more probable than those involving inner-shell electrons, the latter of which can initiate secondary processes such as Auger electron emission or characteristic X-ray production.

The interaction of radiation with matter falls into two categories, depending on whether the radiation is "directly ionising" or "indirectly ionising". The first category includes charged particles that ionise matter as they pass through it, such as protons, electrons, alpha particles and muons. The second category concerns neutral particles that only interact with matter through nuclear interactions, not with the electron cloud of atoms. This is the case with neutrons for example. While these particles themselves are not ionising, the secondary particles they generate can ionise matter. Therefore, the case of neutrons requires studying both their direct interaction with the atomic nucleus and the

ionisation caused by the secondary particles they generate.

The Table 1.2 synthesizes the different radiations, and their effects.

1.3.1. Charged particles: Stopping Power

The material acts as a decelerator, characterised by its stopping power. A screen with sufficient correct thickness will stop all incident charged particles. Total stopping power is generally expressed in $\mathrm{MeV}\cdot\mathrm{cm}^{-1}$, as:

$$S = -\frac{dE}{dx} = \left(\frac{dE}{dx}\right)_{elec} + \left(\frac{dE}{dx}\right)_{nucl} \tag{1.33}$$

This depends on the type of particle, its energy and the properties of the material it passes through, such as density and charge number.

The Figure 1.15 shows the variation of the mass stopping power of proton and alpha in polycarbonate, i.e. $(C_{15}H_{16}O_2)$n which has a density of $1.2\,\mathrm{g}\cdot\mathrm{cm}^{-3}$. The plot is generated based on PSTAR[1] and ASTAR[2] utilities. This polymer is used notably for Solid State Nuclear Track detectors, used in rapid neutron detection, see chapter 2.

The figure presents also the CSDA (Continuous-Slowing-Down Approximation), this is an approximation to the average path length travelled by a charged particles as they slow down to rest. In this approximation, the rate of energy loss at every point along the track is assumed to be equal to the total stopping power. Energy-loss fluctuations are neglected. The CSDA range is obtained by integrating the reciprocal of the total stopping power with respect to energy.

1.3.2. Neutrons and Photons: Absorption law

Unlike charged particles, indirectly ionising radiation is not subject to mandatory interactions. The interaction of a photon, or neutron, with matter, for example, is random and there is a non-zero probability that it will pass through any thickness of matter without interacting.

We refer rather to attenuation law, rather than linear energy transfer. The attenuation of a beam of intensity I_0 in a medium of thickness x depends on the nature of the medium and the energy of the incident photon, following:

$$I(x) = I_0 e^{-\mu x} = I_0 e^{-N\sigma x} \tag{1.34}$$

where N is the number of target centres per unit volume, μ the attenuation coefficient, and σ the total cross-section of interaction.

For photons, the total cross-sections mainly accounts for photo-electric, Compton and pair-production effects. Neutrons reactions are split between absorption (capture and fission) and scattering. The absorption predominates for thermal neutrons and the scattering cross section predominates for fast neutrons.

[1] https://physics.nist.gov/PhysRefData/Star/Text/PSTAR.html
[2] https://physics.nist.gov/PhysRefData/Star/Text/ASTAR.html

Table 1.2.: Direct and Indirect Ionising radiations [25][a]

Radiation	Type	Radiation emitted after interaction
Charged particles (α, electrons)	Ionization	• an atomic electron in the material traversed is set in motion • relaxation of the electron cloud (X-rays, and/or Auger electrons)
	Excitation	• relaxation of the electron cloud (X-rays, and/or Auger electrons)
	Bremsstrahlung	• X-ray emission (bremsstrahlung)
	Annihilation (end of path for positrons)	• emission of 2×511 keV photons at 180°
Electromagnetic radiation (γ, X)	Photoelectric effect (low energies)	• ejection of an atomic electron from inner shells • relaxation of the electron cloud (X-rays, and/or Auger electrons)
	Compton effect (intermediate E)	• ejection of an atomic electron from outer shells • scattering of the incident photon • relaxation of the electron cloud (X-rays, and/or Auger electrons)
	Pair production ($E > 1.022$ MeV)	• generation of a electron–positron pair
Neutrons	Absorption	• emission of a secondary radiation (neutron, proton, α, γ, …)
	Scattering	• scattering of the incident neutron • propulsion of recoil nucleus

[a] Youbba Ould Salem. 'Etude expérimentale et modélisation Monte Carlo des grandeurs opérationnelles en métrologie des rayonnements ionisants: application à la dosimétrie neutrons par radiophotoluminescence'. français. Thèse de doctorat. Institut pluridisciplinaire Hubert Curien: Université de Strasbourg, 2014.

(a) Protons.

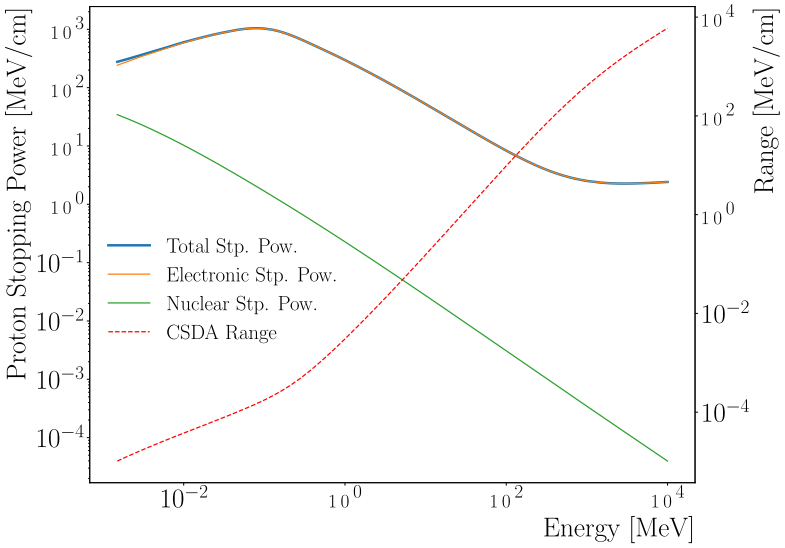

(b) Alphas.

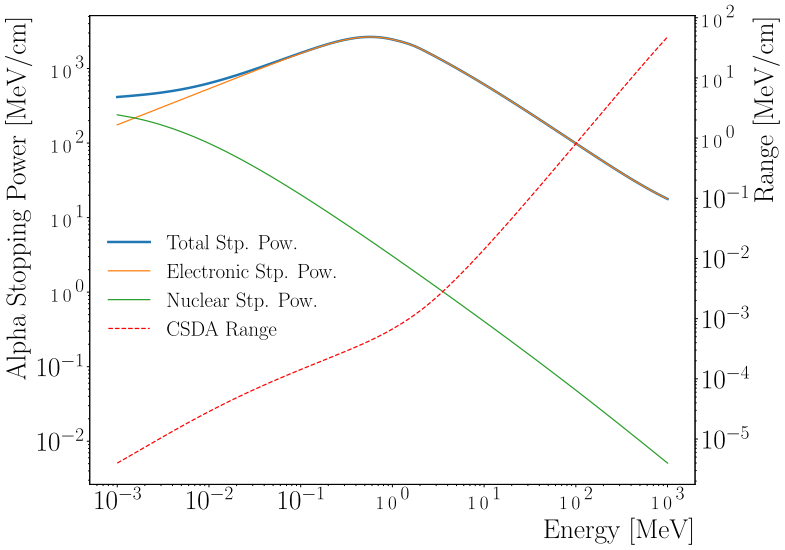

Figure 1.15.: Stopping power and range in polycarbonate for proton (top) and alpha (bottom), according respectively to PSTAR and ASTAR

1.4. Photon-matter interaction

When interacting with matter, a photon can either disappear completely (e.g. photo-electric effect, pair creation or triplet production), or scatter (e.g. Rayleigh scattering, Thomas scattering or the Compton effect).

Here, we will focus on the Photoelectric (PE), the Compton (C) and Pair Production (PP) processes that predominate within our energy range of interest, as depicted in Figure 1.16 (taking the example of Germanium, used in chapter 2) using X-ray Mass attenuation and energy absorption DATa (XMuDat) [26][1].

The attenuation coefficient can be reduced to:

$$\mu_{tot} = \mu_{pe} + \mu_c + \mu_{pp} \tag{1.35}$$

The probability of occurrence for any of these three effects depends on the energy of the electromagnetic radiation involved, and on the nature of the material of the medium concerned.

In order to take into account the contribution of secondary particles, we can define the energy-absorption coefficient (μ_{tot}^{en}). This coefficient involves the further emission of radiation produced by the charged particles in travelling through the medium, and is defined as

$$\mu_{tot}^{en} = (1 - g)\mu_{tot} \tag{1.36}$$

where g is the average fraction of the kinetic energy of secondary charged particles (produced in all the types of interactions) that is subsequently lost in radiative. For example, it includes the contribution of bremsstrahlung of secondary electrons, produced by photo-electric effect.

1.4.1. Photoelectric effect

The interaction of a photon with matter results in the total transfer of its energy to an electron in the electron cloud. This process is predominant below approximately 100 keV.

$$E_e = E_\gamma - B_e \tag{1.37}$$

where E_e is the kinetic energy of the ejected electron, E_γ represents the energy of the incident photon, and B_e is the binding energy of the electron in the deepest layers of the atom as given in Equation 1.4. The latter varies according to the atomic number ($B_e =$ 13.6 eV for $Z = 1$ and $B_e = 142$ keV for $Z = 100$).

As for the cross-section of this effect, we have according to [27][2]:

$$\sigma_{pe} \propto \frac{Z^n}{E_\gamma^m} \tag{1.38}$$

where:

[1] V.G. Pronyaev and Vienna (Austria) International Atomic Energy Agency Nuclear Data Section. *XMuDat: Photon attenuation data on PC. Version 1.0.1 of August 1998. Summary documentation.* Jan. 2025.

[2] Henri Métivier. *Radioprotection et ingénierie nucléaire.* EDP Sciences, 2006.

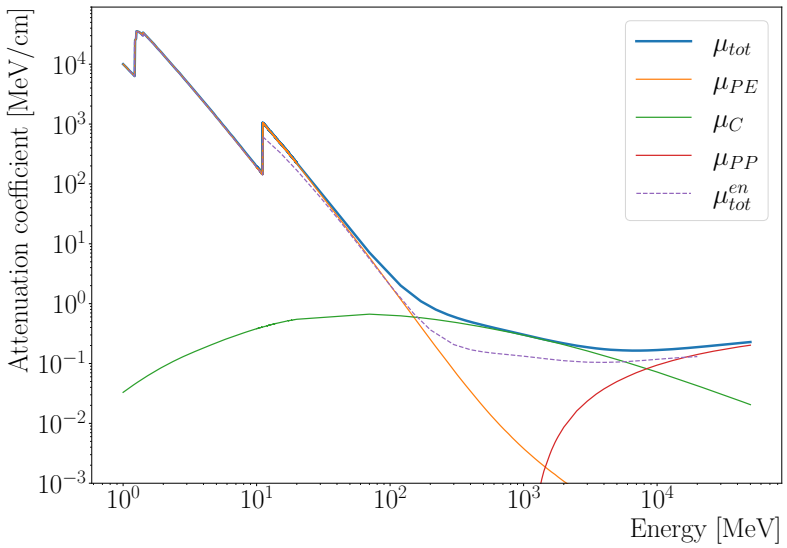

Figure 1.16.: Partial and total attenuation coefficients for γ on Germanium (Z=32), according to XMuDat

- m varies between 1 and 3.5 included.
- n varies between 4 and 5 included

1.4.2. Compton effect

The Compton effect accounts for scattering and absorption effect. The Compton scattering is also known as incoherent scattering. It is the partial transfer of energy from the incident photon to a weakly bound (free) electron in the electron cloud.

The Compton photon can be scattered at an angle between 0 and π rad relative to the incident direction. The conservation of total energy gives

$$E'_\gamma = \frac{E_\gamma}{1 + \epsilon\,(1 - \cos\theta)} \tag{1.39}$$

where E'_γ is the scattered photon energy, $E_0 = m_e c^2 = 511\,\text{keV}$ and $\epsilon = {}^{E_\gamma}/_{E_0}$.

This emission is anisotropic, the Klein et Nishima equation [28][1] formulate the differential cross-sections per unit solid angle of Compton scattering:

$$\frac{d\sigma_{scat}}{d\Omega}(\epsilon,\theta) = \frac{r_0^2}{2}\frac{1}{(1+\epsilon\,(1-\cos\theta))^3}\left(1+\cos^2\theta + \frac{\epsilon^2\,(1-\cos\theta)^2}{1+\epsilon\,(1-\cos\theta)}\right) \tag{1.40}$$

where r_0 is the classical electron radius ($2.817\,940\,326\,2 \times 10^{-15}\,\text{m}$).

[1] Kai Siegbahn. *Alpha-, Beta- and gamma-ray spectroscopy.* en. Vol. 1. North-Holland publishing company, 1965.

The total cross-sections follows:

$$\sigma_{compton} \propto \frac{Z}{E_\gamma} \tag{1.41}$$

1.4.3. Pair production

Pair creation is a process that occurs in the Coulomb field of the nucleus. The incident photon is transformed into an electron-positron pair.

This threshold reaction becomes possible when $E_\gamma \geq 2 \times m_e c^2$. It should be noted that pair production can also occur in the field of an electron, even if the probability is low. In this case, the energy threshold $E_\gamma \geq 4 \times m_e c^2$. If we denote the kinetic energies of the electron and positron by E_e and E_{e^+}, respectively, the law of conservation of energy is written as:

$$E_e + E_{e^+} = E_\gamma - 2E_0 \tag{1.42}$$

The effective cross section is given for a nucleus without and with shielding effect by the relations [29, 30][1]:

$$\sigma_{pp} = \begin{cases} \alpha r_0^2 Z^2 \left[\frac{28}{9}\log\left(\frac{2E_\gamma}{E_0}\right) - \frac{218}{27}\right] & \text{if} \quad 2E_0 << E_\gamma << \frac{E_0}{\alpha} Z^{-1/3} \\ \alpha r_0^2 Z^2 \left[\frac{28}{9}\log\left(183 Z^{-1/3}\right) - \frac{2}{27}\right] & \text{if} \quad E_\gamma << \frac{E_0}{\alpha} Z^{-1/3} \end{cases} \tag{1.43}$$

where α is the hyperfine constant ($1/137.035999084$).

1.5. Neutrons-matter interaction

The neutron was discovered in 1932 by J. Chadwick (who was awarded the Nobel Prize in 1935), following experiments conducted by Bothe and Becker in 1930 and by Joliot-Curie in 1931. Neutrons, which form nuclei together with the proton, has a mass close to that of the proton. Indeed, the $m_n/c^2 = 939.565\,420\,478\,815\,3$ MeV, when the mass of proton is of $938.783\,073\,484\,235\,5$ MeV.

Free neutrons are unstable, β^- emitters, with a lifetime of 886.8 seconds.

Neutrons have no electric charge, as photons, they are hence part of what is known as "indirectly ionising radiation". The ionisation of the medium traversed and therefore the absorbed dose are the responsibility of the charged secondary particles created during the interaction of a neutron with matter.

One often refers neutron as cold or thermal. The link comes from that neutrons cannot be influenced in their motion and energy by magnetic or electric fields but only by nuclear collisions within a medium, which is characterized by its temperature. Under

[1] Samir Dziri. 'Etudes expérimentales et simulations Monte Carlo en spectrométrie gamma: Correction des effets de cascade et de matrice pour des mesures environnementales'. fr. PhD thesis. Université de Strasbourg, May 2013, H. Bethe and W. Heitler. 'On the stopping of fast particles and on the creation of positive electrons'. In: *Proceedings of the Royal Society of London. Series A, Containing Papers of a Mathematical and Physical Character* 146.856 (Aug. 1934), pp. 83–112. ISSN: 0950-1207. DOI: 10.1098/rspa.1934.0140.

equilibrium conditions, the molecular motion in the material corresponds to the averaged energy of the neutrons migrating within the medium. We can derive:

$$E = k_B T \tag{1.44}$$

Where E is the neutron kinetic energy, k_B the Boltzmann constant ($8.617\,343 \times 10^{-5}$ eV·K^{-1}), and T the temperature.

1.5.1. Classification

The probability of neutrons interacting with matter depends on their energy, but when neutrons have sufficiently low energies, thermal equilibrium (due to neutron scattering) can be approximated. Neutrons are therefore classified into families according to their energy. This classification is not clearly established, as with different applications, there are different constraining ranges and if the terminology is the same the ranges vary, especially for fast neutron definitions.

A classification is given in Table 1.3.

Table 1.3.: Category of neutrons per velocity and temperature

Class	Velocity [m·s^{-1}]	Temperature [K]	Energy
Ultra-cold neutrons	< 7.6	$< 3.5 \times 10^{-3}$	< 0.3 µeV
Cold neutrons	$< 1.694 \times 10^3$	< 174	< 15 meV
Thermal neutrons	2.2×10^3	293	25.3 meV
Epithermal neutrons	$6.9 \times 10^3 - 8.7 \times 10^3$	$293 - 4.6 \times 10^3$	0.25 – 0.4 eV
Intermediate neutrons	$1.4 \times 10^4 - 1.4 \times 10^7$	$1 \times 10^4 - 1 \times 10^{12}$	1 eV – 0.1 MeV
Fast neutrons	$1.4 \times 10^7 - 6.2 \times 10^7$	$1.2 \times 10^{12} - 2.3 \times 10^{14}$	0.1 – 20 MeV
Ultra-fast neutrons	$> 6.2 \times 10^7$	$> 2.3 \times 10^{14}$	> 20 MeV

The neutrons depending on their energy may disappear completely (absorption) or simply loose energy (scattering).

The probability of an interaction is referred as cross-sections (σ), the Figure 1.17 summarises the main cross-sections for neutron, which will be detailed in the following sections.

The cross-section may refer, not for one unique nuclide, but rather of 1 cm^3 of matter of this nuclide, it is the macroscopic cross-section:

$$\Sigma = \sigma \frac{N_A}{A} \rho \tag{1.45}$$

where N_A is the Avogadro number, and ρ the atom density. If σ is in cm^2, the macroscopic cross-section is in cm^{-1}.

The Figure 1.18 gives an example of cross-sections of ^{232}Th.

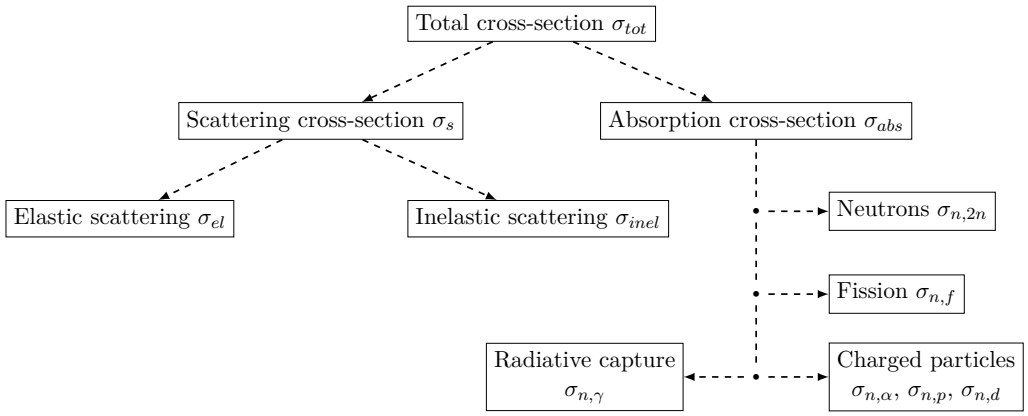

Figure 1.17.: Classification of main neutron cross-sections [31][a]

[a]Raymond Pannetier. *Vade-mecum du technicien*. fr. First. Vol. 1. Vade-mecum du technicien nucléaire : contrôle des rayonnements ionisants, mise en oeuvre des techniques de protection. 1966.

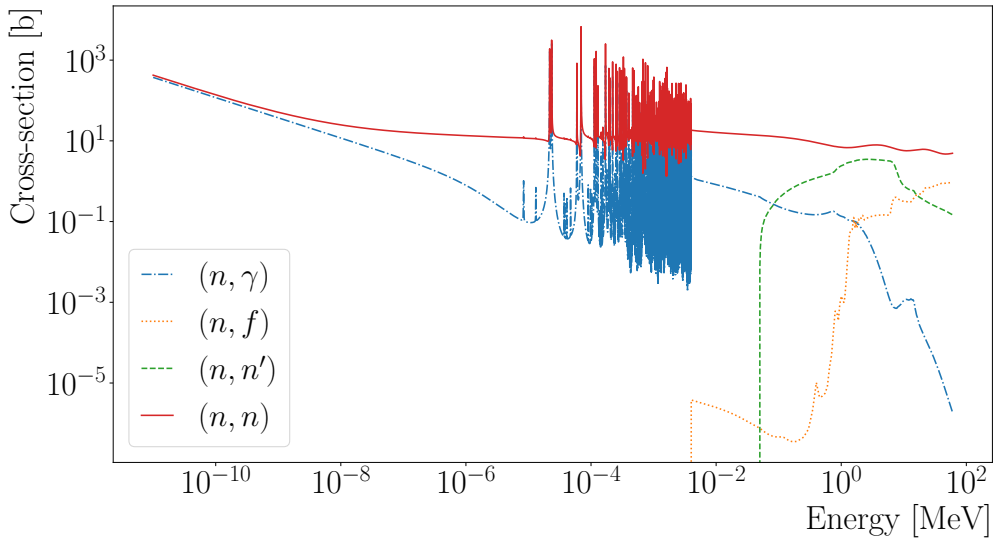

Figure 1.18.: Main neutron interaction on ^{232}Th, based on ENDF/B-VIII.1

1.5.2. Scattering

Neutrons can interact with atomic nuclei in two ways: through scattering reactions, where the neutron is scattered by the nucleus, or absorption reactions, where the neutron is absorbed by the nucleus. There are two types of scattering reaction: "elastic" and "inelastic".

a) Elastic collisions

The scattering of neutron is often referred as "thermalisation".

In elastic collisions, the neutron is simply scattered by the target nucleus with conservation of kinetic energy, and there is no threshold.

Applying the conservation of energy and momentum to the reaction, $X\,(n,n)\,X$, allow us to derive a simple relationship between the energy of the incident neutron, the energy of the recoil nucleus and the scattering angle in the laboratory reference frame:

$$E_X = E_n \left(\frac{4 m_n M_X}{(m_n + M_X)^2} \right) \cos^2 \theta \tag{1.46}$$

where:

- E_X is the recoil energy of the target
- E_n is the incident neutron energy
- M_X the mass of the target
- m_n the mass of the target
- θ the scattering angle

In the case of ^{1}H, as their mass are very similar, the energy transfer is maximal and can be reduced to:

$$E_X = E_n \cos^2 \theta \tag{1.47}$$

This is the reason that light atoms are used as moderator (i.e. medium to reduce neutron energy). Indeed, for instance the fraction of energy transmitted for ^{2}H is of 90 %, when for "heavier" nuclides as ^{16}O already diminish of only 10 %. Such principle is applied for example for the detection of neutrons, notably for SSNTDs (used in chapter 2), which uses polyethylene moderators.

The cross section is relatively well understood: J. L. Gammel [32][1] proposed a semi-empirical formula describing the total elastic scattering cross section of Hydrogen nuclei as a function of incident neutron energy:

$$\sigma_n\,(E_n) = \frac{3\pi}{(a + bE_n + cE_n^2)^2 + dE_n} + \frac{\pi}{(e + fE_n)^2 + dE_n} \tag{1.48}$$

where:

- $a = -1.86$

[1] Jerry B. Marion and J. L. Fowler. *Fast neutron physics.* eng. Vol. 2. Interscience monographs and texts in physics and astronomy. Publication Title: Fast neutron physics. New York: Interscience Publishers, 1960.

- $b = 0.094\,15$
- $c = 0.000\,130\,6$
- $d = 1.206$
- $e = 0.4223$
- $f = 0.13$

This is a good approximation with discrepancies no greater than 0.6% in the 1 to 20 MeV range, as shown in Figure 1.19, compared to ENDF/B.

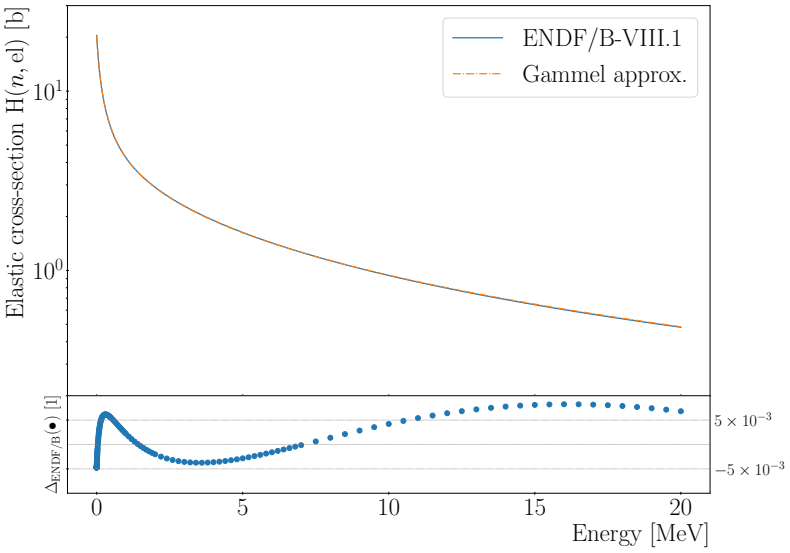

Figure 1.19.: Comparison between ENDF/B-VIII.1 ^{1}H(n,n) and Gammel semi-empirical model

b) Inelastic collisions

Inelastic scattering reactions are threshold reactions that become significant at around a tenth of a MeV.

At this point, the energy of the incident neutron is sufficient to excite the nucleus.

When a compound nucleus is formed, de-excitation radiation is most often emitted, along with a neutron with lower energy than the incident neutron. This (n, n') reaction does not conserve the kinetic energy of the system.

1.5.3. Capture

The absorption of an incident neutron can lead to a compound nucleus. The nucleus is often formed in an excited state, so the nuclides will often relax by emitting gammas. This is called radiative capture.

Below the resonance region, the neutron capture cross-section is inversely proportional to the neutron velocity (we refer this range as the $1/v$ region). Hence for thermal neutron, capture reaction are maximal, as shown in Figure 1.18.

Transmutation The compound nucleus formation does not necessarily ends only with gamma relaxation. In the case, if sufficient energy is available, transmutation reactions as (n,p), (n,α), or other very light nuclides emission can happen.

This transmutation reaction are very useful to detect the neutrons, as it can produce these ionising secondaries which are more easily detected. For instance,

$$n + {}^{6}Li \longrightarrow \alpha + {}^{3}H \tag{1.49}$$

$$n + {}^{10}B \longrightarrow \begin{cases} \alpha + {}^{7}Li & (6\%) \\ \alpha + {}^{7}Li^{*} \longrightarrow {}^{7}Li + \gamma & (94\%) \end{cases} \tag{1.50}$$

$$n + {}^{3}He \longrightarrow p + {}^{3}H \tag{1.51}$$

$$\tag{1.52}$$

which are exoenergetic reactions, with respectively $Q_{n,^6Li} = 4.78\,\text{MeV}$, $Q_{n,^{10}B} = 2.79\,\text{MeV}$ and $Q_{n,^3He} = 0.764\,\text{MeV}$. If the majority of transmutation happens associated with gamma radiations, one can produce directly the daughter in ground states, as mentioned in Equation 1.50.

As an order of magnitude, for thermal neutrons, the cross-sections are 950 b for $(n,^6Li)$ (whereas it is 71 b for ^{nat}Li), and 4000 b for ^{10}B (760 b for ^{nat}B).

Fission When there is a high number of nucleons, the neutron can fragment the target, we refer this as neutron induced fission (n,f)

The resulting compound nucleus will generally split into two fragments. On average, two or three fast neutrons and photons are also released.

For example,

$$^{235}_{92}U + n \rightarrow ^{236}_{92}U^{*} \rightarrow ^{144}_{56}Ba + ^{89}_{36}Kr + 3n$$

The available energy for this fission reaction is of about $Q = 173\,\text{MeV}$, without considering the ^{236}U excitation energy.

The fission fragments may be unstable, and will consequently decay. Hence, when giving fission fragment list, both independent and cumulative yields are given, the latter accounting also of the decay of the fragments.

The fission fragments can have a major roles in the total radioactivity of a fissioning nuclide, see a typical example in Figure 1.20.

1.5.4. Resonance

As seen in previous cross-sections, some structures appear, with large jerk in the cross-sections at certain energies.

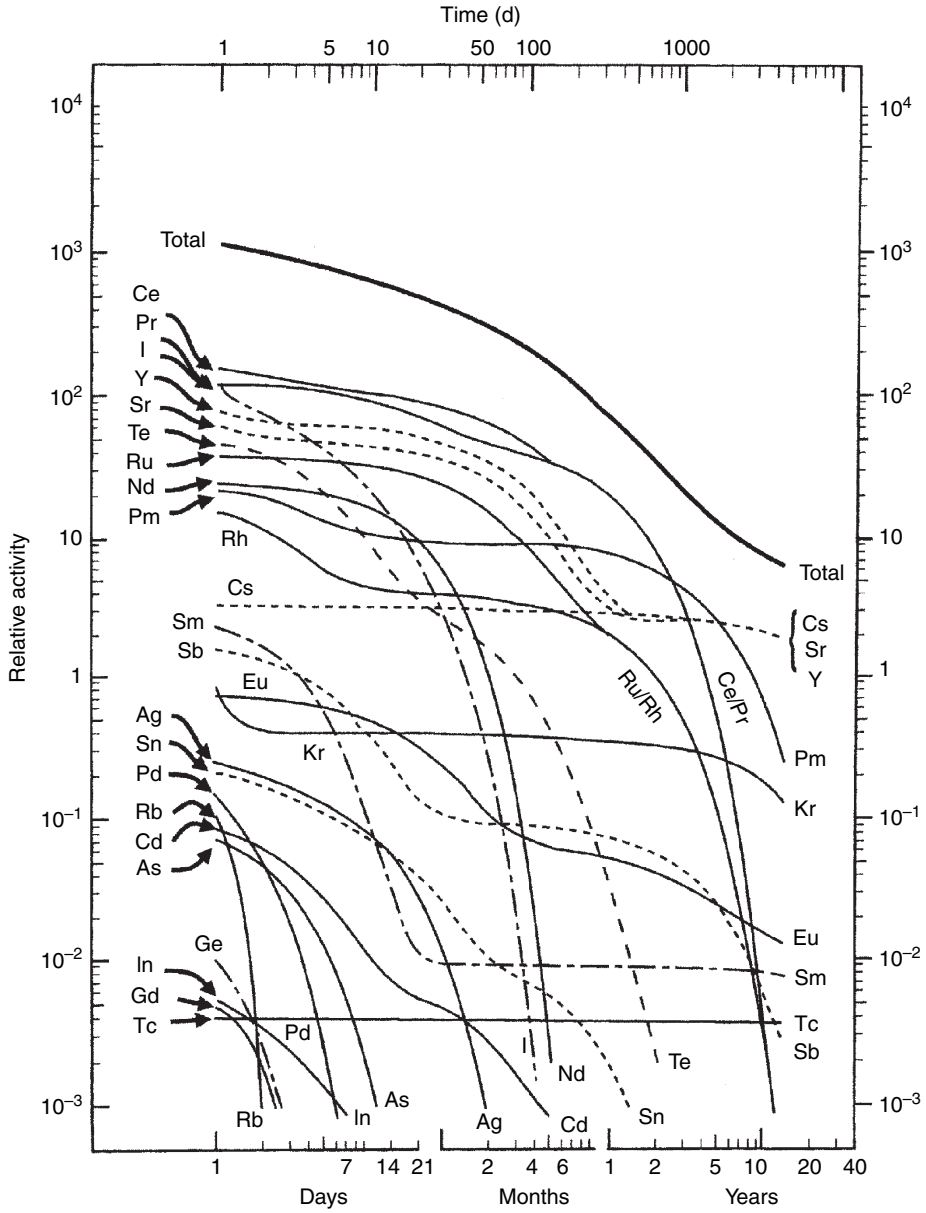

Figure 1.20.: Relative radioactivity from fission products as a function of decay time. Data are for thermal neutron fission of ^{235}U, flux of $1 \times 10^{13}\,\mathrm{n \cdot cm^{-2} \cdot s^{-1}}$ and irradiation time of 2 years. Several different nuclides may contribute to the curve for each element. Extracted from [33][a]

[a] Gordon R. Gilmore. 'Radioactive Decay and the Origin of Gamma and X-Radiation'. en. In: *Practical Gamma-Ray Spectrometry*. John Wiley & Sons, Ltd, 2008, pp. 1–24. ISBN: 978-0-470-86198-1.

The Figure 1.21 highlights that resonances are dependent on the atom mass, the higher the mass the more we expect resonance peaks. It should be noted that when considering even number of neutrons, the cross-section is more stable with average resonance peak distance of 20 eV, whereas odd A number will shorten this distance to the order of 1 eV

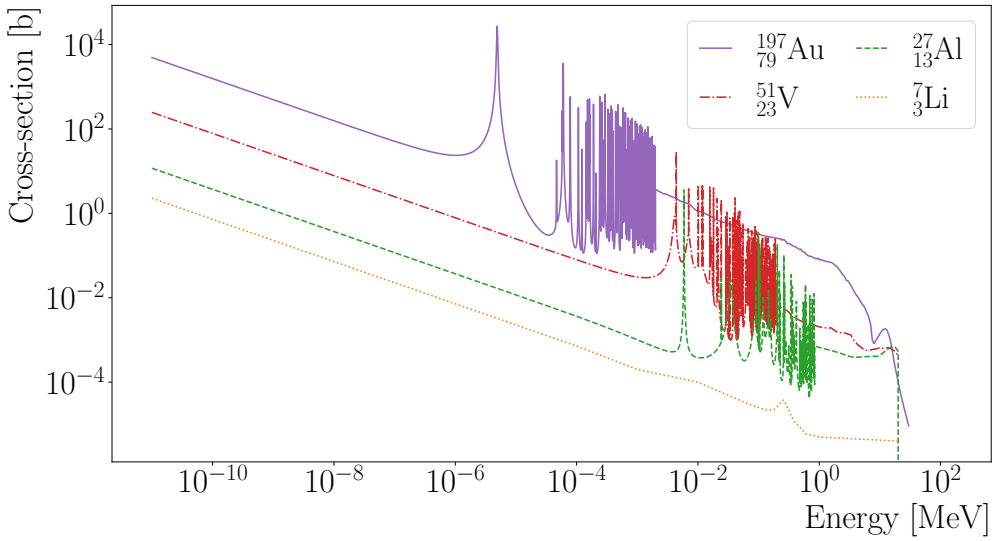

Figure 1.21.: (n, γ) cross-sections for several odd/odd atoms, according to ENDF/B-VIII.1

We distinguish the resolved and the Unresolved Resonance Region (URR). For low energy neutrons, the peaks are well separated: this is the Resolved Resonance Region (RRR).

These peaks can be described by the Breit-Wigner resonance formula:

$$\sigma_i(E_n) = \pi \lambda\!\!\!^{-2} g \frac{\Gamma_n \Gamma_i}{(E_n - E_0)^2 + (\Gamma/2)^2} \tag{1.53}$$

Where:

- $\lambda\!\!\!^{-} = \hbar/p$ the reduced neutron wave-length, where $p = \sqrt{2\mu E_n}$ the impulsion
- μ is the reduced mass, defined as $\frac{1}{\mu} = \frac{1}{\mu_{target}} + \frac{1}{\mu_n}$
- $\Gamma = \hbar/\tau$ resonance width, with τ the meanlife of the compound nucleus
- Γ_n the neutron width
- Γ_i the width for either fission or radiative capture
- E_0 the resonance peak energy
- E_n neutron kinetic energy in the centre of mass

The g-factor is the statistical spin factor:

$$g = \frac{2J+1}{(2s+1)(2l+1)} \tag{1.54}$$

where s is the neutron spin, l the orbital angular momentum and J is the total angular momentum of the resonnance.

Whereas at higher energy, the resonance cannot be discriminated by the measurements, this is the UnResolved Resonance Range (URRR). As shown in the previous figures, inside the unresolved range, the distributed cross-sections are rather the average resonance cross-section.

As most of the application, the neutron spectra are continuous and not mono-energetic, this bias in the cross-section is negligible.

1.5.5. Sources of neutrons

There are two main methods of producing neutron fields. The first method uses radioactive sources, while the second method involves accelerating charged particles. When these particles interact with a suitable thin target, they produce a neutron field whose characteristics can be predicted by the kinematics of the reactions involved. A large number of facilities worldwide deliver neutron fields, either through radionuclide sources or by accelerating charged particles.

Neutrons induced by fission Within a reactor core, the main producers are the fission reactions. They are mainly from neutron-induced fission. Indeed the spontaneous fission have usually low branching ratios (considering ENDF/B-VIII.1, the branching ratio median is of 8 %).

Neutrons induced by radioactivity If a moderate neutron fluence is necessary, then radioactive source maybe be used and the (α, n), (γ, n), or (e^-, n) harnessed. Due to the threshold of such reactions, the main neutron producing reaction is the (α, n). There is limited reactions available, a few are given in Table 1.4.

One of the neutron source used in chapter 2, the AmBe make use of the exothermic reaction $^{9}\mathrm{Be}(\alpha, n)$, thanks to $^{241}\mathrm{Am}$, which emits an alpha of 5.485 MeV.

Table 1.4.: Main reaction (α, n) available with $^{210}\mathrm{Po}$ (E_α=5.304 MeV)

Reaction	Energy threshold [MeV]
$^{6}\mathrm{Li}(\alpha, n)^{9}\mathrm{B}$	6.64
$^{9}\mathrm{Be}(\alpha, n)^{12}\mathrm{C}$	exothermic
$^{10}\mathrm{B}(\alpha, n)^{13}\mathrm{N}$	exothermic
$^{19}\mathrm{F}(\alpha, n)^{22}\mathrm{Na}$	2.33
$^{23}\mathrm{Na}(\alpha, n)^{22}\mathrm{Al}$	3.48
$^{24}\mathrm{Mg}(\alpha, n)^{27}\mathrm{Si}$	8.45
$^{27}\mathrm{Al}(\alpha, n)^{30}\mathrm{P}$	3.06

Photo-neutrons For high-energy photons, one can produce also neutrons. The threshold for this type of reaction is approximately 10 MeV for most nuclei, except for beryllium and deuterium, for which it is around 2 MeV.

They are considered as unwanted secondary emissions, especially in application such as sterilisation via photons or radiotherapy with gammas.

Neutrons induced by spallation If higher neutron fluence is needed, as it is the case for ADS technology, a particle accelerator is necessary.

These spallation reactions are two-stage processes: intra-nuclear cascade, i.e. nucleons are stripped, via inelastic process (of the order of $1\times10^{-22} - 1\times10^{-21}$ s), and produced by evaporation, i.e. neutron-rich excited nuclides relax by emitting neutrons (1×10^{-16} s).

1.6. Conclusion

This chapter has established a basis for understanding the complex interplay between nuclear structure, radioactive decay and radiation-matter interactions. The classification of nuclides and the intrinsic properties that determine their stability have been examined. The concept of the valley of stability and the various decay modes, such as alpha, beta and gamma decay, as well as more exotic transitions, have been described. This highlighted the probabilistic nature of nuclear transformations and the processes involved.

The ionising radiations have been characterised, distinguishing between direct and indirect ionisation mechanisms. A summary of interactions of charged particles, photons, and neutrons with matter in terms of energy transfer, attenuation laws, and cross-sectional behaviour, has been performed. Particular focus was given to neutron interactions, including scattering, capture and fission. Resonance phenomena and neutron sources were examined for their insight into practical applications and experimental setups. Finally, the chapter introduced the Bateman equations and their generalisations, offering a mathematical framework for modelling radioactive decay and nuclide production. These principles are essential for predicting activity evolution and designing irradiation protocols in research and industry.

This chapter pave the notions, that will appear in the following chapters.

Chapter

2. Assessment of induced activation around particle accelerators: modelling and experimental approaches



— Brett: Qu'est-ce qu'elle goûtait cette soupe à la tomate ?
— Lewis: Elle goûtait la tomate.
— Criquette: Eeeeelle goûtaiiiit la tomaaaate ! Êtes-vous soudainement un spécialiste de la tomate, Lewis ? Votre mère était-elle une tomate ?

(L'ambition de Criquette, Le Coeur a ses raisons – 2006)

2.1. Generalities on Monte Carlo Methods . . . 44
2.1.1. Principle . . . 45
2.1.2. Codes of interest . . . 48
2.2. Experimental methods . . . 56
2.2.1. Gamma spectroscopy . . . 57
2.2.2. Solid State Nuclear Track Detector . . . 64
2.3. Assessment of induced activation . . . 69
2.3.1. Around medical LINAC . . . 69
2.3.2. Around an AmBe source . . . 77
2.3.3. Model assumptions . . . 79
2.3.4. Around CYRCé . . . 84
2.3.5. Conclusions and perspectives . . . 91

The formulation of a decommissioning plan necessitates an estimation of radionuclide production within the facility, as referenced in the Introduction chapter. A modelling approach, particularly a Monte Carlo method (see section 2.1), can provide such estimations. As previously introduced, the issue of pure beta emitters constitutes a particularly

significant aspect to consider. Monte Carlo codes are capable of estimating their presence. Indeed, if the models can adequately reproduce easier-to-measure observables, they may be deemed reliable for estimating the presence and quantity of these emitters. This approach limits the requirement for costly and destructive techniques, such as liquid scintillation counting. This section outlines generalities on Monte Carlo codes and details the specific code used in the presented studies. The value of intercomparison codes and nuclear databases will be demonstrated through three case studies. These cases include a simple benchmark around a reduced model for radiotherapy head component, a neutron activation study around an AmBe calibrator, and an analysis around a radioisotope production cyclotron. The experimental techniques employed, primarily gamma spectroscopy and nuclear track detectors, will also be presented. The latter technique will be introduced alongside its associated data acquisition system, in more depth.

2.1. Generalities on Monte Carlo Methods

The Monte Carlo method is a powerful and versatile computational technique that uses randomness and statistical sampling to solve complex mathematical and physical problems. Its core principle is to estimate numerical values by performing a large number of random simulations, effectively using probability to find solutions that might be too difficult or impossible to derive through purely analytical means.

Origins and History The technique was formally named the "Monte Carlo" method in the late 1940s by scientists Stanislav Ulam, John von Neumann, and Nicholas Metropolis at Los Alamos National Laboratory, alluding to the famous casinos of Monte Carlo as a metaphor for its reliance on random chance [34][1]. While its theoretical roots date back to 19th-century probability and statistics (e.g. Buffon needle problem), the first major practical application often mentioned was in modelling neutron transport for nuclear weapons research. The large-scale use of the Monte Carlo method was fundamentally enabled by the advent of electronic computers. Subsequent progress in computing hardware, notably the rise of high-performance computing clusters, greatly expanded the available processing power. This increase in computational resources, have since facilitated the creation of far more complex and detailed models, broadening access beyond dedicated centralised facilities.

The primary advantage of the Monte Carlo method is its simplicity and intuitive nature. It provides a direct, "brute-force" approach to problem-solving that retains a close relationship to the physical or conceptual system being modelled.

[1] Nicholas Metropolis and S. Ulam. 'The Monte Carlo Method'. In: *Journal of the American Statistical Association* 44.247 (1949). _eprint: https://www.tandfonline.com/doi/pdf/10.1080/01621459.1949.10483310, pp. 335–341. DOI: 10.1080/01621459.1949.10483310.

2.1.1. Principle

A foundational application is in nuclear physics, where it is used to model the transport of, in particular, neutrons, photons, or electrons through a geometry, i.e. a combination of (different) material.

The "history" of a single particle is simulated from its birth (emission) to its death (absorption or escape from the system). At each step, the occurrence and outcome of interactions are randomly sampled based on known physics and probability density functions (e.g., interaction cross-sections). By repeating this for millions of particles, a highly detailed model of the entire transport process is built, albeit at a possible significant computational cost. This process is illustrated in Figure 2.1.

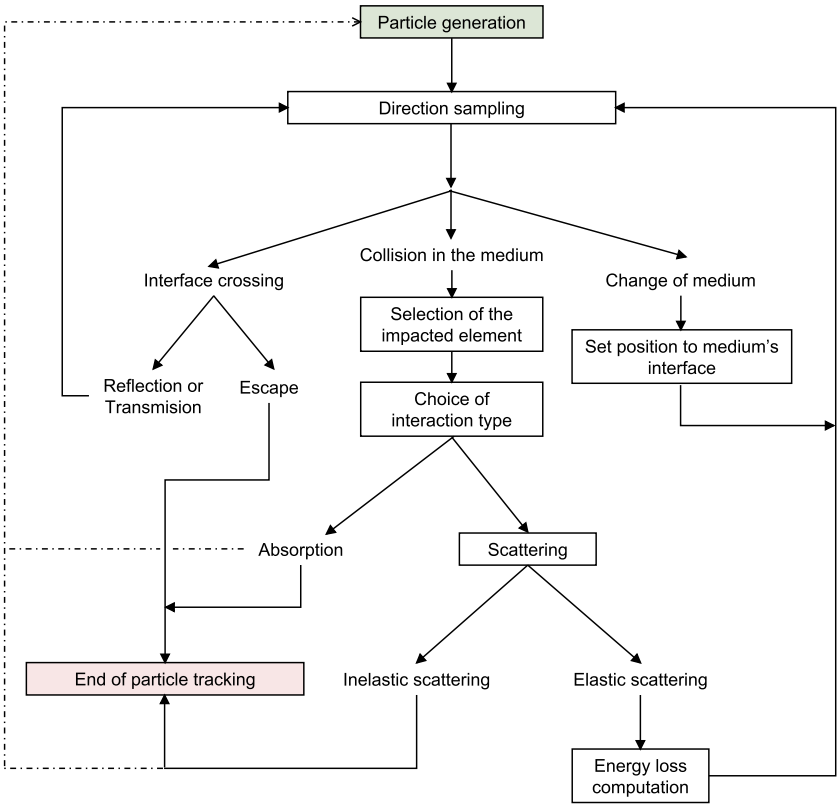

Figure 2.1.: Basic structure of Monte Carlo transport simulation, based on [35][a]

[a] Abdellatif Nachab. 'Etudes expérimentales et modélisations Monte Carlo de l'auto-absorption gamma et de la dosimétrie active par capteurs CMOS'. fr. PhD thesis. Université Louis Pasteur - Strasbourg I, Dec. 2003.

Although the Monte Carlo simulation is a powerful tool, it has its own limitations. The simulation can be computationally intensive, requiring significant processing power to perform a large number of simulations in a reasonable amount of time. Yet as every methods, its accuracy depends on the quality of the entered data and the assumptions made.

Transport The trajectory and interaction probabilities of an incident particle define its history within a medium until its termination. These probabilities are governed by interaction cross-sections, which vary by mode, such as scattering or absorption, see chapter 1.

The likelihood of a particle traversing a medium of thickness l without interaction is expressed as:

$$p(l) = e^{-\Sigma l} \tag{2.1}$$

Here, $\Sigma = n\sigma$ denotes the total macroscopic cross-section, where n is the number density of target nuclei and σ is the microscopic cross-section.

The probability for a collision occurring within an infinitesimal path length dl at a distance l is hence:

$$p(l)dl = e^{-\Sigma l}\Sigma dl \tag{2.2}$$

Integrating this quantity yields the cumulative probability of interaction up to a path length l. This integral is equated to a uniformly distributed random number $\epsilon \in [0, 1]$ for sampling purposes:

$$\epsilon = \int_0^l e^{-\Sigma l'}\Sigma dl' = 1 - e^{-\Sigma l} \tag{2.3}$$

Uncertainty management Simulation results require an estimated reliability in terms of their statistical uncertainty. This uncertainty must be considered during the interpretation of the results. Usually, when considering the law of large number, this estimator is defined as the standard deviation of the mean s_x divided by the estimated mean x.

Considering N primaries, i.e. source particles, the sample mean is calculated as:

$$\overline{x} = \frac{1}{N}\sum_{i=1}^{N}\omega_i x_i \tag{2.4}$$

Where x_i is the measurement related to i-th, with ω_i the weight of the primary. The sample deviation is given by:

$$s_x^2 = \frac{1}{N}\sum_{i=1}^{N}(x_i - \overline{x})^2 \tag{2.5}$$

As a general rule, the statistical uncertainty is proportional to $1/\sqrt{N}$ [36][1]. This uncertainty can therefore be reduced by increasing the total number of simulated events N, albeit at the cost of greater computation time. While such estimators cannot reference the accuracy of an experimental or theoretical result, they aid in assessing the reliability of the Monte Carlo calculation.

[1] Christopher John Werner et al. *MCNP User's Manual Code Version 6.2*. Tech. rep. LA-UR-17-29981. Los Alamos, NM, USA: Los Alamos National Laboratory, Oct. 2017.

Uncertainty on nuclear data Beyond the statistical uncertainty inherent in Monte Carlo simulations, an additional and often dominant source of uncertainty arises from the nuclear data itself, which serves as a primary information to the calculation.

Evaluated nuclear data libraries, such as ENDF/B or JEFF, provide the estimates for fundamental quantities like reaction cross sections, the average number of prompt fission neutrons or resonance parameters. These uncertainties for these datasets are stored in the libraries as covariance matrices, which characterize the variance of each nuclear data point and their correlations across different energy groups or different reaction channels [37][1].

To assess how these nuclear data uncertainties affect a computed response $\mathbf{r}(\alpha)$ (such as the effective multiplication factor k_{eff}), one must propagate the parameter uncertainties through the computational model.

The fundamental approach for this propagation is the "sandwich rule", which combines the sensitivities of the response to each parameter with the parameter covariance matrix:

$$\text{var}\left(\mathbf{r}(\alpha)\right) = \mathbf{S}\mathbf{C}_\alpha\mathbf{S}^T \tag{2.6}$$

where $\mathbf{r}(\alpha)$ is the response of interest, $\mathbf{S}$ is the vector of sensitivities and $\mathbf{C}_\alpha$ is the covariance matrix of the model parameters (α) [38][2].

In order to determine the sensitivity response of the model, Monte Carlo tools as SANDY [39][3] or XSUDA [40][4] have been developped (generating perturbations within the evaluated files, that should be used in the Monte Carlo model rerun, in order to determine the sensitivity vectors). When there are many systems parameters, deterministic approach as Adjoint Sensitivity Analysis Procedure (ASAP) [41, 42][5] can be used.

As it is not an easy feat, such propagation have not been performed during this PhD.

Fundamental components A Monte Carlo simulation for particle transport is defined by several fundamental components.

[1] Pavel Obložinský, Michal Herman, and Said F. Mughabghab. 'Evaluated Nuclear Data'. en. In: *Handbook of Nuclear Engineering*. Ed. by Dan Gabriel Cacuci. Boston, MA: Springer US, 2010, pp. 83–187. ISBN: 978-0-387-98149-9. DOI: 10.1007/978-0-387-98149-9_2.

[2] Dan Gabriel Cacuci and Mihaela Ionescu-Bujor. 'Sensitivity and Uncertainty Analysis, Data Assimilation, and Predictive Best-Estimate Model Calibration'. en. In: *Handbook of Nuclear Engineering*. Ed. by Dan Gabriel Cacuci. Boston, MA: Springer US, 2010, pp. 1913–2051. ISBN: 978-0-387-98149-9. DOI: 10.1007/978-0-387-98149-9_17.

[3] L. Fiorito et al. 'Nuclear data uncertainty propagation to integral responses using SANDY'. in: *Annals of Nuclear Energy* 101 (Mar. 2017), pp. 359–366. ISSN: 0306-4549. DOI: 10.1016/j.anucene.2016.11.026.

[4] W. Zwermann et al. 'NUCLEAR DATA UNCERTAINTY AND SENSITIVITY ANALYSIS WITH XSUSA FOR FUEL ASSEMBLY DEPLETION CALCULATIONS'. in: *Nuclear Engineering and Technology* 46.3 (June 2014), pp. 343–352. ISSN: 1738-5733. DOI: 10.5516/NET.01.2014.711.

[5] Dan G. Cacuci. *Sensitivity & Uncertainty Analysis, Volume 1: Theory*. New York: Chapman and Hall/CRC, May 2003. ISBN: 978-0-429-21009-9. DOI: 10.1201/9780203498798, D. G. Cacuci, Mihaela Ionescu-Bujor, and Ionel Michael Navon. *Sensitivity and uncertainty analysis, Volume 2: Application to Large Scale Systems*. en. Boca Raton: Chapman & Hall/CRC Press, 2003. ISBN: 978-1-58488-115-5 978-1-58488-116-2.

- The Geometry provides the spatial representation of the environment, including detectors, shields, and containers.
- Materials specify the composition of each geometric volume, such as lead, water, or silicon. This definition includes elemental composition, density, and sometimes temperature, which directly influence interaction probabilities.
- Physics data and cross-sections constitute the rules of the simulation. These database contains the probabilities for all possible interactions, such as scattering or absorption, for each particle type and energy. It forms the core of the probabilistic sampling process.
- The Source, that defines the initial conditions for the primary particles. It specifies the particle type, for instance, neutron, photon, or electron. The source also defines the particle energy, which can be a single value or a spectral distribution. Furthermore, it establishes the initial position and direction of the particles.
- Tallies[1] are the specific quantities the user aims to determine through the simulation. These metrics represent the goals of the calculation, such as energy deposited in a detector. Other examples include the number of particles passing through a surface or the rate of a specific nuclear reaction.

2.1.2. Codes of interest

The Monte Carlo method, designed for modelling stochastic phenomena, has revolutionized nuclear physics by enabling the accurate (or at least detailed) simulation of particle transport, radiation interactions, and complex system behaviour.

It serves as a cornerstone technique across several critical domains, including reactor physics, radiation protection, medical physics, and nuclear instrumentation. A wide variety of specialised Monte Carlo codes exist, each with its own application range and optimised use cases. Modelling complex systems, such as particle accelerator facilities, often requires multiphysics codes capable of handling coupled physical phenomena.

The following sections present the primary codes commonly used in the context of the studies presented in this chapter, focusing on their origins, structure, and physics capabilities.

a) Geant4

Geant4 is a Monte Carlo simulation toolkit for modelling the passage of particles through matter [43, 44, 45][2]. Its development was initiated in the mid-1990s by the European Or-

[1] Using MCNP designation.

[2] J. Allison et al. 'Recent developments in Geant4'. In: *Nuclear Instruments and Methods in Physics Research Section A: Accelerators, Spectrometers, Detectors and Associated Equipment* 835 (2016), pp. 186–225. ISSN: 0168-9002. DOI: https://doi.org/10.1016/j.nima.2016.06.125, J. Allison et al. 'Geant4 developments and applications'. In: *IEEE Transactions on Nuclear Science* 53.1 (Feb. 2006), pp. 270–278. ISSN: 1558-1578. DOI: 10.1109/TNS.2006.869826, S. Agostinelli et al. 'Geant4—a simulation toolkit'. In: *Nuclear Instruments and Methods in Physics Research Section A: Accelerators, Spectrometers, Detectors and Associated Equipment* 506.3 (July 2003), pp. 250–303. ISSN: 0168-9002. DOI: 10.1016/S0168-9002(03)01368-8.

ganization for Nuclear Research (CERN) and has since them become worldly as Geant4 toolkit is free and collabourative. It was conceived as a successor to the FORTRAN-based Geant3 program, aiming to leverage modern software engineering practices, specifically object-oriented design implemented in C++, to address the increasingly complex needs of High-Energy Physics (HEP) experiments [46][1].

Originally developed for HEP applications such as the Large Hadron Collider (LHC) experiments, its scope has vastly expanded. Geant4 is now a cornerstone application in diverse fields including nuclear physics, space science, medical physics (e.g., radiotherapy treatment planning and dosimetry), and radiation protection. The toolkit is maintained and developed by the international Geant4 Collaboration, but any user can, and are invited to, contribute.

Its object-oriented architecture provides a flexible and extensible framework for simulating complex geometries, modelling a wide spectrum of physics processes across a broad energy range, handling detector responses (hits and digitization), and visualizing simulations and results. The design supports both sequential and multithreaded execution, enabling efficient utilization of modern computing resources.

Physics Lists A central concept in Geant4 is the *physics list*, a user-constructed selection of particles and physics processes that defines the simulation's behaviour. The toolkit provides pre-configured, self-consistent physics lists curated for different applications. Some of the main reference physics lists include:

- `QGSP_BIC`: A standard list for hadron therapy and general-purpose simulations, combining the Quark-Gluon String (QGS) model for high-energy hadronic interactions with the Binary Cascade (BIC) model for intermediate energies.
- `QGSP_BERT`: A common choice for high-energy physics calorimetry, pairing the QGS model with the Bertini Cascade (BERT) for intermediate energies.
- `FTFP_BERT`: The recommended list for many LHC applications, using the Fritiof (FTF) string model and the Bertini Cascade, providing a smooth transition between models.
- `Shielding`: Optimized for shielding applications, featuring improved low-energy neutron cross-sections.
- `EmStandard`: A set of options for electromagnetic physics, offering different levels of accuracy and performance (e.g., `EmStandard_opt4` for high accuracy in calorimetry).
- *High Precision (HP)*: Provides high-precision neutron tracking using evaluated nuclear data libraries at thermal and epithermal energies, crucial for applications like reactor physics and neutron shielding.
- *Low Energy Nuclear Data (LEND)* (Low Energy Nuclear Data): An alternative package for low-energy neutron interactions, utilizing evaluated data and specifically developed for photonuclear precise modelling.

[1] Geant4 Collaboration. *Introduction to Geant4*. en. Tech. rep. Release 11.3 - Rev9.2. June 2025, p. 17.

Users can also construct custom physics lists by selecting specific models for different particles and energy ranges, tailoring the simulation to their precise requirements.

b) MCNP

MCNP is a general-purpose Monte Carlo simulation code developed by Los Alamos National Laboratory (LANL) starting in the 1970s, merging previous special-purpose Monte Carlo software, developped by the institute. The development of MCNP began as a means to support the design and analysis of nuclear reactors and weapons, but its applications have since expanded to include radiation shielding, dosimetry, medical physics, and more. MCNP's versatility is partly due to its ability to handle complex three-dimensional geometries and its extensive libraries of nuclear and atomic data.

It is designed for modelling the transport of neutrons, photons, and electrons through various materials and geometries. MCNP is written primarily in Fortran and is maintained by LANL with a global user community, which is protected under a strict individual licence. Over the decades, MCNP has become a reference tool in numerous scientific and engineering applications.

MCNP's architecture supports both continuous-energy and multi-group transport methods, making it suitable for a variety of simulation scenarios. The code also includes advanced features such as variance reduction techniques, criticality calculations, and the ability to simulate coupled neutron-photon-electron transport.

MCNP provides extensive capabilities for detailed 3D geometry modelling (using Combinatorial Geometry) and source definition, making it highly versatile for a wide range of applications.

Physics Models A central concept in MCNP is the possibility to select physics models and data tables that defines the simulation's behavior for particle transport and interactions. The code allows users to choose between pre-configured options or custom-tailored selections for different particles and energy ranges.

MCNP-6 is able to transport 37 particle types, as well as arbitrary nuclei. The code allows to controls physics models thanks to several cards (`LCA`, `LCB`, `LCC`, `LEA`, `LEB`), enabling several models in many combination:

- Bertini/Dresner evaporation model
- ISABEL/Dresner for reactions induced by d, t, 3He, 4He, and antinucleons at energies up to 1 GeV per nucleon
- INCL4/Dresner
- Bertini/ABLA
- ISABEL/ABLA
- INCL4/ABLA
- CEM03.03 default event generator
- LAQGSM03.03
- Several fission models are available from simpler sine/cosine sampling model, to Lawrence Livermore National Laboratory (LLNL), Fission Reaction Event Yield

Algorithm (FREYA) or Cascading Gamma-ray Multiplicity and Fission (CGMF) fission models

c) Fluka

FLUKA (from the german, meaning "Fluctuating Cascade") is a fully integrated Monte Carlo simulation package for the interaction and transport of particles and nuclei in matter [47, 48][1]. The code, based on the work of J. Ranft, has been first introduced in 1989, as part of a collaboration between CERN and Istituto Nazionale di Fisica Nucleare (INFN), in collaboration with other international institutions. Initially focused on high-energy physics applications such as accelerator shielding and calorimetry, FLUKA has evolved into a general-purpose tool used across a wide spectrum of scientific and applied fields.

The code is written primarily in Fortran, many of its physical models are based on microscopic theories and are consistently applied across all energy ranges and particle types. A key design philosophy of FLUKA is to minimize the number of free parameters, ensuring predictive power even in regions where experimental data are scarce. Its capabilities span from the simulation of hadronic and electromagnetic showers to the detailed treatment of low-energy neutron transport, heavy-ion interactions, and the generation of optical photons.

Originally developed for particle physics, FLUKA's application base has expanded dramatically. It is now a critical tool in medical physics (e.g., proton and ion radiotherapy, dosimetry, and treatment planning), cosmic ray studies, radiation protection and shielding or also accelerator design [49][2]. The code is maintained and developed by the FLUKA Collaboration, with core development led by its original authors and key contributors.

FLUKA provides a flexible, though not object-oriented, framework for simulating complex geometries using an enhanced version of Combinatorial Geometry (CG). It features a rich set of biasing techniques for variance reduction, and offers numerous scoring options for estimating fluence, dose, energy deposition, and other quantities. While for most application, the regular American Standard Code for Information Interchange (ASCII) input is sufficient, user customization can be achieved through set of Fortran routines, for which templates are provided.

It should be mentioned, that since 2019, two separate version coexist, when maintained by the INFN (which will be referred as FlukaINFN) and second version maintained by CERN (referred as FlukaCERN).

[1] A. Ferrari et al. *FLUKA: A Multi-Particle Transport Code*. English. Tech. rep. SLAC-R-773. SLAC National Accelerator Lab., Menlo Park, CA (United States), Dec. 2005. DOI: 10.2172/877507, G. Battistoni et al. 'The FLUKA code: description and benchmarking'. In: *AIP Conference Proceedings* 896.1 (Mar. 2007), pp. 31–49. ISSN: 0094-243X. DOI: 10.1063/1.2720455.

[2] T. T. Böhlen et al. 'The FLUKA Code: Developments and Challenges for High Energy and Medical Applications'. In: *Nuclear Data Sheets* 120 (2014), pp. 211–214. ISSN: 0090-3752. DOI: https://doi.org/10.1016/j.nds.2014.07.049.

Physics Capabilities and Models A distinctive feature of FLUKA is its integrated and consistent approach to physics modelling, often using a single unified model across a wide energy range rather than a patchwork of different models. Key components of its physics repertoire include:

- **Hadronic Interactions:** The PreEquilibrium Approach to Nuclear Thermalization) (PEANUT) model provides a unified description of hadron-nucleus interactions from a few GeV down to the reaction threshold, combining a generalized intra-nuclear cascade with pre-equilibrium and equilibrium (evaporation, fission, Fermi break-up) stages. At higher energies (up to thousands of TeV), the Dual Parton Model (DPM) and a Glauber-Gribov multiple scattering approach are used. Interfaces to external generators like DPMJET-III and RQMD extend its capabilities to nucleus-nucleus collisions.
- **Electromagnetic Interactions:** Features detailed models for electron, positron, and photon transport, including the Landau-Pomeranchuk-Migdal effect, delta-ray production, and polarized photon interactions. The emission of Cherenkov, transition radiation, and scintillation photons is also supported.
- **Low-Energy Neutrons:** Offers two complementary approaches: a multi-group (260-neutron, 42-gamma group) library with P_5 Legendre expansion for rapid calculations, and a fully correlated pointwise cross-section library for event-by-event detailed simulations, including Doppler broadening and thermal scattering laws. The FlukaCERN version has integrated a pointwise treatment based on Geant4 data libraries (G4NDL), providing an alternative to the traditional multigroup method.
- **Heavy Ions and Special Particles:** Can transport heavy ions with or without nuclear interactions and includes specialized treatment for muons (including photonuclear interactions) and neutrinos.
- **Biasing and Scoring:** Includes a comprehensive suite of variance reduction techniques (e.g., importance sampling, weight windows, leading particle biasing) and a vast array of estimators for scoring physical quantities, from simple fluence and dose to more advanced metrics like Non-Ionizing Energy Loss (NIEL) and Displacement Per Atom (DPA).

Users can configure simulations through an input file system that controls physics settings, geometry, materials, source definition, and scoring, using what are called cards.

While FLUKA provides sensible defaults grouped into pre-configured settings (e.g., for hadrontherapy, shielding, or electromagnetic showers), one can have fine-grained control over most aspects of the simulation via a comprehensive set of input options.

d) PHITS

PHITS (Particle and Heavy Ion Transport code System) is a Monte Carlo simulation toolkit designed for modelling the transport of particles through matter. Its development was initiated in the early 2000s by the Japan Atomic Energy Agency (JAEA). PHITS was conceived to address the needs of diverse fields such as radiation shielding, radiological

protection, and medical physics.

In a similar manner as MCNP, as does FLUKA, PHITS have a versatile geometry handling capabilities and comprehensive physics models that cover a broad spectrum of particles and energy ranges. The design supports both sequential and parallel execution, enabling efficient use of modern computing resources.

Physics Models A central concept in PHITS is the use of comprehensive physics models that define the behaviour of particles in simulations. The toolkit provides pre-configured physics models optimized for different applications.

PHITS integrates a variety of physics models tailored to specific particle interactions and energy ranges. The Figure 2.2 synthesize this highly modular structure.

- `Jaeri Quantum Molecular Dynamics (JQMD)/Generalied Evaporation Model (GEM)`: Models for describing heavy ion interactions through the intranuclear cascade model and subsequent evaporation processes.
- `EVAPORATION`: Focused on low-energy nuclear reactions, essential for modelling neutron and light ion interactions in shielding applications.
- `Electron Gamma Shower (EGS) model`: A comprehensive framework for simulating electromagnetic interactions, critical for medical physics and radiation therapy planning.
- `Biological dose model`: Specialized models for calculating biological doses, particularly useful in radiation protection and space missions.

e) OpenMC

OpenMC is a modern Monte Carlo particle transport code primarily developed by the Computational Reactor Physics Group at the Massachusetts Institute of Technology (MIT), starting in 2011. OpenMC is designed to facilitate neutral-particle radiation transport simulations with capabilities for fixed source, k-eigenvalue, and subcritical multiplication calculations. The code is notable for its flexibility, accuracy, and open-source nature, which has fostered a growing community of users and developers.

The development of OpenMC was motivated by the need for a versatile and user-friendly tool that could handle complex geometries and advanced physics models. It supports both continuous-energy and multi-group transport methods, making it suitable for a wide range of applications in nuclear engineering and beyond. OpenMC's architecture is built with modern software practices in mind, utilizing C++ and Python interfaces to provide users with powerful and intuitive tools for simulation setup and analysis.

Physics Capabilities and Models OpenMC's comprehensive physics models cover a wide range of particle interactions and transport phenomena. Key components of its physics repertoire include:

- **Neutron Transport:** OpenMC employs detailed neutron transport models that utilize evaluated nuclear data libraries to simulate neutron interactions across a

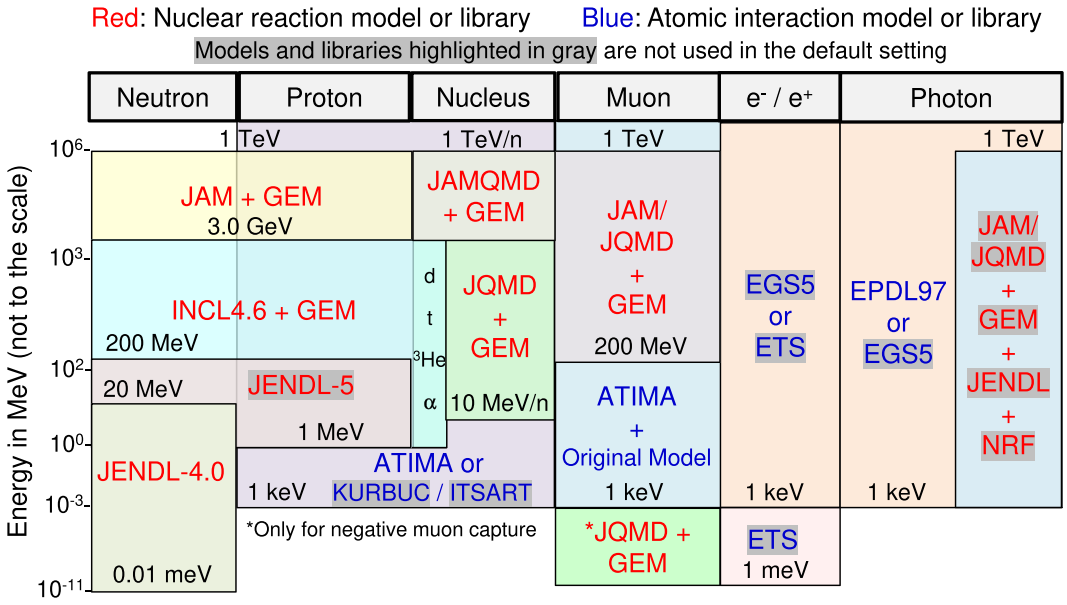

Figure 2.2.: Cartography of physics model of PHITS, from [50][a]

[a]Tatsuhiko Sato et al. 'Recent improvements of the particle and heavy ion transport code system – PHITS version 3.33'. In: *Journal of Nuclear Science and Technology* 0.0 (2023), pp. 1–9. ISSN: 0022-3131. DOI: 10.1080/00223131.2023.2275736.

wide energy spectrum. This includes thermal scattering and resonance absorption processes.

- **Photon Transport:** Comprehensive models for photon interactions, including Compton scattering, photoelectric absorption, and pair production, are integrated into OpenMC, enabling accurate simulations of photon transport.
- **Electron Transport:** OpenMC includes models for electron transport, accounting for processes such as ionization, bremsstrahlung, and positron annihilation.
- **Criticality Calculations:** The code features advanced algorithms for criticality safety analysis, which are essential for nuclear reactor design and safety studies.
- **Variance Reduction Techniques:** OpenMC provides a suite of variance reduction techniques to improve the efficiency and accuracy of simulations, particularly in complex or deep-penetration problems.

Users can configure OpenMC simulations through a flexible input file system that allows for detailed control over geometry, material definitions, source specifications, and output parameters. The code also supports parallel processing, enabling large-scale simulations to be performed efficiently on modern high-performance computing systems.

f) TRIPOLI

TRIPOLI is a Monte Carlo particle transport code that has been developed and maintained by the French Atomic Energy Commission (CEA). It is designed to simulate the

transport of neutrons, photons, and charged particles in complex three-dimensional geometries. TRIPOLI is widely recognized for its accuracy and efficiency in modelling particle interactions across a wide range of energies and materials. The development of TRIPOLI began in the 1970s, with the goal of providing a versatile tool for nuclear physics and engineering applications. Over the years, TRIPOLI has evolved to incorporate advanced physics models and computational techniques, making it suitable for a broad spectrum of applications in nuclear science and technology. TRIPOLI is written primarily in Fortran and is characterized by its robust and comprehensive physics models, which cover neutron, photon, and electron transport. The code's architecture supports both continuous-energy and multi-group transport methods, and it includes advanced features such as variance reduction techniques and criticality calculations.

Physics Capabilities and Models TRIPOLI's comprehensive physics models cover a wide range of particle interactions and transport phenomena. Key components of its physics repertoire include:

- **Neutron Transport:** TRIPOLI employs detailed neutron transport models that utilize evaluated nuclear data libraries to simulate neutron interactions across a wide energy spectrum. This includes thermal scattering and resonance absorption processes.
- **Photon Transport:** Comprehensive models for photon interactions, including Compton scattering, photoelectric absorption, and pair production, are integrated into TRIPOLI, enabling accurate simulations of photon transport.
- **Electron Transport:** TRIPOLI includes models for electron transport, accounting for processes such as ionization, bremsstrahlung, and positron annihilation.
- **Criticality Calculations:** The code features advanced algorithms for criticality safety analysis, which are essential for nuclear reactor design and safety studies.
- **Variance Reduction Techniques:** TRIPOLI provides a suite of variance reduction techniques to improve the efficiency and accuracy of simulations, particularly in complex or deep-penetration problems.

Users can configure TRIPOLI simulations through a flexible input file system that allows for detailed control over geometry, material definitions, source specifications, and output parameters. The code also supports parallel processing, enabling large-scale simulations to be performed efficiently on modern high-performance computing systems.

g) SERPENT

SERPENT is a continuous-energy Monte Carlo reactor physics code developed by VTT Technical Research Centre of Finland and later also by the Department of Nuclear Engineering at Texas A&M University. It is designed primarily for simulations related to nuclear reactor physics, including neutron transport calculations, criticality safety, and reactor core analysis. The development of SERPENT began in the early 2000s with the aim of providing a versatile and efficient tool for nuclear reactor simulations. It has since evolved into a comprehensive code that supports a wide range of applications in nuclear

science and engineering. SERPENT is written primarily in C, which contributes to its computational efficiency and portability across different platforms. SERPENT is widely recognized for its ability to handle complex reactor geometries and its comprehensive set of nuclear data libraries. The code supports both continuous-energy and multi-group neutron transport methods, offering flexibility in modelling various types of reactors, including thermal and fast reactors. Additionally, SERPENT includes advanced features such as depletion calculations, sensitivity analysis, and uncertainty quantification, making it a powerful tool for reactor physics studies.

Physics Capabilities and Models SERPENT's physics capabilities are centreed around neutron transport and the associated nuclear reactions. Key components of its physics repertoire include:

- **Neutron Transport:** SERPENT employs detailed neutron transport models that utilize evaluated nuclear data libraries to simulate neutron interactions across a wide energy spectrum. This includes thermal scattering and resonance absorption processes.
- **Depletion Calculations:** The code features advanced depletion calculation capabilities, allowing users to simulate the evolution of reactor cores over time. This is essential for studies related to fuel management and reactor operation.
- **Sensitivity and Uncertainty Analysis:** SERPENT includes tools for performing sensitivity and uncertainty analysis, helping users to assess the impact of various parameters on reactor performance and safety.
- **Multi-physics Coupling:** SERPENT can be coupled with other codes for multi-physics simulations, such as thermal-hydraulics and fuel performance calculations, providing a more comprehensive analysis of reactor systems.
- **Variance Reduction Techniques:** The code provides a suite of variance reduction techniques to improve the efficiency and accuracy of simulations, particularly in complex or deep-penetration problems.

Users can configure SERPENT simulations through a flexible input file system that allows for detailed control over geometry, material definitions, source specifications, and output parameters. The code also supports parallel processing, enabling large-scale simulations to be performed efficiently on modern high-performance computing systems.

2.2. Experimental methods

This section covers the basics for the two type of detectors used in this work. First gamma spectroscopy, and in particular high resolution spectroscopy using high purity germanium detectors. And in a second part, the more exploratory solid state nuclear track detectors (SSNTD).

2.2.1. Gamma spectroscopy

The gamma spectroscopy is a non-destructive technique used to identify and quantify radionuclides based on the energy and intensity of gamma rays they emits. It is widely used in nuclear physics, medical applications, or even environmental monitoring or geosciences. The first gamma spectrum obtained using a cylindrical lithium-diffused germanium PN junction (h = 8 mm, = 18 mm) operating at 77 K was published by Freck and Wakefield [51][1].

A spectrum is a set of peaks originating from the various interaction processes described in section 1.4, see a typical example in Figure 2.3.

There are some key structure that should be mentioned, synthesised in Figure 2.4:

- A total absorption peak that occurs when the incident photon's energy is completely deposited in the detector. This energy deposition can occur through one or more successive interactions carried out within a time interval shorter than the detector's resolution time. This corresponds to the time taken to collect the charges set in motion in the detection volume.
- The Compton background, which is defined as the partial deposition of the incident photon's energy. This extends from the backscattering peak ($\theta = \pi$ rad, maximum transfer to the Compton electron), located at $E_{min} = 0.226$ MeV, to the photoelectric peak ($\theta = 0$, no energy transfer). The Compton front, located at 1.774 MeV, corresponds to the difference $E_\gamma - E_{min}$. The backscattering peak is mainly due to the influence of the environment surrounding the active part of the detector.
- The backscattering peak corresponds to the backscattering of photons in the environment surrounding the active part of the detector.
- Escape peaks: these result from the materialisation effect (if $E_\gamma \geq 1.022$ MeV) and are located at $E_\gamma - 0.511$ MeV and $E_\gamma - 1.022$ MeV for single and double escape peaks, respectively.
- The annihilation peak is due to the annihilation of a positron with an electron in the traversed medium and is located at 0.511 MeV for $E_\gamma \geq 1.022$ MeV.

Semiconductors Semiconductors are materials with an electrical conductivity intermediate between that of conductors and insulators.

According to band theory, the electronic properties of a semiconductor are defined by its valence band and conduction band, separated by a forbidden energy gap (see Figure 2.5). The valence band is populated with electrons that do not contribute to electrical conduction. For conduction to occur, electrons must be excited across the band gap into the conduction band, where they are free to move, simultaneously leaving behind positively charged holes in the valence band.

The width of this band gap is a critical material property and varies between different

[1] D. V. Freck and J. Wakefield. 'Gamma-Ray Spectrum obtained with a Lithium-drifted p–i–n Junction in Germanium'. en. In: *Nature* 193.4816 (Feb. 1962), pp. 669–669. ISSN: 1476-4687. DOI: 10.1038/193669a0.

(a) Typical spectrum for ^{137}Cs

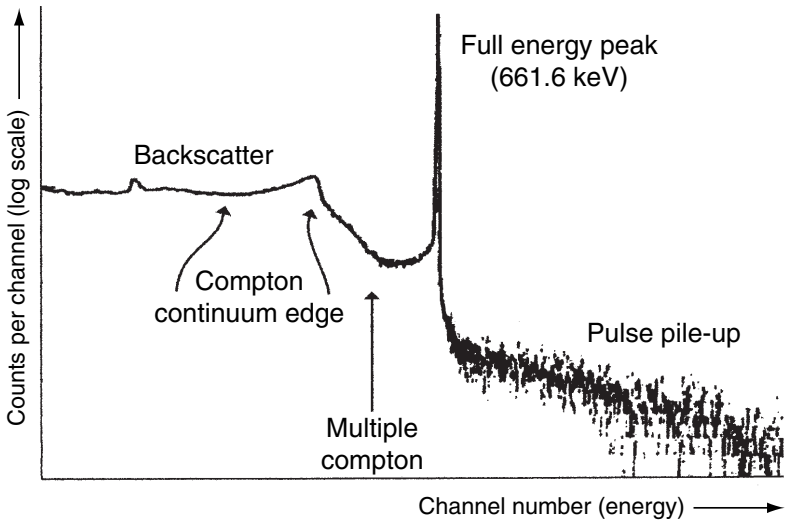

(b) Typical spectrum for ^{28}Al

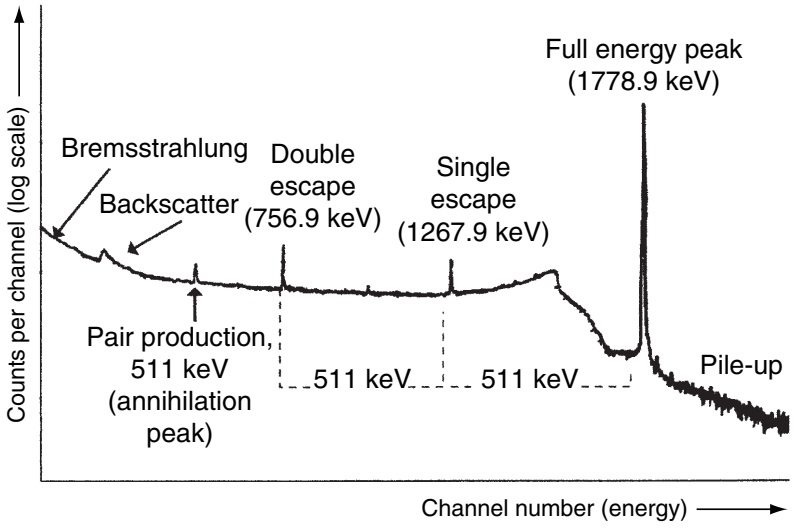

Figure 2.3.: Example spectra illustrating the various spectral features expected, from [52][a]

[a] Gordon R. Gilmore. 'Interactions of Gamma Radiation with Matter'. en. In: *Practical Gamma-Ray Spectrometry*. John Wiley & Sons, Ltd, 2008, pp. 25–38. ISBN: 978-0-470-86198-1.

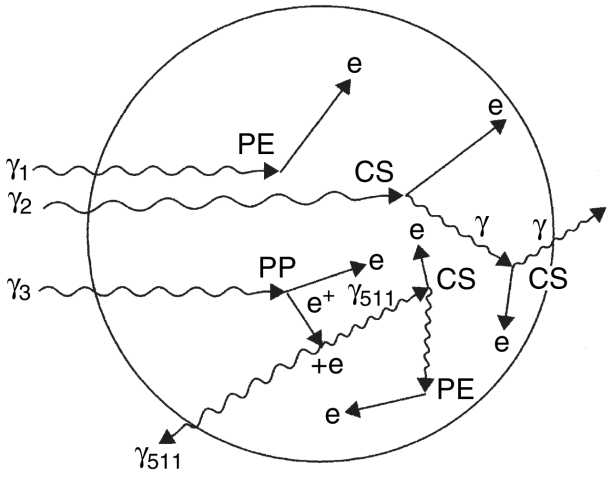

Figure 2.4.: Reaction of interest for gamma spectroscopy, from [52][a]

[a]Gordon R. Gilmore. 'Interactions of Gamma Radiation with Matter'. en. In: *Practical Gamma-Ray Spectrometry*. John Wiley & Sons, Ltd, 2008, pp. 25–38. ISBN: 978-0-470-86198-1.

semiconductors, as illustrated in Table 2.1. When a photon interacts with the material, it can transfer energy to a bound electron. If the photon energy exceeds the band gap energy, this interaction can promote an electron from the valence band to the conduction band, creating an electron-hole pair.

These charge carriers can be collected under an applied electric field, producing a measurable electrical signal that is proportional to the energy deposited by the photon. Due to their relatively small band gaps compared to insulators, semiconductors provide a highly precise means of measuring photon energy, as the amount of charge generated is directly related to the incident energy.

The band gap can be further controlled, through a process called doping, which involves the intentional incorporation of impurity atoms into the crystal lattice. The probability of an electron transitioning across the band gap depends primarily on the material's band gap energy and its temperature.

Hence, for example, germanium has a narrow band gap of approximately 0.67 eV. Since the thermal energy of electrons at room temperature is sufficient to bridge this gap, germanium-based detectors must be cooled to reduce background noise from thermally generated electron-hole pairs.

a) Resolution

Energy resolution is a very important parameter in gamma spectrometry, as it is tantamount to identify each ray to associate them to a correct nuclide. Ideally, an absorbed gamma peak should be as narrow as possible.

In practice, the peak broadening arises mainly from three factors: the statistical fluc-

Table 2.1.: Properties of semi-conductors materials for γ-ray detectors [53][a]

Material	Z	Gap [eV]	$\epsilon^{\dagger}$[eV]	Density [g·cm^{-3}]	e^- [cm^2·V^{-1}·s^{-1}]‡	Holes [cm^2·V^{-1}·s^{-1}]‡
Ge$^{\bullet}$	32	0.67	2.96	5.32	36 000	42 000
Si	14	1.106	3.62	2.33	1350	480
CdTe	48, 52	1.47	4.43	6.06	1000	80
HgI_2	80, 53	2.13	4.22	5.78	1000	50–80
GaAs	31, 33	1.45	4.51	5.35	8000	400
PbI_2	82, 53	2.60	7.68	6.16	8	2

† Average energy to create an electron-hole
‡ Mobility
$^{\bullet}$ Mobility is given at 77K rather than 300K

[a] Gordon R. Gilmore. 'Semiconductor Detectors for Gamma-Ray Spectrometry'. en. In: *Practical Gamma-Ray Spectrometry*. John Wiley & Sons, Ltd, 2008, pp. 39–60. ISBN: 978-0-470-86198-1.

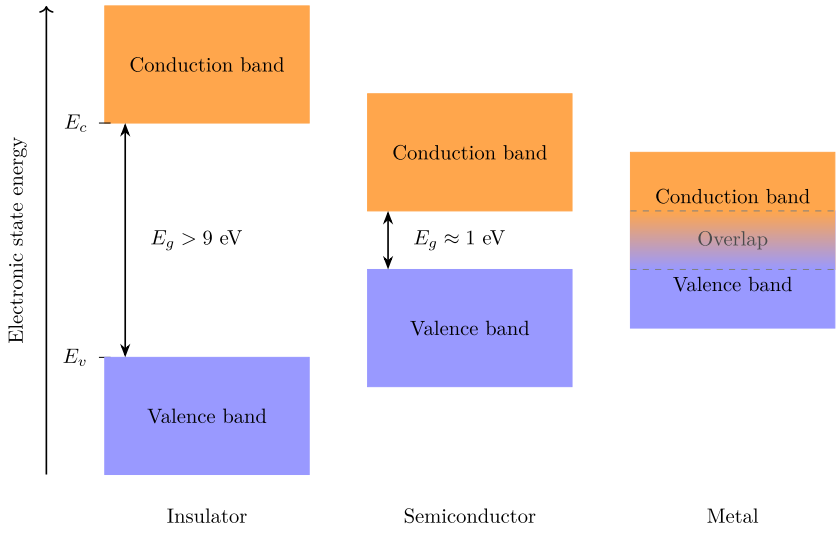

Figure 2.5.: Schematics of the electronic band structures in insulators, semiconductors and metals

tuations in the number of generated charge carriers, the noise from the electronic components, and the charge trapping phenomenon inherent to the semiconductor material. The total peak width can be expressed as the sum of these three contributions.

For an order of magnitude, one gamma-ray of 661.67 keV energy completely absorbed in germanium can be expected to create 3.9 million electron–hole pairs. The same gamma-ray absorbed in sodium iodide will only give rise to 3.9 thousand photoelectrons [54][1]. A Ge detector produces more electron-hole pairs for a given gamma ray that is totally absorbed in its active volume than any other detector material. By consequence, energy resolutions are obtained that are more than 10 times better than by competing gamma detector technologies [55][2].

b) Germanium detectors

In nuclear instrumentation, there are two types of widely used germanium detectors: lithium-compensated Ge(Li) and hyper-pure germanium (HPGe). Ge(Li) detectors are manufactured in the same way as Si(Li) detectors. This generation of detectors was marketed from the early 1960s to the early 1980s [56][3]. As the Lithium diffuse at room temperature, Ge(Li) detectors require a cryogenic cooling system.

Germanium detectors are available in three configurations: planar, coaxial and BEGe (Broad Energy Germanium), which characteristics are summarised in Table 2.2.

Table 2.2.: Characteristics of different gamma spectrometers

Type	Geometry	Key strength	Primary applications
Planar	Flat, parallel plates	Best energy resolution (at low energy)	X-ray and low energy γ-ray
Coaxial	Cylindrical with central hole	High efficiency for high-energy γ	General-purpose, γ-ray
BEGe	Thick planar with small anode	High resolution and high count rates	Low background counting, high-rate environments

[1] Gordon R. Gilmore. 'Resolution: Origins and Control'. en. In: *Practical Gamma-Ray Spectrometry*. John Wiley & Sons, Ltd, 2008, pp. 131–141. ISBN: 978-0-470-86198-1.

[2] Ramkumar Venkataraman. 'Chapter 4 - Semiconductor detectors'. In: *Handbook of Radioactivity Analysis (Fourth Edition)*. Ed. by Michael F. L'Annunziata. Fourth Edition. Academic Press, 2020, pp. 409–491. ISBN: 978-0-12-814397-1. DOI: https://doi.org/10.1016/B978-0-12-814397-1.00004-2.

[3] Glenn F. KNOLL. *Radiation Detection and Measurements*. Fourth. Wiley, 2010. ISBN: 978-0-470-13148-0.

c) Spectral analysis

Gamma spectrometry is a relative measurement method. Detector efficiency is thus typically calibrated using standard sources, whose activity is determined by direct measurement.

Analysis is usually based on studying total absorption peaks observed in the recorded spectrum.

Calibration Prior to any measurements, two essential calibration steps must be performed: energy calibration for qualitative analysis and efficiency calibration for quantitative analysis.

Energy calibration Calibrating the energy of a gamma spectrometer requires a number of radioactive sources that emit gamma radiation. The resulting spectra correspond to the energy lines of these sources. Total absorption lines are classified by their amplitude. Each channel is associated with a specific energy. The channels and energies are linked by a polynomial relationship: The energy calibration of a gamma spectrometer is achieved using a set of radioactive sources that emit gamma radiation at well-defined energies. The resulting spectra exhibit total absorption peaks corresponding to the characteristic energies of these sources. Each peak is associated with a specific channel, and the relationship between channel number C and energy E is established via a polynomial fit:

$$E = A_0 + A_1 C + A_2 C + A_3 C^3 + \cdots \tag{2.7}$$

where A_k are the polynomial coefficients determined during calibration. The higher-order terms account for non-linearities in the detector response.

To accurately characterise the calibration curve, multiple calibration points are required. Commonly used sources, listed in ascending order of gamma-ray energy, include ^{241}Am, ^{109}Cd, ^{57}Co, ^{139}Ce, ^{51}Cr, ^{113}Sn, ^{85}Sr, ^{137}Cs, ^{60}Co, and ^{88}Y. Multi-rays sources, such as ^{152}Eu, may also be employed due to their broad energy coverage. However, their use complicates peak identification owing to the increased spectral complexity.

Efficiency calibration In order to establish an efficiency calibration, it is necessary to use standard sources that are similar in nature and form to the sample to be analysed. These sources are identified by their specific, or volumic activity, or their γ-ray lines emission rate.

A yield curve is obtained as a function of energy for a given geometry and matrix. The detection efficiencies of the different peaks in the sample spectrum are then used to calculate the activity from this curve. If the energy calibration matrix is a polynomial fit, such yields curve are usually fitted with a log-log polynomial fit, see an example on Figure 2.6.

However, if the sample differs from the standard, the efficiency must be corrected for matrix effects and the peak-sum effect due to cascade transitions and pile-up (for high count rates). Monte Carlo models of the detector can be used to estimate such factors.

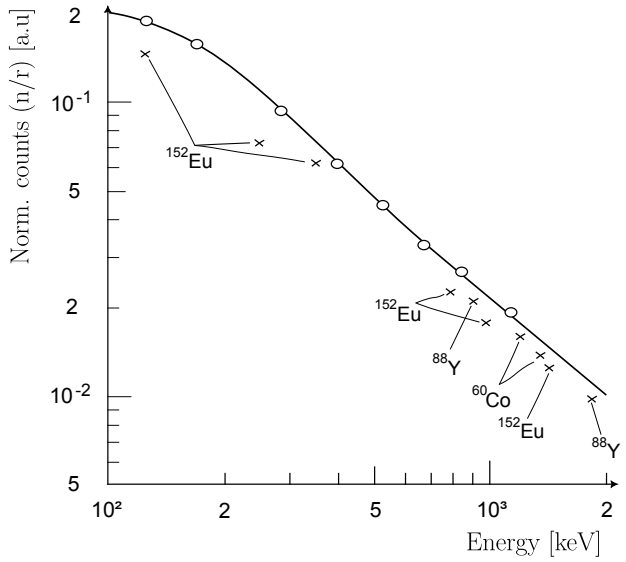

Figure 2.6.: Efficiency calibration and representation of multi-energy gamma emitters (× symbol), from [57][a]

[a]K. Debertin and R.G. Helmer. *Gamma- and X-ray spectrometry with semiconductor detectors*. North-Holland., Jan. 2025.

Activity computation Once the detector is fully calibrated, the activity of a sample can be estimated by identifying its characteristic gamma-ray emissions. According to ISO [58][1], the specific activity is given by:

$$A_m = \frac{N_{net}(E)}{V \times \epsilon_E \times t \times I_\gamma \times f_d \times f_{C-1,E} \times f_{S,E} \times f_{att,E}} \tag{2.8}$$

where:

- A_m is the specific activity;
- N_{net} is the net count rate of the detected gamma-ray peak at energy E;
- V is the volume of the sample;
- ϵ_E is the detection efficiency at E;
- t is the measurement duration;
- I_γ is the intensity of the ray of interest;
- f_d is the decay correction factor;
- $f_{C-1,E}$ is the coincidence-summing correction factor at E;
- $f_{S,E}$ is the self-absorption correction factor at E;
- $f_{att,E}$ is the attenuation correction factor;

While the above equation specifies the emission rate for a single gamma-ray transition,

[1]International Organization for Standardization (ISO). *Measurement of radioactivity in the environment — Soil — Part 3: Test method of gamma-emitting radionuclides using gamma-ray*. Geneva, Switzerland, July 2023.

radionuclides typically emit multiple characteristic gamma rays. To enhance statistical reliability, the activity can be therefore computed as a weighted average of the values derived from the principal gamma-ray emissions:

$$\langle A_m \rangle = \frac{\sum_i {}^{A_i}/_{\sigma^2_{A_i}}}{\sum_i {}^{1}/_{\sigma^2_{A_i}}} \tag{2.9}$$

where A_i represents the activity estimated from the i-th detected gamma-ray transition associated with the nuclide. The relative uncertainty in each activity estimate is determined by:

$$\frac{\sigma_{A_i}}{A_i} = \sqrt{\left(\frac{\sigma_{\epsilon_E}}{\epsilon_E}\right)^2 + \left(\frac{\sigma_m}{m}\right)^2 + \left(\frac{\sigma_{I_\gamma}}{I_\gamma}\right)^2 + \left(\frac{\sigma_{N_{net}}}{N_{net}}\right)^2 + \left(\frac{\sigma_{C_i}}{C_i}\right)^2} \tag{2.10}$$

The coefficient C_i represents the product of the individual correction factors for the i-th gamma-ray transition, accounting for decay, coincidence summing, self-absorption, and attenuation effects. This combined correction factor is expressed as:

$$C_i = f_d \times f_{C-1,E} \times f_{S,E} \times f_{\text{att},E}, \tag{2.11}$$

2.2.2. Solid State Nuclear Track Detector

A detector that can record tracks of charged particles can be categorised as a Nuclear Track Detector. When the medium is solid, e.g., nuclear emulsions, etched track detectors, or fluorescent detectors, then it is usually named a Solid-State Nuclear Track Detector (SSNTD). Vapours, liquids, or gases can also be used for nuclear track detection, with examples including cloud chambers, bubble chambers, or spark chambers. In this section, we will focus solely on SSNTDs.

For a brief historical perspective, Young was the first to reveal and identify fission fragment tracks in lithium fluoride (LiF) by etching in 1958 [59][1]. However, it was Price and Walker who discovered a way to stabilise the tracks and allow them to be seen with an ordinary optical microscope via chemical etching four years later [60][2], which gave birth to the current SSNTD.

Since then, they have been used to detect protons, antiprotons, alpha particles, fission fragments, and a variety of other heavy ions [61, 62][3]. When coupled with converters,

[1] D. A. Young. 'Etching of Radiation Damage in Lithium Fluoride'. en. In: *Nature* 182.4632 (Aug. 1958), pp. 375–377. ISSN: 1476-4687. DOI: 10.1038/182375a0.

[2] P. B. Price and R. M. Walker. 'A new track detector for heavy particle studies'. In: *Physics Letters* 3.3 (1962), pp. 113–115. ISSN: 0031-9163. DOI: https://doi.org/10.1016/0031-9163(62)90051-3.

[3] C. Baccou et al. 'CR-39 track detector calibration for H, He, and C ions from 0.1-0.5 MeV up to 5 MeV for laser-induced nuclear fusion product identification'. In: *Review of Scientific Instruments* 86.8 (Aug. 2015), p. 083307. ISSN: 0034-6748. DOI: 10.1063/1.4927684, Mukhtar Ahmed Rana. 'Summary of a comprehensive data bank for nuclear track research using CR-39 detectors'. In: *Nuclear Instruments and Methods in Physics Research Section A: Accelerators, Spectrometers, Detectors and Associated Equipment* 944 (2019), p. 162590. ISSN: 0168-9002. DOI: https://doi.org/10.1016/j.nima.2019.162590.

this passive detector can also be used for neutron dosimetry [63][1].

Any insulator transparent to photons can serve as an SSNTD medium. The mechanism for track generation and how they react to etching will vary between materials. The usual classification used is shown in Figure 2.7.

In this chapter, only the polyallyldiglycol carbonate CR-39 will be mentioned and used.

a) Track Formation Mechanism and Chemical Etching Process

When a charged particle traverses through a solid material like CR-39, it loses energy primarily through ionisation and excitation of the atoms along its path. This energy loss results in the creation of a trail of damaged material, known as a latent track. This trail consists of broken chemical bonds and displaced atoms. The latent track consists of regions where the material's structure has been altered due to the high linear energy transfer (LET) of the charged particle.

The formation of latent tracks is influenced by several factors, including the type and energy of the charged particle, the material properties of the detector, and the environmental conditions during exposure.

Chemical Etching Process Chemical etching is a critical step in revealing the latent tracks formed by charged particles in SSNTDs.

The etching process involves immersing the detector material in a chemical solution that preferentially attacks the damaged regions along the latent tracks. Making them visible under an optical microscope.

Common etchants for CR-39 include sodium hydroxide (NaOH) and potassium hydroxide (KOH) solutions. The choice of etchant depends on factors such as the material properties of the detector and the desired etching characteristics. The process is influenced by several parameters, including the concentration of the etchant, the temperature of the etching solution, and the duration of the etching process. These parameters must be carefully controlled to achieve optimal track visibility.

The damaged regions along the latent tracks etch at a faster rate compared to the bulk material. This differential etching rate results in the formation of conical or cylindrical pits that correspond to the paths of the charged particles. Proper control of etching parameters ensures that the tracks are sufficiently enlarged for accurate analysis while minimising excessive etching that could damage the detector material.

The shape of the revealed tracks depends on the simultaneous action of the chemical solution along the particle trajectories and on the detector's thickness, leading to the consideration of two main physical parameters: the bulk chemical etch rate of the de-

[1] F. Castillo et al. 'Fast neutron dosimetry using CR-39 track detectors with polyethylene as radiator'. In: *Radiation Measurements*. 25th ICNTS 50 (Mar. 2013), pp. 71–73. ISSN: 1350-4487. DOI: 10.1016/j.radmeas.2012.09.007.

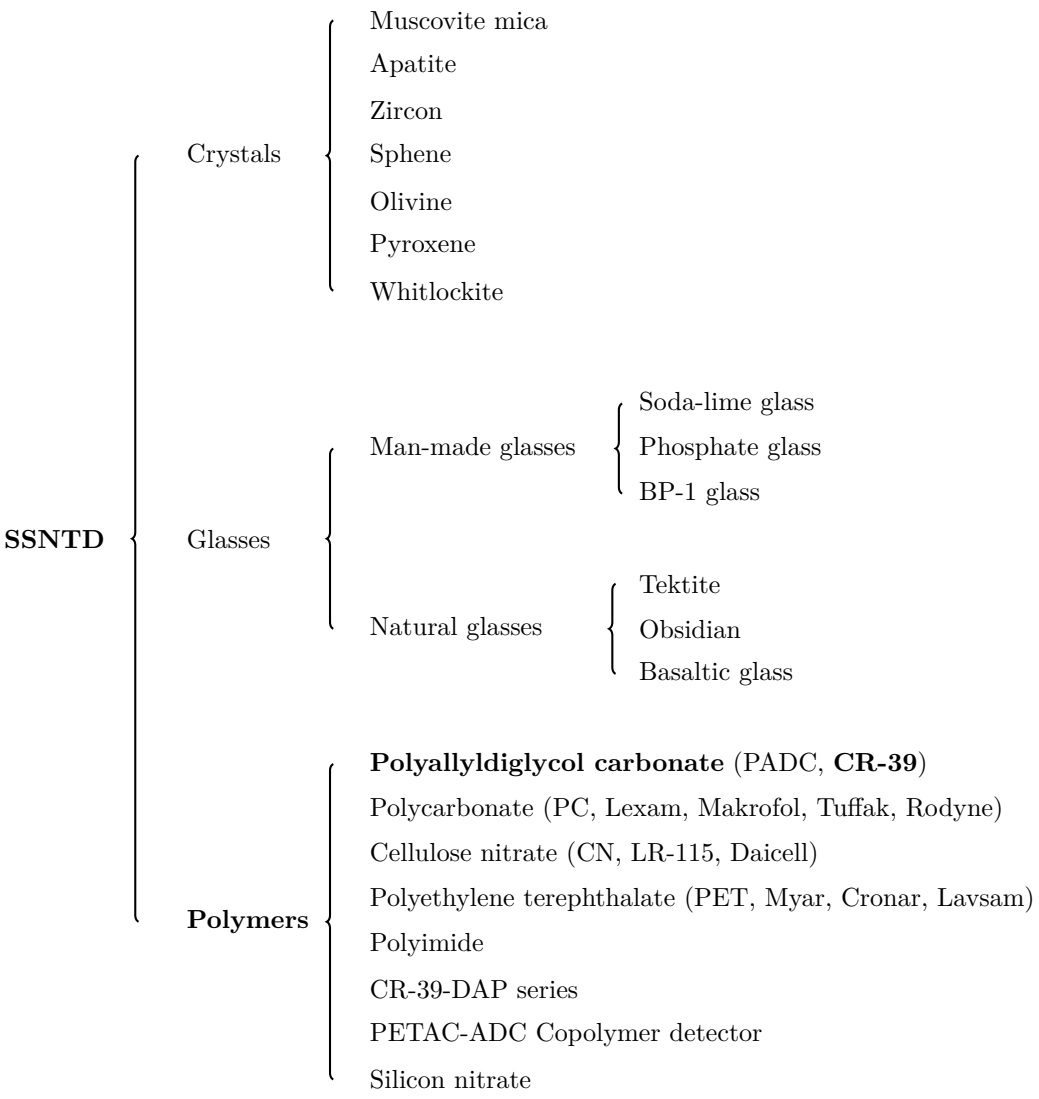

Figure 2.7.: General classification of SSNTD materials, per track formation and etching properties [64][a]

[a] Shi-Lun Guo, Bao-Liu Chen, and S. A. Durrani. 'Chapter 3 - Solid-state nuclear track detectors'. In: *Handbook of Radioactivity Analysis (Fourth Edition)*. Ed. by Michael F. L'Annunziata. Fourth Edition. Academic Press, 2020, pp. 307–407. ISBN: 978-0-12-814397-1. DOI: https://doi.org/10.1016/B978-0-12-814397-1.00003-0.

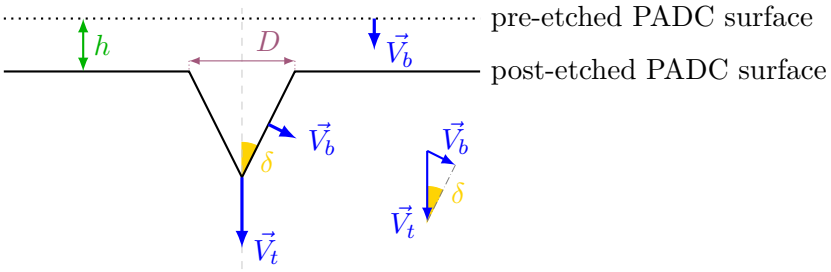

Figure 2.8.: Geometry of the track development. The incident angle is normal with respect to the detector surface, and V_T is constant [66, 67][a]

[a]D. Nikezic and K.N. Yu. 'Formation and growth of tracks in nuclear track materials'. In: *Materials Science and Engineering: R: Reports* 46.3 (Dec. 2004), pp. 51–123. ISSN: 0927-796X. DOI: 10.1016/j.mser.2004.07.003, M. Bolzonella et al. 'Neutron personal dosimetry using polyallyl diglycol carbonate (PADC): Current status, best practices and proposed research'. In: *Physics Open* 12 (2022), p. 100114. ISSN: 2666-0326. DOI: https://doi.org/10.1016/j.physo.2022.100114.

tector (V_B) and the chemical etch rate of the latent tracks (V_T) [65][1]. The parameter are represented on Figure 2.8.

The easiest velocity to measure is V_B, using the classical expression $\frac{h}{t}$ is sufficient if h is the average loss of bulk. As the height may be difficult to measure, the mass before and after and etching can be used:

$$V_B = \frac{\Delta m}{2A\rho t} \tag{2.12}$$

where A is the etched area, Δm the mass loss after etching, ρ the density of the detector and t the etching time.

The etch rate V_T is more difficult to determine. When considering an incident charged particle [66][2], it can be expressed as:

$$V_T = V_B \frac{4h^2 + D^2}{4h^2 - D^2} \tag{2.13}$$

Tracks can only be read if the ratio between the two V_T/V_B is greater than 1.

b) Neutron Detection and Energy Estimation

One of the significant advantages of using SSNTDs, particularly CR-39, is the ability to infer the energy of neutrons indirectly.

[1]Paul Henderson. '(R. L.) Fleischer, (P. B.) Price, and (R. M.) Walker. Nuclear Tracks in Solids: Principles and Applications. Berkeley and London (Univ. California Press), 1975. xxii+605 pp., 205 figs., I pl. Price'. In: *Mineralogical Magazine* 42.322 (1978), pp. 306–307. DOI: 10.1180/minmag.1978.042.322.40.

[2]D. Nikezic and K.N. Yu. 'Formation and growth of tracks in nuclear track materials'. In: *Materials Science and Engineering: R: Reports* 46.3 (Dec. 2004), pp. 51–123. ISSN: 0927-796X. DOI: 10.1016/j.mser.2004.07.003.

Since neutrons are neutral particles, they do not create tracks directly in the detector material. Instead, they are detected through their interactions with converter materials that produce charged particles.

A typical example, that will be used in this work, are the TechnoTrak2 (Chiyoda Technologies, Japan), and their Wide range NeutonPit (WNP), see Figure 2.9.

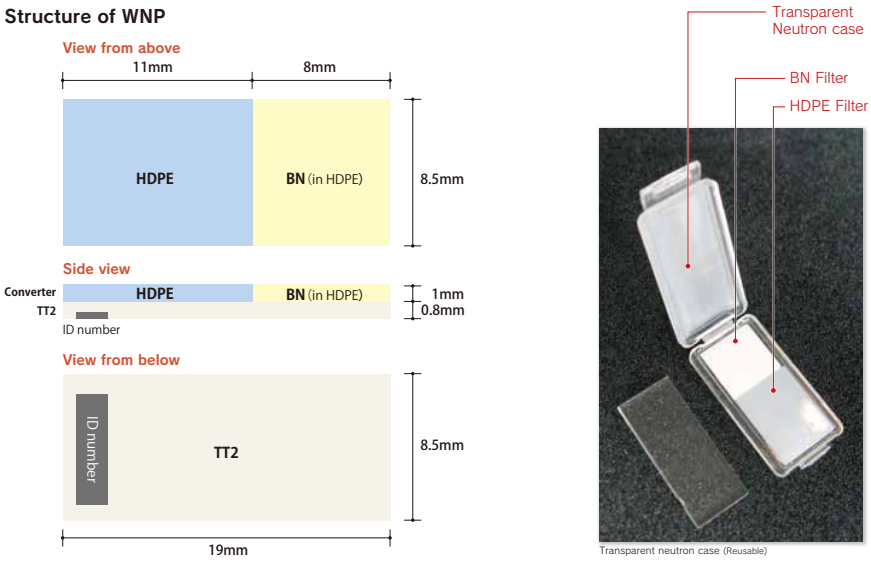

Figure 2.9.: Schematic of the Wide Range Neutronpit (left) and the TechnoTrack2 detector (right) [68][a]

[a]Chiyoda Technologies. *Solid-state Track Detector – TechnoTrak 2.* en.

The dosimeter holder is equipped with two types of radiators and converters to detect neutrons with a wide range of energies, from thermal neutrons to fast neutrons (between 0.25 eV and 15 MeV neutrons [69][1]).

Indeed, a radiator in high density polyethylene, produce recoil protons, as depicted in Figure 2.10. When the second part, the convertor, make use of the reaction:

$$ {}^{1}_{0}n + {}^{10}_{5}B \rightarrow {}^{4}_{2}He + {}^{7}_{3}Li \tag{2.14} $$

As the capture cross-section of Boron follows a $1/v$ shape, as neutron energy tends towards thermal energy, the probability of reaction is increasing. At thermal energy, $\sigma_{^{10}\mathrm{B}(n,\alpha)} \simeq 3870\,\mathrm{b}$, whereas $\sigma_{^{1}\mathrm{H}(n,\mathrm{el})} \simeq 20\,\mathrm{b}$. The α tracks are hence in majority produced by the thermal neutrons, whereas, recoil protons are much more probable for fast neutrons.

[1]H. Ohguchi et al. 'New pre-soaking technique for PADC and application to wide-range personal neutron dosimeter'. In: *Radiation Measurements*. Proceedings of the 23rd International Conference on Nuclear Tracks in Solids 43 (Aug. 2008), S500–S503. ISSN: 1350-4487. DOI: 10.1016/j.radmeas.2008.03.015.

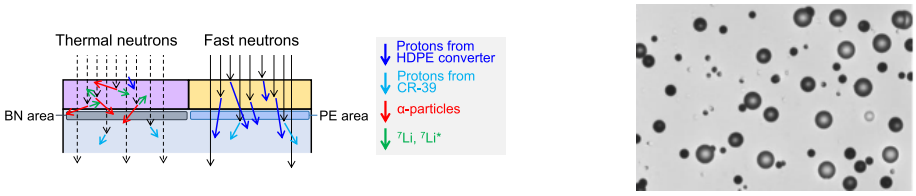

Figure 2.10.: Cross-sectional view with radiator material irradiated by incident neutrons (left) and image of pits due to recoil protons in a CR-39 track detector (right) [70, 71][a]

[a]Takuya Hashizume et al. 'Development of a high-speed and precise automatic reading system of CR-39 plastic nuclear track detector for neutron dose measurements'. en. In: *Radiation Measurements* 191 (Feb. 2026), p. 107572. ISSN: 13504487. DOI: 10.1016/j.radmeas.2025.107572, Youbba Ould Salem et al. 'RPL Neutron Dosimetry in n- Fields in Comparison with Polymer Detectors Type CR-39'. In: *Polymers* 14.9 (2022). ISSN: 2073-4360. DOI: 10.3390/polym14091801.

2.3. Assessment of induced activation

Nuclear activation affects all operating, future, or dismantled particle accelerators used in various fields, from medical applications to industrial applications.

As mentioned in the introduction, modelling is one way to tackle the estimation of a radionuclides inventory in a particle accelerator facility. This section is the synthesis of two papers [72, 73][1]. Three study cases will be presented, the main interest were activation estimation:

- around a medical LINAC, especially the treatment head, with a focus on β-pure emitters.
- around a thermalised neutron source (AmBe), with a comparison deploying most of the Monte Carlo code mentioned.
- finally around a radioisotope production cyclotron, in this case SSNTD have also been used to characterize the secondary neutron field.

2.3.1. Around medical LINAC

Medical LINACs are widely used for radiotherapy. These accelerators can produce hard Bremsstrahlung photons from 6 to 25 MeV when high-energy electrons hit a thick target of copper and tungsten. Photonuclear reactions occur at such energies, including the photoneutrons production (γ, n). The production of secondary neutrons within the treatment head activates the accelerator components and surrounding materials. To decommission these accelerators, waste disposal management institutions need to know the amount of radioactivity in the accelerator parts, and especially the presence of pure

[1]Jonathan Collin et al. 'Validation of Monte Carlo simulations by experimental measurements of neutron-induced activation in cyclotrons'. en. In: *EPJ Web of Conferences*. Vol. 288. Italy: EDP Sciences, 2023, p. 04025. DOI: 10.1051/epjconf/202328804025, Abdel-Mjid Nourreddine et al. 'Assessment of photon and proton-induced activation in particles accelerators'. In: *Radiation Protection Dosimetry*. Vol. 200. 16-18. Japan, Nov. 2024, pp. 1507–1513. DOI: 10.1093/rpd/ncae146.

β emitters.

This section, published in [73][1], objective was to evaluate the feasibility of estimating the γ and β activities in LINAC parts by calculations.

a) Geometry

Such device is quite complex to model, there are numerous parts for which the exact composition is not known. As for intellectual properties, manufacturers cannot share extensive details on the geometry nor the composition that may vary for one module to another. Yet the basic designed is entailed to the technology are a usually as depicted in Figure 2.11. Meaning an electron-beam will impinge on a copper target, to produce bremsstrahlung, the gamma beam will be shaped through several jaws.

For this study only the production of photoneutrons, and the appearance of related atoms, the model was simplified to the one of Figure 2.12. The electron beam is impinging on a copper slab, and the activation of a steel block is checked. The steel is regular SS316LN, and a polluted copper is considered. The compositions are detailed in Table 2.3 and Table 2.4.

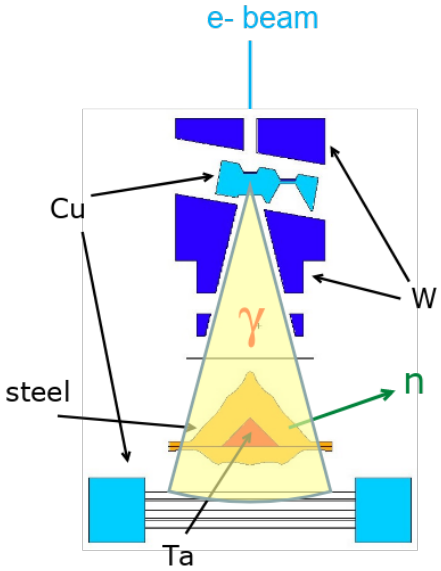

Figure 2.11.: Simplified head of radiotherapy accelerator

b) Neutron production

In the energy region that concerns most LINACs, the Giant Dipolar Resonance (GDR) dominates photonuclear reaction cross-sections, see a representation in Figure 2.13. For

[1] Abdel-Mjid Nourreddine et al. 'Assessment of photon and proton-induced activation in particles accelerators'. In: *Radiation Protection Dosimetry*. Vol. 200. 16-18. Japan, Nov. 2024, pp. 1507–1513. DOI: 10.1093/rpd/ncae146.

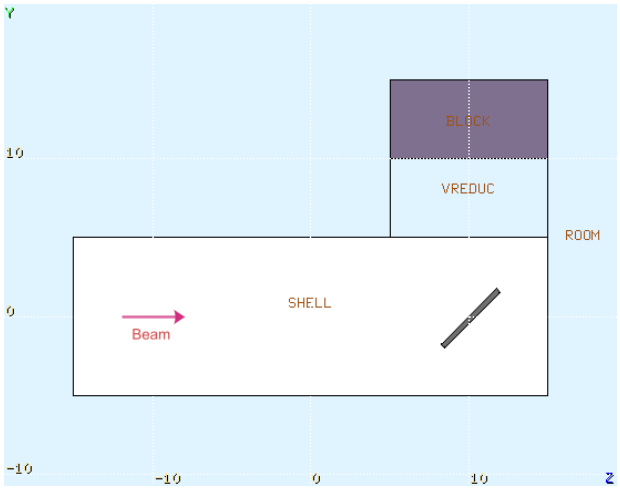

Figure 2.12.: Benchmark geometry

Table 2.3.: Composition of SS316LN, of $8\,\mathrm{g\cdot cm^{-3}}$ density

Atom	Massic [%]	Isotope	[%]	Isotope	[%]	Isotope	[%]
Iron	69.118	^{54}Fe	5.845	^{56}Fe	91.754	^{57}Fe	2.119
		^{58}Fe	0.282				
Chromium	16.83	^{50}Cr	4.345	^{52}Cr	83.789	^{53}Cr	9.501
		^{54}Cr	2.365				
Nickel	10.06	^{58}Ni	68.077	^{60}Ni	26.223	^{61}Ni	1.1399
		^{62}Ni	3.6346	^{64}Ni	0.9255		
Molybdenum	2.03	^{92}Mo	14.53	^{94}Mo	9.15	^{95}Mo	15.84
		^{96}Mo	16.67	^{97}Mo	9.60	^{98}Mo	24.39
		^{100}Mo	9.82				
Manganese	1.43	^{55}Mn	100				
Silicon	0.385	^{28}Si	92.223	^{29}Si	4.685	^{30}Si	3.092
Nitrogen	0.076	^{14}N	99.636	^{15}N	0.364		
Carbon	0.03	^{12}C	98.93	^{13}C	1.07		
Phosphorus	0.03	^{31}P	100				
Sulfur	0.025	^{32}S	94.99	^{33}S	0.75	^{34}S	4.25
		^{36}S	0.01				

Table 2.4.: Composition of polluted Copper, of 8.96 g·cm^{-3} density

Atom	Massic [%]	Isotope	[%]	Isotope	[%]	Isotope	[%]
Copper	99.9917	^{63}Cu	69.15	^{65}Cu	30.85		
Silver	0.0025	^{107}Ag	51.839	^{109}Ag	48.161		
Bismuth	0.0002	^{209}Bi	100				
Lead	0.0005	^{204}Pb ^{208}Pb	1.4 52.4	^{206}Pb	24.1	^{207}Pb	22.1
Antimony	0.0004	^{121}Sb	57.21	^{123}Sb	42.79		
Tin	0.0002	^{112}Sn ^{116}Sn ^{119}Sn	0.97 14.54 8.59	^{114}Sn ^{117}Sn ^{120}Sn	0.66 7.68 32.58	^{115}Sn ^{118}Sn	0.34 24.22
Zinc	0.0001	^{64}Zn ^{68}Zn	49.17 18.45	^{66}Zn ^{70}Zn	27.73 0.61	^{67}Zn	4.04
Arsenic	0.0005	^{75}As	100				
Iron	0.001	^{54}Fe ^{58}Fe	5.845 0.282	^{56}Fe	91.754	^{57}Fe	2.119
Nickel	0.001	^{58}Ni ^{62}Ni	68.077 3.6346	^{60}Ni ^{64}Ni	26.223 0.9255	^{61}Ni	1.1399
Sulfur	0.0015	^{32}S ^{36}S	94.99 0.01	^{33}S	0.75	^{34}S	4.25
Selenium	0.0002	^{74}Se ^{78}Se	0.89 23.77	^{76}Se ^{80}Se	9.37 49.61	^{77}Se ^{82}Se	7.63 8.73
Tellurium	0.0002	^{120}Te ^{124}Te ^{128}Te	0.09 4.74 31.74	^{122}Te ^{125}Te ^{130}Te	2.55 7.07 34.08	^{123}Te ^{126}Te	0.89 18.84

a few isotopes like ^{186}W and ^{64}Cu or ^{208}Pb, the (γ,n) reaction cross-sections, the GDR can reach several hundred mbarns. The kinetics relation determines the photoneutron energy E_n:

$$E_n = \frac{A-1}{A}\left[E_\gamma - E_{th} - \frac{E_\gamma^2}{1862(A-1)}\right] + E_\gamma\sqrt{\frac{2(A-1)(E_\gamma - E_{th})}{931A^2}}\cos\theta$$

where: A is the mass number of the target, E_γ is the energy of the incident photon (MeV), E_{th} is the threshold energy of the (γ,n) reaction, and θ is the angle of photoneutron emission relative to the beam axis [74][1].

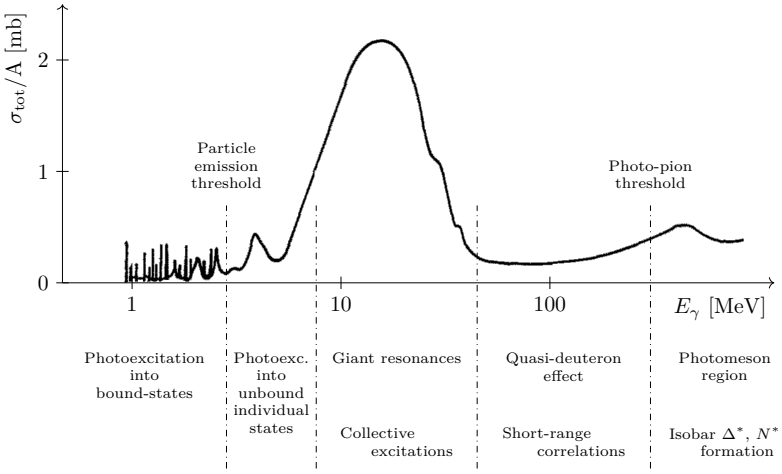

Figure 2.13.: Schematic representation of the total photonuclear cross section per nucleon as a function of photon energy E_γ. [75][a]

[a] D. J. S. Findlay. 'Applications of photonuclear reactions'. In: *Nuclear Instruments and Methods in Physics Research Section B: Beam Interactions with Materials and Atoms* 50.1 (Apr. 1990), pp. 314–320. ISSN: 0168-583X. DOI: 10.1016/0168-583X(90)90374-4.

Table 2.5 shows the energy thresholds and the maximum GDR cross section (γ,n) for stable isotopes of copper and tungsten. Thresholds are between 6 and 11 MeV and the GDR peak is between 12 and 20 MeV.

c) Expected activation

Table 2.6 presents a detailed list of the activation products at the energy considered (25 MeV photons), comparing the activation chains. The available techniques to confirm the presence of the elements listed are mainly gamma spectrometry and liquid scintillation.

[1] Douglas A. Fynan. 'Photoneutron reaction kinematics and error of commonly used approximations'. In: *Nuclear Instruments and Methods in Physics Research Section A: Accelerators, Spectrometers, Detectors and Associated Equipment* 977 (Oct. 2020), p. 164271. ISSN: 0168-9002. DOI: 10.1016/j.nima.2020.164271.

Table 2.5.: Energy threshold and photonuclear cross section for stable isotopes of Copper and Tungsten [76][a]

Isotope	Abundance [%]	E_{th} [MeV]	σ [mb]	$E_{th}(\gamma, 2n)$ [MeV]	$E_{th}(\gamma, 3n)$ [MeV]
^{63}Cu	69.17	10.85	81	19.74	31.45
^{65}Cu	30.83	9.91	73.5	17.83	28.68
^{182}W	0.12	8.07	440	14.75	23.16
^{183}W	14.28	6.19	450	14.26	20.94
^{184}W	30.70	7.41	425	13.60	21.67
^{186}W	28.60	7.19	437	20.36	20.36

[a]B. J. Patil et al. 'Estimation of neutron production from accelerator head assembly of 15 MV medical LINAC using FLUKA simulations'. In: *Nuclear Instruments and Methods in Physics Research Section B: Beam Interactions with Materials and Atoms*. Proceedings of the 10th European Conference on Accelerators in Applied Research and Technology (ECAART10) 269.24 (Dec. 2011), pp. 3261–3265. ISSN: 0168-583X. DOI: 10.1016/j.nimb.2011.04.013.

As the pure beta emitters are challenging to detect, we will focus on gamma detection during the modelling.

d) Monte Carlo photonuclear calculation

We have focused our studies on the parts of a typical accelerator being dismantled and, in particular, the main components of the LINAC head. The dimensions and materials have been modelled in MCNP6.2 [36][1] to simulate photon and neutron spectra. Electrons impinge on two-layered tungsten/copper targets to produce Bremsstrahlung photons, which are directed mainly along the beam axis. The elemental compositions used for the simulations, including impurities [77][2], are W, Fe, Ni, Cu; Pb with Sb, Fe with Ni, Cr, and Cu. Above the photonuclear energy threshold, 6.19 MeV according to Table 2.5, we estimated the Bremsstrahlung flux at the isocentre produced by a 20 mA and 18.8 MeV electron beam to be 3.06×10^{12} photons/s/cm^2. The "isocentre" is a reference point on the treatment table located on the axis of the electron beam, 100.1 cm from the target.

Figure 2.14 compares the neutron spectra at the isocentre obtained by MCNP, PHITS and FLUKA. There is good agreement between PHITS and MCNP, but we see a slight deviation with FLUKA, with a shift of $\sim$ 500 keV in the maximum of the neutron spectrum. The mean energy is 764 keV, representing the main contribution (excluding the albedo of the concrete bunker walls) of the radiation spectra near a medical LINAC. The total flux of photoneutrons in the isocentre is 1.48×10^9 neutrons/s/cm^2. This

[1]Christopher John Werner et al. *MCNP User's Manual Code Version 6.2*. Tech. rep. LA-UR-17-29981. Los Alamos, NM, USA: Los Alamos National Laboratory, Oct. 2017.

[2]Francois Begin, Addil Sellam, and Abdel-Mjid Nourreddine. 'Monte Carlo simulations of photoneutron activation in a medical LINAC'. en. In: *2015 4th International Conference on Advancements in Nuclear Instrumentation Measurement Methods and their Applications (ANIMMA)*. Lisbon, Portugal: IEEE, Apr. 2015, pp. 1–4. ISBN: 978-1-4799-9918-7. DOI: 10.1109/ANIMMA.2015.7465550.

Table 2.6.: Radionuclides activation products of linear medical accelerator of 25 MeV

Electron incident maximal energy [MeV]	Neutron Activation	Photon Activation	Emission	Pure β-emitters
6	^{10}Be		β^-	✓
	^{14}C		β^-	✓
	^{54}Mn		γ	
	^{55}Fe		γ	
	^{59}Ni		X-ray	
	^{60}Co		γ, β^-	
	^{63}Ni	^{63}Ni	β^-	✓
	^{65}Zn		γ, β^+	
		^{182}Hf	γ, β^-	
15	^{10}Be		β^-	✓
	^{14}C	^{14}C	β^-	✓
		^{32}Si	β^-	✓
		^{49}V	$e.c$	
		^{53}Mn	$e.c$	
	^{54}Mn	^{54}Mn	γ	
	^{55}Fe		γ	
		^{57}Co	$e.c$, γ	
	^{59}Ni	^{59}Ni	X-ray	
		^{60}Fe	γ, β^+	
	^{60}Co	^{60}Co	γ, β^-	
	^{63}Ni	^{63}Ni	β^-	✓
	^{65}Zn	^{65}Zn	γ, β^+	
		^{179}Ta	$e.c$	
		^{182}Hf	γ, β^+	
		^{204}Tl	β^-	✓
	^{205}Pb	^{205}Pb	$e.c$	
25	^{10}Be		β^-	✓
	^{14}C	^{14}C	β^-	✓
		^{26}Al	γ, β^+	
		^{32}Si	β^-	✓
		^{49}V	$e.c$	
		^{50}V	γ, β^-	
		^{53}Mn	$e.c$	
	^{54}Mn	^{54}Mn	γ	
	^{55}Fe	^{55}Fe	γ	
	^{57}Co	^{57}Co	$e.c$, γ	
	^{59}Ni	^{59}Ni	X-ray	
		^{60}Fe	γ, β^+	
	^{60}Co	^{60}Co	γ, β^-	
	^{63}Ni	^{63}Ni	β^-	✓
	^{65}Zn	^{65}Zn	γ, β^+	
		^{121m}Sn	γ, β^-	
		^{179}Ta	$e.c$	
		^{182}Hf	γ, β^+	
		^{204}Tl	β^-	✓
	^{205}Pb	^{205}Pb	$e.c$	

information was used in CINDER'90 [78][1] to calculate the nuclide inventory in irradiated material.

We simulated the neutron fluxes in the LINAC parts and calculated each element's activation (major and minor) with MCNPX/CINDER'90 and FLUKA [47][2]. The spectral shapes of the photons and neutrons are similar to those reported in neutron studies around a medical LINAC [79][3]. The irradiation times used, were determined irradiation times from an inquiry from users of this kind of accelerator, and estimated an irradiation time of 100 s per working day, with 7 months of cooling time.

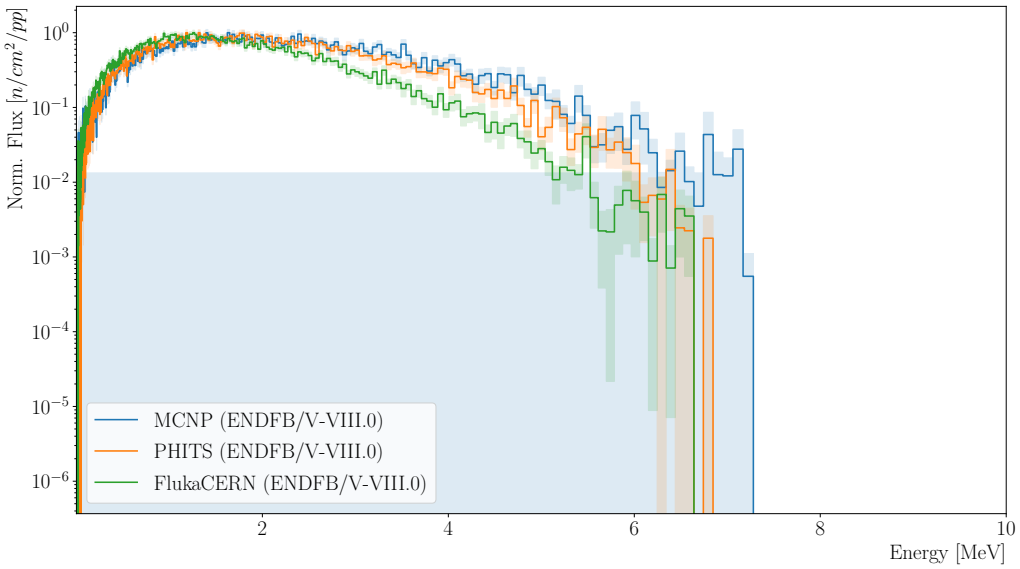

Figure 2.14.: Neutron spectrum in the copper target simulated by MCNP, PHITS and FLUKA

e) Measurements on real irradiated parts

The beam flattening filter from a dismantled LINAC (operated for 18.8 MeV electrons) were analysed in situ by high-resolution gamma-ray spectrometry (Falcon 5000® Portable

[1] M. Fassbender et al. 'Proton beam simulation with MCNPX: Gallium metal activation estimates below 30 MeV relevant to the bulk production of 68Ge and 65Zn'. In: *Nuclear Instruments and Methods in Physics Research Section B: Beam Interactions with Materials and Atoms*. The Application of Accelerators in Research and Industry 261.1 (Aug. 2007), pp. 742–746. ISSN: 0168-583X. DOI: 10.1016/j.nimb.2007.03.099.

[2] A. Ferrari et al. *FLUKA: A Multi-Particle Transport Code*. English. Tech. rep. SLAC-R-773. SLAC National Accelerator Lab., Menlo Park, CA (United States), Dec. 2005. DOI: 10.2172/877507.

[3] A. Esposito et al. 'Determination of the neutron spectra around an 18 MV medical LINAC with a passive Bonner sphere spectrometer based on gold foils and TLD pairs'. In: *Radiation Measurements*. Proceedings of the 15th Solid State Dosimetry (SSD15) 43.2 (Feb. 2008), pp. 1038–1043. ISSN: 1350-4487. DOI: 10.1016/j.radmeas.2007.10.035.

HPGe-Based Radionuclide Identifier). The efficiency of the sample was simulated with MCNPX (with the entire geometry of both detector and sample in measurement conditions) to obtain an accurate activity.

In stainless steel, ^{54}Mn remains a few months after the end of accelerator operations. Table 2.7 lists the radionuclides identified and their activities in the stainless steel lower part of the flattening filter induced by the photonuclear reaction in the 18.8 MeV LINAC.

The large uncertainties appearings are due to the lack of knowledge of the actual beam profile. Indeed, this profile as been estimated after surveying several facilities, and an average use-time considered. This information is actually a critical knowledge for the correct estimation of induced activity in the facility.

Table 2.7.: Measured activities in the 18 MeV LINAC flattening filter

Radionuclide	Activity [kBq]	Origin
^{54}Mn	11400 ± 1300	^{54}Fe(n,p)^{54}Mn
^{57}Co	178 ± 200	^{57}Co(γ,2n)^{57}Co
^{58}Co	15.6 ± 2.7	^{58}Fe(n,p)^{58}Co
^{60}Co	15.4 ± 2.8	^{60}Ni(n,p)^{60}Co
^{182}Ta	25300 ± 1300	^{181}Ta(n,γ)^{182}Ta

Figure 2.15 shows experimental results (in blue) and calculations (in red) with CINDER90 for the main radionuclides in the three pieces "upper," "lower," and "inner" parts of the filter (^{54}Mn and ^{182}Ta). Calculations give a good prediction of real activity for ^{54}Mn, slightly worse for ^{182}Ta; this discrepancy could be due to the other ^{182}Ta production channel i.e, ^{183}W(γ,p) ^{182}Ta (direct photo-activation).

f) Discussions

The coupling of Monte Carlo and deterministic code for activity estimation can predict the main activities in parts of decommissioned accelerators coming from neutron activation. A significant source of uncertainty is the lack of knowledge of the accelerator use (energy, operation schedule, and so on) and the precise date of decommissioning. Accurate information on alloy compositions (primary materials and impurities) could help for the radionuclide inventory, particularly pure β-emitters. Some analysis by acidic dissolution and liquid scintillation analysis would help demonstrate the method's reliability of the method for these emitters.

2.3.2. Around an AmBe source

In this section, the four main MC tools (MCNP, FLUKA, PHITS and Geant4) will be compared for neutron capture and activation computation. If most of them can do a radionuclides inventory natively, the access to an activity value is limited. Hence, the analytical code `FISPACT-II` will be systematically used in association to the neutron

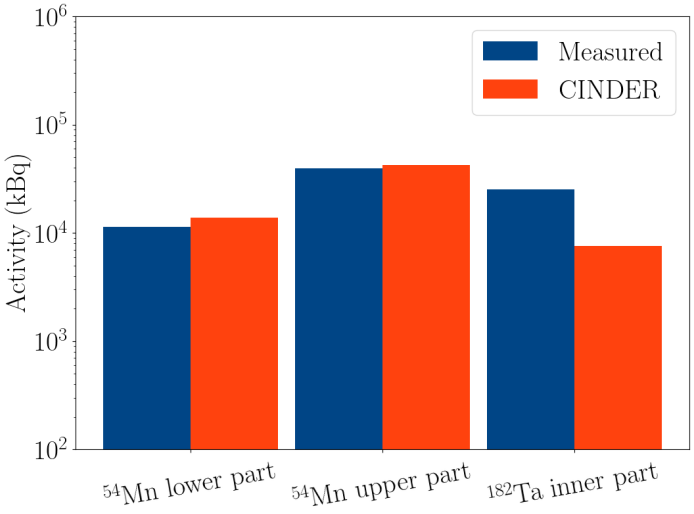

Figure 2.15.: Measured and simulated activities in 18 MeV flattening filter LINAC, [73][1]

spectra obtained via the mentioned MC tools. The comparison has been validated by experimental measurements, using high-resolution gamma spectrometry.

a) Material and Methods

From the typical isotopes found around activated components of particle accelerated, a few materials have been selected V, Sc, Tb, Ta, W and Au samples to expose them to the AmBe source (and latter to secondary neutron field from cyclotron). These samples were chosen according to the following criteria:

- Preferably only one stable nucleus.
- Materials available in foils and at high purity.
- Activation products half-life are compatible with gamma spectrometry and measures of radioprotection (access to irradiation zone, ...)

In this work, the measurements were performed with a HPGe LABSOCS from Canberra. The sensitivity of the setup used spans from 40 keV to 2650 keV with a relative efficiency of about 40%, while the resolution is 1.9 keV at 1.33 MeV. The system had been previously characterized using an ^{152}Eu source. The activities were computed using the software Genie2000, considering the decay scheme compiled by the National Laboratory Henri Becquerel (LNHB) [21][2]. An example of measured spectra is provided Figure 2.17.

[2] M.-M. Bé et al. *Table of Radionuclides*. Vol. 1. Monographie BIPM-5. Pavillon de Breteuil, F-92310 Sèvres, France: Bureau International des Poids et Mesures, 2004. ISBN: 92-822-2206-3.

Experimental set-up Two samples were irradiated with the AmBe source: Au and V. The isotropic ^{241}AmBe neutron source used has an activity of 3.7×10^{10} Bq and a nominal neutron emission rate of $2.24 \times 10^{6}\,s^{-1}$ [80][1]. The AmO2-Be powder is double-encapsulated within welded stainless-steel cylinders, which are inside of a Pb cylinder. The source was placed inside a paraffin (CH_2) barrel of 75 cm diameter and height, with 5 extruded cylinders, allowing to guide safely the source in the middle of the barrel, see Figure 2.16a.

The V (1.5x3x0.1cm^2) and Au (Ø1.2x0.1cm^2) samples were placed for respectively 32 and 6027 minutes inside the barrel and gamma spectrometry analysis were performed. One of the gamma spectra acquired is shown in Figure 2.17.

2.3.3. Model assumptions

Physics choices To conduct this study, the options used for the MC tools will be detailed in the following:

- FLUKA 2021.2.9 Neutrons are managed group-wise below 20 MeV (with 260 groups). ENDF/B-VIII.0 [81][2] cross-sections is used for all materials.
- FLUKA-CERN 4-3.2 In this case, the neutron point-wise cross-sections JEFF-3.3 library [82][3] is used for all materials.
- Geant4 11.0.3 The high precision models and cross-sections for neutron below 20 MeV is used (for elastic and inelastic scattering, capture and fission) through the physics lists ShieldingLEND [83][4] and QGSP_BIC_HP[84][5].
- PHITS 3.32 The photon transport EGS is activated. The library JENDL-4.0 [85][6] is used for neutron cross-sections.
- MCNP6.2 The neutron, proton and photon mode are activated in this simulation. The library ENDF/B-VII.1 [86][7] were privileged.

[1] K. Amgarou et al. 'Characterization of the neutron field from the 241Am-Be isotopic source of the IPHC irradiator'. en. In: *Radiation Measurements*. 25th ICNTS 50 (Mar. 2013), pp. 61–66. ISSN: 1350-4487. DOI: 10.1016/j.radmeas.2012.11.015.

[2] D. A. Brown et al. 'ENDF/B-VIII.0: The 8th Major Release of the Nuclear Reaction Data Library with CIELO-project Cross Sections, New Standards and Thermal Scattering Data'. In: *Nuclear Data Sheets*. Special Issue on Nuclear Reaction Data 148 (Feb. 2018), pp. 1–142. ISSN: 0090-3752. DOI: 10.1016/j.nds.2018.02.001.

[3] A. J. M. Plompen et al. 'The joint evaluated fission and fusion nuclear data library, JEFF-3.3'. en. In: *The European Physical Journal A* 56.7 (July 2020), p. 181. ISSN: 1434-601X. DOI: 10.1140/epja/s10050-020-00141-9.

[4] Geant4 Collaboration. *Shielding — PhysicsListGuide 11.4 documentation*.

[5] Geant4 Collaboration. *QGSP_BIC — PhysicsListGuide 11.4 documentation*.

[6] Keiichi SHIBATA et al. 'JENDL-4.0: A New Library for Nuclear Science and Engineering'. In: *Journal of Nuclear Science and Technology* 48.1 (Jan. 2011). _eprint: https://doi.org/10.1080/18811248.2011.9711675, pp. 1–30. ISSN: 0022-3131. DOI: 10.1080/18811248.2011.9711675.

[7] M. B. Chadwick et al. 'ENDF/B-VII.1 Nuclear Data for Science and Technology: Cross Sections, Covariances, Fission Product Yields and Decay Data'. In: *Nuclear Data Sheets*. Special Issue on ENDF/B-VII.1 Library 112.12 (Dec. 2011), pp. 2887–2996. ISSN: 0090-3752. DOI: 10.1016/j.nds.2011.11.002.

For the first irradiation run, TENDL-21 [87][1] neutron cross-section library was mainly used, excepted for ^{nat}C (ENDF/B-VII.1), ^{nat}Mg, ^{nat}S (ENDF/B-VI.8) and ^{nat}Si (ENDF/B-VI). TENDL-19 proton cross-section library is used for all materials instead of physics models excepted for H, ^{nat}C, ^{nat}Mg, ^{nat}S and ^{nat}Si.

– `FISPACT-II` Is used in a two-step process, using the average neutron fluxes in the volume of interest. All computations were done with TENDL-19 library.

Geometrical choices In the case of the direct irradiation, only the barrel and the surrounding air were modelled in the simulations. And for the AmBe, the ISO8529-1:2021 (small source Figure 2.16b) spectrum was assumed [88][2].

(a) Barrel geometry

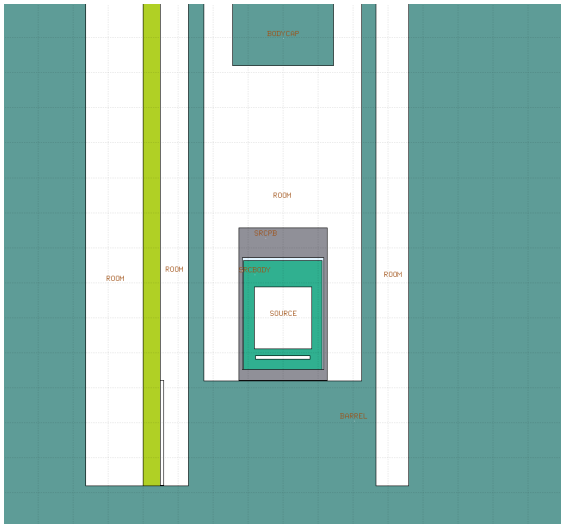

(b) AmBe source capsule dimensions

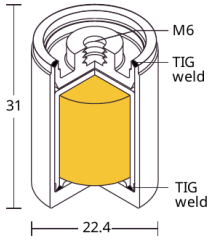

Figure 2.16.: Barrel geometry and source characteristics

The value of interest for these simulations were the incoming neutron spectra on the sample, as well as the production yield of nuclides inside the samples. This last value has been compared to experimental values acquired via gamma spectrometry and computed through `FISPACT-II`

a) Results

The neutrons produced by the Am-Be source are thermalized inside the paraffin barrel, maximizing the neutron capture rate in the vanadium and gold samples. The energy

[1] A. J. Koning et al. 'TENDL: Complete Nuclear Data Library for Innovative Nuclear Science and Technology'. In: *Nuclear Data Sheets*. Special Issue on Nuclear Reaction Data 155 (Jan. 2019), pp. 1–55. ISSN: 0090-3752. DOI: 10.1016/j.nds.2019.01.002.

[2] International Organization for Standardization (ISO). *Part 1: Characteristics and methods of production*. Standard ISO 8529-1:2021. Geneva, CH, Nov. 2021, p. 30.

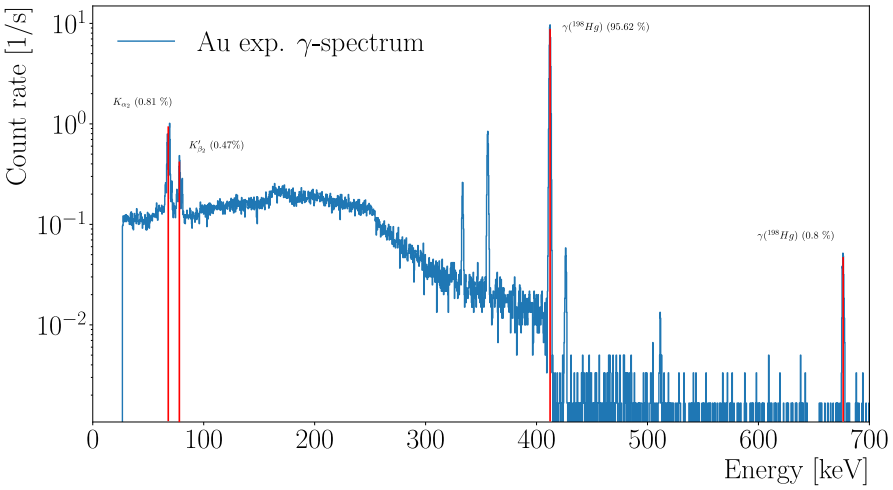

Figure 2.17.: ^{198}Au activated gamma spectra

differential neutron flux calculated by various codes is reported in Figure 2.19. We found an agreement of all simulation for the energy spectrum of the neutron arriving on the sample, but for Geant4-ShieldingLEND which seems to have a different thermalization behaviour. At thermal energy, the LEND (Low Energy Nuclear Data) model deviates of 43% from the MCNP value, when FLUKA, PHITS and the High Precision (HP) from Geant4 stays below 8% of difference. For the fast neutron component, the standard deviation is within 5% for all models.

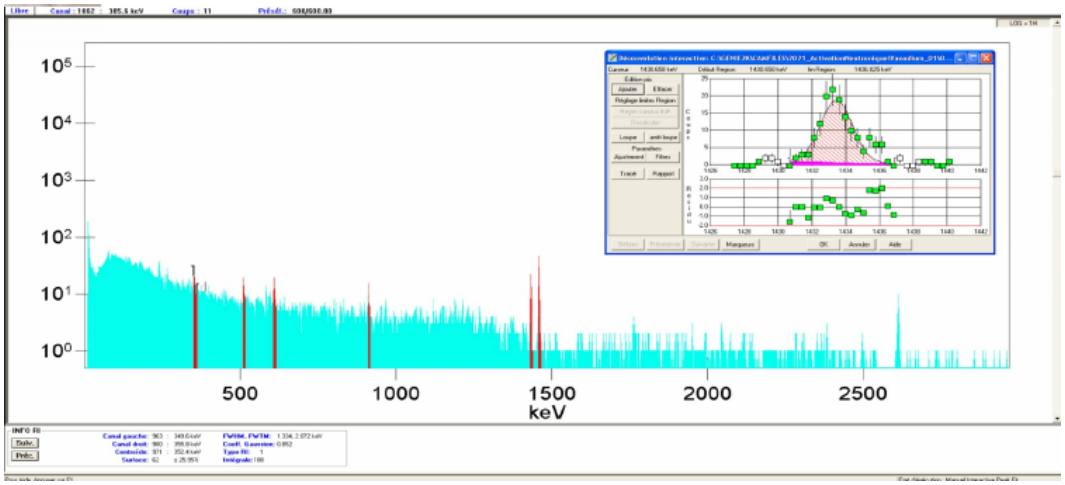

Figure 2.18.: V52 acquired gamma spectrum

The four codes allow scoring the yield of the radioactive nuclei of interest. The simulation results are synthetised in Table 2.8. FLUKA, PHITS and MCNP well agree within

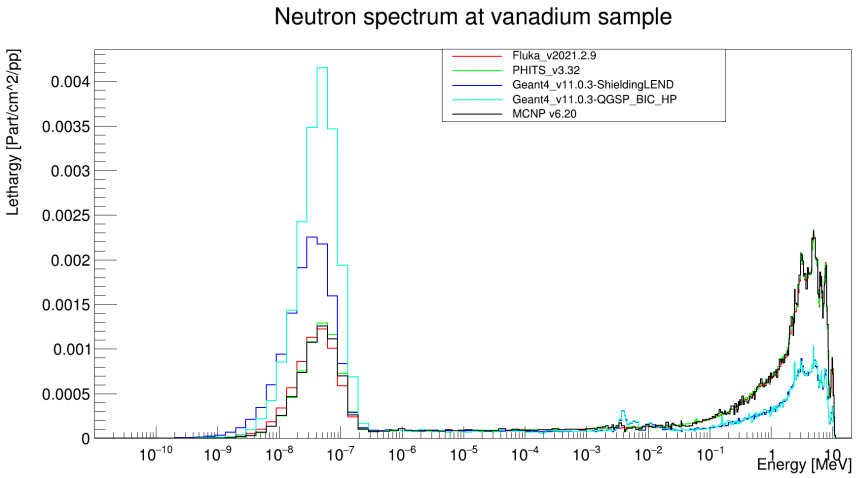

Figure 2.19.: Track-length estimation of the neutron fluence inside the vanadium sample irradiated by the direct neutron field

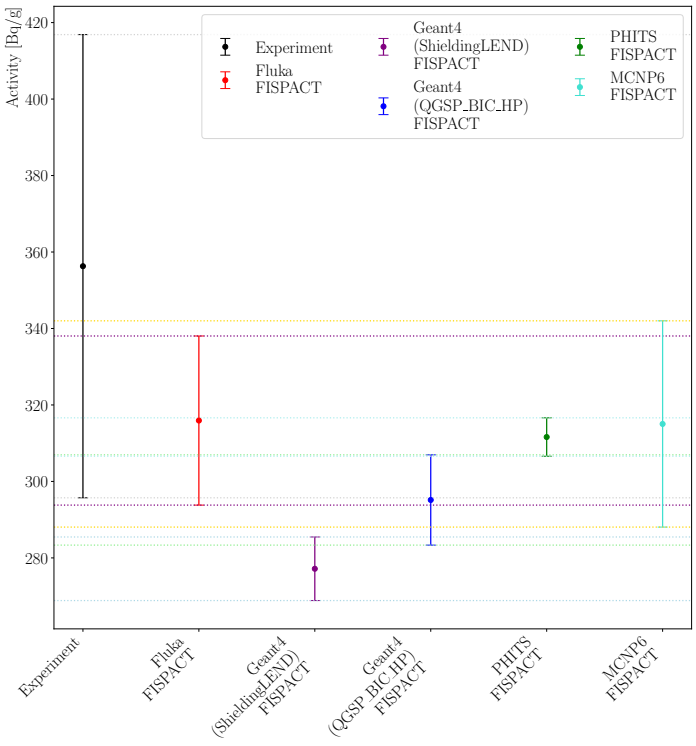

Figure 2.20.: Compilation of measured vs estimated activities for the direct field experiment with the vanadium sample

Table 2.8.: Comparison of expected yield in the irradiated samples

Vanadium	
Code	Production rate [$\times 10^{-4}$ ^{52}V/*pp*]
FlukaINFN	4.08 ± 0.01
Geant4 (ShieldingLEND)	3.78 ± 0.04
Geant4 (QGSP_BIC_HP)	4.24 ± 0.15
PHITS	4.05 ± 0.02
Gold	
Code	Production rate [$\times 10^{-3}$ ^{198}Au/*pp*]
FlukaINFN	0.99 ± 0.01
Geant4 (ShieldingLEND)	0.87 ± 0.01
Geant4 (QGSP_BIC_HP)	1.02 ± 0.01
PHITS	1.02 ± 0.01

1% (3% for Au). As for Geant4, while QGSP_BIC_HP stays within 3.9% (and 1% for Au), ShieldingLEND gives the most discrepancies with as much as 14% of difference for gold. We note that when using the physics list QGSP_BIC_HP the computation's speed is a factor 10 slower.

The same agreement has been found when considering `FISPACT-II`, as shown in Figure 2.20. When comparing native Fluka and Fluka coupled with `FISPACT-II`, we obtain same results within the given statistical uncertainties as well (respectively 332 versus 315 $\mathrm{Bq \cdot g^{-1}}$).

Experimental data points were taken with V and Au, the samples were respectively activated at $357 \pm 61 \mathrm{Bq g^{-1}}$ and $318 \pm 21 \mathrm{Bq g^{-1}}$. Considering uncertainties, the simulations are validated by the experimental data points.

If one can compare codes through the yield of nuclei per primary atoms, to confront to experimental value with ease, `FISPACT-II` remains essential. As well as for the intercomparison of codes, this analytical allows to compare radionuclides inventories with the neutron spectra as the only input, restraining the number of influences.

b) Conclusion

The objective of this work was to compare several MC codes, including a coupling with `FISPACT-II`, for two experimental scenarios: neutrons from AmBe source and secondary neutrons generated in a low energy cyclotron environment irradiated a set of samples and induced activations have been compared. For the AmBe experiment, there is a good agreement between all the codes, and experimental values as well. While the Fluka, MCNP and PHITS agree within less than 3 %, Geant4 and its ShieldingLEND physics list strays to 15%. This difference could be explained by a difference in the thermalization process of neutron (Neutron managed with Geant4 physics lists, not marked with "_HP" i.e., not with high precision models are not able to thermalize).

2.3.4. Around CYRCé

Another widespread usage of particle accelerators is the production of radionuclide for imaging and therapy medical applications. We conducted the second study was conducted inside the (p,n) field of a facility. Cyclotron pour la ReCherche et l'Enseignement (CYRCé) is a TR24 from Advanced Cyclotron System Inc (ACSI) used, in parallel to research activities, for radionuclide production. This machine can produce ^{18}F, ^{64}Cu and ^{89}Y, with a higher current ($\simeq$100 μA). This work will present the characterization of the neutron field generated during the production of ^{18}F via activation foils (measured with gamma spectrometry) and SSNTD.

a) Facility

CYRCé platform (Cyclotron pour la ReCherche et l'Enseigment), housed within the Institut Pluridisciplinaire Hubert Curien (IPHC) in Strasbourg. CYRCé is a TR24 from Advanced Cyclotron System Inc (ACSI), made in 2010 and installed in 2012. There are three beam line :

- one for scientific use, low current but controllable energy ;
- the other for isotopes production (^{18}F, ^{64}Cu, ^{89}Zr), high current.
- A dedicated sensor testing line, notably used for evaluating detectors developed for high-energy physics experiments such as CMS at CERN.

Production line Located in the "casemate", i.e. room containing the cyclotron made of 2-meter-thick concrete walls. Isotopes (see Table 2.9) are produced in a 10 cm-thick lead shielded case ($\simeq$ 60cm cube) installed next to the cyclotron.

The beam is of 2 kW power, with a 100 µA current.

Table 2.9.: Characteristics of CYRCé beam for the three targets

Target	Product	Energy [MeV]	Current [μA]
H_2 ^{18}O	^{18}F	18	80
H_2 ^{18}O	^{18}F	18	80

These isotopes are essential for the synthesis of radiolabelled compounds used in diagnostic imaging, therapeutic monitoring, and targeted treatment protocols.

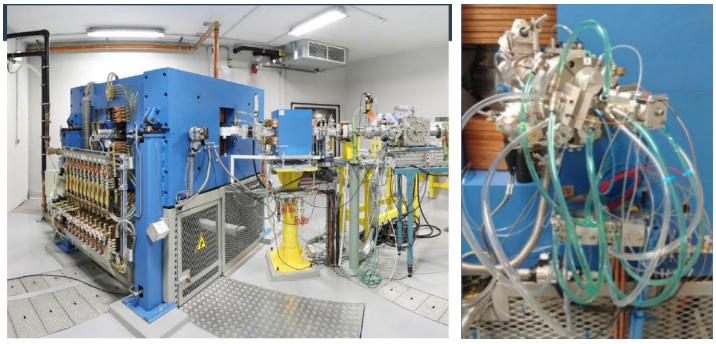

Figure 2.21.: CYRCé and its target selector for radioisotope production

b) Methodology

We will compare the prediction of activity measurements of four Monte Carlo codes, FLUKA-CERN [89][1] FlukaINFN [47][2], Geant4 [43][3], and PHITS [90][4], extending preliminary results from [72][5]. As each of these codes uses different ways to solve the Bateman equation for activity evaluation, `FISPACT-II` [91][6] will be systematically used to report the radionuclide inventory from the estimated neutron spectra of each simulation code.

An experiment was done inside the cyclotron room, with a liquid target of enriched water ($H_2{}^{18}O$) during the production of 90 GBq of ^{18}F, with a proton beam of 18 MeV and a current of 75 μA for 45 minutes. We estimate the neutron field through the activation of metallic samples (Au, Sc Tb, Ta), chosen because their cross-sections and half-lives are compatible with the time constraints for access to the room after irradiation (radio-safety issues). The standard dimensions of the samples are 2.5x2.5cm^2, with thicknesses of 0.2 cm for Ta, 0.1 cm for Tb and Au, and 0.055 cm for Sc.

The activation was measured using HPGe LABSOCS from Canberra. The sensitivity of the setup spans from 40 keV to 2650 keV with a relative efficiency of 40%, while the resolution is 1.9 keV at 1.33 MeV. We computed the activities considering the decay

[1] C. Ahdida et al. 'New Capabilities of the FLUKA Multi-Purpose Code'. In: *Frontiers in Physics* 9 (2022). ISSN: 2296-424X.

[2] A. Ferrari et al. *FLUKA: A Multi-Particle Transport Code*. English. Tech. rep. SLAC-R-773. SLAC National Accelerator Lab., Menlo Park, CA (United States), Dec. 2005. DOI: 10.2172/877507.

[3] J. Allison et al. 'Recent developments in Geant4'. In: *Nuclear Instruments and Methods in Physics Research Section A: Accelerators, Spectrometers, Detectors and Associated Equipment* 835 (2016), pp. 186–225. ISSN: 0168-9002. DOI: https://doi.org/10.1016/j.nima.2016.06.125.

[4] Tatsuhiko Sato et al. 'Features of Particle and Heavy Ion Transport code System (PHITS) version 3.02'. In: *Journal of Nuclear Science and Technology* 55.6 (June 2018), pp. 684–690. ISSN: 0022-3131. DOI: 10.1080/00223131.2017.1419890.

[5] Jonathan Collin et al. 'Validation of Monte Carlo simulations by experimental measurements of neutron-induced activation in cyclotrons'. en. In: *EPJ Web of Conferences*. Vol. 288. Italy: EDP Sciences, 2023, p. 04025. DOI: 10.1051/epjconf/202328804025.

[6] J. -Ch. Sublet et al. 'FISPACT-II: An Advanced Simulation System for Activation, Transmutation and Material Modelling'. In: *Nuclear Data Sheets*. Special Issue on Nuclear Reaction Data 139 (Jan. 2017), pp. 77–137. ISSN: 0090-3752. DOI: 10.1016/j.nds.2017.01.002.

scheme compiled by the National Laboratory Henri Becquerel (LNHB) [15][1].

We placed the samples in four different locations (see Figure 2.22) with expected neutron fluence between 10^9 n/cm^2/s and 10^6 n/cm^2/s.

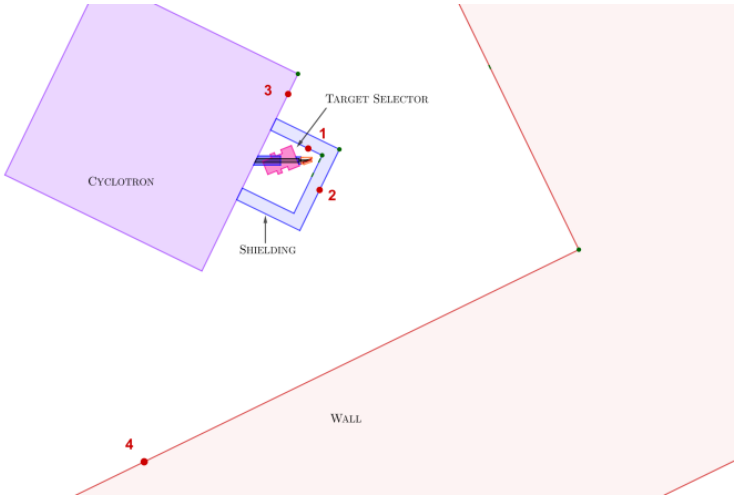

Figure 2.22.: Locations for the irradiated samples. In red, the room walls. In purple the cyclotron, in blue the biological shield, and in pink the target selector. Red dots correspond to sample positions

The neutron libraries used for the MC codes chosen were:

- FlukaINFN 2023.3.1 : this last version manages point-wise neutrons and uses a mix of ENDF/B-VIII.0 [81][2] and TENDL-2021 [87][3] databases. ENDF/B was the sole library used in this case.
- FLUKA-CERN 4-3.2: the two available libraries ENDF/B-VIII.0 and JEFF-3.3 [82][4] were used, with point-wise management
- Geant4 11.0.3: we used both high precision physics list ShieldingLEND and QGSP_BIC_HP, based respectively on ENDF/B-VII.1 and JEFF-3.3.
- PHITS 3.33: allows the usage of JENDL5. We used the former with ENDF/B-VIII.0, JENDL5 [92][5], JEFF-3.3 and TENDL-2021.

[1] Laboratoire National Henri Becquerel. *Nucléide – Lara Application – Laboratoire National Henri Becquerel*. en-GB.

[2] D. A. Brown et al. 'ENDF/B-VIII.0: The 8th Major Release of the Nuclear Reaction Data Library with CIELO-project Cross Sections, New Standards and Thermal Scattering Data'. In: *Nuclear Data Sheets*. Special Issue on Nuclear Reaction Data 148 (Feb. 2018), pp. 1–142. ISSN: 0090-3752. DOI: 10.1016/j.nds.2018.02.001.

[3] A. J. Koning et al. 'TENDL: Complete Nuclear Data Library for Innovative Nuclear Science and Technology'. In: *Nuclear Data Sheets*. Special Issue on Nuclear Reaction Data 155 (Jan. 2019), pp. 1–55. ISSN: 0090-3752. DOI: 10.1016/j.nds.2019.01.002.

[4] A. J. M. Plompen et al. 'The joint evaluated fission and fusion nuclear data library, JEFF-3.3'. en. In: *The European Physical Journal A* 56.7 (July 2020), p. 181. ISSN: 1434-601X. DOI: 10.1140/epja/s10050-020-00141-9.

[5] Osamu Iwamoto et al. 'Japanese evaluated nuclear data library version 5: JENDL-

As for FISPACT-II v5.0.0 used to infer induced activity, the library TENDL-2021 was chosen. Prior to that every neutron spectra were converted into a 1102 multigroup structure, thanks to GRPCONVERT utility from FISPACT-II.

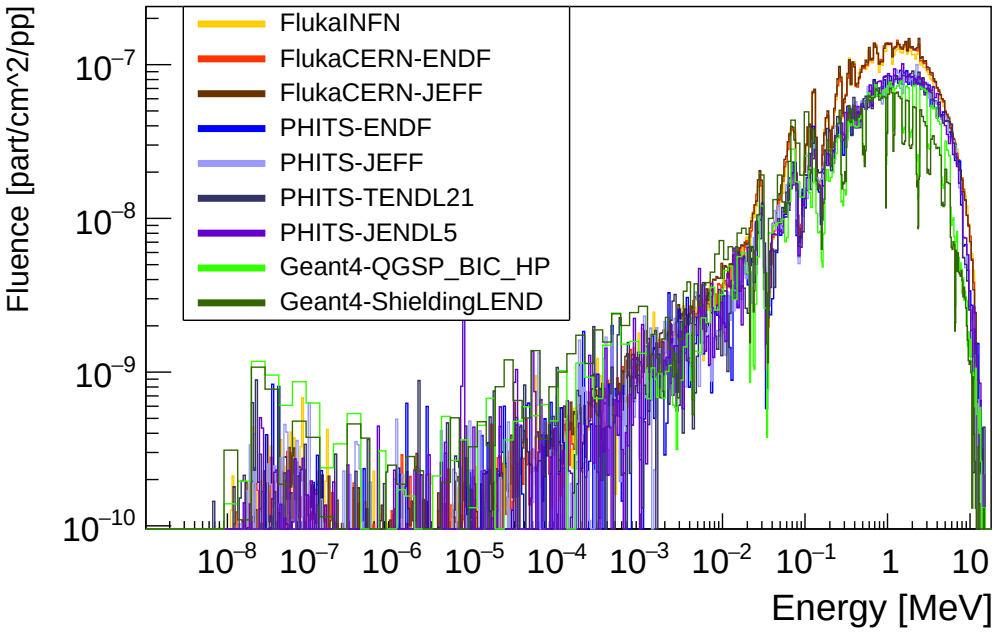

Figure 2.23.: Comparison of simulated neutron lethargy spectra inside the biological shielding using ENDF library

c) Results and interpretations

Whereas PHITS reproduces the 90 GBq ^{18}F production well (5% error), this is not true for FLUKA. We get an overproduction of Fluorine (250% increase). This overestimation is likely due to the use of physics model implemented in FLUKA for the reaction of proton on nuclei.

Yet when looking at the secondary neutron spectra, especially in the closest position to the target (see Figure 2.23), the neutron spectra of all codes agree, except for a minor shift with Geant4 ShieldingLEND. As pointed out in [72][1] for the AmBe experiment, the thermalization behaviours of the MC codes agree, except for Geant4, where, especially at the cyclotron position (Loc. 3), the fast component maximum is 150% higher than FLUKA and PHITS.

5'. In: *Journal of Nuclear Science and Technology* 60.1 (Jan. 2023). _eprint: https://doi.org/10.1080/00223131.2022.2141903, pp. 1–60. ISSN: 0022-3131. DOI: 10.1080/00223131.2022.2141903.

[1] Jonathan Collin et al. 'Validation of Monte Carlo simulations by experimental measurements of neutron-induced activation in cyclotrons'. en. In: *EPJ Web of Conferences*. Vol. 288. Italy: EDP Sciences, 2023, p. 04025. DOI: 10.1051/epjconf/202328804025.

d) Activation detector

We performed activation calculations with all codes and evaluated libraries reported in the last paragraph of the Methodology section, estimated a week after the irradiation, corresponding to the average experimental acquisition time. Figure 2.24 presents the summary for the ENDF/B library. In this comparison code to code, PHITS is taking the lead with an average ratio between calculation and measurement of 1.45 ± 0.7. The conclusion is the same if we expand the comparison to all libraries.

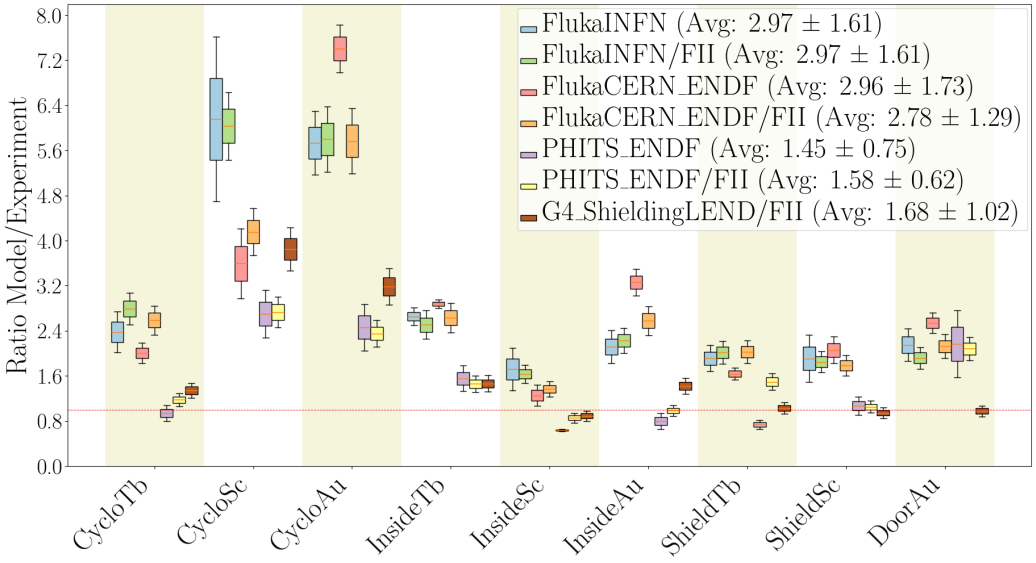

Figure 2.24.: The ratio of estimated over measured activity for FLUKA, PHITS and Geant4 using the ENDF library

FLUKA can perform activation computation, using the RESNUCLEi card. For PHITS, the JAEA developed an independent tool, dchain-sp, that easily communicates with PHITS (yet it can be extended to any coupling if the input is correctly formatted). In both tools in this case agree well within the error bars of `FISPACT-II`.

e) Neutron mapping

The SSNTDs are another interesting technique of neutron field characterization. Several CR-39 (Technol Chiyoda, Japan) were placed inside the casemate, yet farther away from the target, as shown in Figure 2.25. In order not to saturate the detectors (the system used's higher limit is around 150k tr/cm^2), a shorter exposure (13 µA of integrated current, i.e. typically 5 minutes irradiation) was used.

After irradiation, all SSNTDs were etched simultaneously in a KOH^- solution (30 % concentration) for 2.5 hours at 90 °C.

Each CR-39 was enclosed in the previously mentionned WNP, allowing to distinguish

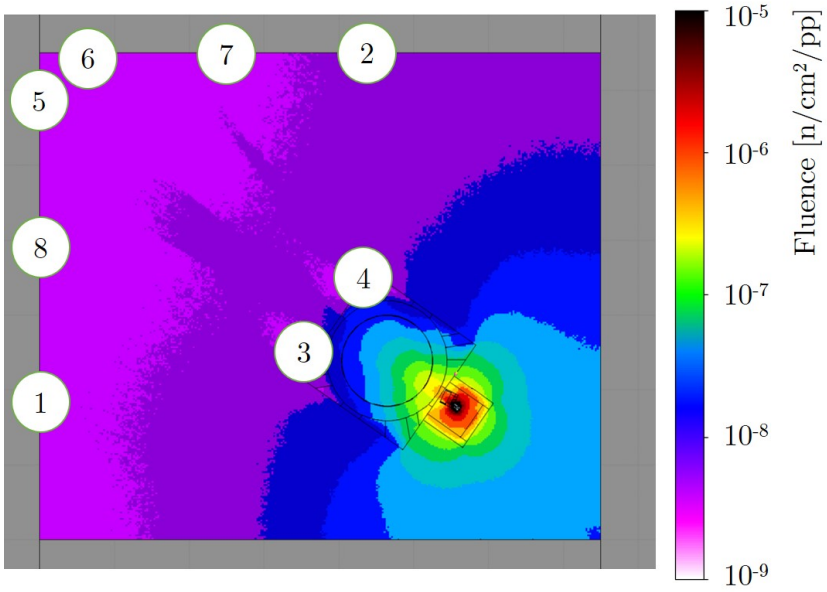

Figure 2.25.: Location for the SSNTD with estimated neutron fluence from FLUKA-CERN

two sections, one impacted by recoil protons and another one with both recoil protons and alphas from boron capture (converter containing 8% boron, and 92 % High Density PolyEthylene). Figure 2.26 present a typical detector acquisition, the two images cut from the global acquisition, are analysed via ImageJ [93][1]. During this PhD, the acquisition have been improved to capture the entire detector, and merge the thousand of pictures obtained. The track detection is still performed using the one developped in previous PhD [94][2].

The Figure 2.27 show the comparison of the thermal over fast component ratio measured experimentally in several location of the "casemate", in addition to two unirradiated detectors (allowing to verify track pollution).

We notice that for locations 5 and 6, the farthest point from the target, the results are of the same magnitude, with the thermal component prominent as expected. For other positions, we can only conclude that the tendency (results taken relatively to the other) is quite similar, yet simulation does overestimate the thermal component. The simulation ratio does not consider the efficiency of the detector, such computation could enhance the simulation results.

[1]Caroline A. Schneider, Wayne S. Rasband, and Kevin W. Eliceiri. 'NIH Image to ImageJ: 25 years of image analysis'. en. In: *Nature Methods* 9.7 (July 2012), pp. 671–675. ISSN: 1548-7105. DOI: 10.1038/nmeth.2089.

[2]Halima Elazhar. 'Dosimétrie neutron en radiothérapie: étude expérimentale et développement d'un outil personnalisé de calcul de dose Monte Carlo'. français. Thèse de doctorat. Université de Strasbourg, 2018.

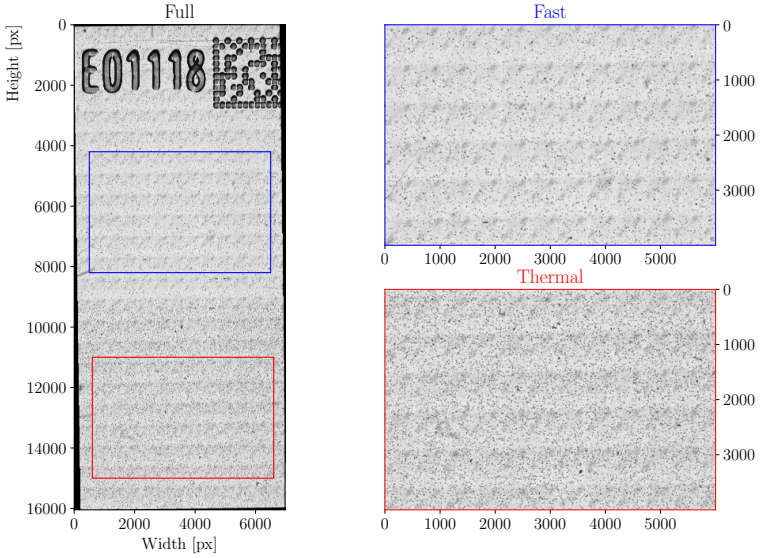

Figure 2.26.: Typical SSNTD image acquisition, with splitting between Fast (HDPE) and Thermal area (BN)

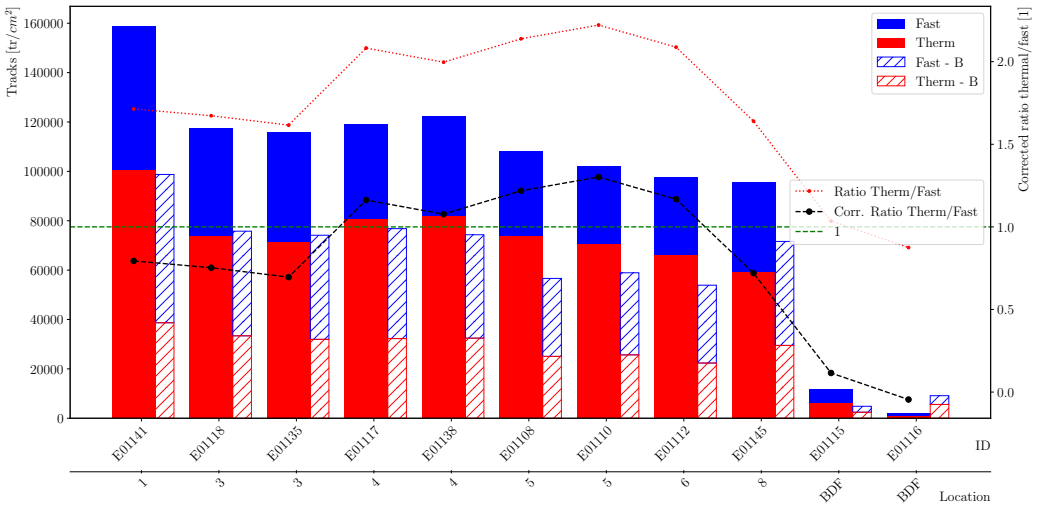

Figure 2.27.: Stacked histogram of measured average track densities. The ratio of Track density BN (thermal) over HDPE (fast) is presented, with and without correction from HDPE composition in thermal converter

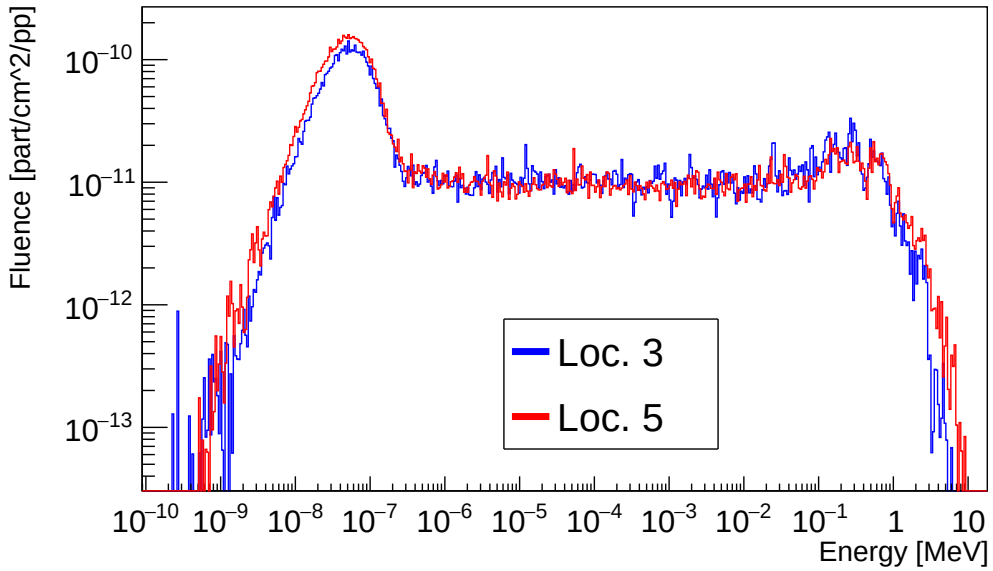

Figure 2.28.: Expected neutron spectrum at Location 3 and Location 5

f) Discussions

Activity were estimated with three Monte Carlo codes. FLUKA and PHITS have the advantage for calculating the activity without the need for another code. Geant4 also allows to estimate such activity observable, yet one must complexify quite largely the model used, to avoid the extra step well validated by `FISPACT-II`, as such it was preferred to use it directly.

The estimations are well in agreement with the thoroughly validated `FISPACT-II`. The advantage of using these MC tools, in addition to their mandatory use to obtain the secondary spectra, is the easiness of considering many secondary particles interactions (and not solely neutrons). Yet `FISPACT-II` stays the reference for such inventory, especially when making multi-code comparison. In the case of ^{18}F production modelling, PHITS is currently the most adequate.

The SSNTD technique is an appropriate passive tool for measurements at a low fluence, but for more precise characterization of neutron field the gamma spectrometry via activation detectors remains the most adequate.

2.3.5. Conclusions and perspectives

This work could serve as a basis for users of medical LINACs or of cyclotrons for the production of radioisotopes. In order to be able to receive and manage waste at a storage site, ANDRA in France, requires information on the nature of the radioelements and their composition. In the first part, we assessed the activities β and γ of the various components of the accelerator likely to be irradiated in order to classify them

radiologically as waste. Pure β emissions are very difficult to detect, and the resources required are both costly and time-consuming. This type of characterisation would save a great deal of time if beta activity could be determined from gamma activity, which is easy to measure. In its second part, this work presents the first strategies for obtaining numerical modelling of the installation of interest, in this case from the outside. The aim is to validate the source term during the life of the installation, so as to be able to question dismantling in a pre-emptive manner. The aim is to establish criteria for validating or not the model used, using active and passive gamma/neutron spectrometry methods.

This work aimed to compare several MC codes, including coupling with `FISPACT-II` and CINDER'90, to estimate the gamma radioactivity. The first scenario concerned the photoneutrons in the treatment head of decommissioned medical LINAC, using FLUKA and MCNP/CINDER'90. The second scenario focused on the neutron field of an operating proton cyclotron using FLUKA, Geant4, and PHITS coupled with `FISPACT-II`. For the first scenario, FLUKA and MCNP/CINDER'90 give similar results for the main radionuclides produced by neutron activation of copper and even all the trace elements included except ^{65}Zn. Despite the uncertainty on this LINAC's operation life of this LINAC, the residual radioactivity estimation well matches the measurements. As for the activation evaluation around CYRCé cyclotron, the activity was estimated after a week to circumvent the metastable impact.

Passive characterization of neutron field using SSNTDs is cheap and easy to implement and allows an interesting relative position to position knowledge about the neutron field. Combining the gamma spectrometry technique, based on activation foils, at some specific locations and wider spread CR-39 probes would enable to expand easily the field of interest to create a neutron mapping.

Conclusion

This chapter investigates how particle accelerators –particularly medical LINACs and cyclotrons– induce radioactivity in surrounding materials through secondary radiation. It combines Monte Carlo simulations with experimental validation to assess activation levels, which is essential for radiation safety, waste classification, and facility decommissioning. In the first part, a comprehensive presentation of four major Monte Carlo-based simulation tools (Geant4, FLUKA, PHITS, and MCNP) which were employed to model radiation transport and activation phenomena. These tools represent the cornerstone of modern computational physics, offering robust frameworks for simulating the behaviour of particles as they interact with matter. Each of these codes is designed to tackle highly complex systems, where deterministic approaches are insufficient due to the inherent stochastic nature of particle interactions. By relying on probabilistic algorithms, they allow for the accurate modelling of phenomena such as scattering, absorption, secondary particle generation, and induced radioactivity. The second part of this study uses a variety of experimental techniques and case analyses to investigate radiation transport and activation phenomena in detail and with great precision. A

key component of the experimental approach is gamma spectroscopy, which identifies radionuclides through their characteristic gamma emissions. This technique uses high-purity germanium (HPGe) detectors, which are renowned for their spectral resolution and sensitivity. This method is complemented by SSNTD, which are passive devices that map neutron fields by recording the tracks left by charged particles resulting from neutron interactions.

These techniques were applied across several targeted case studies. In the context of medical linear accelerators (LINACs), activation was observed in structural components made of copper and steel. This activation results from exposure to high-energy Bremsstrahlung photons and secondary photoneutrons generated during therapeutic procedures. Another case involved an AmBe neutron source, where vanadium and gold samples were irradiated to study neutron-induced activation. The experimental results, obtained via gamma spectroscopy, were compared with simulations from multiple Monte Carlo codes to assess consistency and validate modelling accuracy. Further investigation was conducted at the CYRCé cyclotron, particularly during the production of 18F. Here, the neutron field was characterized through activation measurements in metallic foils, with spatial mapping performed using SSNTDs to capture the distribution and intensity of neutron flux. To support these simulations, a variety of nuclear data libraries were utilized, including ENDF, JEFF, JENDL, and TENDL. Due to proprietary constraints, certain simplifications in geometry were necessary, which were carefully considered to maintain the integrity of the modelling process. Finally, neutron mapping was refined using CR-39 detectors, which allowed for the differentiation between thermal and fast neutron components. While simulation results generally aligned with experimental observations, a tendency to overestimate thermal neutron contributions was noted, highlighting areas for further refinement in computational modelling. Together, these methodologies and case studies form a cohesive framework for understanding activation mechanisms and validating simulation tools in diverse radiation environments. Looking ahead, this study opens several promising avenues for research and practical application in the field of radiation transport and activation modelling. One of the key contributions lies in the domain of waste management and decommissioning, where the proposed framework enables accurate estimation of residual radioactivity in accelerator components. This approach supports institutions such as ANDRA in the classification and handling of radioactive waste, facilitating safer and more efficient disposal strategies. A particularly innovative perspective involves the challenge of detecting pure beta emitters, which are notoriously difficult to measure directly. The study suggests that beta activity could potentially be inferred from gamma measurements, offering a streamlined method for waste characterization that could significantly reduce the complexity and cost of radiological assessments. In terms of model validation, the work outlines a dual approach combining active techniques, such as gamma spectroscopy, with passive methods, notably Solid-State Nuclear Track Detectors (SSNTDs). This integrated strategy enhances the reliability of source term estimations and activation models, ensuring that simulations align closely with experimental data. The study also lays foundational work for benchmarking in Accelerator Driven Systems (ADS). By leveraging EXFOR datasets, future efforts will focus on validating Monte Carlo simulation codes and nuclear data

libraries, a critical step toward improving predictive accuracy in ADS design and operation. On the development front, the TRANSMUTEX project is advancing its own simulation platform, TMX-MC, built on the Geant4 framework. This tool is specifically tailored to address the unique challenges of dismantling ADS facilities, incorporating detailed physics models and flexible geometry handling. Finally, the scope of future research will extend to the study of (x,n) reactions in proton accelerators, particularly at energies reaching the GeV scale. These investigations hold significant relevance for both medical isotope production and nuclear waste transmutation, bridging fundamental research with impactful real-world applications. Together, these perspectives chart a dynamic and multidisciplinary path forward, blending theoretical modelling, experimental validation, and technological innovation to tackle some of the most pressing challenges in nuclear science and engineering.

Chapter

3. Tracking radionuclide vector through time: Bateman equations

I have given a name to my pain,
and it is Batman.

(Joker, Batman – 1989)

3.1. The interest of developing a new Bateman solver . . . 96
3.2. Bateman equations resolution . . . 97
3.2.1. Livermore Solver for Ordinary Differential Equations . . . 98
3.2.2. Chebyshev Rational Approximation Method . . . 99
3.2.3. Transmutation Trajectory Analysis . . . 100
3.3. TMX_Bateman . . . 100
3.3.1. Implementation of the decay and transmutation equation . . . 103
3.3.2. Inputs . . . 105
3.3.3. Evaluated databases . . . 106
3.3.4. Outputs . . . 108
3.3.5. Isotopic composition . . . 108
3.3.6. Activity . . . 108
3.3.7. Heat load . . . 111
3.3.8. Committed dose . . . 116
3.3.9. Decay spectra . . . 116
3.4. Benchmark of `TMX_Bateman` against `FISPACT-II` and `DCHAIN-PHITS` . . . 117
3.4.1. Universe material check . . . 117
3.4.2. Decay only . . . 120
3.4.3. Transmutation/depletion considerations . . . 124
3.5. Application . . . 127
3.5.1. Extracting the γ spectra. . . . 127
3.5.2. Extracting the alpha spectrum . . . 129
3.5.3. Identifying β pure emitters. . . . 129
3.6. Conclusion . . . 133

Nuclear inventory analysis is required for many nuclear applications such as fuel depletion in reactors, material activation in nuclear devices, radiation dose assessment or decay calculations. There are different approaches to conduct such analysis, either deterministically or via Monte Carlo. Precise knowledge of radionuclide inventory can only be obtained with well validated nuclear data, to accurately reproduce the phenomena in question (mostly neutron capture and neutron induced fission in nuclear reactor, as well as photonuclear or even (α, n) channels). This requires precise knowledge of the usage programme of the facility of interest.

3.1. The interest of developing a new Bateman solver

There are a a large number of programs designed to resolve these issues. Historically, the US Department of Energy's ORIGEN then ORIGEN2 [95][1] were the reference for such studies. The project has forked several times, for instance, with KIT version, KIT-ORIGEN (KORIGEN) [96][2]. The ORNL (Oak Ridge National Laboratory) continues its development under the Standardized Computer Analyses for Licensing Evaluation (SCALE) [97][3] ecosystem (and the name ORIGEN). We should also mention some other more generalist codes (considering also accelerator activation) with more modern interface such as Fusion-Induced Spallation and Activation Code Tool (FISPACT) [91][4], Decay Chain Analysis code (DCHAIN) [98][5] or Nuclear Inventory Uncertainty Tool (NUIT) [99][6], which are also continuously developed. Such developments mostly consist of ergonomic improvements and minor bug fixes, as the equation have been well described since a century, even if new strategies for faster computation are created, as [100][7] or [101][8].

[1] C V Parks and P O Box. *Overview of ORIGEN2 and ORIGEN-S: capabilities and limitations*. en. Tech. rep.

[2] U. Fischer and H. W. Wiese. 'Verbesserte konsistente Berechnung des nuklearen Inventars abgebrannter DWR-Brennstoffe auf der Basis von Zell-Abbrand-Verfahren mit KORIGEN'. de. In: *Karlsruher Institut für Technologie*. Institut für Neutronenphysik und Reaktortechnik (INR) (1983). DOI: 10.5445/IR/270018961.

[3] W. A. Wieselquist and R. A. Lefebvre. *SCALE 6.3.1 User Manual*. en. Tech. rep. Oak Ridge National Laboratory, 2023.

[4] J. -Ch. Sublet et al. 'FISPACT-II: An Advanced Simulation System for Activation, Transmutation and Material Modelling'. In: *Nuclear Data Sheets*. Special Issue on Nuclear Reaction Data 139 (Jan. 2017), pp. 77–137. ISSN: 0090-3752. DOI: 10.1016/j.nds.2017.01.002.

[5] Hunter N. Ratliff et al. 'Modernization of the DCHAIN-PHITS activation code with new features and updated data libraries'. In: *Nuclear Instruments and Methods in Physics Research Section B: Beam Interactions with Materials and Atoms* 484 (Dec. 2020), pp. 29–41. ISSN: 0168-583X. DOI: 10.1016/j.nimb.2020.10.005.

[6] Jian Li et al. 'The NUIT code for nuclide inventory calculations'. In: *Annals of Nuclear Energy* 148 (Dec. 2020), p. 107690. ISSN: 0306-4549. DOI: 10.1016/j.anucene.2020.107690.

[7] Maria Pusa and Jaakko Leppänen. 'Computing the Matrix Exponential in Burnup Calculations'. In: *Nuclear Science and Engineering* 164.2 (Feb. 2010), pp. 140–150. ISSN: 0029-5639. DOI: 10.13182/NSE09-14.

[8] Kai Huang et al. 'Improvements to the Transmutation Trajectory Analysis of depletion evaluation'. In: *Annals of Nuclear Energy* 87 (Jan. 2016), pp. 637–647. ISSN: 0306-4549. DOI: 10.1016/j.anucene.2015.10.013.

The main Monte Carlo tools also possess activation and decay chain resolution modules, as FLUKA [47][1], MCNP6 [102][2], PHITS [50][3] (with its association with `DCHAIN-PHITS`), TRIPOLI-4 [103][4]. Yet only TRIPOLI or MCNP among those, allows for criticality simulation, necessary to estimate the spectrum and fluences when concerned with nuclear facilities.

When using FLUKA, which allows to get every observables possible, thanks to its standard detectors (USRBIN, USRBDX, USRDUMP), it is necessary to rerun the entire simulation, if the irradiation profiles changes. Only decoupled tools as `FISPACT-II` or `DCHAIN-PHITS` allow to modify the irradiation profile at lower costs in term of computation time, as the projectile spectra (and extra yields) are already computed when using them. Yet not all observables that can be extracted from the decay data are exploited by the aforementioned code.

Hence, there is a need for a module, that can extract any secondary particle spectra. The programme usually provides the three main heat channels (from light and heavy particles or from electromagnetic radiations; see subsection 3.3.7). From the available spectra, one can decompose all specific channels to better estimate, and alleviate, the origin of the heat.

The available spectra could also be fully extracted, especially the alpha spectra, to ascertain whether there is a reaction threshold, and whether this should be considered, see subsection 3.5.1. Indeed, `FISPACT-II` only considers the interaction of the projectile particle (primary or secondary). `DCHAIN-PHITS` expanded it this to include photonuclear reactions.

3.2. Bateman equations resolution

The generalised Bateman equation for tracking an inventory can be written in the form referenced in Equation 3.1. Some of the solving strategies are listed in the following subsections.

$$\frac{dN_j(t)}{dt} = -\left[\lambda_j + \xi_j\right] N_j + \sum_{\substack{i=1 \\ i\neq j}}^{J} \left[\lambda_{i\to j} + \xi_{i\to j}\right] N_i + S_j \tag{3.1}$$

$$\xi_j = \int_0^{+\infty} \sigma_j(E)\phi_n(E)dE \tag{3.2}$$

[1] A. Ferrari et al. *FLUKA: A Multi-Particle Transport Code*. English. Tech. rep. SLAC-R-773. SLAC National Accelerator Lab., Menlo Park, CA (United States), Dec. 2005. DOI: 10.2172/877507.

[2] Joel Aaron Kulesza et al. *MCNP® Code Version 6.3.0 Theory & User Manual*. Tech. rep. LA-UR-22-30006, Rev. 1. Los Alamos, NM, USA: Los Alamos National Laboratory, Sept. 2022. DOI: 10.2172/1889957.

[3] Tatsuhiko Sato et al. 'Recent improvements of the particle and heavy ion transport code system – PHITS version 3.33'. In: *Journal of Nuclear Science and Technology* 0.0 (2023), pp. 1–9. ISSN: 0022-3131. DOI: 10.1080/00223131.2023.2275736.

[4] François-Xavier Hugot et al. 'Overview of the TRIPOLI-4 Monte Carlo code, version 12'. en. In: *EPJ Nuclear Sciences & Technologies* 10 (2024), p. 17. ISSN: 2491-9292. DOI: 10.1051/epjn/2024018.

$$\xi_{i\to j} = \sum_{q=1}^{M} \int_0^{+\infty} \sigma_{q,i\to j}(E)\phi_n(E)dE \tag{3.3}$$

where:

- $N_j(t)$ is the number of nuclei of isotope j at time t with an initial value $N_{j,0}$;
- J is the total number of isotopes present in the database ;
- M is the total number of reactions capable of transmuting an isotope ;
- $\sigma_j(E)$ is the microscopic absorption cross-section of isotope j at energy E [b] ;
- $\sigma_{q,i\to j}(E)$ is the microscopic cross-section of transmutation reaction q from isotope i to isotope j at energy E [b] ;
- $\phi_n(E)$ is the energy spectrum of the neutron flux in the material considered $\left[\text{cm}^{-2}\cdot\text{MeV}^{-1}\cdot\text{s}^{-1}\right]$;
- λ_j is the decay constant of isotope j $\left[\text{s}^{-1}\right]$;
- ξ_j is the total transmutation rate of isotope j under the neutron flux $\left[\text{s}^{-1}\right]$;
- $\lambda_{i\to j}$ is the decay constant from isotope i to isotope j $\left[\text{s}^{-1}\right]$;
- $\xi_{i\to j}$ is the production rate of isotope j under the neutron flux from isotope i $\left[\text{s}^{-1}\right]$;
- S_j is the external production rate of isotope j $\left[\text{s}^{-1}\right]$.

One of the preferred solving strategy is to transform the Equation 3.1 into a matrix equation of the form:

$$\frac{d\mathbf{n}(t)}{dt} = \mathbf{A}\mathbf{n}(t) \tag{3.4}$$

where:

- $\mathbf{n}$ is the radiological vector, at time t with an initial value $\mathbf{n_0}$;
- $\mathbf{A}$ is the burnup matrix

3.2.1. Livermore Solver for Ordinary Differential Equations

The Bateman equation is reduced to a simple ordinary differential equation, expressed as follows:

$$\begin{cases} \dfrac{dy_i}{dt} = f_i\left(y_j, t\right) \\ y_i\left(t{=}0\right) = y_{i,0} \end{cases}$$

This system of equation is considered "stiff", as the eigenvalues of such matrices can differ by large order of magnitude. Therefore, methods such as the explicit Runge-Kutta are not appropriate, as in order to satisfy stability conditions, the step size must be of the order of $1/max(-Re(\lambda_i))$, where λ_i are the eigenvalues. This implies a high computation time, so the use of a backward differentiation formula method is recommended, as their stability is not impacted by the step-size, only their accuracy [104][1].

[1] Krishnan Radhakrishnan. 'Description and Use of LSODE, the Livermore Solver for Ordinary Differential Equations'. en. In: ().

Such resolution strategy has been implemented in tool such as the FORTRAN Livermore Solver for Ordinary Differential Equations (LSODE). Specifically with the sixth order three steps Gear's method, that is expressed in its general form in Equation 3.5.

$$\begin{cases} y^{p}_{n+1} = -18y_n + 9y^{c_1}_{n-1} + 10y^{c_2}_{n-2} + 9hy'_n + 18hy'_{n-1} + 3hy'_{n-2} \\ hy'^{p}_{n+1} = -57y_n + 24y^{c_1}_{n-1} + 33y^{c_2}_{n-2} + 24hy'_n + 57hy'_{n-1} + 10hy'_{n-2} \\ F = hy'^{p}_{n+1} - hf(x_{n+1}, y^{p}_{n+1}) \\ y_{n+1} = y^{p}_{n+1} - \dfrac{95}{288}F \\ y^{c_1}_{n} = y_n + \dfrac{3}{160}F \\ y^{c_2}_{n-1} = y^{c_1}_{n-1} - \dfrac{11}{1440}F \\ hy'_{n+1} = hy'^{p}_{n+1} - F \end{cases} \tag{3.5}$$

where:

- c_1 and c_2 are correction factors;
- $y' = f(x, y)$;

This method and tool are used by `FISPACT-II`, with minor modifications made to take advantages of the new capabilities of FORTRAN95.

3.2.2. Chebyshev Rational Approximation Method

The solution to the differential expression of Equation 3.4 can be expressed simply as the Equation 3.6. The difficulty lies in the estimation of the $e^{\mathbf{A}t}$ term.

From the Taylor expansion definition Equation 3.7 of order k, the numerical error can improved with the Quadrature-based Rational Approximation Method (QRAM) (Equation 3.8), or with the Chebyshev Rational Approximation Method (CRAM) (Equation 3.8), which is more deployed in burn-up solvers, due to its computation efficiency.

$$\mathbf{n}(t) = \mathbf{n_0} \times e^{\mathbf{A}t} \tag{3.6}$$

$$e^{\mathbf{A}t} = \mathbf{I} + \sum_{i=1}^{k} \frac{1}{i!}\mathbf{A}^i t^i + o\left(\mathbf{A}^k\right) \tag{3.7}$$

$$= \sum_{i=1}^{k} c_i e^{z_i} \left(z_i - \mathbf{A}t\right)^{-1} + o\left(\mathbf{A}^k\right) \tag{3.8}$$

$$= \alpha_0 \mathbf{I} + 2\,\Re\mathrm{e}\left\{\sum_{i=1}^{k/2} \alpha_i \left(\theta_i + \mathbf{A}t\right)^{-1}\right\} + o\left(\mathbf{A}^k\right) \tag{3.9}$$

where:

- $\mathbf{I}$ is the identity matrix;

- k is the order of the serie ;
- c_i and z_i are respectively the quadrature weight and point ;
- α_i and θ_i are the CRAM coefficients.

The CRAM is used for cyclic channels that cannot be linearized directly (see subsection 3.2.3). In addition, the computation speed is minimal, but it will fail for low appearance nuclides, as illustrated in Table 3.1 from [101][1].

The CRAM strategy is used by the SERPENT MC code [105][2] (14-order by default) for transmutation computation, as well as NUIT (16-order by default).

While QRAM is less susceptible to numerical instability, its convergence speed is the hurdle of this method, see Table 3.1.

3.2.3. Transmutation Trajectory Analysis (TTA)

Transmutation Trajectory Analysis (TTA) is the "original" solution of the Bateman equation is the linearization of the system. This methods is illustrated in Figure 3.1.

This implementation consists to split all the decay path until one obtain a stable element. If there are no cycle, i.e. only decay, the solution obtained is exact.

However, when cycle appears, see Figure 3.1b, a cut-off is necessary to stop the chain.

The main issue with the method, when considering decay only, is the high computational time required to linearized the decay path. However due to its precision, it is used by `DCHAIN-PHITS`, SERPENT (when not considering any transmutation) and the code of interest of this chapter `TMX_Bateman`.

3.3. TMX_Bateman

The core implementation of `TMX_Bateman` was originally developed by Transmutex. During the course of this work, the code has been significantly enhanced with several critical features, including:

- Implementation of ENDF-6 decay data parsing capabilities
- Development of secondary particle spectra export functionality
- Expansion of measurements
- Integration of HDF5-formatted ENDF-6 database parsing
- Incorporation of neutron interaction physics

[1] Kai Huang et al. 'Improvements to the Transmutation Trajectory Analysis of depletion evaluation'. In: *Annals of Nuclear Energy* 87 (Jan. 2016), pp. 637–647. ISSN: 0306-4549. DOI: 10.1016/j.anucene.2015.10.013.

[2] Jaakko Leppänen et al. 'The Serpent Monte Carlo code: Status, development and applications in 2013'. In: *Annals of Nuclear Energy*. Joint International Conference on Supercomputing in Nuclear Applications and Monte Carlo 2013, SNA + MC 2013. Pluri- and Trans-disciplinarity, Towards New Modeling and Numerical Simulation Paradigms 82 (Aug. 2015), pp. 142–150. ISSN: 0306-4549. DOI: 10.1016/j.anucene.2014.08.024.

Table 3.1.: Comparison of Bateman solving algorithm, extracted from [101][a].

Methods[†]	Time [ms]	max(E_i) for i satisfying $F_{ref,i} \in$ $[-20,-10)$	$[-10,-5)$	$[-5,0)$[‡]
1 million year of only decay of uranium oxyde fuel				
TTA [10^{-30}]	39.41	ref.	ref.	ref.
QCRAM [64]	405.3	-11.1502	-5.6023	-1.4819
CRAM [14]	2.109	-9.3630	> 0	> 0
50 days irradiation of uranium oxyde fuel				
QCRAM [64]	2387	ref.	ref.	ref.
CRAM [14]	4.742	-11.4616	-6.9242	-3.6610
TTA [10^{-15}]	77.30	-7.9819	-4.0320	> 0
TTA [10^{-20}]	645.8	-12.1997	-8.1636	-0.4280
TTA [10^{-30}]	9.394×10^5	-14.6170	-11.4003	-8.4262

[†] The order (or cut-off for TTA) is indicated between the brackets

[‡] E_i is the absolute relative error ($\log_{10}$), and $F_{ref,i}$ is the number density fraction of i-th nuclide ($\log_{10}$)

[a] Kai Huang et al. 'Improvements to the Transmutation Trajectory Analysis of depletion evaluation'. In: *Annals of Nuclear Energy* 87 (Jan. 2016), pp. 637–647. ISSN: 0306-4549. DOI: 10.1016/j.anucene.2015.10.013.

(a) Decay network

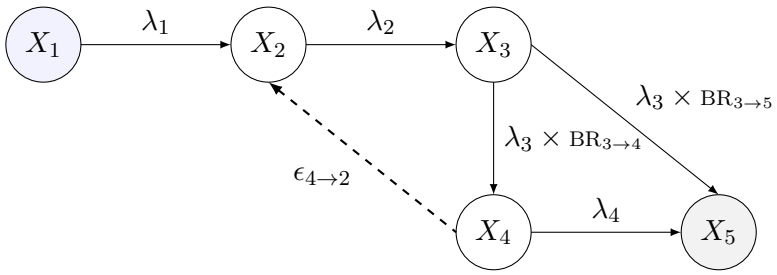

(b) Linearised decay path

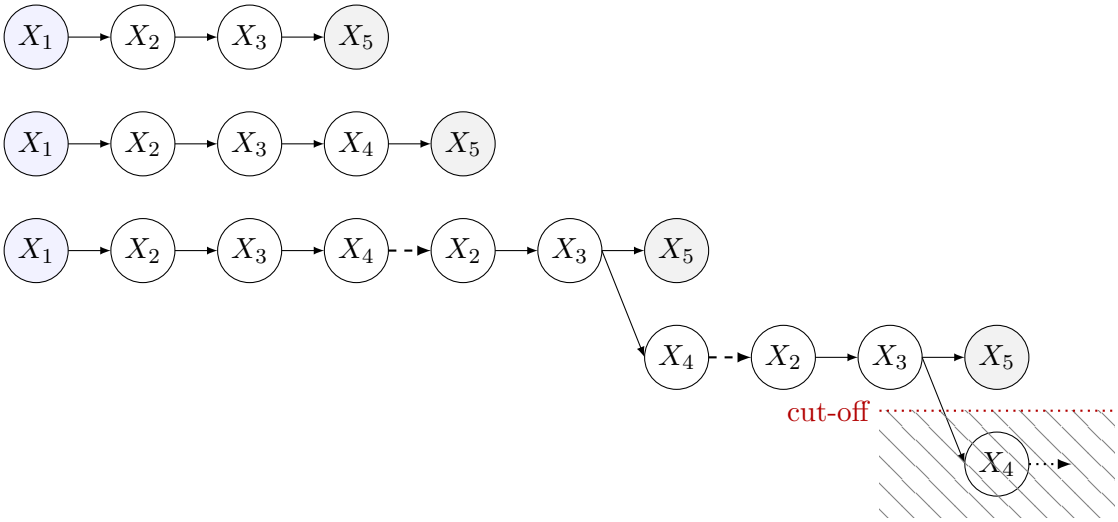

Figure 3.1.: Principle of TTA

3.3.1. Implementation of the decay and transmutation equation

Motivation for TTA choice Table 3.1 is an excerpt of a comparison, by [101][1], of the Transmutation Trajectory Analysis, the Quadrature-based and the Chebyshev Rational Approximation methods. According to this table, the TTA is well suited for depletion calculations, as the analytical solution of the Bateman equation can be obtained. Whereas CRAM will fail for low appearance nuclides, but will be the most suitable for transmutation. As the main interest, for the development of `TMX_Bateman` was the depletion only for fuel cycle analysis, the TTA was chosen.

Main principle As previously mentioned, the goal is to track a nuclide vector (B_1^0, B_2^0, ..., B_n^0), after a Δ_t of irradiation and/or cooling time. `TMX_Bateman` was developed from [106][2], based on [107][3]

If only decay is considered, one can simply linearize the decay path by following decay products until finding a stable element[4].

The transmutation part is considered in a two steps. First, disregarding the decay and inventory evolution over time step, the maximum yield is computed. Then, the maximum yielded inventory is decayed for the time step duration. When considering transmutation, one can create cycling path. This choice implies that the material irradiated does not evolve during the given time period, and that the by-products from irradiation do not interact with the external projectile (i.e. neutrons, depending on the given cross-section tables).

The initial inventory can then be split into an initial decay term and a transmutation term, which corresponds to the maximum nuclides yielded from irradiation. The two inventories are followed separately and then summed up.

a) Decay of nuclides

After linearization of the decay path, the exact equation implemented in `TMX_Bateman` is the solution proposed by [106][5].

$$N_i(t) = \sum_{m=1}^{i} N_m^0 \sum_{j=m}^{i} d_{ijm} e^{-\lambda_j \Delta_t} \tag{3.10}$$

where:

[1] Kai Huang et al. 'Improvements to the Transmutation Trajectory Analysis of depletion evaluation'. In: *Annals of Nuclear Energy* 87 (Jan. 2016), pp. 637–647. ISSN: 0306-4549. DOI: 10.1016/j.anucene.2015.10.013.

[2] Pertti A Aarnio. *Decay and Transmutation of Nuclides*. Place: Geneva. 1999.

[3] Kanji Tasaka. 'DCHAIN2 : A COMPUTER CODE FOR CALCULATION OF TRANSMUTATION OF NUCLIDES'. en. In: (1980), p. 171. DOI: 10.11484/jaeri-m-8727.

[4] In `TMX_Bateman` for nuclide decaying into an unknown nuclide, are identified via a Xx symbol in the ZSYMAM representation in the outputs, and considered as stable

[5] Pertti A Aarnio. *Decay and Transmutation of Nuclides*. Place: Geneva. 1999.

– if $i = 1$, $d_{111} = 1$, else:

$$d_{ijm} = \frac{\prod_{k=m}^{i-1} \lambda_k}{\prod_{\substack{k=m \\ k \neq j}}^{i} (\lambda_k - \lambda_j)}, \; 1 \leq m \leq j \leq i \tag{3.11}$$

– $N_i(t)$ is the number of ith isotope in the decay chain at time t ;
– $\sum_{m=1}^{i}$ is the contribution to $\mathrm{N_i}$ from all the linearized decay chains ;
– N_m^0 is the number of mth isotope in the chain at time $t = 0$;
– $\sum_{j=m}^{i}$ is the build-up of $\mathrm{N_i}$ from other isotopes higher in the decay chain and its decays ;
– $e^{-\lambda_j \Delta_t}$ is the classical exponential decay function, which is characteristic of every unstable nucleus, with the decay constant λ_j.

The supported decays are hardcoded, and listed in Table A.2.

b) Source term

When the material of interest is submitted to an external fluence, nuclides have an alternative build-up and depletion. This process can be expressed, in a similar form of Equation 3.10, as :

$$N_i(t) = \sum_{m=1}^{i} S_m \int_0^{\Delta_t} d\tau \sum_{j=m}^{i} d_{ijm} e^{-\lambda_j \tau} \tag{3.12}$$

where $S_m d\tau$ is the ammount of nuclide m produced during a fraction of Δ_t $(d\tau)$ [106][1].

To estimate the creation rate, the nuclide vector is assumed to remain constant for the duration of the irradiation, and the interaction of by-products resulting from irradiation are disregarded. With these constraints, the transmuted amount can be easily computed from reaction rate according to Equation 3.13.

$$S_m = \int_0^{+\infty} y_m(E)\, \phi(E)\, dE \tag{3.13}$$

where:

– y_m is the yield of nuclide m;
– $\phi(E)$ is neutron fluence in s^{-1};

The supported reactions are listed in Table A.1. Among the listed channels, the MT=5[2] and MT=18[3] reactions are treated differently as there is no exact secondaries associated with them, see subparagraph a.

[1] Pertti A Aarnio. *Decay and Transmutation of Nuclides*. Place: Geneva. 1999.
[2] (z, anything)
[3] (z, f)

c) Management of fission fragments

To appear, from either spontaneous or induced fission, the fragments must be explicitly detailed. Once such a channel is available, the code will check if there is such data, and include them to the nuclides vector.

Fission of excited isomers In the case, that the isotope is in an excited state and there is no associated Fission Fragments (FF) listing, but a listing is available for the ground state, this latter table will be used.

Fission fragment not available When adding the FF, if certain excited fragments are not registered inside the decay database, preventing the code from tracking their decay path, they will be directly set to their ground state. However, this assignment will not be accounted in the isomeric transition activity or with any photon spectra, as there is no information on their exact excitation.

Renormalisation for SF Spontaneous fission typically result in a two-body emission, which explains why the table of fission fragments sums up to two. This yield is systematically renormalized to reflect this, and a warning is raised to flag any discrepancy before renormalization.

3.3.2. Inputs

The C++ application is controlled by a JavaScript Object Notation (JSON), and will output Comma-Separated Values (CSV) or JSON depending on the option used.

The most simple input would be Listing 3.1, one can indicate a nuclide spectrum, in moles (and/or grams) thanks to their ZAI code[1], and the time steps in absolute time.

Listing 3.1: Simple input file for `TMX_Bateman`

```
{
    "moles" : {
        "922350": 1,
        "922380": 1
    },
    "time_bins" : [
        0,
        1,
        100,
        200
    ],
    "json": true,
    "csv_per_meas": true,
    "csv_per_step": true,
    "hdf5_decay": "/path/to/decay_db_file.hdf5",
    "hdf5_sff": "/path/to/sff_db_file.hdf5",
    "hdf5_xs": "/path/to/xs_db_file.hdf5",
```

[1] Z*1000 + A*10 + I, where Z is the atom number, A the atom mass and I the isomeric state

```
18      "hdf5_nff": "/path/to/nff_db_file.hdf5"
19      }
```

Such input can be completed with an irradiation spectrum, see Listing A.2. Alternatively, the reaction rate can be directly indicated, see Listing A.3.

The outputs can also be controlled, as the energy binning for the spectra and which one to produce (see Listing A.4). As the JSON output is more modular, a threshold section can also be implemented to filter out the obtained inventory, see Listing A.6.

The most extensive input, Listing A.1, can be quite large but allows for some fine tuning.

3.3.3. Evaluated databases

The most important part of this type of code is the evaluated databases, which contains the nuclear properties of nuclides.

The most basic information is the decay constants and the decay types (limited to a combination of the one listed in Table 3.2). Such data is commonly released in the Evaluated Nuclear Data File 6 (ENDF-6) [108][1]; see more details in section 5.1.

In addition, in such files, contain the nuclides mass (in neutron mass units), the associated decay spectra (limited to those listed in Table 3.4), or yet the average secondary particle energies.

For radioprotection purposes, it may also be necessary to determine the committed dose per intake for workers in the vicinity. For such estimation tables released by the ICRP are available i.e. ICRP72 [109][2] or ICRP151 [110][3] to get from the activity a committed dose (via constant coefficients).

a) HDF5 library

As ENDF-6 files are generated for all end-users, whether interested in a single nuclide, or to the whole database, information can be redundant due to the history of the format. Also because `C++`is not the most optimised ASCII parser, the mentioned databases have been stripped down and reorganised into four Hierarchical Data Format 5 (HDF5) files, in order to access the nuclear decay properties, the fission fragment properties and the cross-sections.

Decay parsing The splitting of electron-capture and positron emission is implemented, at the generation of this file. In addition, the branching are also systematically renormalized to one.

[1] David A. Brown. *ENDF-6 Formats Manual - Data Formats and Procedures for the Evaluated Nuclear Data Files ENDF/B-VI, ENDF/B-VII and ENDF/B-VIII*. English. Tech. rep. BNL-224854-2023-INRE. Brookhaven National Laboratory (BNL), Upton, NY (United States), Sept. 2023. DOI: 10.2172/2007538.

[2] 'ICRP Publication 72: Age-dependent Doses to Members of the Public from Intake of Radionuclides - Part 5 Compilation of Ingestion and Inhalation Coefficients'. en. In: *Annals of the ICRP* 26.1 (Jan. 1996), pp. 1–91. ISSN: 0146-6453. DOI: 10.1016/S0146-6453(00)89192-7.

[3] *ICRP Publication 151: Occupational Intakes of Radionuclides: Part 5.*

Table 3.2.: `RTYP` translation table.

RTYP	Symbol	Decay mode
1	β^-	Beta decay
2	e.c./β^+	Electron capture and/or positron emission
3	IT	Isomeric transition
4	α	Alpha decay
5	n	Neutron emission
6	SF	Spontaneous fission
7	p	Proton emission
10		Unknown origin

Table 3.4.: `STYP` translation table.

STYP	Symbol	Radiation type
0	γ	Gamma rays
1	β^-	Beta rays
2	e.c./β^+	Electron capture and/or positron emission
4	α	Alpha particles
5	n	Neutrons
6	SF	Spontaneous fission fragments
7	p	Protons
8	e^-	'Discrete electrons', including Auger and conversion electrons
9	x	X-rays and annihilation radiation
10	$\bar{\nu_e}$	Electron anti-neutrinos
11	ν_e	Electron neutrinos

Cross-section parsing In ENDF-6 files, cross-section are part of the `MF=3` reaction cross-sections sub-library. For such applications, the by-products are the most relevant. As being 0D, the elastic reactions are irrelevant. The only reactions that requires special treatment are:

MT=5 this part of the ENDF-6 file, includes all reactions that are not included in other MT codes. As the reaction does not provide information on the by-products as the other, the `MF=6` part of the file must be parsed to get the list of yields (which must be multiplied by the cross-section).

MT=18 similarly, the (n,f) reaction does not include on its own the fragments produced, for that one must rely on the `MF=8` sub-library (neutron induced fission fragments). This reaction will deplete the target nuclides, but will not produce any residuals unless external table of fragments is given.

The presence of an external file allows to overcome limitation as of `FISPACT-II`, which cannot follow elements that does not have an attached cross-section and decay data (and necessitate an index file).

Neutron-induced and spontaneous fission fragments The list of fragments is provided in the `MF=8`, and in `MT=454` or `MT=458`, respectively independent and cumulative yields[1] Both components are translated and available, but it is recommended not to use the cumulative yields as they might not be consistent with the decay database otherwisely chosen.

3.3.4. Outputs

All basic observables are extracted from the composition in moles and the decay constant.

3.3.5. Isotopic composition

If the quantity followed by the Equation 3.10 is in moles, one can easily derive the mass as:

$$m_i(t) = M_i \times N_i(t) \tag{3.14}$$

where:

- $m_i(t)$ is the mass of isotope i in [g] ;
- M_i is the molar mass of isotope i in [g/mol] ;
- $N_i(t)$ is the number of nuclei of isotope i in [mol].

3.3.6. Activity

The total activity is obtained according to the following equation:

$$a_i(t) = \frac{N_i(t) \times N_A \times (1 - e^{-\lambda_i \Delta t})}{\Delta t} \tag{3.15}$$

[1] They will consider the decay path to stable nuclides in addition to the first fragment list.

where:

- $a_i(t)$ is the activity of isotope i in [Bq] ;
- $N_i(t)$ is the number of nuclei of isotope i [mol] ;
- N_A is the Avogadro number in [mol^{-1}] (i.e. $6.02214076 \times 10^{23}$ mol^{-1})

a) α emission rate

Like all the following observables, the alpha emission rate is computed from the total activity, according to the following equation:

$$a_i^{\alpha}(t) = a_i(t) \times \mathrm{BR}_{\alpha} \tag{3.16}$$

where:

- $a_i^{\alpha}(t)$ is the alpha emission rate of isotope i in $[\alpha/s]$;
- $a_i(t)$ is the activity of isotope i in [Bq] ;
- BR_{α} is the branching ratio of decays that generates alpha particle as a decay product.

b) β emission rate

We compute the beta emission rate according to the following equation:

$$a_i^{\beta}(t) = a_i(t) \times \mathrm{BR}_{\beta} \tag{3.17}$$

where:

- $a_i^{\beta}(t)$ is the beta emission rate of isotope i in $[\beta/s]$;
- $a_i(t)$ is the activity of isotope i in [Bq] ;
- BR_{β} is the branching ratio of decays that generates beta particle (β^- and β^+) as a decay product.

Positron emission intensity For the β^+ decay, the positron emission and electron-capture are distinguished, and electron-capture is not accounted in BR_{β}. To obtain this split ratio, two strategies are assumed in `TMX_Bateman`. Such treatment have been applied during the generation of the *TMXElements* dataset, rather than inside the `C++` implementation.

Empirical splitting function To estimate the ratio between positron emission and electron-capture, the empiric formula determined in [98][1] is used, and given in explicit form in Equation 3.18.

[1] Hunter N. Ratliff et al. 'Modernization of the DCHAIN-PHITS activation code with new features and updated data libraries'. In: *Nuclear Instruments and Methods in Physics Research Section B: Beam Interactions with Materials and Atoms* 484 (Dec. 2020), pp. 29–41. ISSN: 0168-583X. DOI: 10.1016/j.nimb.2020.10.005.

$$I_{\beta^+} = \begin{cases} 0.0 & Q < Q_{th} \\ \frac{Q}{2Q_{th}} - \frac{1}{2} & Q_{th} < Q < 2Q_{th} \\ \frac{Q-2Q_{th}}{10-2Q_{th}} & Q > 2Q_{th} \end{cases} \tag{3.18}$$

with Q_{th} expressed, in MeV, as $2 \times m_e + A \times 5 \times 10^{-3}$.

Evaluated splitting ratio The splitting can be precised in the decay sub-library, but they are attached to the β^+ spectrum (`STYP` $= 2$), within the positron emission rate `RIS`. This splitting is mostly never experimentally measured but rather estimated via LogFT [111][1] or BetaShape [22][2].

When such spectra is available, the intensity from Equation 3.18 is replaced by the value:

$$I_{\beta^+} = \texttt{FD} \times \sum_i \texttt{RIS}_i + \texttt{FC} \times \int_0^\infty \texttt{RP}(E)dE \tag{3.19}$$

where:

- `FD` is the discrete ray scaling factor ;
- `FC` is the continuous bins scaling factor ;
- $\texttt{RIS}_i$ is the positron intensity of discrete ray i ;
- $\texttt{RP}(E)$ is the description of the continous spectrum.

c) γ emission rate

We compute the gamma emission rate according to the following equation:

$$a_i^\gamma(t) = a_i(t) \times \sum_k^n I_k \tag{3.20}$$

where:

- $a_i^\gamma(t)$ is the gamma emission rate of isotope i in $[\gamma/s]$;
- $a_i(t)$ is the activity of isotope i in [Bq] ;
- I_k are the intensities of gammas (and X-rays) for the isotope i, see Equation 3.19.

d) IT activity

We compute the isomeric transition activity according to the following equation:

$$a_i^{\mathrm{IT}}(t) = a_i(t) \times \mathrm{BR}_{\mathrm{IT}} \tag{3.21}$$

where:

[1] N. B. Gove and M. J. Martin. 'Log-f tables for beta decay'. In: *Atomic Data and Nuclear Data Tables* 10.3 (Nov. 1971), pp. 205–219. ISSN: 0092-640X. DOI: 10.1016/S0092-640X(71)80026-8.

[2] Xavier Mougeot. 'Atomic exchange correction in forbidden unique beta transitions'. In: *Applied Radiation and Isotopes* 201 (Nov. 2023), p. 111018. ISSN: 0969-8043. DOI: 10.1016/j.apradiso.2023.111018.

- $a_i^{\mathrm{IT}}(t)$ is the isomeric transition activity of isotope i in $[\mathrm{IT}/s]$;
- $a_i(t)$ is the activity of isotope i in [Bq] ;
- $\mathrm{BR}_{\mathrm{IT}}$ is the branching ratio of isomeric transition for the isotope.

e) n emission rate

We compute the neutron emission rate according to the following equation:

$$a_i^n(t) = a_i(t) \times (\mathrm{BR}_n + \nu \times \mathrm{BR}_{\mathrm{SF}}) \tag{3.22}$$

where:

- $a_i^n(t)$ is the neutron emission rate of isotope i in $[n/s]$;
- $a_i(t)$ is the activity of isotope i in [Bq] ;
- BR_n is the branching ratio of decays that generates neutron as a decay product ;
- ν is the average number of neutron emitted during fission, i.e. neutron multiplicity ;
- $\mathrm{BR}_{\mathrm{SF}}$ is the branching ratio of decays that does spontaneous fission.

3.3.7. Heat load

Observable relevant in particular for nuclear reactors, the heat refers to the sum of average energy generated by the secondary particle within the core to estimate the thermal power. If primarily due to nuclear reaction and decay processes. It is crucial to manage the heat for energy production and management of fuel waste.

There are several ways to compute the heat load, either as the maximum energy available from the Q_{value}, or from the average energy available.

a) Total heat

The total is computed from the sum of the heavy and light particle heat and the electromagnetic radiation heat:

$$P_i^{\mathrm{heat_{tot}}} = a_i(t) \times \left(\left\langle \mathrm{ER}_i^{\mathrm{HP}} \right\rangle + \left\langle \mathrm{ER}_i^{\mathrm{Rad}} \right\rangle + \left\langle \mathrm{ER}_i^{\mathrm{LP}} \right\rangle \right) \tag{3.23}$$

where:

- $P_i^{\mathrm{heat_{tot}}}$ is the total heat (not accounting for neutrinos) available for the decay of isotope i in $[W]$;
- $a_i(t)$ is the activity of isotope i in [Bq] ;
- $\left\langle \mathrm{ER}_i^{\mathrm{HP}} \right\rangle$ is the heavy particle average energy for the decay of isotope i in $[J]$;
- $\left\langle \mathrm{ER}_i^{\mathrm{Rad}} \right\rangle$ is the electromagnetic radiation average energy for the decay of isotope i in $[J]$;
- $\left\langle \mathrm{ER}_i^{\mathrm{LP}} \right\rangle$ is the light particle average energy for the decay of isotope i in $[J]$.

b) Heavy particle heat

The heavy particle heat, defined according to the ENDF-6 format (see subsection 5.2.5), is computed using:

$$P_i^{\text{heat}_{\text{HP}}} = a_i(t) \times \left\langle \text{ER}_i^{\text{HP}} \right\rangle \tag{3.24}$$

where:

- $P_i^{\text{heat}_{\text{HP}}}$ is the heat available from heavy particle for the decay of isotope i in $[W]$;
- $a_i(t)$ is the activity of isotope i in [Bq];
- $\left\langle \text{ER}_i^{\text{HP}} \right\rangle$ is the heavy particle average energy for the decay of isotope i in $[J]$.

c) Light particle heat

The light particle heat, defined according to ENDF-6 format (see subsection 5.2.5), is computed using:

$$P_i^{\text{heat}_{\text{LP}}} = a_i(t) \times \left\langle \text{ER}_i^{\text{LP}} \right\rangle \tag{3.25}$$

where:

- $P_i^{\text{heat}_{\text{LP}}}$ is the heat available from light particle for the decay of isotope i in $[W]$;
- $a_i(t)$ is the activity of isotope i in [Bq];
- $\left\langle \text{ER}_i^{\text{LP}} \right\rangle$ is the light particle average energy for the decay of isotope i in $[J]$.

d) Electromagnetic radiation heat

The electromagnetic radiation heat, defined according to ENDF-6 format (see subsection 5.2.5), is computed using:

$$P_i^{\text{heat}_{\text{Rad}}} = a_i(t) \times \left\langle \text{ER}_i^{\text{Rad}} \right\rangle \tag{3.26}$$

where:

- $P_i^{\text{heat}_{\text{Rad}}}$ is the heat available from light particle for the decay of isotope i in $[W]$;
- $a_i(t)$ is the activity of isotope i in [Bq];
- $\left\langle \text{ER}_i^{\text{Rad}} \right\rangle$ is the electromagnetic radiation average energy for the decay of isotope i in $[J]$.

e) α heat

The alpha heat is computed from the average energy of the alpha discrete spectrum, available in the ENDF-6 format (see Table 3.4), according to:

$$P_i^{\text{heat}_\alpha} = a_i(t) \times \langle \text{ER}_i^{\alpha} \rangle \tag{3.27}$$

where:

- $P_i^{\text{heat}_\alpha}$ is the heat available from ${}_2^4\text{He}$ for the decay of isotope i in $[W]$;
- $a_i(t)$ is the activity of isotope i in [Bq];
- $\langle \text{ER}_i^{\alpha} \rangle$ is the alpha average energy during the decay of isotope i in $[J]$.

Note If no average energy is available, but alphas are indicated as secondary product, the code will raise a warning.

f) Spontaneous fission heat

The spontaneous fission (SF) heat is computed from the average energy of the SF spectrum, available in the ENDF-6 format (see Table 3.4), according to:

$$P_i^{\text{heat}_{\text{SF}}} = a_i(t) \times \left\langle \text{ER}_i^{\text{SF}} \right\rangle \tag{3.28}$$

where:

- $P_i^{\text{heat}_{\text{SF}}}$ is the heat available from SF decay $[W]$;
- $a_i(t)$ is the activity of isotope i in [Bq] ;
- $\left\langle \text{ER}_i^{\text{SF}} \right\rangle$ is the SF average energy for the decay of isotope i in $[J]$.

Note If there is no average energy available, but spontaneous fission is indicated as potential decay channel, the code will raise a warning.

g) n heat

The neutron heat is computed from the average energy of the neutron spectrum, available in the ENDF-6 format (see Table 3.4), according to:

$$P_i^{\text{heat}_n} = a_i(t) \times \langle \text{ER}_i^n \rangle \tag{3.29}$$

where:

- $P_i^{\text{heat}_n}$ is the heat available from ${}^1_0\text{n}$ for the decay of isotope i in $[W]$;
- $a_i(t)$ is the activity of isotope i in [Bq] ;
- $\langle \text{ER}_i^n \rangle$ is the neutron average energy during the decay of isotope i in $[J]$.

Note If no average energy is available, but neutrons are indicated as secondary product, the code will raise a warning.

h) p heat

The proton heat is computed from the proton spectrum's average energy, available in the ENDF-6 format (see Table 3.4), according to:

$$P_i^{\text{heat}_p} = a_i(t) \times \langle \text{ER}_i^p \rangle \tag{3.30}$$

where:

- $P_i^{\text{heat}_p}$ is the heat available from ${}^1_1\text{H}$ for the decay of isotope i in $[W]$;
- $a_i(t)$ is the activity of isotope i in [Bq] ;
- $\langle \text{ER}_i^p \rangle$ is the proton average energy during the decay of isotope i in $[J]$.

Note If no average energy is available, but protons are indicated as secondary product, the code will raise a warning.

i) β^- heat

The β^- heat is computed from the average energy of the β^- spectrum, available in the ENDF-6 format (see Table 3.4), according to:

$$P_i^{\text{heat}_{\beta-}} = a_i(t) \times \left\langle \text{ER}_i^{\beta^-} \right\rangle \tag{3.31}$$

where:
- $P_i^{\text{heat}_{\beta-}}$ is the heat available from e^- for the decay of isotope i in $[W]$;
- $a_i(t)$ is the activity of isotope i in [Bq];
- $\left\langle \text{ER}_i^{\beta^-} \right\rangle$ is the β^- average energy during the decay of isotope i in $[J]$.

Note If no average energy is available, but β^- are indicated as secondary product, the code will raise a warning.

j) β^+ heat

The β^+ heat is computed from the average energy of the β^+ spectrum, available in the ENDF-6 format (see Table 3.4), according to:

$$P_i^{\text{heat}_{\beta+}} = a_i(t) \times \left\langle \text{ER}_i^{\beta^+} \right\rangle \tag{3.32}$$

where:
- $P_i^{\text{heat}_{\beta+}}$ is the heat available from e^- for the decay of isotope i in $[W]$;
- $a_i(t)$ is the activity of isotope i in [Bq];
- $\left\langle \text{ER}_i^{\beta^+} \right\rangle$ is the β^+ average energy during the decay of isotope i in $[J]$.

Note If no average energy is available, but β^+ are indicated as secondary product, the code will raise a warning.

Warning β^+ heat does not account for electron capture heat (as the code distinguish the two channels).

k) "Discrete" e^- heat

The discrete electron heat is computed from the integral of the "discrete" electron spectrum (including Auger, conversion electron, ...), which is available in the ENDF-6 format (see Table 3.4), according to:

$$P_i^{\text{heat}_{e-}} = a_i(t) \times \int S_i^{e^-}(E)dE \tag{3.33}$$

where:

- $P_i^{\text{heat}_{e^-}}$ is the heat available from Auger and conversion e$^-$ for the decay of isotope i in $[W]$;
- $a_i(t)$ is the activity of isotope i in [Bq];
- $S_i^{e^-}(E)$ is the discrete e^- spectrum for the decay of isotope i.

Note This information is only available if a "discrete" electron spectrum is present.

l) γ heat

The gamma heat is computed from the integral of the γ, and X-ray, spectra, available in the ENDF-6 format (see Table 3.4), according to:

$$P_i^{\text{heat}_\gamma} = a_i(t) \times \int S_i^\gamma(E)dE \tag{3.34}$$

where:

- $P_i^{\text{heat}_\gamma}$ is the heat available from γ (and X-ray) for the decay of isotope i in $[W]$;
- $a_i(t)$ is the activity of isotope i in [Bq];
- $S_i^\gamma(E)$ is the photon spectrum for the decay of isotope i.

Note This information is only provided if either a γ or X-ray spectrum is available. These two spectra are summed, when the spectrum is output.

Warning Hence, if an isomeric transition is registered without any photon rays indicated, gamma heat will be null (and vice-versa).

m) Maximum available energy

The maximum heat load is computed according to the following equation:

$$P_i^{\text{heat}_{\max}} = a_i(t) \times \sum_k (BR_k \times Q_{\text{value},\,k}) \tag{3.35}$$

where:

- $P_i^{\text{heat}_{\max}}$ is the maximum heat available for the decay of isotope i in $[W]$;
- $a_i(t)$ is the activity of isotope i in [Bq];
- BR_k is the branching ratio of the kth decay channel of isotope i;
- $Q_{\text{value},\,k}$ is the decay energy of the kth decay channel of isotope i.

Note This value corresponds to the total available energy, that will be shared by the secondary products such as alphas, neutrons, neutrinos, as well as gammas, electrons, or recoil energy.

3.3.8. Committed dose

Committed dose is a concept used in radiological protection to estimate long-term health risks from radioactive materials entering the body. Committed doses from inhalation and ingestion are considered using the dose coefficient given in ICRP151 [110][1], which are used in occupational and public exposure scenarios.

a) Ingestion dose

The committed ingestion dose is computed according to the following equation:

$$D_i^{\text{inh}} = a_i(t) \times d_i^{\text{ing}} \tag{3.36}$$

where:

- D_i^{ing} is the ingestion committed dose of isotope i in [Sv] ;
- $a_i(t)$ is the activity of isotope i in [Bq] ;
- d_i^{ing} is the ingestion coefficient of isotope i in [Sv/Bq]

b) Inhalation dose

The committed inhalation dose is computed according to the following equation:

$$D_i^{\text{inh}} = a_i(t) \times d_i^{\text{inh}} \tag{3.37}$$

where:

- D_i^{inh} is the inhalation committed dose of isotope i in [Sv] ;
- $a_i(t)$ is the activity of isotope i in [Bq] ;
- d_i^{inh} is the inhalation coefficient of isotope i in [Sv/Bq]

3.3.9. Decay spectra

The last observables are the decay spectra, each radiation described in Table 3.4 is potentially available as an output.

The ENDF-6 `MF`=8 does contain the discrete and continuous spectra, the code allows to output any of them, with any binning desired.

In current application, if no ray (be it discrete or continuous) is available, but average energy is non-null, no attempt to estimate rays are done. Hence if working with exotic nuclides, not much measured, such secondary spectra will be underestimated.

It should be noted that beta spectra is described through its transitions, rather than their continuous spectra in standard libraries, so there is no interest in extracting it (except when using chapter 5).

[1] *ICRP Publication 151: Occupational Intakes of Radionuclides: Part 5.*

3.4. Benchmark of TMX_Bateman against FISPACT-II and DCHAIN-PHITS

To check, and compare the different approaches of Bateman resolution, this section will benchmark TMX_Bateman against the two codes in several decay only and transmutation applications.

Versions TMX_Bateman used in this section is the v4.0.0. FISPACT-II version 5.1 was used, and DCHAIN-PHITS version 3.3.5 was used[1]

For all, unless specified, the ENDF/B-VIII.0 evaluated library was chosen in priority, for decay, cross-section and fission fragment data.

a) Conversion table

While the Bateman system solving enables the calculation of isotopic composition as a function of time, the solver can leverage nuclear properties to provide additional outputs: activity, decay spectra, inhalation intake, average energy of decay particles . The naming system and unit convention vary with codes; this differences are summarised in Table 3.6.

3.4.1. Universe material check

Accurate parsing of decay data is a key requirement for the reliability of such computational codes. As a preliminary step, all material properties must be carefully checked. In this study, we examined the selected material — one mole of each isotope listed in NUBASE2020 [16][2], including both ground and excited states— at the initial time.

The results of TMX_Bateman are compared to FISPACT-II and DCHAIN-PHITS in Figure 3.2 and Table 3.7. As shown Figure 3.2, there is perfect agreement with an error margin of 1×10^{-5} % relative difference with FISPACT-II. The discrepancy is larger with DCHAIN-PHITS for the number of atoms (-2.69×10^{-2} %), but is most probably due to a numerical error in the sum. The other observable error average to 1×10^{-3} %, which is in consistent with the four significant digits used by DCHAIN-PHITS outputs.

This plot does not include the emission rate that can be quite different, as synthesised in Table 3.7.

- The discrepancy in alpha emission rate originates from a bug of FISPACT-II (v5.1) that affects decay channel involving alpha delayed emission, e.g. $\beta^{\pm} + \alpha$. This results in the emission rates[3] being underestimated by a factor two for such decays (see ^{8}Li or ^{8}B). It is important to note that only the reported output rate is affected, yet the total alpha particle count, and the residuals, in the inventory remain accurate.

[1] The number of channels imax was extended to 5000 before compilation.

[2] F.G. Kondev et al. 'The NUBASE2020 evaluation of nuclear physics properties *'. en. In: *Chinese Physics C* 45.3 (Mar. 2021), p. 030001. ISSN: 1674-1137, 2058-6132. DOI: 10.1088/1674-1137/abddae.

[3] The β-rate is also divided by two for those.

Table 3.6.: Correspondance table between `TMX_Bateman`, `FISPACT-II` and `DCHAIN-PHITS`.

Quantity	`TMX_Bateman`	`FISPACT-II`[†]	`DCHAIN-PHITS`
Header (totals)			
Number of atoms	atm & mol	atm	atm cm^{-3}
Number of activated atoms	∅	∅	atm cm^{-3}
Mass	g	kg	g
Activity	Bq	kBq	Bq & Bq·cm^{-3}
α emission rate	$\alpha\,s^{-1}$	Bq	∅
$\beta^{\pm}$ emission rate	$e^{\pm}\,s^{-1}$	Bq[‡]	∅
γ emission rate	$\gamma\,s^{-1}$	∅	$\gamma\,s^{-1}$·cm^{-2}
Annihilation γ emission rate	∅	∅	$\gamma\,s^{-1}$·cm^{-2}
Isomeric Transition rate	Bq	Bq	∅
Total heat	W	kW	W & W cm^{-3}
Light particle heat	W	kW	W & W cm^{-3}
Electromagnetic Radiation heat	W	kW	W & W cm^{-3}
Heavy particle heat	W	kW	W & W cm^{-3}
Channel heat[A]	W	∅	∅
Ingestion intake	Sv	Sv	∅
Inhalation intake	Sv	Sv	∅
Gamma-ray dose rate	∅	Sv	Sv·m^2·h^{-1}
Gamma spectrum	$\gamma\,s^{-1}$	$\gamma\,s^{-1}$[B]	$\gamma\,s^{-1}$
Gamma power spectrum	∅	γ MeV·s^{-1}	$\gamma\,s^{-1}$ & γ MeV·s^{-1}
Body (per nuclide)			
Number of atoms	atm & mol	atm	atm cm^{-3}
Mass	g	g	g
Activity	Bq	Bq	Bq & Bq·cm^{-3}
α emission rate	$\alpha\,s^{-1}$	Bq	∅
$\beta^{\pm}$ emission rate	$e^{\pm}\,s^{-1}$	Bq[‡]	∅
γ emission rate	$\gamma\,s^{-1}$	∅	∅
Isomeric Transition rate	Bq	Bq	∅
Total heat	W	kW	W cm^{-3}
Light particle heat	W	kW	W cm^{-3}
Electromagnetic Radiation heat	W	kW	W cm^{-3}
Heavy particle heat	W	kW	W cm^{-3}
Channel heat[A]	W	∅	∅
Ingestion intake	Sv	Sv	∅
Inhalation intake	Sv	Sv	∅
Gamma-ray dose rate	∅	Sv	Sv·m^2·h^{-1}
Half-life	s	s	s

∅ indicates that the measurement is not available.

[†] Considering the modern JSON output of `FISPACT-II`.

[‡] `FISPACT-II` does not distinguish the electron-capture and positron emission, contrary to `TMX_Bateman` and `DCHAIN-PHITS`.

[A] i.e. α, β^+, β^-, discrete e^-, γ, SF, neutron and proton heat.

[B] only in the legacy (`.out`) output.

– The difference in β emission rate comes from the fact that TMX_Bateman distinguishes the positron/electron emission from the electron capture, which is not the case for FISPACT-II. Hence, the e.c. only ^{7}Be will have null β-rate for TMX_Bateman, but 100 % of its activity with FISPACT-II.
– The large γ emission rate difference is due to the way γ-rate is computed in DCHAIN-PHITS. The rate is scored via the energy weighted fluence, and divided at the end by the average energy within the bin, which generate such a significant difference.

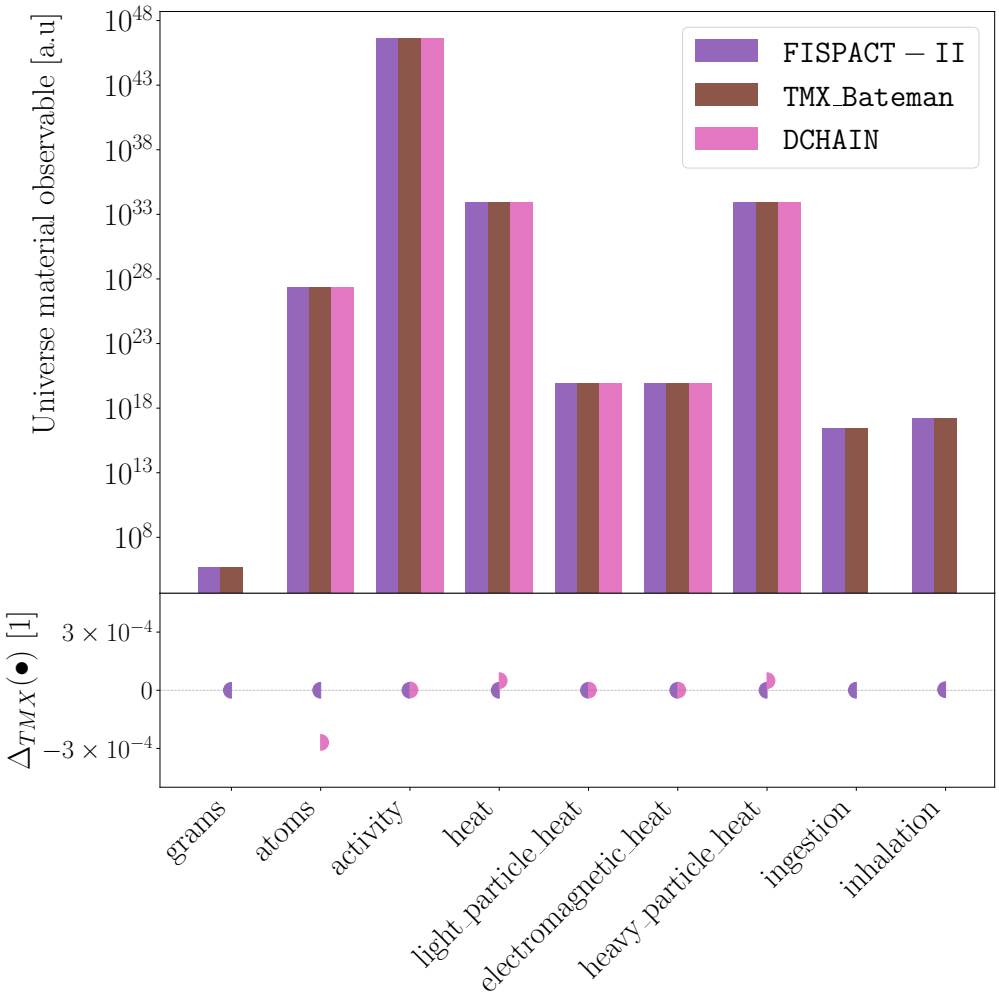

Figure 3.2.: Check for main observables correct parsing

Table 3.7.: Comparison of emission rate of FISPACT-II and DCHAIN-PHITS with respect to TMX_Bateman.

Quantity	$\Delta_{\texttt{TMX}}$ (FII) [%]	$\Delta_{\texttt{TMX}}$ (DCHAIN) [%]
Total activity	2.37×10^{-13}	1.86×10^{-4}
Total α-emission rate	40.4	$\emptyset$
Total β-emission rate	$0.422^{\dagger}$	$\emptyset$
Total γ-emission rate	$\emptyset$	5009
Total isomeric transition activity	4.44×10^{-10}	$\emptyset$

$\emptyset$ indicates that the measurement is not available.
† When the $\beta^{+}/e.c.$ is not distinguished by TMX_Bateman, the error reduces to -4.13×10^{-6} %.

3.4.2. Decay only

If the previous section demonstrated the correct parsing of all the properties. In this section, the tracking capacities of TMX_Bateman will be compared to FISPACT-II and DCHAIN-PHITS. It is unnecessary to check anything other than the amount of nuclides, as the other measurements have been validated in the subsection 3.4.1.

The different inputs used can be found in section A.4.

a) Decay of simple decay channels

Decay of one-size decay path The Figure 3.6 compares the β^{+} decay of ^{48}V, according to the decay scheme represented in Figure 3.3.

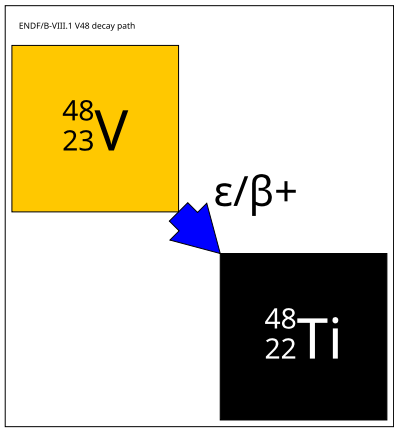

Figure 3.3.: Decay path of ^{48}V based on ENDF/B-VIII.0, produced with JANIS-4.0

The discrepancies are within numerical error with the two other codes, with the absolute relative difference for the ^{48}Ti number of atoms, from start to hundred period of Vanadium, respectively within $[1.8 \times 10^{-9}; 9.7 \times 10^{-2}]$% and $[0.0; 5.1 \times 10^{-4}]$% for

FISPACT-II and DCHAIN-PHITS.

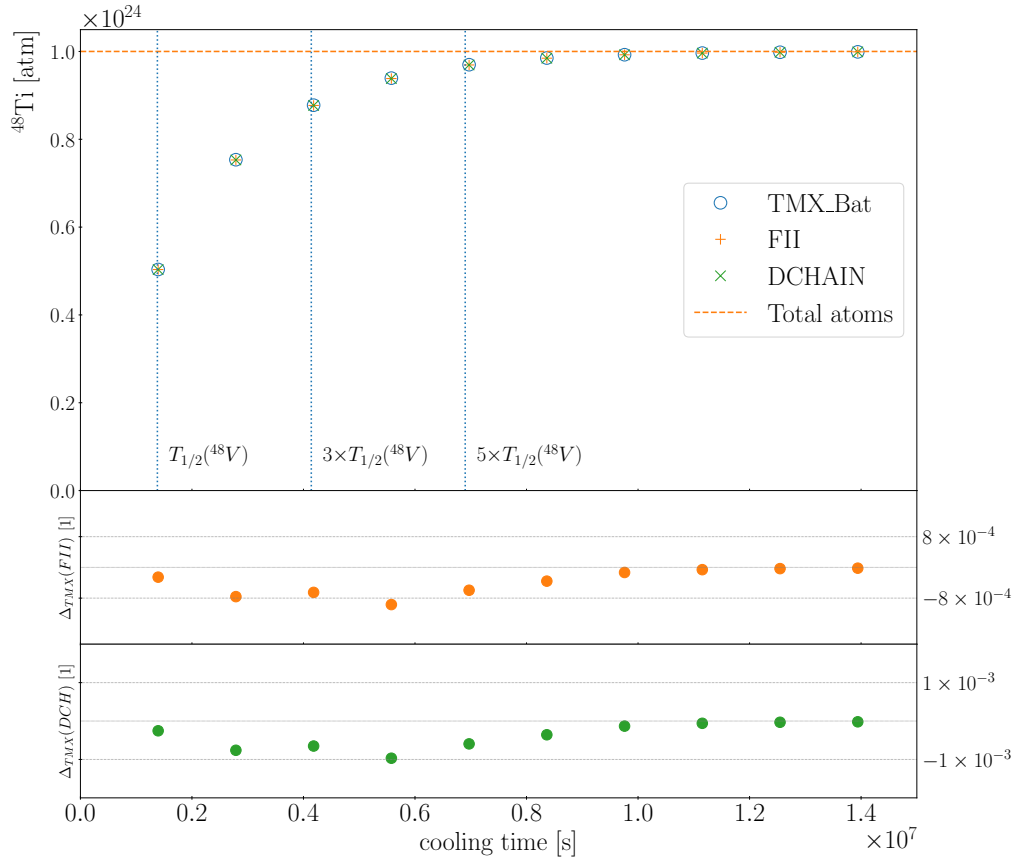

Figure 3.4.: Comparison for the decay of $^{48}\mathrm{V} \rightarrow {}^{48}\mathrm{Ti}$. Relative difference of FISPACT-II and DCHAIN-PHITS with respect to TMX_Bateman

Decay of n-size decay path The Figure 3.6 shows a slightly more complex case with the decay of ^{211}Tl in three stages into ^{207}Pb, according to the decay scheme represented in Figure 3.5. As shown, there is a small mass loss due to binding energy loss and β particle emission, the number of atoms will augment due to emission (and listing) of alphas.

Considering the absolute relative difference, for the amount of final stable nuclide ^{207}Pb, up to 125 times the half-life of ^{211}Tl, is bounded respectively by $[8.3 \times 10^{-9}; 2.8 \times 10^{-3}]\%$ and $[6.9 \times 10^{-6}; 3.1 \times 10^{-3}]\%$ for FISPACT-II and DCHAIN-PHITS.

b) Decay of uranium oxyde fuel

The remaining decay to verify is the spontaneous fission.

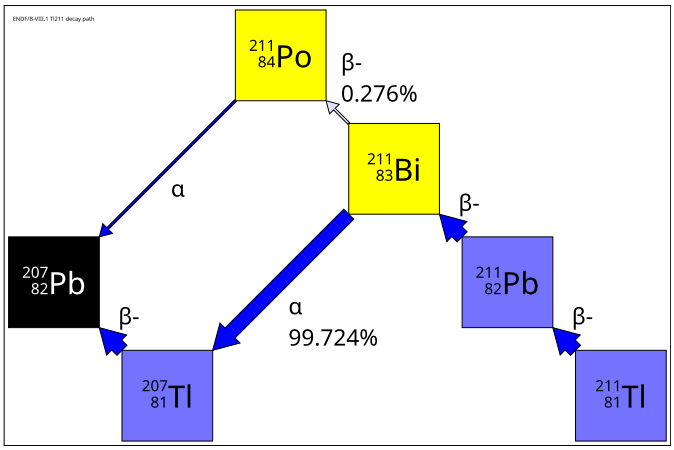

Figure 3.5.: Decay path of ^{211}Tl based on ENDF/B-VIII.0, produced with JANIS-4.0

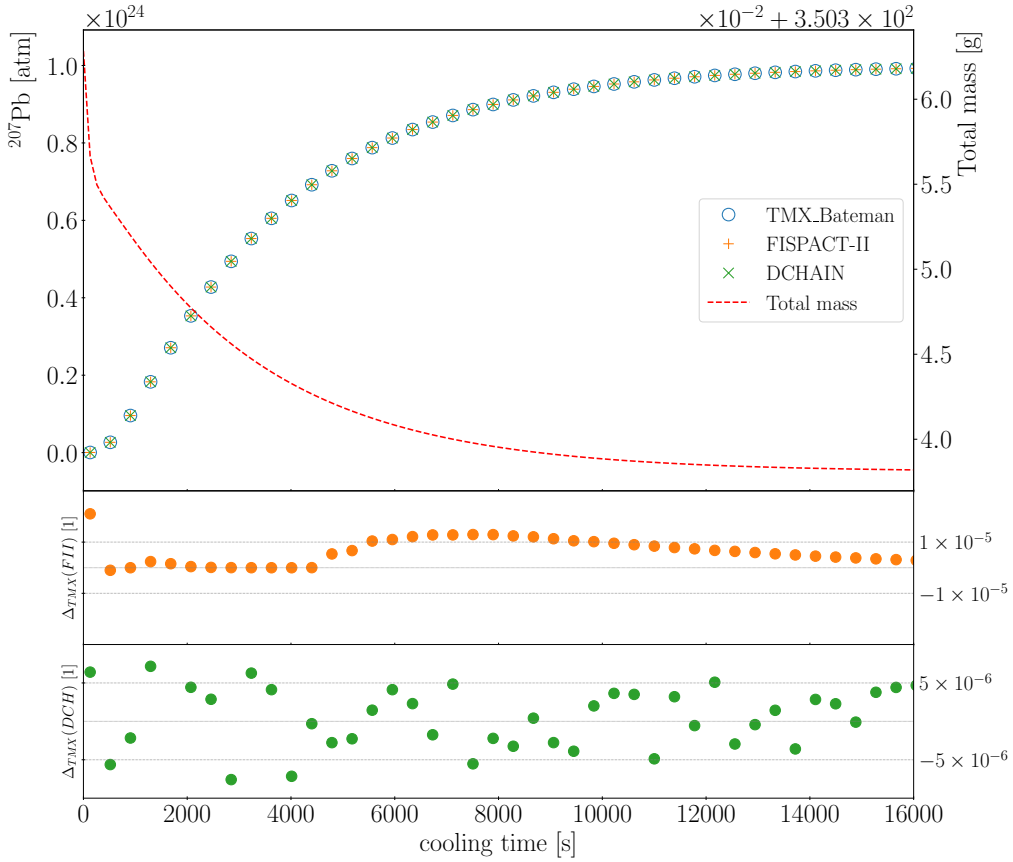

Figure 3.6.: Comparison for the decay of ^{211}Tl → ^{211}Pb → ^{211}Bi → ^{207}Tl → ^{207}Pb. Relative difference of `FISPACT-II` and `DCHAIN-PHITS` with respect to `TMX_Bateman`

Figure 3.7 presents the decay of a typical uranium oxyde fuel, which contains isotope that does such spontaneous fission, with at initial instant : ^{230}Th, ^{232}Th, ^{231}Pa, ^{232}U, ^{234}U, ^{235}U, ^{236}U, ^{238}U, ^{236}Pu, ^{238}Pu, ^{239}Pu, ^{240}Pu, ^{242}Pu, ^{244}Pu, ^{241}Am, ^{242}Am, ^{243}Am, ^{242}Cm, ^{244}Cm, ^{246}Cm, ^{248}Cm, ^{249}Bk, ^{249}Cf, ^{250}Cf, ^{252}Cf that does such decay. Of which only ^{238}U, Cm, ^{250}Cf and ^{252}Cf are present in the Spontaneous Fission Fragment sub-library used to produce the figure.

Error over all nuclides stays below 10^{-5}, except for a few discrepancies due to numerical error and different treatments of extra long half-lives. As an example, the global discrepancies reaches a maximum of 8 % for one of the stable isotope (^{126}Te with DCHAIN-PHITS). We can also see in Figure 3.7 an expected loss of the total mass, as energy is lost with heat emissions.

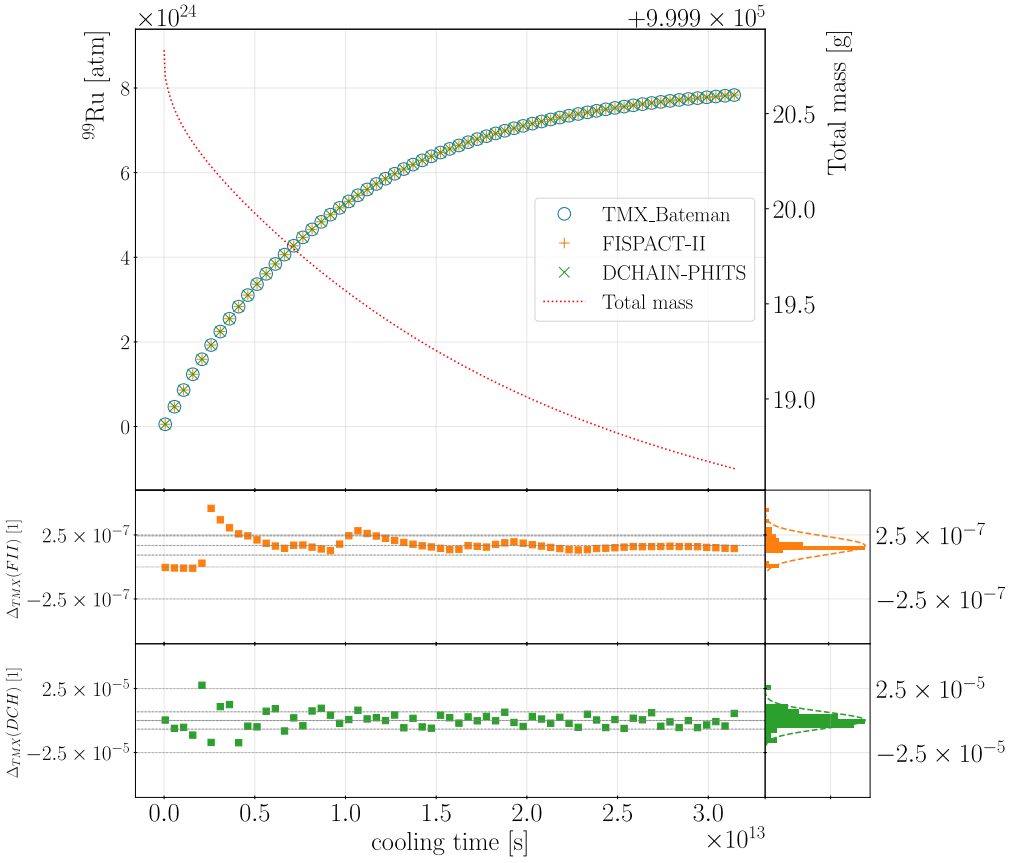

Figure 3.7.: Comparison for the decay of uranium oxyde fuel, with trace of nuclides up to Californium. Relative difference of FISPACT-II and DCHAIN-PHITS with respect to TMX_Bateman

To describe this decay, one needs an additional datasets to extract the fission fragments. As mentioned in subsubsection a, the general ENDF-6 databases provide only

fission fragment list for around 10 nuclides (whereas JEFF-3.3 list 147 nuclides doing such fission).

It is recommended to use a sub-library as GEFY, in order to have better estimation of nuclide vector full composition. But one should beware the discrepancies between nuclides `ZAI` identifiers, see subsection 5.4.1.

c) Time step effect

As the benchmark mentioned previously do not contain any decay cycle, and all path can be linearized without any cut-off, there is no impact whether one hundred steps or only one step are used.

This check, as well as switching from grams to moles input, allow to find the correct output precision to use (currently 16 digits).

3.4.3. Transmutation/depletion considerations

In this section, the source term computation will be validated only with simple irradiation.

a) Irradiation of Vanadium

In this section, we compare the results of the capture of neutron of ^{51}V, resulting in ^{52}V, which finally decays into ^{52}Cr. The comparison is well within acceptable ranges, as seen in Figure 3.8. We see an deviation at early time, that resorbs. This discrepancy is expected and not found in `DCHAIN-PHITS` as the irradiation treatment is similar. Indeed, currently `TMX_Bateman` does not consider the interaction of residuals from the interaction of the neutrons (with the material at start time), this imply that the irradiation profile should be splitted in several small substeps in order to consider the "intermediary" interactions.

In Figure 3.8, there are two `TMX_Bateman` mentions, as there are actually two possibility for neutron cross-sections integration. Either one generates the HDF5 files from the evaluated data source, or one can parse the post-processed ENDF-6 files used by `FISPACT-II` (only useful for direct comparison).

In this configuration, rather than computing linear interpolation when reading cross-sections, the cross-sections will be considered as histogram. We see here a small deviation (less than a percent), as there are not many interactions considered, especially when irradiating V with quasi-monoenergetic neutrons. Yet this feature allow to have interesting insight on the multi-group binning used when preprocessing cross-sections, and when considering more complex cases.

b) Fast neutron irradiation

To validate the irradiation and depletion calculation chain of `TMX_Bateman`, we compared our results against the systematic decay heat experiment conducted by Maekawa et al. at the FNS/JAERI facility m[112]. This benchmark is particularly valuable because it

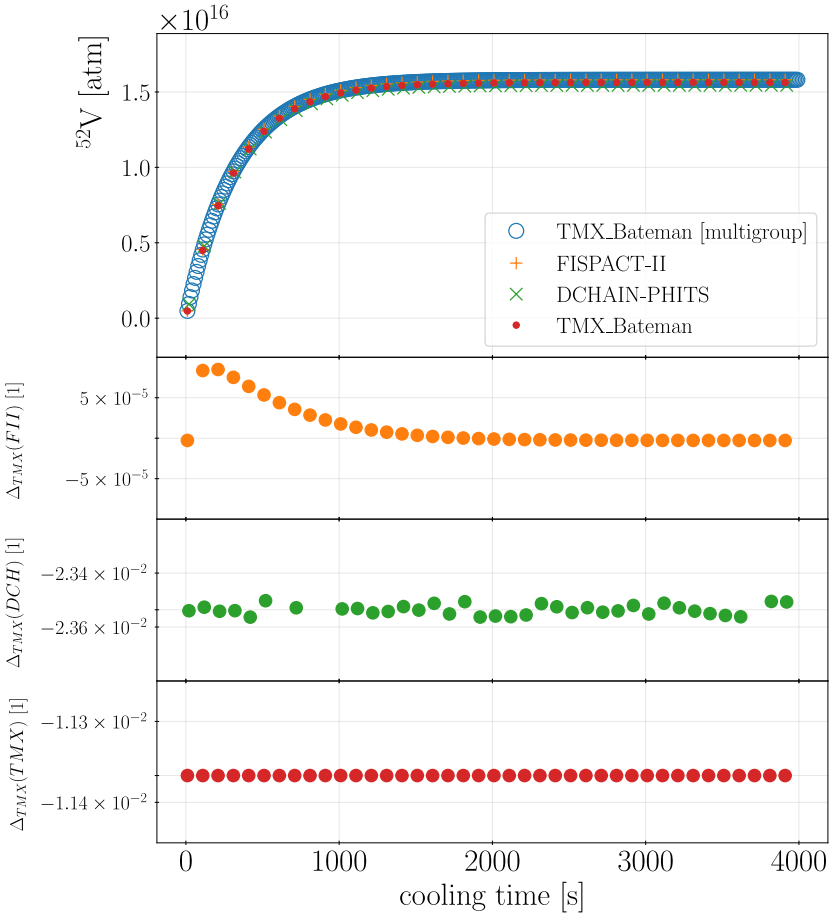

Figure 3.8.: Comparison of ^{52}V build-up from ^{51}V irradiation between FISPACT-II, DCHAIN-PHITS and TMX_Bateman

provides direct measurements of decay heat (including both beta and gamma contributions) for 32 fusion-relevant materials irradiated by 14 MeV D-T neutrons, with cooling times ranging from 1 minute to 400 days.

The experiment used the Whole Energy Absorption Spectrometer (WEAS), accurately measuring total decay heat. Among the 32 materials, stainless steel SS316, aluminum, chromium, and iron have been selected. The comparisons focus on short irradiations (5 minutes).

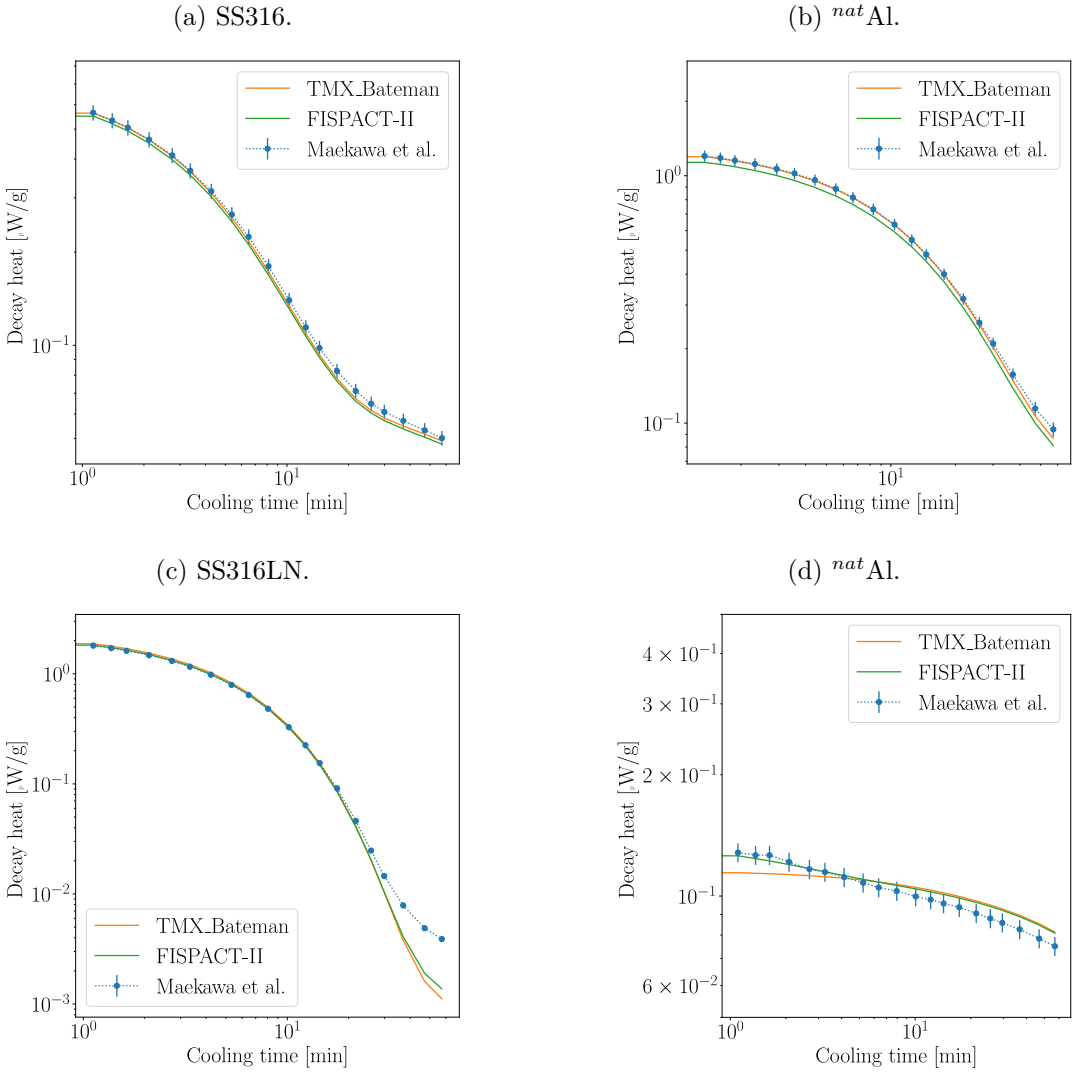

Figure 3.9.: Comparison of several 5 minutes irradiation with fast neutron sources, between `FISPACT-II` and `TMX_Bateman`

Figure 3.9 presents the calculated decay heat (per gram, normalized to a neutron flux of $10 \times 10^{10}\,\mathrm{cm}^{-2} \cdot \mathrm{s}^{-1}$ compared to the experimental data for four samples. In

all cases, TMX_Bateman shows great agreement with FISPACT-II, as well as against the experimental values.

c) Pu fission only heat

Another very usual benchmark is a 1 µs of thermal pulse (with a fluence of $10 \times 10^{22}\,\mathrm{s}^{-1}$) on pure ^{239}Pu, estimated by Dickens [113][1] and Tobias [114][2].

In this benchmark, Figure 3.10, we have still perfect agreement with FISPACT-II, but the discrepancies with respect to experimental data is quite important (more than 10 % relative difference).

Rather than pointing faults in the Bateman engine, it shows that there are issues in the decay data, especially in the heat evaluations. This discrepancies is actually due to the underestimation of heat, due to the continuous band in higher energy levels (related to the pandemonium effect [115][3]).

3.5. Application

As mentioned, TMX_Bateman can provide any decay spectra (which are present in the ENDF-6 file, with a dedicated STYP entry). Both the energy-weighted and the particle count can be obtained, with any binning desired. In addition, efficiency function can be applied[4].

3.5.1. Extracting the γ spectra.

A typical application, would be from a Monte Carlo model, acquiring the expected radionuclide inventory, and using TMX_Bateman obtaining the gamma relaxation spectra, to compare it to the one experimentally obtained.

If the FISPACT-II and DCHAIN-PHITS cannot provide neither neutron nor alpha spectra, the gamma spectrum can be obtained, as such this one will be compared.

But there are limitations, DCHAIN-PHITS can only output the spectra in a fixed 44 group, as does FISPACT-II (but in 24 sized group). Actually for the latter, in the case the API interface is used, the binning can be changed but only the energy weighted spectra is then accessible (as only the JSON output is generated).

In Figure 3.11a, the energy-weighted gamma-rate spectra from TMX_Bateman is compared with DCHAIN-PHITS (using the latter crude binning) and compared with FISPACT-

[1] J. K. Dickens et al. 'Fission-Product Energy Release for Times Following Thermal-Neutron Fission of Plutonium-239 and Plutonium-241 Between 2 and 14 000 s'. In: *Nuclear Science and Engineering* 78.2 (June 1981). _eprint: https://doi.org/10.13182/NSE81-A20099, pp. 126–146. ISSN: 0029-5639. DOI: 10.13182/NSE81-A20099.

[2] A. Tobias. 'Decay heat'. In: *Progress in Nuclear Energy* 5.1 (Jan. 1980), pp. 1–93. ISSN: 0149-1970. DOI: 10.1016/0149-1970(80)90002-5.

[3] J.C. Hardy et al. 'The essential decay of pandemonium: A demonstration of errors in complex beta-decay schemes'. en. In: *Physics Letters B* 71.2 (Nov. 1977), pp. 307–310. ISSN: 03702693. DOI: 10.1016/0370-2693(77)90223-4.

[4] Four different polynomial functions are available (log/lin).

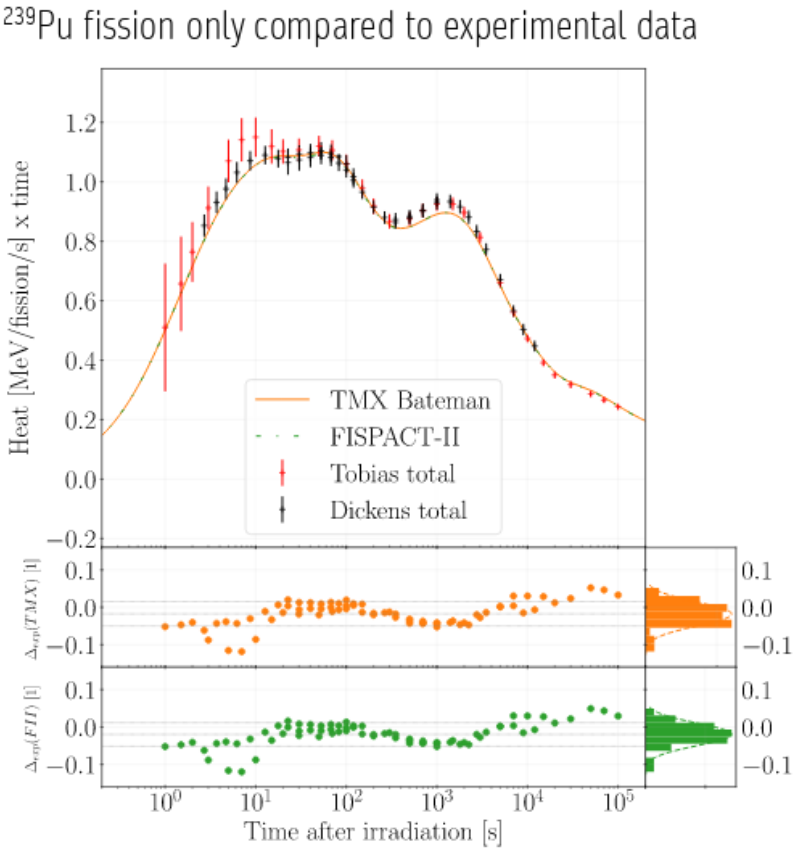

Figure 3.10.: Comparison of ^{52}V build-up from ^{51}V irradiation between `FISPACT-II`, `DCHAIN-PHITS` and `TMX_Bateman`

II, as it is energy-weighted the binning of FISPACT-II can be set to the one of DCHAIN-PHITS. We can see, that DCHAIN-PHITS does not account for the $x - rays$, and that for both codes, there are quasi no discrepancies with respect to TMX_Bateman. When comparing, not energy-weighted gamma spectra, but actual gamma rate (this mandates to use the legacy binning of FISPACT-II), 1.5 % average discrepancy is observed. The difference is due to the fact that these two alternative codes, score the energy-weighted spectra rather than the gamma rate. And in order to get the gamma rate back, they divide by the average energy of the bin, rather than the actual rays energy, creating a slight error.

When reviewing the expected spectra for all known isotopes, Figure 3.11b (see subsection 3.4.1 for details on composition), further issues are found. Notably, some rays corruption in DCHAIN-PHITS, when FISPACT-II cannot consider continuous spectra.

Therefore, TMX_Bateman is the only code, mentioned here to provide a variable binned gamma spectra, which can account[1] for X-ray. The energy weighted spectra, useful for radioprotection issue can also be output.

Yet it should be noted, that for all the codes only the rays inherent to the atom are included. To account for any other phenomenon, as compton background or backscatter is only possible when considering the geometry which is not possible: as FISPACT-II, TMX_Bateman is a 0D code (i.e. it does not account for geometry).

A possible use, of this spectra is a direct comparison between Monte Carlo (and the spectra produced from it) and what was experiemtally obtained. This can help to renomarlise or correct the simulation using the spectra to access the beta pure-estimate. To this end, efficiency functions can be indicated (as in Listing A.5)

As an example, the experimental spectra obtained in campaign lead in chapter 2 of Tantalum is compared to TMX_Bateman output in Figure 3.12.

3.5.2. Extracting the α spectrum.

As mentioned, TMX_Bateman can also extract other secondary particle spectras, see Figure 3.13, for an example of alpha spectrum. This output are as limited as the decay databases. For example, in ENDF/B latest version, there are 820 isotopes that can potentially emits alphas (799 if limiting to only pure alpha emitters). For these isotopes, the experimental alpha rays are limited to 256 isotopes.

In order to truly harness this feature, the current decay databases must be re-evaluated in order to explicitate the alpha rays. This task is easily feasible when considering alpha only decay, with the knowledge of total energy available and simple kinematics, one can explicitate the potential alpha emitted, especially as alpha are emitted through tunnel effect, so have low probabilities to be in excited states.

3.5.3. Identifying β pure emitters.

TMX_Bateman allows to identify the beta-pure emitters (a flag is raised in the output

[1] Considered by default but can be deactivated if wanted. As the continous spectra, easing the comparison to FISPACT-II

(a) ^{52}V

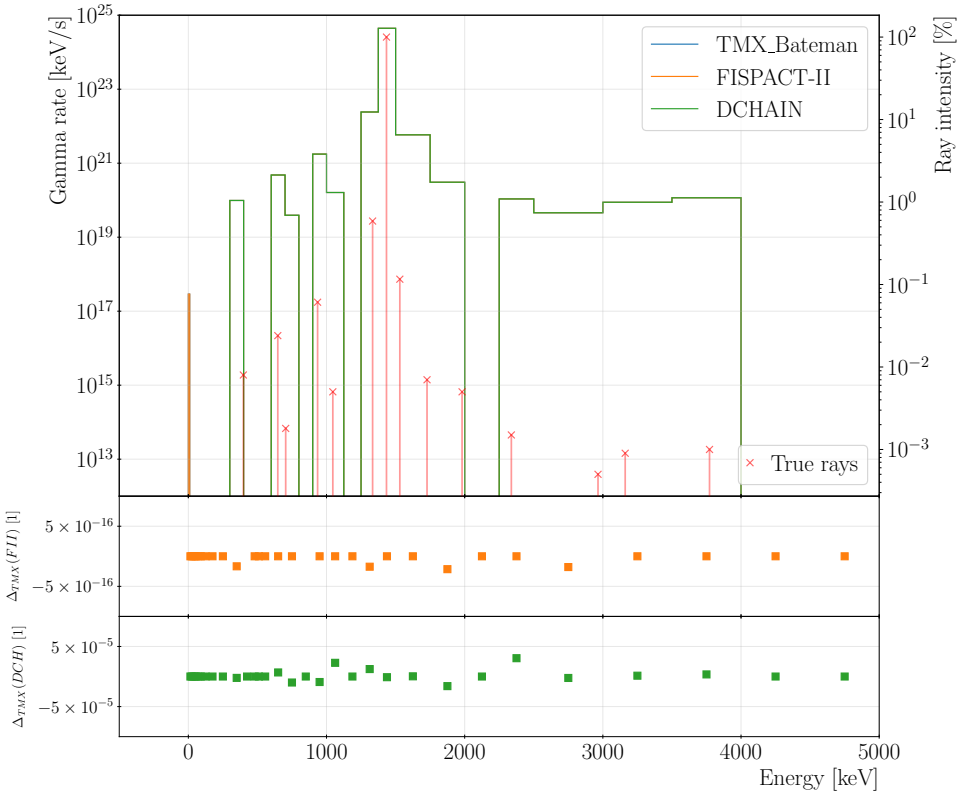

(b) Universe material



Figure 3.11.: Comparison of expected gamma-rate (energy-weighted) spectra for `FISPACT-II` and `DCHAIN-PHITS` with respect to `TMX_Bateman`

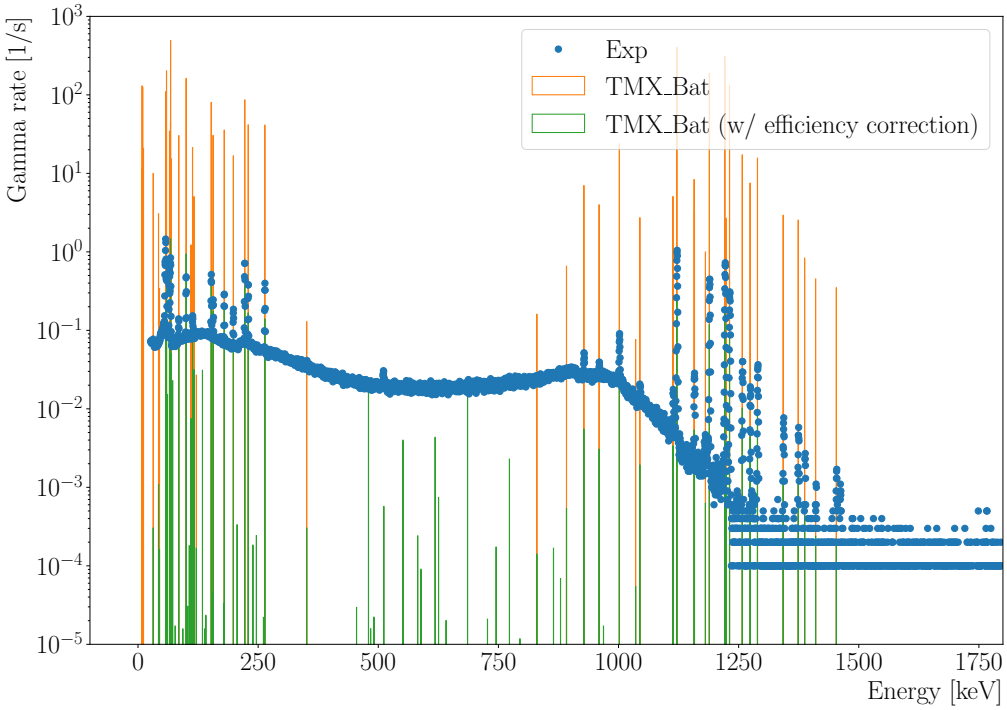

Figure 3.12.: Comparison of experimental Tantalum spectra, against estimation from `TMX_Bateman` (with and without efficiency considerations)

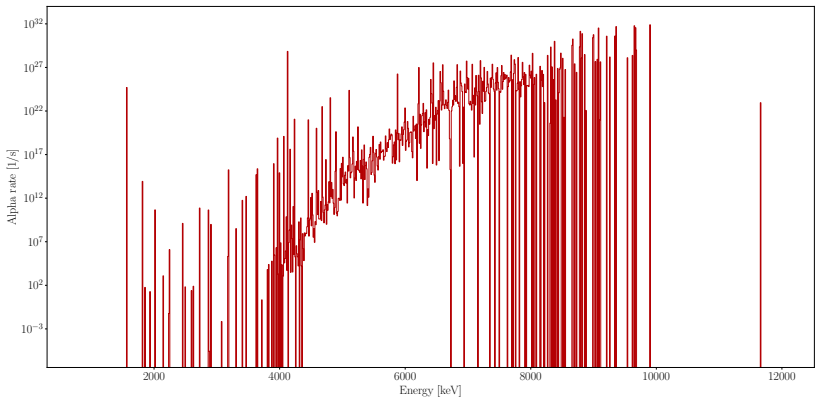

Figure 3.13.: Estimated alpha spectrum for Universe material according to `TMX_Bateman` and ENDF/B-VIII.1 database

JSON). On should note that the definition of β-pure nuclides can vary.

This criteria is an experimental consideration: one does not measure any gamma allowing to identify (or detect) the emitter nuclide. At first, one could consider that any nuclides with mention of β decay, without any information on the gamma could be a sufficient discriminative attribute. Yet most of known nuclides (especially NUBASE-2020) have not be experimentally observed (or at least on its own) limiting the knowledge of gamma rays.

If we consider, only the nuclides with experimental information on the β spectrum, the accounting is easier.

There are 62 nuclides in ENDF/B-VIII.1 that does β decay, with knowledge on the electron or positron spectra, but without any gamma registered. It raises to 67 and 107 for respectively JEFF-4.0 and JENDL-5, as the latter registers more nuclides, and the former limits full mass chain evaluation (prefering "targeted" evaluation).

One could extend the criteria, by listing nuclides with also very low gamma emissions (for example of less than 1 % of intensity). The class of beta pure raises of 58, 59 and 60 nuclides for respectively ENDF/B, JEFF and TENDL. The distribution of those isotopes is given in Figure 3.14

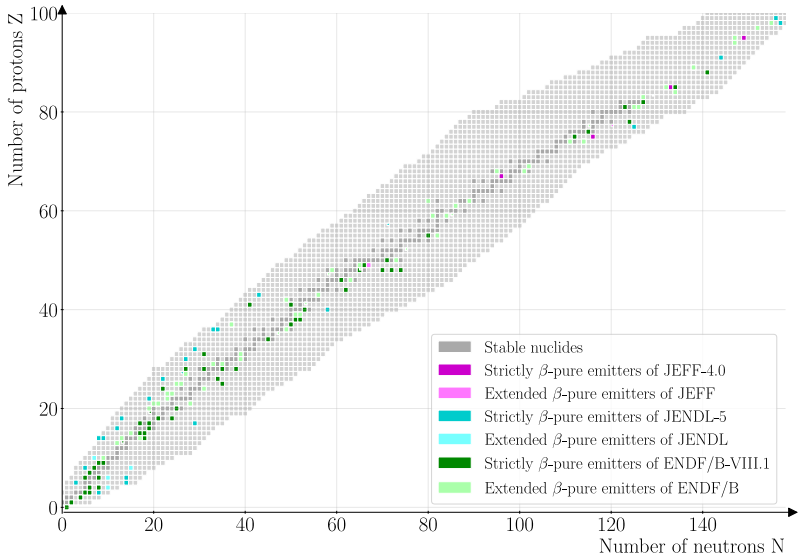

Figure 3.14.: Map of β-pure emitters, identifiable through `TMX_Bateman`, considering ENDF/B-VIII.1 database

Hence, if this additional information could be considered anecdoctal, it does raise the attention of the user to this problematic. It should be noted that strict definition of β-purity is used by the code (at HDF-5 formation), i.e. considering them pure when description of β spectrum is given, but no γ spectrum available.

3.6. Conclusion

This work presents a versatile nuclear inventory tool that advances decay chain modelling and radiation spectrum completeness for radioprotection applications. The solver provides critical capabilities for nuclear facility decommissioning planning and spent fuel shielding design by delivering comprehensive nuclear data, including:

- Radionuclide emission rates and decay heat estimates,
- Complete secondary particle spectra (γ, β, α, proton, neutron),
- Flexible input interfaces for seamless coupling with arbitrary simulation codes.

Compared to existing solutions, this implementation introduces two key innovations:

- Mitigation of information loss from unclosed decay paths through *dummy* metadata retention, ensuring full traceability of all transmutation branches (including those with incomplete nuclear data);
- Unified access to all secondary decay emissions, with customizable binning, to fit the used detector.

Database considerations The solver's capabilities are inherently constrained by the underlying nuclear data libraries:

- ENDF-6 format (or custom HDF5 equivalent) defines the observable limits;
- For optimal results, use of the decay database from **??** to fill critical gaps (e.g., internal bremsstrahlung or beta spectra) is recommended;
- For cross-sections, TENDL is recommended for completeness, though the compiled library in chapter 4 should be considered to ensure reaction channel coverage. Note: isomeric state consistency between decay and cross-section databases is not guaranteed.

Future enhancements While significant progress has been made, further developments would expand the solver's applicability:

- **Uncertainty integration**: Incorporate uncertainty on observables, as well has half-life and branching;
- **Solver optimization**: Implement recent Bateman equation advances like TTA methods [101][1] or Chebyshev resolvent techniques for complex irradiation profiles;
- **Dose analysis**: Develop dedicated functionality for accelerator decommissioning challenges, especially for worker safety.

This chapter delivers a comprehensive framework for tracking radionuclide evolution over time, grounded in the Bateman equations. At its core is the development of `TMX_Bateman`, an advanced solver engineered by Transmutex to address the limitations of legacy tools such as `FISPACT-II`, Oak Ridge Isotope Generation and Depletion Code (ORIGEN), and `DCHAIN-PHITS`. While these conventional platforms are widely adopted,

[1] Kai Huang et al. 'Improvements to the Transmutation Trajectory Analysis of depletion evaluation'. In: *Annals of Nuclear Energy* 87 (Jan. 2016), pp. 637–647. ISSN: 0306-4549. DOI: 10.1016/j.anucene.2015.10.013.

they fall sometimes short in flexibility, spectral completeness, and computational efficiency –particularly when modelling intricate decay chains or extracting secondary particle spectra essential for nuclear safety and design assessments. The increasing demand for precision in nuclear fuel cycle analysis, radiation protection, and waste management underscores the need for a next-generation solver. `TMX_Bateman` meets this challenge by implementing TTA –a method that linearizes decay pathways and yields exact solutions, outperforming traditional approaches like LSODE and CRAM in both fidelity and adaptability. Built on a modular architecture, `TMX_Bateman` leverages structured JSON inputs and HDF5 databases derived from ENDF-6 nuclear data. It supports the separation and recombination of decay and transmutation chains, and accounts for a wide spectrum of nuclear phenomena including spontaneous fission, isomeric transitions, and exotic decay modes. The solver also exports secondary particle spectra, enabling high-resolution analysis across multiple domains. Input parameters encompass initial nuclide inventories, irradiation profiles, and solver configurations; outputs include isotopic compositions, activity levels, emission rates, decay heat contributions, and committed dose estimates based on ICRP standards.

Benchmarking results demonstrate strong alignment with existing tools in pure decay scenarios, while also revealing `TMX_Bateman`'s greater detail in modelling delayed alpha emissions and gamma spectra. These validations affirm its reliability and highlight its potential for broader deployment in nuclear science and engineering. Looking ahead, the works outlines key development pathways: integration of reaction spectra, optimization of complex irradiation scenarios, and the creation of specialized modules for pure beta emitters and clearance obligations.

In the next chapter, we will present a robust methodology for selecting and evaluating data on nuclear cross sections, which are essential for accurate nuclear modelling. We will discuss the main international libraries (ENDF/B, JEFF, JENDL, TENDL), validated by reference experiments. We will present a Python-based tool for systematic data analysis, highlighting the impact of library choice and advocating a hybrid approach to validated data compared to EXFOR in order to improve future nuclear applications.

In the following chapter, the discussion of a new database generation will be done and we will introduce GENF/D.

Chapter

4. A strategy to choose the cross-sections

— Comment imaginez-vous l'abscisse et l'ordonnée ?
— La personne ordonnée, sa maison est toute de suite bien rangée et bien organisée. Et puis, c'est aussi, peut-être, une personne qui a les pieds sur Terre.
— Qui ça ?
— Et bien, l'ordonné
— Et l'abscisse ?
— L'abscisse, bon bah, elle s'en va: elle aime mieux courrir dehors. Et, évidemment, elle est peut-être plus utile à la société. C'est certain, mais il faut les deux, monsieur.
— Vous faîtes une nette différence entre l'abscisse et l'ordonnée ?
— Oh oui, exactement, exactement. M'enfin, on a peut-être plus confiance dans l'ordonné.

(Anonyme, Micro-trottoir de Gérard Pabiot – 1986)

4.1. Systematic access tool for evaluations : eval_explorer 140
4.2. Applications 141
4.2.1. Comparison of (n, γ) cross-sections 141
4.3. Impact of evaluated library on models 142
4.3.1. Comparison of cross-sections models 143
4.3.2. Simplified case 143
4.3.3. Complex case 145
4.4. Conclusion 148

The ENDF-6 format (Evaluated Nuclear Data File, version 6) is a standardised structure used to store nuclear reaction data that is essential for the design of reactors, radiation shielding and other nuclear applications. It is maintained by the Cross Section Evaluation Working Group (CSEWG) and disseminated by the National Nuclear Data Centre (NNDC).

These databases contain evaluated cross-section data, which is calculated using nuclear models in combination with experimental measurements. This provides reliable access to cross-section data for a wide range of nuclear physics applications. As summarised in Table 4.1, these libraries contain cross-sections for neutron reactions as well as information on fragmentation, angular distributions, neutron scattering and covariance data. Such data is organised in File (MF) and section (MT).

Table 4.1.: Listing of main files available in ENDF6 format.

MF[A]	MT[B]	Description
1	451	General data
1	452/455 456/460	Fission total/delayed/prompt neutron or delayed photons multiplicities
2	*	Resonance parameters (for neutrons)
3	*	Reaction cross-sections
4	*	Angular distributions
5	*	Energy distributions
6	*	Product energy-angle distributions[†]
7	*	Thermal scattering law
8	457 454/459	Decay or Independent/Cumulative fission yields
9	*	Multiplicities for radionuclides products
10	*	Production cross-section for radionuclides
11/12 13/14 15/23/26	*	Photo- and electro-atomic related data
31	*	Covariance for fission multiplicity (related to MF=1)
32	*	Covariance of resonance parameters (related to MF=2)
33	*	Covariance for neutron cross-sections (related to MF=3)
34	*	Covariance for angular distributions (related to MF=4)
35	*	Covariance for energy distributions (related to MF=5)
40	*	Covariance for radionuclide production (related to MF=10)

[A] File
[B] Section with the associated file
[†] Often stores list of residuals

These databases are the result of the effort of various national and international nuclear data working groups. Notable examples include ENDF/B [81][1], JEFF [82][2], JENDL [92][3], TENDL [116][4], and TENDL [87][5], along with more specialised databases such as Library of Russian Evaluated Neutron Data (BROND) [117][6], Fusion Evaluated Nuclear Data Library (FENDL) [118][7], Brookhaven National Laboratory (BNL), International Nuclear Data Evaluation Network (INDEN), and several IAEA databases (including ADS [119][8], Medical [120][9] and standards), as well as Ion Beam Applications (IBA) and Waste Incineration Nuclear Data (WIND). The libraries are distributed by their originating institutions, as well as through the NEA[10] and the IAEA[11].

The validity of key-nuclides in these libraries is usually confirmed through integral benchmark experiments, as the ones peer-reviewed and compiled in the International Reactor Physics Evaluation Project (IRPhEP) [121][12], the International Criticality Safety Benchmark Evaluation Project (ICSBEP) [122][13], or the Shielding Integral Benchmark Archive and Database (SINBAD) [123][14].

[1] D. A. Brown et al. 'ENDF/B-VIII.0: The 8th Major Release of the Nuclear Reaction Data Library with CIELO-project Cross Sections, New Standards and Thermal Scattering Data'. In: *Nuclear Data Sheets*. Special Issue on Nuclear Reaction Data 148 (Feb. 2018), pp. 1–142. ISSN: 0090-3752. DOI: 10.1016/j.nds.2018.02.001.

[2] A. J. M. Plompen et al. 'The joint evaluated fission and fusion nuclear data library, JEFF-3.3'. en. In: *The European Physical Journal A* 56.7 (July 2020), p. 181. ISSN: 1434-601X. DOI: 10.1140/epja/s10050-020-00141-9.

[3] Osamu Iwamoto et al. 'Japanese evaluated nuclear data library version 5: JENDL-5'. In: *Journal of Nuclear Science and Technology* 60.1 (Jan. 2023). _eprint: https://doi.org/10.1080/00223131.2022.2141903, pp. 1–60. ISSN: 0022-3131. DOI: 10.1080/00223131.2022.2141903.

[4] Zhigang Ge et al. 'CENDL-3.2: The new version of Chinese general purpose evaluated nuclear data library'. en. In: *EPJ Web of Conferences* 239 (2020), p. 09001. ISSN: 2100-014X. DOI: 10.1051/epjconf/202023909001.

[5] A. J. Koning et al. 'TENDL: Complete Nuclear Data Library for Innovative Nuclear Science and Technology'. In: *Nuclear Data Sheets*. Special Issue on Nuclear Reaction Data 155 (Jan. 2019), pp. 1–55. ISSN: 0090-3752. DOI: 10.1016/j.nds.2019.01.002.

[6] Russia Blokhin et al. 'NEW VERSION OF NEUTRON EVALUATED DATA LIBRARY BROND-3.1 (in Russian), published in Voprosy At. Nauki i Tekniki, ser Yadernye Konstanty, issue 2, p. 92 (2016)'. In: *Voprosy atomnoj nauki i techniki = Pytannja atomnoï nauky i techniky = Problems of atomic science and technology* 2016 (Aug. 2016), p. 92.

[7] G. Schnabel et al. 'FENDL: A library for fusion research and applications'. In: *Nuclear Data Sheets*. Special Issue on Nuclear Reaction Data 193 (Feb. 2024), pp. 1–78. ISSN: 0090-3752. DOI: 10.1016/j.nds.2024.01.001.

[8] Daniel Lopez Aldama. *ADS-HE: Evaluated Nuclear Data Library up to 1 GeV for 202Hg, 208Pb, 209Bi, 232Th, 235U, 238U, 237Np, 239Pu, 242Am and 245Cm*. en. Tech. rep. IAEA-Nuclear Data Section, Dec. 2013. DOI: 10.61092/iaea.r81b-0sjz.

[9] *Index of /public/download-endf/IAEA-Medical*.

[10] https://www.oecd-nea.org/dbforms/data/eva/evatapes/

[11] https://www-nds.iaea.org/public/download-endf/

[12] *IRPhEP Handbook Online - OECD Nuclear Energy Agency*.

[13] *Nuclear Energy Agency*.

[14] Ivan A. Kodeli and Enrico Sartori. 'SINBAD – Radiation shielding benchmark experiments'. In: *Annals of Nuclear Energy* 159 (Sept. 2021), p. 108254. ISSN: 0306-4549. DOI: 10.1016/j.anucene.2021.108254.

These libraries were initially developed to facilitate the modelling of neutron interactions, particularly given the challenges in accurately simulating such reactions below 20 MeV (see subsubsection b). Consequently, the integral benchmarks used are related in majority to nuclear reactor application, and criticity measurements. However, the format has since been extended to describe higher energy interactions and charged particles. Current efforts, particularly with the TENDL model and the PADF library (for protons), aim to expand the range and quality of these evaluations. Table 4.2 presents statistics on the coverage of different projectiles in evaluated libraries. The main advantage of this approach is its ability to temporarily adjust the treatment of specific projectile-material interactions to better match experimental data.

Nuclear Data Management in Radiation Transport Codes Modern radiation transport codes offer extensive control over nuclear data selection through their library management systems. In PHITS, SERPENT, and MCNP, the `xsdir` mechanism enables the precise selection of different evaluated libraries for each projectile-nuclide combination. This is done within defined energy ranges, that can be varied, and will defaulting to their native physics engines outside of them.

Geant4 and FlukaCERN provide analogous functionality, though implemented at the global library level rather than with per-reaction granularity. While library selection is principally restricted to neutron interactions below 20 MeV, Geant4's ParticleHP model offers additional access to parts of the TENDL evaluations.

Historical Library Preferences and Modern Developments The Monte Carlo community has historically followed regional preferences in the default nuclear data choices: MCNP prioritises ENDF/B (U.S. evaluations), PHITS defaults to JENDL (Japanese evaluations), and Geant4 typically employs JEFF (European evaluations). These preferences reflect both the codes' national origins and the nuclear data infrastructure available during their development. However, contemporary versions increasingly support cross-library comparisons, facilitating more rigorous uncertainty quantification in nuclear simulations.

Experimental Validation of Nuclear Data The EXperimental FORmat (EXFOR) library, maintained by the IAEA's Network of Nuclear Reaction Data Centres (NRDC), is the primary repository for experimental nuclear reaction data. This comprehensive database aggregates:

- Experimentally measured cross-sections from published literature
- Unpublished data from laboratory reports
- Quality-controlled submissions from international collaborators

Methodological Considerations for Nuclear Data Selection Comprehensive modelling requires systematic variation of nuclear databases, which is a time-intensive process involving verification of reaction existence across different evaluations. Code-to-code comparisons further necessitate fixed database selections with maximum projectile-material

Table 4.2.: Synthesis of number of nuclides for neutron, proton and alpha incident cross-sections of main ENDF6 sub-libraries.

Library	n	p	α
TENDL-2023	2830	2855	2835
TENDL-2023.s0[†]	0	2850	2835
TENDL-2023.s60	2830	0	0
TENDL-2023.600MeV[‡]	0	553	0
JEFF-4.0	2842	2855[•]	2835[•]
JENDL-5	795	239	0
ENDF/B-VIII.1	558	49	5
CENDL-3.2	268	0	0
BROND-3.1	362	0	0
FENDL-3.2c	190	0	0
ROSFOND-2010	658	0	0
MENDL-2.0	501	504	0
ADS-2.0	142	0	0
PADF-2	0	62	0
IAEA-Therapeutic	23	16	0
IRDFF-II	45	0	0
INDEN-Aug23	24	0	0
IAEA-Medical	0	23	0
WIND-1.0	18	1	0
LA-100	7	6	0
HEL-0.0	4	4	0
Standards	7	0	0
BNL-1GeV	0	2	0

[†] The pure TALYS-based version of TENDL, without substitution by other libraries when the model fails

[‡] The TENDL.s0 library extended up to 600 MeV projectile energy

[•] JEFF-4.0 distributes TENDL-2023 for α (except for ^{9}Be), γ, p, ^{2}H, ^{3}H and ^{3}He.

coverage. The extensive coverage is of particular importance for deterministic codes, as `FISPACT-II` or `TMX_Bateman` are limited to ENDF6-defined reactions, without alternative nuclear models.

To address these challenges, this work involved the development of a Python toolset for library processing and comparing. This framework enables:

- Cross-validation of models against experimental data (via EXFOR)
- Systematic evaluation of reaction-specific performance
- Generation of optimized compiled databases through selective library merging

In addition, EXFOR provides critical experimental benchmarks for validating evaluated libraries. This enables two complementary approaches: direct comparison between models and experimental measurements and inter-model comparisons anchored to experimental data. Those approaches can inform the selection of optimal evaluations for specific reaction channels

4.1. Systematic access tool for evaluations : eval_explorer

A dedicated analysis environment was required to enable systematic benchmarking across nuclear data libraries. While existing solutions, like the JANIS [12][1] web interface, are available. This latter solution face limitations in maintaining current datasets (the latest available TENDL evaluation dates from 2017), and only facilitate the visual access to cross-sections.

Python was chosen as the optimal programming language for this toolset due to:

- Its robust capabilities for file parsing and data processing
- The language's growing adoption in scientific computing
- Simplified integration with modern analysis workflows

The toolsets is built around to the MIT licenced IAEA tools: `endf_parserpy` [124][2] and X4Pro [125][3]. It is built around pandas.DataFrame, to mimic the structure of the EXFOR SQL dump associated with XPro[4].

a) Data access

As for the tool presented here, the EXFOR data is accessed via SQL query, while the evaluated data can be accessed either via web-request or locally from ENDF/ACE format files. This data is then transcribed into `pandas.DataFrame` objects, allowing filtering by projectiles, reactions but also by isotope properties (atomic mass, number, half-life, ...)

[1] N. Soppera, M. Bossant, and E. Dupont. 'JANIS 4: An Improved Version of the NEA Java-based Nuclear Data Information System'. In: *Nuclear Data Sheets* 120 (June 2014), pp. 294–296. ISSN: 0090-3752. DOI: 10.1016/j.nds.2014.07.071.

[2] Georg Schnabel, Daniel Lopez Aldama, and Roberto Capote. *How to explain ENDF-6 to computers: A formal ENDF format description language*. Dec. 2023.

[3] Viktor Zerkin. *X4Pro – universal, fully relational EXFOR database*. English. Publication Title: EPJ Web of Conferences Volume: 284. 2023.

[4] https://www-nds.iaea.org/cdroms/x4pro1

thanks to additional access to Nubase2020. Only the cross-section data (MF3 section) is acquired.

This Pythonic analyser is also able to automatically extract similar cross-sections (MT, projectile, ...) from the SQL database, or the local file catalogue.

Dataframe structure The SQL dump of cross-sections is organised in a one line per incident energy fashion, with dataset ID based on a an entry and subentry ID, in addition to MF and MT numbers (same as the one defined in ENDF6 format).

Hence, `eval_explorer` produces such structure for data, with each reaction cross-sections dataset is identified by a unique string (DatasetID), and the properties of the target and projectile are stored (Z, A, I, projectile, MT code). The id number is based on the library, release, version and modification number, and for the global ID (DatasetID) the MF/MT value is also appended to ensure each reactions can be followed independently.

This structure, with an example in **??** and **??**, allows to make use of the filter features available of the pandas.DataFrame objects.

b) Neutron cross-sections

Specific attention should be given when parsing neutron cross-section, especially when resonance is expected. To represent, "resonating" cross-section both the MF=3 and MF=2 are used. If only one of them is read, as in the neutron capture[1] represented in Figure 4.1, missing component is expected. Where as the (n, n+p)[2] is directly available in the ENDF6.

A warning will be raised, when a `MF`=2 is expected, but not applied.

Preprocessing files Currently the resonance contribution, nor Doppler broadening, is not fully implemented in the `eval_explorer` toolset. To get valid cross-sections, one should run code as `prepro`, part of NJOY. At least the LINEAR, then RECENT should be used To get the standard output, the PREPRO software is one of the reference tool for such data processing.

4.2. Applications

4.2.1. Comparison of (n, γ) cross-sections

Scoring system of single dataset Regardless of the type of data (experimental or evaluated data), a scoring system must be defined to compare and contrast datasets. As the availability over the range of interest is of great importance, a coverage interval is defined. For a given range of energies (which may be discontinuous), the interval is segmented in one hundred bins (either linearly or logarithmically) in order to obtain

[1] `MT`=102
[2] `MT`=28

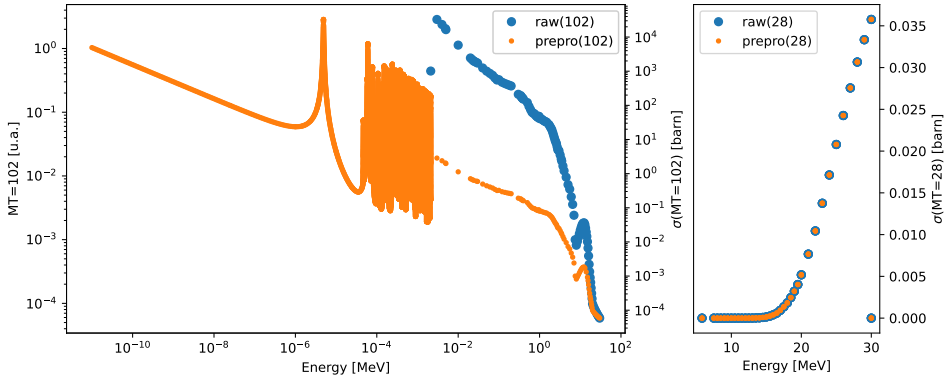

Figure 4.1.: Comparison of distributed and preprocessed partial cross-section of ^{197}Au from TENDL-2023. On the left, neutron-capture, and on the right, neutron and proton emission

a coverage percentage. Secondly, especially for experimental data the distribution of points is of importance, hence the average distance between coverage bins is computed into a contiguity index (one can also directly compute the average distance between data points of the abscissa).

Comparison of two datasets The usual comparer (deltas and ratios are available) as well as data collapser (integer, summation or average) have been implemented. Especially for evaluated data, when the abscissa do not correspond, the user can either choose for logarithmic or linear interpolation between the two nearby neighbours. For cross-section axis, the uncertainties are propagated via the usual rules, unless there is also an energy uncertainty. In this case, the method implemented here consists in doing three comparisons and averaging the results, for the three positions.

When comparing EXFOR data, which may be unevenly distributed and with large energy gaps, the mentioned interpolation method cannot be considered. Hence, we avoid the interpolation over the uncovered bins (explained in the previous paragraph), and only compare over the contiguous intervals, providing the same output as expected when comparing models (with sum, average done over the truncated range) at the end.

4.3. Impact of evaluated library on models

This section will discuss the differences between libraries and their consequences on multi-physics tools, especially with FISPACT-II and PHITS. The developed methodology in the previous section will be applied. And afterwards, the impact will be discussed based on an arbitrary situation for neutron capture only and then in a more complex model based on an experiment done in the neutron field of a particle accelerator. The material list is reduced to the one available for the experiment i.e., Sc, Tb, Ta, W and Au. The mono-isotopic composition was one of the criteria for the choice of materials.

4.3.1. Comparison of cross-sections models

We extracted the cross-sections for the materials of interest ^{45}Sc, ^{159}Tb, ^{181}Ta, ^{197}Au and ^{nat}W for the (n,γ) reaction (coded MT102).

The scoring of the EXFOR presence for the MT102 reaction is summarised in Table 4.3. The evaluated data, with the four main libraries in their latest version, is compared (via an average of the ratio with ENDF/B as reference) in Table 4.4. The average was weighted by the normalised ENDF/B data.

As we can see in Table 4.3, for the gold and scandium isotopes, the former has the most experimental data and greatest coverage. Yet the latter possesses greater agreement between models. This is explained by the presence of a large number of resonant energies for the gold, which are not all described by experimental data, and push the limits of the nuclear models, as shown in Figure 4.2.

We can also check the difference between models and EXFOR, the difference between cross-sections implemented in PHITS and EXFOR data is show in Table 4.5. We observe again the similarities pointed by Table 4.4. The largest differences are between version of models e.g., ENDF/B-VIII versus ENDF/B-V.I. The average distance considering the full range is determined in this table, with all available EXFOR points. Yet as seen in Figure 4.2(b), some data maybe deprecated, the point straying from the models are from 1977, a discussion with respect to acquisition date and uncertainties should be done to check further the discrepancies.

Table 4.3.: Scoring the available experimental data for neutron capture of several materials

Reaction	**Points**	**Coverage [%]**	**Contiguity [a.u.]**
^{45}Sc(n,γ)	80	14	10
^{181}Ta(n,γ)	1394	78	5.75
^{184}W(n,γ)	92	16	21.25
^{186}W(n,γ)	198	73	9.34
^{182}W(n,γ)	54	16	21.25
^{183}W(n,γ)	41	15	21.5
^{197}Au(n,γ)	8966	100	0.

4.3.2. Simplified case

This trial is based on FISPACT-II and PHITS. The activation of 1 cm^3 cubes of the 5 materials mentioned, via a neutron beam was considered. The cubes were irradiated at a current of 10^9 n/cm^2/s^{-1} for 3 hours and the activation checked after 1 second of cooling. An arbitrary neutron spectrum was defined based on the constraints from FISPACT-II which processes particles group-wise. The spectrum is simply defined at 1 n/cm^2/s for each 1102 bins. When necessary, the spectrum was converted into 709 groups (using

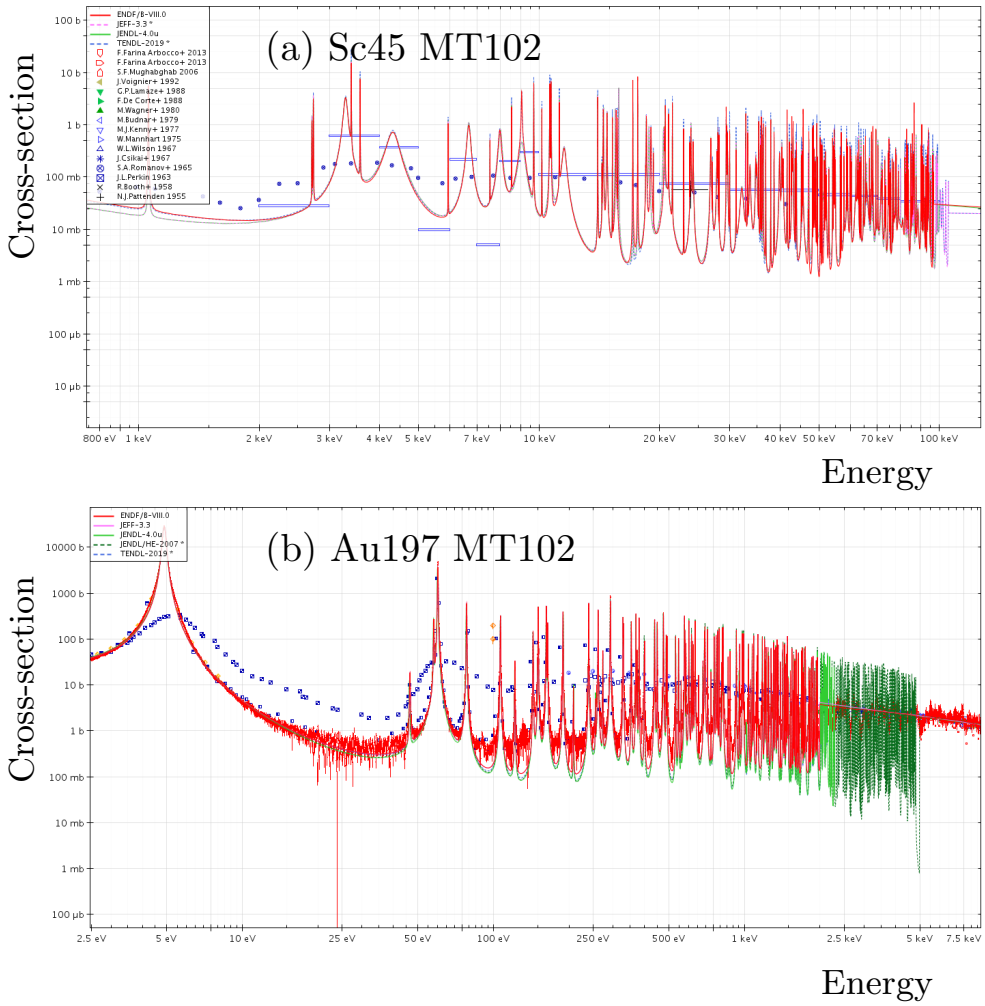

Figure 4.2.: Comparison of ^{45}Sc (a) and ^{197}Au (b) cross-sections (evaluation and experiment)

Table 4.4.: Averaged weighted ratio of cross-sections available over the full energy range, with ENDF/B as reference

	^{45}Sc	^{159}Tb	^{181}Ta	^{nat}W	^{197}Au
ENDF	1.0	1.0	1.0	1.0	1.0
JENDL	0.999	0.977	0.868	1.022	1.003
JEFF	0.999	0.978	0.884	1.006	1.000
TENDL	1.002	1.015	0.819	1.024	1.003

Table 4.5.: Averaged weighted ratio of cross-sections available over the full energy range, with EXFOR as reference

	^{45}Sc	^{159}Tb	^{181}Ta	^{nat}W	^{197}Au
ENDF/B-VIII	0.04	0.10	0.46	0.01	-0.02
ENDF/B-VII	0.04	0.10	0.46	0.00	-0.01
JENDL-5	0.05	-0.14	0.02	0.41	-0.02
JENDL-4	0.05	-0.14	0.45	0.02	-0.01
JEFF	0.05	-0.14	0.45	0.01	-0.02
TENDL	0.06	-0.18	0.47	0.03	-0.02

`GRPCONVERT` from FISPACT).

The natural composition was used for each material, and the activation estimation was extracted from the product of neutron capture on the main isotope (e.g. ^{46}Sc for ^{45}Sc). The discussion of results appears in the Figure 4.3.

As we can see, the difference between models are no more than 5 to 10%, which is in perfect agreement with the expected model differences obtained in the previous section.

4.3.3. Complex case

An experiment, furthering , was carried out inside the cyclotron room of the proton accelerator available at the IPHC laboratory, CYRCé a TR24 from Advanced Cyclotron System Inc (ACSI). The liquid target of enriched water ($H_2{}^{18}O$) during the production of 90 GBq of ^{18}F was with a 18 MeV proton beam at a current of 75 μA for 45 minutes. The resulting secondary neutron field was used to activate the mentioned materials, which were placed around the inside the biological shield (Loc. 1: Sc, Ta, W, Au), on the outside of the lead shield (Loc. 2: Sc, Tb), on the yoke of the cyclotron (Loc. 3: Sc, Ta, W, Au) and farther away : on one of the room wall (Loc. 4: Ta, Au). These positions were considered because of the expected neutron fluence ranging from 10^9 n/cm^2/s and 10^6 n/cm^2/s.

The activation was measured using HPGe LABSOCS and computed considering the

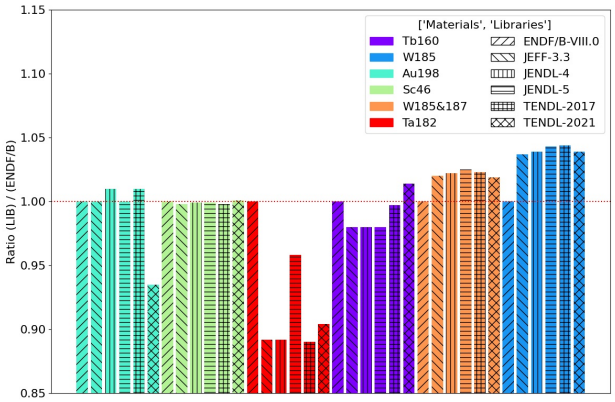

Figure 4.3.: Ratio of estimated activity varying evaluated library using FISPACT-II, with ENDF/B as ratio reference

Table 4.6.: Comparison of expected activity inside the samples considering materials, using PHITS, with ENDF/B library as reference

Library \ Material	**Sc**	**Tb**	**Ta**	**Au**
ENDF/B-VIII.0	1.0	1.0	1.0	1.0
JENDL-5	1.15	1.39	0.86	1.14
JEFF-3.3	1.26	0.96	1.0	1.44
TENDL-2021	1.15	1.37	0.89	1.14

decay scheme compiled by the National Laboratory Henri Becquerel (LNHB).

The model of CYRCé was simulated for ENDF/B-VIII.0, JENDL5, JEFF-3.3 and TENDL-21. The activation calculations were performed with DCHAIN-SP after a week of decay in order to avoid most metastable states, which are one of the most delicate items to accurately be model via MC codes.

The average ratio between models taking reference of the ENDF/B is shown in Figure 4.4. The synthesis of ratios by material is shown respectively with ENDF/B reference and with experimental reference in Table 4.6 and Table 4.7. In the former, we observe a proximity of both ENDF/B and JEFF models for Tb and Ta. If we check systematically the difference between models, we get that JENDL and TENDL agree on Sc, Tb and Ta.

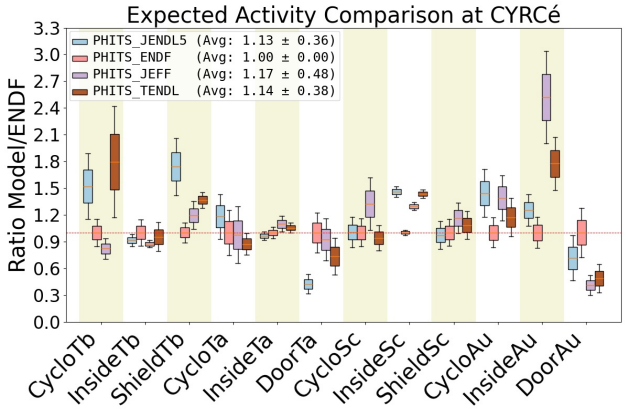

Figure 4.4.: Comparison of expected activity inside the samples using PHITS with ENDF/B library as reference

Table 4.7.: Comparison of expected activity inside the samples considering materials, using PHITS, with experimental measurements as reference. *In blue, the best of four*

Library \ Material	**Sc**	**Tb**	**Ta**	**Au**
ENDF/B-VIII.0	1.47	1.08	6.24	1.81
JENDL-5	1.56	1.37	5.37	2.03
JEFF-3.3	1.88	1.00	6.47	2.10
TENDL-2021	1.54	1.39	5.9	1.78

4.4. Conclusion

In conclusion, we have attempted to develop a methodology in order to choose the best database for activation computation, around particle accelerators.

A Pythonic tool was built in order to compare evaluated data for the same nuclear reaction. The provided comparison method (doing the ratio between models, weighting by the reference cross-section) shows a hierarchy between models, which is maintained when running FISPACT-II or PHITS. The interest of such discussion is to pick the library that provides more accurate models. Hence, the basic showcase was applied to an experimental situation involving a proton accelerator. As not only neutronic capture is taking place, reporting the hierarchy between models is more difficult.

The CYRCe experiment should be extended to the other target available (^{64}Ni and ^{89}Y), especially for the nickel target, as the (p,n) reaction is available in ENDF/B, JENDL and TENDL, unlike to the other two which are solely available in TENDL.

Additionally, the distance between model and EXFOR data must be calculated, considering acquisition year and distance between other experimental points in the same area, to corroborate the finding of the most relevant database, allowing to base oneself one the large databank that is EXFOR. Yet we have highlighted, the resonance problematic with the gold case.

The full characterization of models via EXFOR would enable the possibility to create a customized mixture of databases, a cocktail, dedicated to neutron capture and activation studies. Enabling to provide for a more accurate estimate of radionuclide inventory, thanks to the indirect corroboration via EXFOR data. And one could expand the model comparison to angular distribution when available to compare more in depth models, and make it available to the tool presented here. Offering an easy entry to most databases in most format.

This task is one step to provide a software module for the decommissioning consideration, via radionuclide inventories, of the ADS future prototype from TRANSMUTEX, belonging to the digital twin strategy of the company.

Chapter

5. Global Evaluated Nuclear File GENF/D: a decay database for extensive radionuclide inventories

Qui aurait pu prédire que ···

(Emmanuel Macron, *Allocution présidentielle – 2022)*

5.1. Overview of decay databases . . . 151
5.1.1. ENSDF . . . 152
5.1.2. ENDF6 Decay Sub-libraries . . . 152
5.1.3. NUBASE . . . 154
5.1.4. RIPL . . . 156
5.2. Generation of the decay database . . . 157
5.2.1. Procedure Summary and Tools . . . 157
5.2.2. Step 1: Generation of basic ENDF6 database. . . . 161
5.2.3. Step 2: Insertion of decay spectra. . . . 168
5.2.4. Step 3: Addition of spontaneous fission properties . . . 172
5.2.5. Average energy estimations . . . 173
5.3. Comparison to evaluated databases . . . 175
5.3.1. Extensiveness considerations . . . 175
5.3.2. Energetics considerations . . . 176
5.4. Validation against integral measurements . . . 183
5.4.1. Fission fragments difficulties . . . 184

As mentioned in section 3.4, the usual Bateman deterministic codes can only follow isotopes that are presents in the decay database linked, and the majority of the measurements extracted from a specific inventory come only from the properties explicited in the source database.

To extend the capacities of such programme, one could modify their source code to introduce additional datasets and nuclear models to cover all necessary physics. But this means making large changes, introducing libraries that may not have been coded in the same language, generating a high number of controls, breaking the ergonomy of such tools. It creates also an opacity on the origin and which data is used in the end.

For inventory analysis, obtaining precise beta distributions (unlike other secondary particles) requires additional utilities like LogFT [126][1] or BetaShape [127][2], as only maximum energy levels are typically provided in the standard ENDF-6 file. Systematic data for internal bremsstrahlung are often unavailable. Yet the contribution of high-energy β-particle bremsstrahlung to the total dose rate can be significant [128][3]. Consequently, by including it systematically, the Bateman solver needs only to compute the external bremsstrahlung component.

To circumvent the extensiveness issues, the `FISPACT-II` and `DCHAIN-PHITS` projects have made hybridation of decay databases, mixing JEFF, ENDF/B and JENDL in different orders. Yet this strategy can be dangerous as it may introduces incoherence in the data, gamma rays of very short lived decay chains may not be associated to the same isotopes, the average energy estimates may differ...

In addition, the evaluated databases are not updated as regularly as the experimental data, as they are often only released jointly with the neutron cross-sections evaluations, which are the primary interest. The ENSDF project evaluates fully about 220 nuclides yearly, with partial updates made available each month [129][4]. It is estimated that a given mass chain is revisited every seven years, on average [86][5].

The major libraries can exhibit even longer revision cycles, with seven years between JEFF-3.3 and JEFF-4.0, or between ENDF/B-VIII.0 and ENDF/B-VIII.1, and eleven years between JENDL-4 and JENDL-5. Moreover, these distributions aim to serve a different purpose than broader databases such as NUBASE or the Reference Input Parameter Library (RIPL) [130][6], which prioritise comprehensiveness.

To address these release delays and reduce reliance on external utilities during inventory analysis (especially for `TMX_Bateman`), a Python-based toolset that generates

[1] NNDC. *IAEA-NSDDNetwork/LOGFT*. original-date: 2021-11-09T14:47:14Z. National Nuclear Data Center, May 2025.

[2] X. Mougeot. 'Erratum: Reliability of usual assumptions in the calculation of beta and nu spectra'. In: *Physical Review C* 92.5 (Nov. 2015), p. 059902. DOI: 10.1103/PhysRevC.92.059902.

[3] Greg Baily et al. *FISPACT-II User Manual*. en. Manual UKAEA-CCFE-RE(21)02. United Kingdom Atomic Energy Authority, May 2023.

[4] *Evaluated Nuclear Structure Data File (ENSDF)*. en. Artwork Size: 0.45 GB Pages: 0.45 GB. 2022. DOI: 10.18139/NNDC.ENSDF/1845010.

[5] M. B. Chadwick et al. 'ENDF/B-VII.1 Nuclear Data for Science and Technology: Cross Sections, Covariances, Fission Product Yields and Decay Data'. In: *Nuclear Data Sheets*. Special Issue on ENDF/B-VII.1 Library 112.12 (Dec. 2011), pp. 2887–2996. ISSN: 0090-3752. DOI: 10.1016/j.nds.2011.11.002.

[6] R. Capote et al. 'RIPL – Reference Input Parameter Library for Calculation of Nuclear Reactions and Nuclear Data Evaluations'. In: *Nuclear Data Sheets*. Special Issue on Nuclear Reaction Data 110.12 (Dec. 2009), pp. 3107–3214. ISSN: 0090-3752. DOI: 10.1016/j.nds.2009.10.004.

an extensive and up-to-date decay database, compiling several nuclear databases, was developed. The Global Evaluated Nuclear File Decay sub-library (GENF/D) combines the NUBASE2020 evaluation with the latest ENSDF distribution, accessed via IAEA Livechart API, augmented by calculated quantities from BetaShape for beta spectra, from the GEneral description of Fission observables (GEF) code [131][1] for fission properties, from the Band-Raman Internal Conversion Coefficients (BrIcc) code [132][2] for conversion electron data, and the from the RadiationReport of the NSDD network [23][3] for internal bremsstrahlung estimates.

This database generation goes towards the modern calls of open data, allowing to conserve ownership of the code, but making available the datasets for other uses and especially ease validation by the peers.

This chapter proposes the in-depth discussion of the decay databases, and the generation of a state-of-the-art decay database, including the latest estimation of several metrics.

This compiled dataset has been checked against the other evaluated databases, as well as established international benchmarks using the deterministic Bateman equation solver in FISPACT-II.

5.1. Overview of decay databases

Nuclear decay data is disseminated across a variety of databases, each characterized by distinct formats that differ in structure and adoption by simulation tools. There is no single prevailing standard; instead, major Monte Carlo and inventory codes depend on customised adaptations: Geant4 primarily processes decay data from ENSDF; FLUKA incorporates evaluations from NUBASE; MCNP utilises Reference Input Parameter Library (RIPL) for nuclear structure parameters.

Despite this fragmentation, the ENDF6 format maintains its prevalence, particularly for activation and inventory codes such as `FISPACT-II`, SERPENT, `DCHAIN-PHITS`, NUIT, and SCALE.

This section offers a review of the principal decay databases, with an emphasis on their coverage and accessibility within modelling workflows.

[1] K. -H. Schmidt et al. 'General Description of Fission Observables: GEF Model Code'. In: *Nuclear Data Sheets*. Special Issue on Nuclear Reaction Data 131 (Jan. 2016), pp. 107–221. ISSN: 0090-3752. DOI: 10.1016/j.nds.2015.12.009.

[2] T. Kibédi et al. 'Evaluation of theoretical conversion coefficients using *BrIcc*'. In: *Nuclear Instruments and Methods in Physics Research Section A: Accelerators, Spectrometers, Detectors and Associated Equipment* 589.2 (May 2008), pp. 202–229. ISSN: 0168-9002. DOI: 10.1016/j.nima.2008.02.051.

[3] Jun Chen. *IAEA-NSDDNetwork/RadiationReport*. original-date: 2022-08-25T19:42:34Z. Apr. 2025.

5.1.1. ENSDF

The majority of modern decay data originates from the U.S. Evaluated Nuclear Structure Data File (ENSDF) database, which provides critically reviewed experimental results supplemented by systematic trend analyses and theoretical models. ENSDF contains comprehensive nuclear structure information including:

- Nuclear level properties (energy, half-life, spin/parity, decay modes)
- Gamma-ray characteristics (energies, intensities, multipolarities, conversion coefficients)
- Detailed radiation data for various emission types (α, β, γ, n)

Approximately 220 nuclides undergo full evaluation annually, with numerous partial updates. This effort is primarily supported by the U.S. Nuclear Data Program, coordinated by Brookhaven National Laboratory's National Nuclear Data Center for both evaluation and dissemination.

Unlike the computer-oriented ENDF-6 format which provides summarized data, ENSDF retains raw experimental values alongside evaluated results, resulting in a complex format that remains challenging to parse. Modernization efforts, including migration from ASCII to JSON, are underway, though no comprehensive tools currently exist for full data access.

Yet, the database is available via the IAEA's LiveChart API. Based on February 2023 cut-off, ENSDF contains 2491 ground states (see Table 5.1), with BrIcc estimates supplementing conversion electron data (*discrete electron* category).

Table 5.1.: Livechart API summary with cut-off from May 2025.

Radiation	Isotopes with rays[a]	Number of rays
γ	2162	128671
X-ray	1533	12775
α	684	2723
β^-	815	12601
β^+	797	13675
"discrete" $e^{-\dagger}$	1533	168062
β^- (BetaShape)	783	313181[‡]
β^+ (BetaShape)	612	250907[‡]

[a] Not distinguishing the isomers
† Conversion and Auger electrons
‡ Number of bins

5.1.2. ENDF6 Decay Sub-libraries

Among the various files comprising the ENDF6 format, File 8 specifically contains the decay data sub-library.

The main distributors of such sub-libraries are the JEFF [82][1], the ENDF/B [81][2], and the JENDL [92][3]. However, there exist some more restrictive or specialised databases, such as the European Activation File (EAF) [133][4], the FENDL [118][5], the International Reactor Dosimetry and Fusion File (IRDFF) [134][6], the United Kingdom Heavy Decay Data (UKHEDD)/United Kingdom Product Decay Data (UKPADD) [135][7], and the WIND [136][8], amongst others.

All aforementioned databases are accessible via the IAEA Nuclear Data Services (NDS) website[9], with key statistics summarised in Table 5.2.

The evaluated nuclear data cover 4219 isotopes (including 3337 ground states) and document 27 distinct decay modes. Focusing specifically on the most recent major evaluations –JENDL-5, ENDF/B-VIII.1, and JEFF-3.3 – these provide complete decay data for 3281 ground states and 833 excited isomeric states, characterised by 25 decay modes.

Data Inconsistencies. The comparative analysis of nuclear databases reveals several issues, ranging from simple parsing errors to more fundamental data representation problems.

Neutrino Spectrum Classification. While the ENDF-6 format specification provides distinct neutrino spectrum designations (`STYP = 10/11`), current evaluations still categorise neutrino emissions under β-decay spectral type (`STYP = 1/2`).

[1] A. J. M. Plompen et al. 'The joint evaluated fission and fusion nuclear data library, JEFF-3.3'. en. In: *The European Physical Journal A* 56.7 (July 2020), p. 181. ISSN: 1434-601X. DOI: 10.1140/epja/s10050-020-00141-9.

[2] D. A. Brown et al. 'ENDF/B-VIII.0: The 8th Major Release of the Nuclear Reaction Data Library with CIELO-project Cross Sections, New Standards and Thermal Scattering Data'. In: *Nuclear Data Sheets*. Special Issue on Nuclear Reaction Data 148 (Feb. 2018), pp. 1–142. ISSN: 0090-3752. DOI: 10.1016/j.nds.2018.02.001.

[3] Osamu Iwamoto et al. 'Japanese evaluated nuclear data library version 5: JENDL-5'. In: *Journal of Nuclear Science and Technology* 60.1 (Jan. 2023). _eprint: https://doi.org/10.1080/00223131.2022.2141903, pp. 1–60. ISSN: 0022-3131. DOI: 10.1080/00223131.2022.2141903.

[4] L W Packer and J-Ch Sublet. *The European Activation File: EAF-2010 biological, clearance and transport libraries*. en. Tech. rep. CCFE-R (10)04. Culham Science Centre: Culham Centre for Fusion Energy, 2010, p. 46.

[5] G. Schnabel et al. 'FENDL: A library for fusion research and applications'. In: *Nuclear Data Sheets*. Special Issue on Nuclear Reaction Data 193 (Feb. 2024), pp. 1–78. ISSN: 0090-3752. DOI: 10.1016/j.nds.2024.01.001.

[6] A. Trkov et al. 'IRDFF-II: A New Neutron Metrology Library'. In: *Nuclear Data Sheets* 163 (Jan. 2020), pp. 1–108. ISSN: 0090-3752. DOI: 10.1016/j.nds.2019.12.001.

[7] R. J. Perry, C. J. Dean, and A. L. Nichols. 'Actinide, Activation Product and Fission Product Decay Data for Reactor-based Applications'. In: *Nuclear Data Sheets* 120 (June 2014), pp. 261–263. ISSN: 0090-3752. DOI: 10.1016/j.nds.2014.07.062.

[8] Enrico Sartori. 'Nuclear data for radioactive waste management'. In: *Annals of Nuclear Energy* 62 (Dec. 2013), pp. 579–589. ISSN: 0306-4549. DOI: 10.1016/j.anucene.2013.02.003.

[9] https://www.oecd-nea.org/dbforms/data/eva/evatapes/

This inconsistency is illustrated in Listing 5.1, showing ^{51}Cr data from ENDF/B-VIII.1. Despite ^{51}Cr undergoing pure electron capture (emitting neutrinos without β particles), its spectrum remains classified as `STYP = 2` rather than the physically correct `STYP = 11`. The distinction is maintained through the `RIS` parameter (set to 0 for no positron emission), which serves as a workaround rather than a proper solution.

Incomplete Spontaneous Fission Data. ENDF/B-VIII.1 documents spontaneous fission for only 128 isotopes (compared to 338 in NUBASE2020), with complete Q-value and energy data available for only 28 of them. This discrepancy stems primarily from missing experimental data on fission fragments.

While "light" isotopes contribute minimally (the average branching ratio below Americium is 8.4×10^{-5} %), the collective omission of hundreds of spontaneous fission channels can create substantial inaccuracies in full-system modelling—particularly for non-standard scenarios like exotic target irradiation or advanced fuel cycles—as the average branching is 32 %, with some channels at 100 %.

Listing 5.1: Excerpt of ^{51}Cr β decay spectrum (ENDF/B-VIII.1) (JSON-ised)


```
"STYP": 2.0,
"LCON": 0, "LCOV": 0,
"NER": 2,
"FD": 1.0, "dFD": 0.0,
"ERAV": 0.0, "dERAV": 0.0,
"FC": 0.0, "dFC": 0.0,
"discrete": {
    "energysec": {
        "1": {
            "ER": 432496.5, "dER": 240.0003,
            "NT": 6,
            "RTYP": 2.0,
            "TYPE": 1.0,
            "RI": 0.0994, "dRI": 0.0005,
            "RIS": 0.0, "dRIS": 0.0
        }, "2": {
            "ER": 752580.0, "dER": 240.0,
            "NT": 6, "RTYP": 2.0,
            "TYPE": 1.0,
            "RI": 0.9006, "dRI": 0.0005,
            "RIS": 0.0, "dRIS": 0.0
        }
    }
}
```


5.1.3. NUBASE

The Atomic Mass Evaluation (AME) Project, which provides comprehensive nuclear mass data, began consolidating its evaluations into a unified publication starting in 1983. With the 1993 update, the Nuclear DataBase (NUBASE) database was created

Table 5.2.: List of ENDF6 Decay Databases with MF=8, MT=457.

Name	Author(s)[†]	Latest[‡] evaluation year	Number of entries	Number of ground states	Number of channels	Number of decay modes
decay2020[a]	Mix[b]	2018	4035	3238	5699	22
decay2012[a]	Mix[b]	2010	3875	3107	5470	22
EAF-2010	Mix[c]	2009	2222	1744	2794	16
ENDF/B-VIII.1[d]	**NNDC**	**2018**	**3821**	**3083**	**5457**	**20**
ENDF/B-VIII.0	NNDC	2018	3821	3083	5457	20
ENDF/B-VII.1	BNL/NNDC	2007	3821	3083	5458	20
ENDF/B-VII.0	BNL	2006	3838	3104	5326	19
ENDF/B-VI.8	INEL/LANL	1990	979	805	1463	7
FENDL-2.0	NEA	1983	1569	1179	1928	10
IRDFF-II	IAEA	2015	90	61	115	3
IRDFF-2002	IAEA	2015	85	58	110	3
JEFF-4.0	**CEA/ENSDF**	**2025**	**3852**	**3084**	**5546**	**23**
JEFF-3.3	CEA/ENSDF	2017	3852	3084	5546	23
JEFF-3.1.1	CEA/ENSDF	2007	3852	3084	5545	23
JEFF-3.1	CEA/ENSDF	2005	3852	3084	5568	23
JENDL-5	**ENSDF**	**2022**	**4071**	**3274**	**5634**	**22**
JENDL-DDF15	JAEA	2015	2993	2343	4309	13
JENDL-FPD-2011	JAEA	2013	1142	890	1682	5
JENDL-FPD-2000	JAEA	2000	1087	890	1405	5
UKHEDD-2.6[d]	WTC	2004	125	111	187	7
UKHEDD-2.4	WTC	2004	125	111	187	7
UKPADD-6.12	WTC	2012	595	401	792	7
UKPADD-6.11	WTC	2012	593	399	790	7
UKPADD-6.10	WTC	2010	589	396	785	7
UKPADD-6.9	WTC	2009	582	392	773	7
UKPADD-6.8	WTC	2008	573	388	762	7
UKPADD-6.5	WTC	2005	521	358	696	7
UKPADD-6.1	WTC	2000	456	317	615	7

[†] Or greatest contributor from `[1][451][ALAB]`

[‡] Considering `[1][451][EDATE]/[RDATE]` or `[1][451][DDATE]`

[a] Released by `FISPACT-II` team (adviced to be used by FENDL evaluators)

[b] Merge of mostly JEFF then ENDF/B (and ENDF/A), UKPADD (and UKHEDD) and CULHAM, and EAF

[c] Merge of mostly JEFF then ENDF/B (and ENDF/A), UKPADD (and UKHEDD) and CULHAM

[d] Format update mostly

to ensure consistent treatment of isomeric states and was first published in 1997 [137][1]. This database includes not only nuclear masses but also decay modes, branching ratios, and total available energy—key properties for radionuclide tracking.

Since its initial 1997 release (3891 isotopes, 3010 ground states), NUBASE has expanded significantly, with the 2020 edition containing 5565 isotopes, 3558 ground states, and 43 unique decay modes (see Table 5.3 for full historical data).

Table 5.3.: Summary of NUBASE channels.

Version†	Number ‡ of entries	Number of ground states	Number of channels	Number of § decay modes
2020	5565	3558	8736	43
2016	5346	3436	8237	42
2012	5202	3379	7811	31
2003	4366	3179	6413	42
1997	3891	3010	5679	39

† NUBASE is merged, with its associated AME except for 1997 version which is merged with the AME1995

‡ Only ground and isomeric states are listed, no IAS or resonance levels

§ Cluster decays, as ^{14}C or ^{28}Mg+^{30}Mg, are counted, but electronic capture and positron emission are accounted as one mode.

5.1.4. RIPL

The RIPL serves as a curated compilation of nuclear level schemes, primarily derived from ENSDF data and supplemented with information from NUBASE. The library employs sophisticated completion methods:

- Missing spins are reconstructed using statistical spin distributions based on known levels
- Unmeasured Internal Conversion Coefficients (ICC) are calculated using available or inferred spin values
- Non-electromagnetic decay modes are included when experimental data exists

The current RIPL-3.23 release contains comprehensive data for 3557 ground states (RIPL excludes the neutron, hence has one less entry than NUBASE2020) and documents an extensive collection of 177422 nuclear levels. This represents one of the most complete sets of evaluated nuclear structure parameters available for theoretical modeling and reaction calculations.

[1] G. Audi. 'The History of Nuclidic Masses and of their Evaluation'. en. In: *International Journal of Mass Spectrometry* 251.2-3 (Apr. 2006). arXiv:physics/0602050, pp. 85–94. ISSN: 13873806. DOI: 10.1016/j.ijms.2006.01.048.

5.2. Generation of the decay database

As highlighted in section 5.1, current evaluated decay data exhibit notable inconsistencies in both coverage and alignment with reference databases such as NUBASE and ENSDF. These inconsistencies include missing isotopes and decay channels, which can significantly impact the accuracy and reliability of nuclear data modelling. Additionally, issues identified in subsection 5.1.2 can be addressed through supplementary estimations and trend studies, underscoring the need for a more comprehensive and precise decay database.

The gaps in coverage have profound implications for modelling tools like `FISPACT-II` and `TMX_Bateman`, which are unable to follow isotopes lacking associated decay files. This limitation effectively excludes most isomeric states, despite their documented presence in NUBASE (subsection 5.1.3). For critical applications such as fission or neutron-induced reactions, these omissions can lead to substantial inaccuracies in inventory calculations, thereby necessitating the development of an improved decay database.

This section describes the development of an enhanced decay database designed to:

- Prioritise the inclusion of missing isomers and decay channels.
- Rectify spectral misclassifications, such as the disentanglement of ν_e from $\beta^{\pm}$ emissions.
- Ensure compatibility with major simulation workflows to bolster the precision of nuclear data modelling.

This new decay sublibrary will be termed the Global and Extensive Nuclear File or GENF/D.

The methodology employed will follow that of JEFF-3.1, involving the creation of a skeleton sub-library based on NUBASE and its expansion using ENSDF data. Additional evaluations will be conducted using tools such as BetaShape and BrIcc, which are part of the ENSDF Analysis and Utility Programs maintained by the NSDD network, as well as the GEF code.

5.2.1. Procedure Summary and Tools

A Pythonic toolbox has been developed to handle the relevant data and to offer an interface for all databases and code outputs of interest. The environment is built on the IAEA's `endf_parserpy` package [124][1], together with the pandas [138][2] and pint (for uncertainty propagation) [139][3] packages.

The raw data is processed in several stages to produce a full and valid ENDF6 formatted decay sublibrary:

[1] Georg Schnabel, Daniel Lopez Aldama, and Roberto Capote. *How to explain ENDF-6 to computers: A formal ENDF format description language.* Dec. 2023.

[2] The pandas development team. *pandas-dev/pandas: Pandas.* Aug. 2025. DOI: 10.5281/zenodo.16918803.

[3] Hernan E. Grecco et al. *Pint: a Python units library.* 2015.

Step 1: Conversion of NUBASE2020 to an ENDF-6 decay library, supplemented with RIPL-3.23 spin estimates.

Step 2: Implementation of decay spectra from ENSDF, accessed via the IAEA LiveChart API, supplemented with BetaShape and BrIcc estimates.

Step 3: Implementation of Spontaneous Fission (SF) Q-values and associated neutron and photon spectra from the GEF code.

The Figure 5.1 illustrates these steps in a general flowchart.

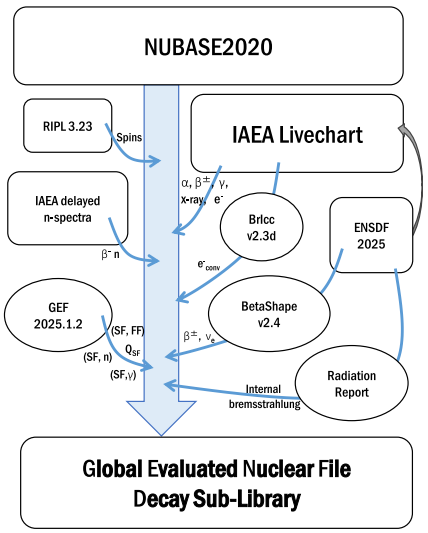

Figure 5.1.: Flowchart of data source for GENF/D generation

Parsed databases. The library is constructed using the NUBASE/AME 2020 database as its core source. Spin values are updated with those from RIPL-3.23 when available. A Python parser was created for both, using raw data files. Additional nuclear structure data is integrated through API-extracted ENSDF datasets, along with compiled delayed neutron spectra from the works of [140][1] and [141][2].

Beta and neutrino spectra For decades, the estimation of beta spectra for nuclear data evaluations has primarily relied on the `LogFT` code. Although capable of handling beta and electron capture transitions and propagating uncertainties from input parameters, `LogFT` used simple analytical models to ensure fast calculations, which led to a lack

[1] J. Liang et al. 'Compilation and Evaluation of Beta-Delayed Neutron Emission Probabilities and Half-Lives for Z > 28 Precursors'. In: *Nuclear Data Sheets* 168 (Sept. 2020), pp. 1–116. ISSN: 0090-3752. DOI: 10.1016/j.nds.2020.09.001.

[2] M. Birch et al. 'Evaluation of Beta-Delayed Neutron Emission Probabilities and Half-Lives for Z = 2–28'. In: *Nuclear Data Sheets* 128 (Sept. 2015), pp. 131–184. ISSN: 0090-3752. DOI: 10.1016/j.nds.2015.08.002.

of precision, particularly in screening effect corrections and shape factors for forbidden transitions.

To overcome these limitations, the BetaShape code was developed. BetaShape brings improved physical models, a database of experimental shape factors, and provides more detailed information such as beta and neutrino spectra. BetaShape is a code developed by the Laboratoire National Henri Becquerel (LNHB/CEA) to compute beta decays with the goal to improve theoretical predictions of beta decays, electron capture, neutrinos and capture probabilities. The programme also calculates beta and neutrino energies, together with log-ft values for each transition. It includes an analytical screening correction, which leads to satisfactory results above a few keV, but lacks of precision at very low energies for an accurate description of the beta spectrum. From version 2.3, more accurate atomic effects are included (via extensive tabulation of numerical solving): screening, exchange, overlap [22][1]. BetaShape version 2.2 was used by the Livechart API maintainers, using default parameters. In this work, the version 2.4 has been used together with the ENSDF data as of May 2025, as present in the IAEA Livechart. The default parameters have also been systematically used.

BetaShape is specifically used to produce the continuous β spectra, the average energy, and the positron emission rate.

Internal conversion factors BrIcc, distributed by the Australia National University (ANU), allows the computation of theoretical coefficients for internal conversion electrons (ICC), electron-positron pair conversion coefficients (IPC), and electronic factors Ω(E0) for nuclear transitions of pure or mixed multipolarity. BrIcc leverages state-of-the-art theoretical models to provide reliable calculations of these coefficients.

The code employs a self-consistent relativistic Dirac-Fock (DF) approach, representing a significant advancement in theoretical precision, with results now rivalling experimental accuracy at the percent level. Comparisons with experimental data demonstrate superior agreement with BrIcc's DF-based calculations compared to older tabulations such as HsIcc (Hager and Seltzer) and RpIcc (Rösel et al.). The default implementation, BrIccFO, incorporates the *frozen orbital approximation* to account for atomic vacancies during conversion processes, showing better alignment with experiments than the *no-hole approximation* (BrIccNH) [132][2]. Adopted internationally by the NSDD network, BrIcc is now the standard tool for new evaluations in *Nuclear Data Sheets* and *Nuclear Physics A* [142][3]. It spans broad transition energy ranges (1–6000 keV for ICC;

[1] Xavier Mougeot. 'Atomic exchange correction in forbidden unique beta transitions'. In: *Applied Radiation and Isotopes* 201 (Nov. 2023), p. 111018. ISSN: 0969-8043. DOI: 10.1016/j.apradiso.2023.111018.

[2] T. Kibédi et al. 'Evaluation of theoretical conversion coefficients using *BrIcc*'. In: *Nuclear Instruments and Methods in Physics Research Section A: Accelerators, Spectrometers, Detectors and Associated Equipment* 589.2 (May 2008), pp. 202–229. ISSN: 0168-9002. DOI: 10.1016/j.nima.2008.02.051.

[3] T. Kibédi et al. 'Internal conversion coefficients - How good are they now?' en. In: *ND2007*. Nice, France: EDP Sciences, 2007, p. 017. DOI: 10.1051/ndata:07771.

Table 5.4.: `BrIcc` default mixing ratio, when no mixing ratio is given [132]

Multipolarity	Mixing ratio
E2/M1	1.0
M2/E1, M3/E2, E4/M3, M4/E3, E5/M4	0.1
E3/M2	1.0

1100–8000 keV for IPC) and atomic numbers ($Z = 5$–110), exceeding the scope of earlier tabulations. Additionally, BrIcc systematically evaluates conversion coefficient uncertainties by incorporating theoretical errors, transition energy uncertainties, and mixing ratio uncertainties.

The version 2.3d of BrIcc slave program has been ran, with default parameters (e.g. Frozen Orbital approximation, or using Table 5.4 for missing mixing ratios), using the gamma information available in the Livechart API. Compared to the total coefficients already available through the Livechart, some deviations have been identified but none greater than 4%.

Internal bremsstrahlung The RadiationReport Java programme is among the code recommended by the NSDD network and part of the ENSDF Analysis and Utility Programs, as BetaShape and BrIcc. It allows the calculation of energies, intensities and doses of all radiations as well as log-ft values for a decay dataset. It is an alternative to the RADLIST and LogFT Fortran codes combined. This code has been run in order to obtain the internal bremsstrahlung continuous spectrum not available through the Livechart API.

The version released in April 2025 have been used in this work, and as for BetaShape rerun, the ENSDF files as of May 2025 were used as inputs. The default parameters have been systematically used.

Conversion electron. If conversion electron can be predicted by this tools, the atomic data used for GENF/D are evaluated data present through the API: with the atomic shell transition yields from [143][1] and atomic shell energies from the Evaluated Atomic Data Libraries EPICS2023 [144][2]

Spontaneous fission The GEF model (*GEneral description of Fission observables*) is designed to deliver a comprehensive and self-consistent description of fission observables for spontaneous fission, neutron-induced fission, and compound-nucleus fission across

[1] E. Schönfeld and H. Janßen. 'Calculation of emission probabilities of X-rays and Auger electrons emitted in radioactive disintegration processes'. In: *Applied Radiation and Isotopes* 52.3 (Mar. 2000), pp. 595–600. ISSN: 0969-8043. DOI: 10.1016/S0969-8043(99)00216-X.

[2] D.E. Cullen. *EPICS2023: August 2023 Status Report*. en. Tech. rep. Vienna: IAEA Nuclear Data Section, Aug. 2023. DOI: 10.61092/iaea.cfw1-fws6.

arbitrary entrance channels, over a wide range of excitation energies and angular momentum states. Designed to supply nuclear data for reactor technology and engineering applications, GEF covers an extensive isotopic range ($Z = 80$ to 112 and beyond) and excitation energies up to ∼100 MeV, including multi-chance fission processes.

The GEF code employs a Monte-Carlo framework to simulate fission dynamics while preserving correlations between observables, offering critical insights into the fission process. Unlike empirical models that directly parametrise observables, GEF integrates approximations rooted in microscopic system properties, with parameters globally optimised to minimise deviations from experimental data. This physics-based approach ensures robust predictive power for nuclei near experimentally characterised cases, though localised structural effects may introduce exceptions. The model successfully reproduces key features such as delayed neutron probabilities – linked to fragment yields and excitation energies – and provides detailed predictions for total kinetic energy (TKE) distributions as functions of fragment mass. By combining general physical principles with empirical constraints, GEF achieves superior predictive accuracy and evaluative capability compared to alternative methods, enabling reliable extrapolations for unmeasured fission quantities across a broad range of nuclei.

One should note that, GEF does not include ternary fission.

This code was chosen over other codes, such as FREYA [145][1] or FIFRELIN [146][2], as it allows to directly obtained an ENDF-6 formatted output for fission fragment list, as well as access to the secondary spectra (neutron, photons, fission fragments energy). Further motivations are available in the validation subsubsection a.

The latest version (2025.1.2) has been used for this project. In addition, a nuclear property table and branching table have been generated based on GENF/D to ensure consistency in the excited states, and for the cumulative yields generation.

5.2.2. Step 1: Generation of basic ENDF6 database.

The NUBASE/AME database contains:

- mass excess;
- isomer excitation energy;
- half-life;
- spin and parity;
- decay modes and their intensities;
- atomic mass;
- β^-, α, $2\beta^-$, $4\beta^-$, $\beta^- n$, e.c.+p available decay energy.

This is sufficient to define an ENDF6 library. However, some filtering and post-processing is necessary; see the raw data excerpt in Listing 5.2.

[1] J. M. Verbeke, J. Randrup, and R. Vogt. 'Fission Reaction Event Yield Algorithm FREYA 2.0.2'. In: *Computer Physics Communications* 222 (Jan. 2018), pp. 263–266. ISSN: 0010-4655. DOI: 10.1016/j.cpc.2017.09.006.

[2] Olivier Litaize, Olivier Serot, and Léonie Berge. 'Fission modelling with FIFRELIN'. en. In: *The European Physical Journal A* 51.12 (Dec. 2015), p. 177. ISSN: 1434-601X. DOI: 10.1140/epja/i2015-15177-9.

Isomeric states. First, only ground and excited isomeric states[1] are kept. 277 entries are ignored with this consideration.

It should be noted that energies can be negative due to the measurements uncertainties. In such a case, the RIPL methodology is applied, i.e. shifting the negative energy by its uncertainty, or alternatively flooring it to zero (if this last attempt was not successful). This happens for 9 excited isotopes, explicitly for: ^{91m}Ru, ^{124m}In, ^{154m}Pm, ^{152m}Tm, ^{164m}Re, ^{194m}At, ^{196m}At, ^{248m}Bk, ^{265m}Sg.

To give an example, the excitation energy of ^{91m}Ru is reported to be -340 ± 500 keV; it can be shifted to 160 keV.

Half-life. If an isotope has no half-life information, it is discarded. This happens for 63 radioisotopes (with 46 ground states). The majority of these radioisotopes, being close to the drip line, are subjected to quite different physics regimes, making an estimation of their half-life impossible. The ignored isotopes are listed in Appendix B.

Spin and parity. In the shell model, multiple spin values are allowed for nuclear states, following the rule explicited by [147][2]:

$$|j_p - j_n| \leq J \leq |j_p + j_n|$$

However, the ENDF6 format restricts spin to a single value.

To refine spin assignments, the RIPL project uses experimental spin distributions and statistical models [148, 149][3]. GENF/D prioritises these estimates.

Nevertheless, RIPL does not provide spin assignments for 607 isotopes. For these cases, NUBASE spins are used as a fallback. If NUBASE lists multiple spins (e.g., ^{10}Li with $(1^-, 2^-)$), the first value (1^-) is selected. The situation arise for 61 isotopes listed in Appendix B.

In the end, 249 isotopes have unknown spins.

Listing 5.2: Excerpt of NUBASE2020

```
001 0010   1H       7288.971064   0.000013                    stbl            1/2+*       06  1920
      ↪ IS=99.9855 78
003 0010   3H       14949.81090    0.00008                     12.32  y 0.02   1/2+*       00  1934 B-=100
003 0030   3Li      28670#       2000#                         p-unst          3/2-#       98       p ?
008 0048   8Be  i   21568          3       16626       3                       2+  frg T=1       2004 A-100
012 0030   12Li     49010         30                                           (1-,2-)     17  2008 n ?
012 0040   12Be     25077.8        1.9                         21.46 ms 0.05   0+          17  1966
      ↪ B-=100;B-n=0.50 3
012 0041   12Be m   27328.8        2.1       2251      1       233    ns 7     0+          17  2007 IT=100
024 0100   24Ne     -5951.6        0.5                         3.38   m 0.02   0+          07  1956
      ↪ B-=100[gs=0,m=100]
```

[1] Excited states up to 6th are registered in NUBASE, noted in order from m, n, p, q, r to x

[2] M. H. Brennan. 'jj Coupling Model in Odd-Odd Nuclei'. In: *Physical Review* 120.3 (1960), pp. 927–933. DOI: 10.1103/PhysRev.120.927.

[3] Torleif Ericson. 'The statistical model and nuclear level densities'. EN. in: *Advances in Physics* (Oct. 1960), p. 425. DOI: 10.1080/00018736000101239, A. Gilbert and A. G. W. Cameron. 'A Composite Nuclear-level density formula with shell corrections'. en. In: *Canadian Journal of Physics* 43 (Aug. 1965). DOI: 10.1139/p65-139.

```
035 0120   35Mg    15640        270                            11.3  ms 0.6    (3/2-,5/2-) 17  1989
      ↪ B-=100;B-n=52 46;B-2n ?
091 0441   91Ru m -68580        500        -340    500     BD*   7.6   s 0.8    (1/2-)      13  1983
      ↪ B+=100;B+p=?;IT ?
098 0391   98Y  m -72118          8         170.78   0.05       615    ns 8      2-          20  1972 IT=100
098 0392   98Y  n -71823          8         465.7    0.7    MD    2.32  s 0.08   (6,7)+      20  1977
      ↪ B-=100;IT ?;B-n=3.44 95
098 0393   98Y  p -71793          8         496.10   0.11       6.90 us 0.054  (4)-        20  1970 IT=100
098 0394   98Y  q -71695         13         594      10         180    ns 7      (3-,4-)         2017 IT=100
098 0395   98Y  r -71317          8         972.17   0.20       450    ns 150    (8+)        20  2017 IT=100
098 0396   98Y  x -71108          8        1181.50   0.18       762    ns 14     (10-)       20  1972 IT=100
230 0920   230U    31615         5                              20.23  d 0.02    0+          12  1948
      ↪ A=100;22Ne=4.8e-12 20;SF ?
230 0930   230Np   35240        60                               4.6   m 0.3     4+#         12  1968 B+<97;A>3
```

a) Decay channels.

The main difficulty of NUBASE conversion is the processing of decay modes and their intensities. Several not so straight-forward choices have been made, and presented in this section.

Decay modes. It should be noted that the ENDF6 format encodes the decay into a real number, called `RTYP`. Each emitted particle is associated with a digit, see Table 5.5. Multiple particle decay is encoded by adding significant digits e.g. a beta decay followed by an alpha emission is registered as 1.4. The delayed neutron emissions can be described in the same manner, e.g. marking 1.55 for a β^- emission followed by two delayed neutrons. In addition, ENDF6 format does not distinguish positron emission and electron capture (except when the beta spectrum is given, with `RIS` value), so the splitting indicated by NUBASE is ignored.

However, NUBASE presents decay modes that cannot be encoded directly into `RTYP`, such as "cluster decays", i.e. emission of ^{12}C, ^{14}C, ^{18}O, ^{20}Ne, ^{20}O, ^{22}Ne, ^{23}F, ^{24}Ne, ^{24}Ne+^{26}Ne, ^{25}Ne, ^{28}Mg, ^{28}Mg+^{30}Mg, ^{30}Mg, ^{32}Si, ^{34}Si.
Amongst all, only the ^{12}C channel is kept (with a maximum branching appearance of 0.0034 %) and translated using `RTYP`=4.44, meaning a 3α decay. The others cannot be described as easily but having a branching ratio lesser than 8.9×10^{-8} %, they can be ignored without much concern.

In addition, the deuterium and tritium emission are converted in their $2p$ and $3p$ `RTYP` equivalents. Such translation is done for the $\beta^- + d$ channel of ^{6}He and ^{11}Li and the $\beta^- + t$ one of ^{6}He, ^{11}Li and ^{14}Be. This does not overlap with any $\beta^- + 2p$ and $\beta^- + 3p$, as they were not amongst already defined decay channels.

All decay modes of NUBASE and their translation into `RTYP` values are presented in Table 5.5.

Daughter nuclide isomeric states. It should be mentioned that the `RFS` flag, i.e. the value indicating the isomeric state for the daughter nuclide, is always set at 0. No information on daughter properties are given in NUBASE, except for a few of them (see ^{24}Ne in Listing 5.2): ^{24}Ne, ^{77}Ga, ^{90}Nb, ^{109n}In, ^{114n}In, ^{116n}In, ^{118n}In, ^{124n}Sb, ^{126n}Sb, ^{148n}Ho, ^{150n}Tm, ^{124n}Sb. For these 14 isotopes, the `RFS` was explicitely defined and not automatically extracted.

Table 5.5.: NUBASE decay mode translation matrix.

Decay mode	RTYP[†]	Description	Decay mode	RTYP	Decay mode	RTYP[‡]
B-	1	Beta decay	2B-	1.1	14C	Ø
B+	2	Electron capture and/or positron emission	B-A	1.4	18O	Ø
EC	2		B-n	1.5	20O	Ø
e+	2		B-2n	1.55	23F	Ø
EC+B+	2		B-3n	1.555	20Ne	Ø
IT	3	Isomeric transition	B-4n	1.5555	22Ne	Ø
A	4	Alpha decay	B-SF	1.6	24Ne	Ø
n	5	Neutron emission	B-p	1.7	25Ne	Ø
SF	6	Spontaneous fission	B-d	1.77	24Ne+26Ne	Ø
p	7	Proton emission	B-t	1.777	28Mg	Ø
␣	10	Unknown origin	2B+	2.2	30Mg	Ø
			B+A	2.4	28Mg+30Mg	Ø
			B+SF	2.6	32Si	Ø
			B+p	2.7	34Si	Ø
			B+pA	2.74		
			B+2p	2.77		
			B+3p	2.777		
			12C	4.44		
			2n	5.5		
			3n	5.55		
			2p	7.7		
			3p	7.77		

[†] Conversion table from ENDF6 manual [108][1]. Contrary to ENDF6 format, NUBASE distinguishes between pure electron capture, pure positron emission and mixed ratio.

[‡] These decays could be marked as unknown in GENF/D, but choice was made to totally ignored them.

Branching ratios. The ENDF6 format requires that the total branching ratio sums up to 100 %, at variance with NUBASE format. For example, for the decay of ^{11}Li, in NUBASE format, the decay channels are given as 100 % emission of β^+ and 86 % of β^+n emission, whereas ENDF6 indicates 14 % of β^+ and 86 % of β^+n, this typical case happens for 529 isotopes. After all such corrections and in any case, the sum of the partial branching ratios is systematically renormalised to 1.

This entails to know every branching for all accounted channels, which is not the case. Indeed, some channels indicated are energically allowed, but not experimentally observed[1], or observed but their intensity are not experimentally known[2].

Discarding the isotopes when no half-life is provided, over the 5248 unstable isotopes available, 1519 have at least one channel without branching. The main actions taken are categorised in the Table 5.6, the last column of this table giving one example for illustration. The different corrections are listed by priority. There are actually 793 nuclei that need renormalisation to obtain 100%. After the prompt emission was corrected, negative Q-value channel, and unknown decays are removed, and the positron/electron-capture splitting is merged.

Table 5.6.: Summary of conversion criteria. Actions ordered by the priority of application..

Action	Occurrence	Example
No action	4358	
Branching ratio set to 0, due to negative Q-value	28	^{224}Th
Removal of channel, due to decays forbidden by the format (cluster decays)	22	^{224}Ra
Uncertain branching (with > or < mention) reduced to obtain 100%	113	^{94m}Tc
One mode only, BR set to 100%	176	^{42}V
Increase of isomer transition branching	113	^{60m}V
All channels with unknown branching, uniform distribution of BR	63	^{169}Au
Uniform distribution of BR to rise to 100%	22	^{175}Au
Global renormalisation of BR to obtain 100%	159	^{176}Lu

In Figure 5.2, the main decay modes available in this library are summarised, not representing the isomeric excited states.

b) Available decay energy.

To produce a minimal decay sub-library, only energetics considerations are lacking. The estimation of average energy, for heat application will be explicited in subsection 5.2.5, as the generation is rather empiric.

[1] Is indicated as $\alpha_{\sqcup}$?
[2] Is indicated as α =?

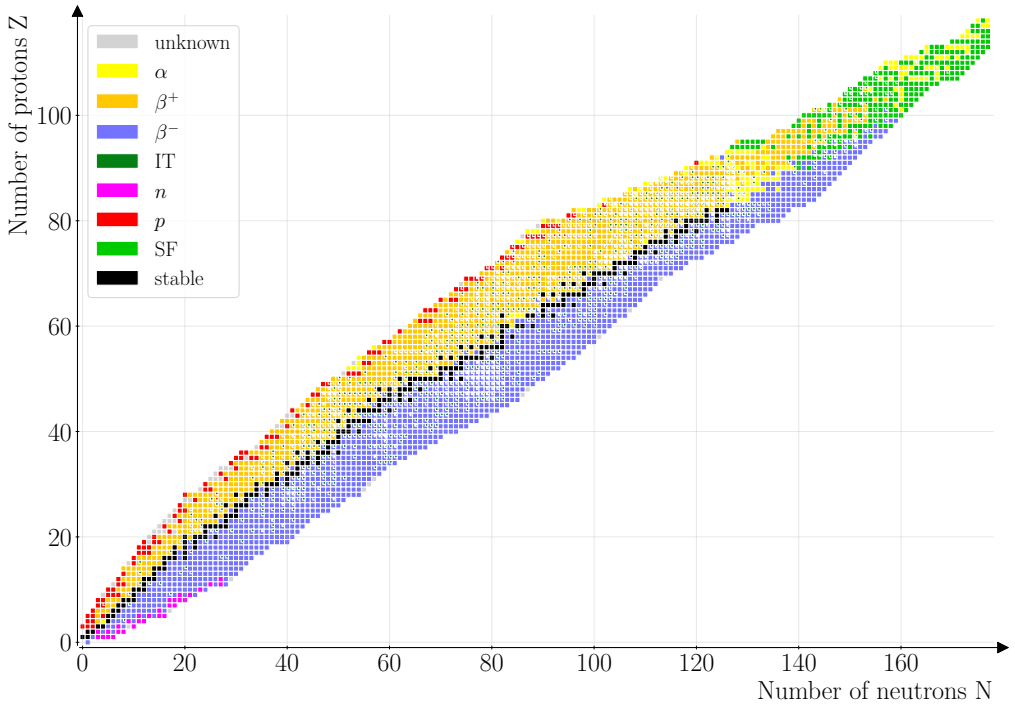

Figure 5.2.: Segrè diagram of available ground states and their main decay mode in the GENF decay sub-library

Q-value. To check for channel availability, as well as heat computation, careful attention must be given for Q-value computation. For a most accurate estimation, this database uses the Q-value computed from atomic masses of AME2020 database (part of NUBASE). The total available energy, for a decay channel, considering the conservation of energy E, is as follows:

$$Q = E(X_i) - \sum_f E(Y_f) \tag{5.1}$$

$$= M_{atm}(X_i)c^2 + E^*(X_i) - \sum_f \left(M_{atm}(Y_f)c^2 + E^*(Y_f) \right) \tag{5.2}$$

where E^* is the excitation energy, X_i the mother nuclide, Y_f the daughter products, and M_{atm} is the atomic mass defined by:

$$M_{atm}({}^A_Z X) = M_N({}^A_Z X) + Z \times m_e - B_e(Z)/c^2 \tag{5.3}$$

where A is the atomic mass number and Z the atomic number. An approximation of

electron binding energy, in electron-volt, is given by the empiric formula [17][1]:

$$B_e(Z) = 14.4381 \times Z^{2.39} + 1.55468 \times 10^{-8} \times Z^{5.35} \tag{5.4}$$

There are 29 decay modes, described by the `RTYP` parameter, available in the generated sub-library, which are β^-, $2\beta^-$, $\beta^- + \alpha$, $\beta^- + n$, β^-+$2n$, β^-+$3n$, β^-+$4n$, β^-+SF, β^-+p, β^-+$2p$, β^-+$3p$, β^+, $2\beta^+$, $\beta^+ + \alpha$, β^++SF, $\beta^+ + p$, β^++p+α, β^++$2p$, β^++$3p$, IT, α, 3α, n, $2n$, $3n$, SF, p, $2p$, $3p$. The electron capture distinction for the β^+ (and extended) are the responsibility of the end-users.

As there is almost no mention of isomeric states of daughters, most Q-values computed in GENF/D consider the daughter at ground states, i.e $E^*(Y_f)$ is null in Equation 5.2. The eleven exceptions are ^{24}Ne, ^{77}Ga, ^{90}Nb, ^{109n}In, ^{114n}In, ^{116n}In, ^{118n}In, ^{124n}Sb, ^{126n}Sb, ^{148n}Ho and ^{150n}Tn.

The available energy for all decays in GENF/D are computed based on the raw definition of decay (and not using the `RTYP` alternative). Following the convention of other evaluated databases, β^+ available energy is rather the e.c. available energy:

$$E_{\beta^+} = Q_{ec} = M_{atm}\left({}^{A}_{Z}X\right) - M_{atm}\left({}^{A}_{Z-1}Y\right)$$

Here are listed all Q-values recomputed (the value for Q_{β^-} and Q_α from NUBASE, available directly, is preferred by GENF/D):

- $Q_{\beta^- xn}/c^2 = M_{atm}\left({}^{A}_{Z}\mathrm{X}\right) - M_{atm}\left({}^{A}_{Z+1}\mathrm{Y}\right) - x \times m_n$
- $Q_{\beta^- xp}/c^2 = M_{atm}\left({}^{A}_{Z}\mathrm{X}\right) - M_{atm}\left({}^{A}_{Z+1}\mathrm{Y}\right) - x \times M_{atm}\left({}^{2}_{1}H\right)$
- $Q_{\beta^- {}^2\mathrm{H}}/c^2 = M_{atm}\left({}^{A}_{Z}\mathrm{X}\right) - M_{atm}\left({}^{A-2}_{Z}\mathrm{X}\right) - M_{atm}\left({}^{2}_{1}H\right)$
- $Q_{\beta^- {}^3\mathrm{H}}/c^2 = M_{atm}\left({}^{A}_{Z}\mathrm{X}\right) - M_{atm}\left({}^{A-3}_{Z}\mathrm{X}\right) - M_{atm}\left({}^{3}_{1}H\right)$
- $Q_{\beta^- \alpha}/c^2 = M_{atm}\left({}^{A}_{Z}\mathrm{X}\right) - M_{atm}\left({}^{A-4}_{Z-1}\mathrm{Y}\right) - M_{atm}\left({}^{4}_{2}He\right)$
- $Q_{\beta^+}/c^2 = M_{atm}\left({}^{A}_{Z}\mathrm{X}\right) - M_{atm}\left({}^{A}_{Z-1}\mathrm{Y}\right)$
- $Q_{2\beta^+}/c^2 = M_{atm}\left({}^{A}_{Z}\mathrm{X}\right) - M_{atm}\left({}^{A}_{Z-2}\mathrm{Y}\right)$
- $Q_{\beta^+ xp}/c^2 = M_{atm}\left({}^{A}_{Z}\mathrm{X}\right) - M_{atm}\left({}^{A}_{Z-1}\mathrm{Y}\right) - x \times M_{atm}\left({}^{1}_{1}\mathrm{H}\right)$
- $Q_{\beta^+ \alpha}/c^2 = M_{atm}\left({}^{A}_{Z}\mathrm{X}\right) - M_{atm}\left({}^{A-4}_{Z-3}\mathrm{Y}\right) - M_{atm}\left({}^{4}_{2}\mathrm{He}\right)$
- $Q_{\beta^+ p\alpha}/c^2 = M_{atm}\left({}^{A}_{Z}\mathrm{X}\right) - M_{atm}\left({}^{A-5}_{Z-4}\mathrm{Y}\right) - M_{atm}\left({}^{4}_{2}\mathrm{He}\right) - M_{atm}\left({}^{1}_{1}H\right)$
- $Q_{xn}/c^2 = M_{atm}\left({}^{A}_{Z}\mathrm{X}\right) - M_{atm}\left({}^{A-x}_{Z}\mathrm{X}\right) - x \times m_n$
- $Q_{xp}/c^2 = M_{atm}\left({}^{A}_{Z}\mathrm{X}\right) - M_{atm}\left({}^{A-x}_{Z-x}\mathrm{Y}\right) - x \times M_{atm}\left({}^{1}_{1}\mathrm{H}\right)$

[1] W.J. Huang et al. 'The AME 2020 atomic mass evaluation (I). Evaluation of input data, and adjustment procedures*'. en. In: *Chinese Physics C* 45.3 (Mar. 2021), p. 030002. ISSN: 1674-1137, 2058-6132. DOI: 10.1088/1674-1137/abddb0.

- $Q_{^2\mathrm{H}}/c^2 = M_{atm}\left({}^{A}_{Z}\mathrm{X}\right) - M_{atm}\left({}^{A-2}_{Z-1}\mathrm{Y}\right) - M_{atm}\left({}^{2}_{1}\mathrm{H}\right)$
- $Q_{^3\mathrm{H}}/c^2 = M_{atm}\left({}^{A}_{Z}\mathrm{X}\right) - M_{atm}\left({}^{A-2}_{Z-1}\mathrm{Y}\right) - M_{atm}\left({}^{3}_{1}H\right)$
- $Q_{^{12}\mathrm{C}}/c^2 = M_{atm}\left({}^{A}_{Z}\mathrm{X}\right) - M_{atm}\left({}^{A-12}_{Z-6}\mathrm{Y}\right) - M_{atm}\left({}^{12}_{6}\mathrm{C}\right)$
- $Q_{SF}/c^2 = M_{atm}\left({}^{A}_{Z}\mathrm{X}\right) - \sum y_i \times M_{atm}\left(\mathrm{Y}_i\right)$, with $\sum y_i = 2$
- $Q_{IT} = E^*\left({}^{A}_{Z}\mathrm{X}\right)$

Of course, the spontaneous fission available energy can only be computed after having run subsection 5.2.4.

RIPL shift. Some decay channels have nonetheless negative values, the same principle for negative excitation energies mentionned in paragraph 5.2.2. There are 13 isotope with issue with Q-values, listed in Appendix B.
For example, the $Q_{\beta^- n}$ of ^{55}Ti given in NUBASE2020 is -6 ± 31 keV, this channel is therefore raised to 25 keV. The flooring to zero was only necessary for ^{154m}Pm.

This procedure produces the minimum required information to track a radionuclide inventory. The description of each file (MF=1/MT=451) gives the raw information from NUBASE in case of doubt on data.

5.2.3. Step 2: Insertion of decay spectra.

If the previous step could be sufficient for simple inventory tracking, for radioprotection and heat estimation, one should register the expected decay spectra. The format allows to indicate dicrete and continous spectra for γ, β^-, β^+, α, neutrons, spontaneous fission, protons, "discrete" electrons (including conversion and Auger electrons), X-rays (and annihilation radiation), neutrinos and anti-neutrinos (electron).

Livechart provides the α, β, γ, X-rays and discrete electrons (conversion and Auger). The main source is the ENSDF archive as of May 2025, with the atomic shell transition yields from [143][1] and atomic shell energies from EPICS2023.

The annihilation rays can be simply deduced from positron emission rate.

If displayed, the internal brehmstrahlung spectra, and delayed particle spectra (protons, neutrons, alpha) cannot be obtained via the webaccess.

The former can be obtained using the RadiationReport utility from NDSS [23][2], but this workflow will not be added to the generation of GENF/D. As for delayed particles,

[1] E. Schönfeld and H. Janßen. 'Calculation of emission probabilities of X-rays and Auger electrons emitted in radioactive disintegration processes'. In: *Applied Radiation and Isotopes* 52.3 (Mar. 2000), pp. 595–600. ISSN: 0969-8043. DOI: 10.1016/S0969-8043(99)00216-X.

[2] Jun Chen. *IAEA-NSDDNetwork/RadiationReport*. original-date: 2022-08-25T19:42:34Z. Apr. 2025.

only the neutron delayed spectra are extracted using the data of the compilation of [140][1] and [141][2].

a) Linkage between isomeric states.

Before mentioning any procedure of appending spectra to GENF/D, correct correspondance between isotopes must be done. If for ground states, the issue is non-existent, excited isomers must be treated with care, as the excitation energy and level index may not correspond. Indeed, the ENSDF does not always quantify the excited levels and will give them as floating levels, but estimated values are always provided in NUBASE.

Connection. There is not a single procedure to create the bridge between the two database. In the case, that no floating point are given in ENSDF, the level are recognised by distance. When floating point exists, the levels will be recognised through the energy shift in priority. The association is also validated against half-life.

For example, with ^{102}Y, which has two entries in NUBASE, and 11 levels registered in NUBASE with two energy shift '+X' and '+Y'

LIS and LISO. The ENDF6 distinguishes the state of the nuclide (excitation state), marked as `LIS`, and the isomeric state number of the nuclide, marked as `LISO`. During the procedure explained in subsection 5.2.2, these two notions have been merged, as there are no listings of levels structure in NUBASE. With the access to ENSDF, the level structure of isotopes is made available, the `LIS` flag is therefore updated.

To link GENF/D and Livechart data, respectively, the `ELIS` and the `p_energy` values are checked. Exact correspondance cannot be always obtained as NUBASE does averaging of the different sources that they considers, but exact match ammounts to 93.6 % of all spectra subsets (spectra splitted per type and mother level energy).

Therefore, the energies are either exactly matched, considering uncertainty, or within 5 %. One can update 3199 isotopes of GENF/D, of which 12 needs care when updating the spectra. Indeed if 3187 have a one to one association, for 12, several excited levels of Livechart correspond to a single level of GENF/D.

Treatement of multiple associated levels. Those 12 isotopes are ^{130p}In, ^{143m}Gd, ^{145m}Gd, ^{150m}Tb, ^{151m}Tb, ^{156m}Tb, ^{176m}Au, ^{191m}Hg, ^{195m}Hg, ^{194m}Tl, ^{215m}Bi, ^{234m}Pa. For them, the multiple spectra are added to their associated GENF/D decay file.

For example, ^{130p}In has four isomeric levels according to ENSDF: 0 keV, 50 keV, 388.3 keV and 400 keV. Whereas, NUBASE20 considers four levels at 0 keV, 66.5 keV

[1] J. Liang et al. 'Compilation and Evaluation of Beta-Delayed Neutron Emission Probabilities and Half-Lives for Z > 28 Precursors'. In: *Nuclear Data Sheets* 168 (Sept. 2020), pp. 1–116. ISSN: 0090-3752. DOI: 10.1016/j.nds.2020.09.001.

[2] M. Birch et al. 'Evaluation of Beta-Delayed Neutron Emission Probabilities and Half-Lives for Z = 2–28'. In: *Nuclear Data Sheets* 128 (Sept. 2015), pp. 131–184. ISSN: 0090-3752. DOI: 10.1016/j.nds.2015.08.002.

(M), 385.4 keV (N) and 388.3 keV (P). When linking both database, the issues arise for the 400 keV level of ENSDF which is associated both with 385.4 keV and 388.3 keV of GENF/D. Any decay which comes from the a mother at 400 keV will be added to the decay file of the N and the P isomeric states. Evidently, the decay spectrum of ENSDF 388.3 keV will only be added to the P state of GENF/D as it was an exact match, even if according to the uncertainty acceptance range rule the N state could have been also updated.

b) γ spectrum

The gamma rays energy and intensities are obtained from ENSDF.The theoretically predicted but not experimentally observed γ, which have an undefined intensity are kept, with a null intensity.

Internal conversion. If the structure of the ENDF6 spectrum section is consistent across all radiation types, the gamma spectra must also indicate the internal conversion coefficients: total, as well as for K- and L-shells. This phenomenon is associated with the probability of the relaxation gamma interacting with the electronic configuration of the atom and knocking one of its electrons.

The coefficients can be, and have been, computed using the BrIcc code.

If the Livechart API maintainers have made the `RICC`, RICK and `RICL` coefficients available, the uncertainties are not. Therefore the programme (in its slave version) was run again during the production of GENF/D. To produce a results, BrIcc requires the transition energy, the multipolarity as well as mixing ratio.

For them, the Livechart values are used, and any NaN values are set to 0 when unknown uncertainties are set to 100 %.

Internal Brehmstrahlung. If the Internal Brehmstrahlung is available through the web interface, it is not available via the API. To generate this theoretical spectra, RadiationReport programme can be used. This code takes an ENSDF file in input, hence the programme was run using the archived ENSDF files of May 2025[1] to be consistent with LiveChart API data.

By running RadiationReport on the 300 ensdf raw files, one can produce 1826 of such continuous gamma spectra (histogram representation) in addition to the discrete rays available in the API.

c) α spectrum

It should be noted that the α considered as delayed particle are not part of those spectras.

Not all isotopes emitting α particles have an associated spectrum. Among the X with missing description, Y have gamma rays information. One could give an estimates of the

[1] https://www.nndc.bnl.gov/ensdfarchivals/distributions/dist25/ensdf_250501.zip

alpha spectra based gamma energy, as the conservation law of energy and momentum of such decay can simply expressed as in Equation 5.5.

$$T_\alpha = \frac{M_{nucl}(Y)}{M_{nucl}(Y) + M_{nucl}(\alpha)} (Q_\alpha - E_Y^* - E_\alpha^*) \tag{5.5}$$

where Y is the daughter isotope, Q_α the available decay energy, T the kinetic energy, M_{nucl} the nuclear mass and E^* the excitation energy. We can consider that $E_Y^* = E_\gamma$, with E_γ the gamma ray energy. This approach was not yet implemented in GENF/D.

d) β and ν spectra

The beta decay produces two particles: in addition to the daughter nuclide, a β particle and (anti-) neutrino are produced. The evaluators usually measure the β end-point energy, and use a theoretical model to deduce the spectra chararacteritics, due to the complexity to measure such spectra.

The legacy approach was to use LogFT through RADLST, since then a new model BetaShape has been recommended by the NSDD Network.

Therefore, the Livechart API provides the two datasets: the LogFT as well as the BetaShape estimates. However, BetaShape version 2.4 was rerun independently (without using the results from the Livechart maintainers, which were based on version 2.2) because it includes more accurate atomic effects. These improvements were achieved through extensive tabulation of numerical solutions, addressing screening, exchange, and overlap effects [22][1]. The same files as for RadiationReport in paragraph b were used.

Default parameters were consistently used throughout the additional generation. This meant that the NUBASE20 Q-value was used rather than the end-point energy present in the raw ENSDF files, consequently ensuring consistency with the GENF/D generation approach.

LogFT vs BetaShape. When available the data of BetaShape is always prioritised. Yet for N isotopes, the original data is used. One should not that the discrete ray description is used, and ray energy corresponds to the max energy of transition and not their average energy.

In the case of BetaShape spectra, the continuous description of ENDF6 format does not allow to separate the transitions, hence only the total spectrum is given.

[1] Xavier Mougeot. 'Atomic exchange correction in forbidden unique beta transitions'. In: *Applied Radiation and Isotopes* 201 (Nov. 2023), p. 111018. ISSN: 0969-8043. DOI: 10.1016/j.apradiso.2023.111018.

Separation of β and ν. The previous versions of ENDF-6 format, as [150][1], described in the β spectra section both the charged particle (e^+, e^-) and the neutrino (or anti-neutrino). According to the 2018 update of the format [151][2], the neutrino part can be removed from the spectra related to beta decay and placed in the dedicated section (STYP=10 or 11). This distinction has been applied within GENF/D.

It means that capture only isotopes will only have a neutrino spectrum entry.

e) Discrete electron spectrum

The discrete rays available in the LiveChart correspond to the Auger and Conversion electrons.

They are theoretically estimated rays. Specifically for conversion electrons, the energies set in GENF/D are the ones averaged over the contributing sub-shells and were calulated, by the API maintainers, using the BrIcc programme.

f) Delayed particles spectra

As mentioned the API only makes available the prompt radiations (and discrete electrons). In its current version, the delayed particle spectra can be displayed on the web interface, but are not available through API requests.

In the GENF/D version from subsection 5.2.2, and not considering delayed fission and xp, xn channels, there are 1426 channels with delayed particles. If we consider only non-null branching ratio, there are 607 delayed channels, detail is given in Table 5.7.

Delayed neutrons. Alternatively, the IAEA distributes some of the known delayed neutron spectra, in two compilations [141][3] and [140][4]. These compilations provide spectra for 44 isotopes. They have been implemented in GENF/D.

5.2.4. Step 3: Addition of spontaneous fission properties

In the last step, the Q-value of spontaneous fission (SF) is computed, as well as the spectra of neutrons, photons and fission fragments. Only a few experimental data is available in ENDF-6 format, with only ten evaluated spontaneous fission fragment lists released altogether in ENDF/B, JEFF and JENDL.

[1] M. Herman. *ENDF-6 Formats Manual Data Formats and Procedures for the Evaluated Nuclear Data File ENDF/B-VI and ENDF/B-VII*. English. Tech. rep. BNL–90365-2009. Brookhaven National Laboratory (BNL) National Nuclear Data Center, June 2009. DOI: 10.2172/981813.

[2] Andre Trkov and David A. Brown. *ENDF-6 Formats Manual: Data Formats and Procedures for the Evaluated Nuclear Data Files*. English. Tech. rep. BNL-203218-2018-INRE. Brookhaven National Laboratory (BNL), Upton, NY (United States), Jan. 2018. DOI: 10.2172/1425114.

[3] M. Birch et al. 'Evaluation of Beta-Delayed Neutron Emission Probabilities and Half-Lives for Z = 2–28'. In: *Nuclear Data Sheets* 128 (Sept. 2015), pp. 131–184. ISSN: 0090-3752. DOI: 10.1016/j.nds.2015.08.002.

[4] J. Liang et al. 'Compilation and Evaluation of Beta-Delayed Neutron Emission Probabilities and Half-Lives for Z > 28 Precursors'. In: *Nuclear Data Sheets* 168 (Sept. 2020), pp. 1–116. ISSN: 0090-3752. DOI: 10.1016/j.nds.2020.09.001.

Table 5.7.: Delayed decay channels with non-null branching in GENF/D.

Decay	Number of non-null channels	Number of channels
$\beta^- + n$	324	704
$\beta^- + 2n$	32	327
$\beta^- + 3n$	5	6
$\beta^- + 4n$	1	1
$\beta^- + p$	1	1
$\beta^- + +3p$	3	3
$\beta^- + 2p$	2	2
$\beta^+ + p$	175	308
$\beta^+ + \alpha$	34	41
$\beta^+ + p + \alpha$	3	3
$\beta^+ + 2p$	13	16
$\beta^+ + 3p$	2	2

The fission fragment lists have been generated using the Monte Carlo GEF code, version 2025.1.2, with 10^9 events simulated, based on the property tables extracted from the GENF/D library, for consistency. The subsequent sub-libraries for spontaneous fission yields (SFY) and neutron-induced fission yields (NFY) were produced, thanks to the GEF features. This parallel dataset is used in the benchmarks, discussed in section 5.4.

The fission fragment list, as well as neutrons and total kinetic energy of fragments spectra have been produced for 338 isotopes (including 279 ground states). The neutron and kinetic energy of fission fragments spectra have been imported in GENF/D as continuous spectra. Moreover, the average neutron multiplicity is also added in the MF=1/MT=452 section.

5.2.5. Average energy estimations

ENDF6 format allows to indicate the global average energy of the emitted particles, one can list three main heat components, i.e. light particles (β^-, β^+, electrons, ...), electromagnetic radiations (γ, X-ray, annihilation radiation, ...) and heavy particles (α, FF, p, n, ...) average energies.

Only with the availability of the information on the emitted gamma, can one solve the energy equations of two body decays. And only with advanced nuclear theories, can one estimate the gamma emitted, or the spectra of three, and more, body decays. This is beyond what is available in NUBASE, and beyond the goals of the pythonic toolbox.

Through the IAEA API, without considering the different isomers, there are 2158 isotopes with information on the associated gamma spectra and 813 with beta-, 797 with beta+, and 683 with alpha information. Therefore, even with ENSDF data, all average energies of particle emitted cannot be computed, and estimates must be done.

From a detailed analysis of ENDF/B heat estimation when no spectra were given, one can extract a convention in order to get the average energies from the total available energy. These rules are presented in Table 5.8. The Figure 5.3 shows the relative difference between original ENDF/B and ENDF/B average energies recomputed with Table 5.8 convention, for the nuclides without any decay spectra information, considering 10^{23} W total heat for each radionuclide.

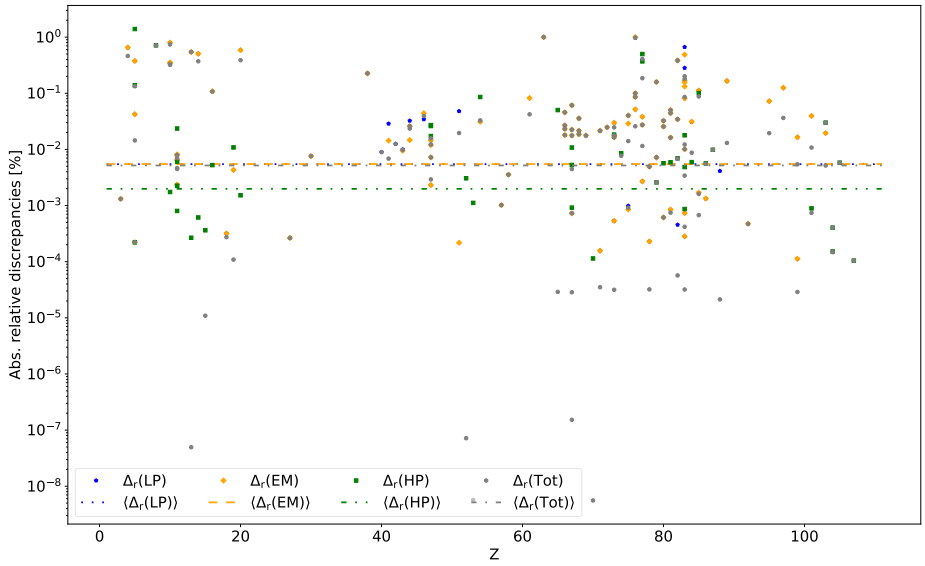

Figure 5.3.: Log-scaled relative difference between ENDF/B original and recomputed from Q-value decay heat by atomic number Z. The discrepancies for the total decay heat (blue hexagon), as well as light particle (yellow diamond), electromagnetic (green square) heavy particle (grey bullet) decay heat are represented, with their global average

For those 1828 nuclides, the average relative error is $0.005 \pm 0.05\%$. The decay heat components from each radionuclide were compared on a normalised basis, assuming a total decay heat output of 10^{23} W per nuclide.

Spontaneous fission heat, and the β followed by spontaneous heat have a null Q-value in the other database, so there is no rule availalble in ENDF/B, JENDL nor JEFF. But as GEF can provide the list of fragments, and their combined kinetic spectra, as well photo-fission spectra, therefore there is no need to find this fraction of Q values.

Table 5.8.: Convention for average energy estimation from Q-value, with $\langle E_{LP} \rangle$ the light particle decay heat, $\langle E_{EM} \rangle$ the electromagnetic decay heat and $\langle E_{HP} \rangle$ the heavy particle decay heat

Decay modes	$\langle E_{LP} \rangle$	$\langle E_{EM} \rangle$	$\langle E_{HP} \rangle$
β^+, β^-	$\frac{1}{3}$Q	$\frac{1}{3}$Q	0
$2\beta^+$, $2\beta^-$	$\frac{1}{2}$Q	$\frac{1}{2}$Q	0
$\beta^\pm\alpha$, $\beta^\pm p$, $\beta^\pm n$	$\frac{1}{4}$Q	$\frac{1}{4}$Q	$\frac{1}{4}$Q
$\beta^\pm xp$, $\beta^\pm xn$ (with $x > 1$)	$\frac{1}{5}$Q	$\frac{1}{5}$Q	$\frac{2}{5}$Q
α, xp, xn	0	0	Q
IT	0	Q	0

When spectra are available, the associated average heat component is superseded, using the Equation 5.6.

$$\langle E \rangle = BR \times \frac{\int P(E) E dE}{\int P(E) dE} \tag{5.6}$$

where BR is the branching ratio of the considered channel, and P is the probability of emission of energy E.

For the 5501 isomers, only 1962 kept the guess estimate for all three values.

5.3. Comparison to evaluated databases

Having generated a full and state-of-the-art decay database, in this section GENF/D will be compared to the three main evaluated decay database, JENDL, ENDF/B and JEFF.

The average energy estimates will also be criticised as well as GEF results.

5.3.1. Extensiveness considerations

The primary design objective for the GENF/D library is extensiveness. A comparison with all other publicly available ENDF-6 format libraries reveals that the combined set contains data for 5583 isotopes (comprising 3567 ground states and 2016 isomers). The GENF/D library is very complete but misses 49 ground states and 33 isomeric states present in other libraries, they are listed in Appendix B.

The majority of these omitted nuclides are meta-stable with very short half-lives falling below the $T_{1/2} \geq 100$ ns validity threshold of the NUBASE2020 evaluation (e.g., ^{12}Li, ^{56}Ga). As for some of the longer-lived nuclides, they simply do not appear in NUBASE2020, i.e. ^{244}U, ^{245}U, ^{246}Np, and ^{250}Am, nor do they appear in ENSDF, making difficult their addition to GENF/D in a direct manner.

A potential solution to these omissions would be to import data for the missing isotopes directly from other evaluated databases. This approach, however, presents significant challenges. Data for some nuclides is only available in outdated distributions (e.g., 5 in ENDF/B-VII.0, 3 in JEFF-2.2, and 1 in JENDL-FPD-2000) and was not carried forward into subsequent updates of those libraries, raising doubts about its reliability.

Furthermore, while more credible modern evaluations – such as JENDL-5 (59 isotopes), JEFF-4.0 (9 isotopes), and EAF-2010 (4 isotopes) – could potentially fill most of the gaps, a conscious decision was made to exclude this data. The priority was to ensure absolute internal consistency within the decay chains and to maintain a uniform methodology for spectral association across the entire library.

5.3.2. Energetics considerations

As a reminder, GENF/D proposal is the translation of the evaluated NUBASE in ENDF-6 format, and compiled with the evaluated ENSDF. Hence, some discrepancies are expected against the other decay sub-libraries as ENDF/B, JEFF or JENDL as they do a second layer of evaluation. Validation of GENF/D can be quite complex due to the high number of nuclides. In this section, global check against ENDF/B, JEFF and JENDL is made. To keep the reference consistent in the relative differences, GENF/D has been chosen as reference, as the most extensive one.

Firstly, in order to check the correct parsing of the half-lives, the ones of GENF/D have been compared in Figure 5.4. As expected, as they are closer in release date and sources, GENF/D half-lives are in better concordance JENDL-5, with 80% of half-lives within 5% agreement. The other main properties have been compared and synthesized in Table 5.9.

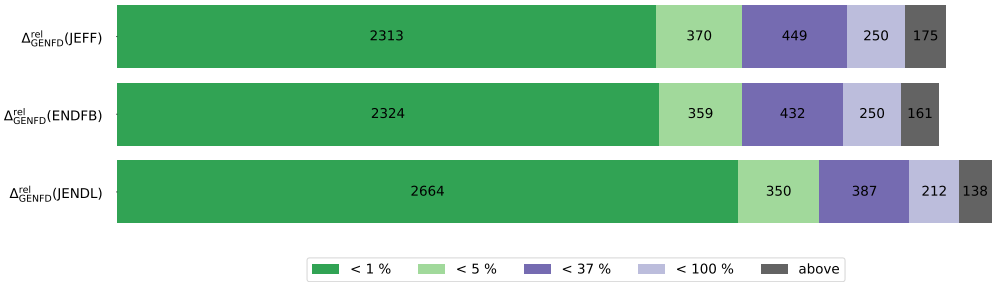

Figure 5.4.: Relative difference between GENF/D half-lives and JENDL-5

Another relevant and easily comparable property is the total available decay energy. The agreement within 5% is of 77% for JEFF-4.0, 82% with ENDF/B-VIII.0 and 81% with JENDL-5. If we consider the maximum decay energy, then the agreement is over 82% for all of them.

As seen in Table 5.9, the decay heat estimates have lesser agreement, especially with JENDL-5. This is mainly due to mistakes in the decay heat estimation of JENDL-5. Indeed, some decays that emit delayed neutrons do not account them in the heavy particle heat.

As for the consideration of delayed neutrons, one should note that, without accounting for fission neutrons, JEFF-3.3 have neutron average decay energy for 80 isotopes, ENDF/B-VIII.1 for 312 isotopes and JENDL-5 for 494 isotopes, whereas GENF/D have data for 44 isotopes. This reduced number of neutron spectra in GENF/D is due to the use of the IAEA compilation, rather than extracting the one from ENSDF, as they are not available through the Livechart API.

Table 5.9.: Comparison of GENF/D against JENDL-5, ENDF/B-VIII.0 and JEFF-3.3 over the main observables available. The proportion, expressed in percent, of common nuclides, which have relative difference below 10% are presented. Only nuclides in their ground states and with half-lives greater than one second are considered

	JENDL-5 [%]	ENDF/B-VIII.0 [%]	JEFF-4.0 [%]
$T_{1/2}$	92.5	91.1	90.7
Q_{tot}	92.3	94.5	93.2
Q_{max}	91.1	92.8	92.4
$\langle E_{LP} \rangle$	78.9	84.9	81.8
$\langle E_{EM} \rangle$	82.2	84.9	83.2
$\langle E_{HP} \rangle$	62.4	77.4	80.6

a) Spontaneous fission considerations

In this section, the comparison of JEFF-4.0 with the results using GEF is done, to confirm the motivation of its use, and validate the GENF/D estimates. The fission data is virtually the same for JEFF, ENDF/B and JENDL when considering the decay data, except for ^{231}Pa that is absent in JENDL-5. Since JEFF-4.0 provides more details on the associated spectra, this database was chosen for comparison.

JEFF indicates 132 channels of SF or β followed by fission, and provides non-null Q value for only 27 of them. In contrast, GENF/D indicates 240 isotopes that undergo spontaneous fission, and provides an estimate of Q-value for all of them, as well as neutron-multiplicity and the neutron, gamma and fission fragment spectra.

When comparing the 27 isotopes, which have detailed data in JEFF-3.3, the available decay energy difference between GENF/D and GEF is within 2%. Hence, even if GEF

does not consider the ternary fission, because the probability of appearance of this phenomenon is very reduced, there is no impact on energy estimations.

If one compare the neutron multiplicity, meaning the average number of neutrons emitted after a spontaneous fission, the discrepancies get larger with a maximum of 21%, and an average discrepancy of 7%. This remains in an acceptable range of difference, which are shown in Figure 5.5.

Table 5.10 illustrates this comparison for ^{238}U and ^{232}Th decays. For these isotopes, the average neutron energies are in perfect agreement, within at most 1.2 % of difference. The gamma spectrum disagrees by only 2% for ^{238}U, but jumps to 14 % for the ^{232}Th. The difference in the gamma spectrum with JEFF-4.0 could come from the fact that the relaxation spectra of such a decay are represented by a very smoothed continuous linear-linear distribution, whereas GEF generates a histogram with 1 keV binning, as shown in Figure 5.6.

It should also be noted that ternary fission is not considered in GEF, leading to the absence of light fragments as protons, helium, lithium, etc. that can be found in the other evaluations.

Table 5.10.: Average energy, in MeV, of gamma $\langle E_\gamma \rangle$, neutron $\langle E_n \rangle$, fission fragments $\langle E_{FF} \rangle$ as well as available energy Q_{SF}, and neutron-multiplicity $\langle xn \rangle$ for the spontaneous fission of ^{238}U and ^{232}Th

	^{238}U		^{232}Th	
	GEF	JEFF-4.0	GEF	JEFF-4.0
$\langle E_\gamma \rangle$	0.881	0.896	0.981	0.843
$\langle E_n \rangle$	3.9	3.7	2.8	2.7
$\langle E_{FF} \rangle$	166.5	162.9	158.9	159.7
Q_{SF}	176.1	173.6	167.1	169.4
$\langle xn \rangle$	1.99	2.00	1.38	1.50

Globally, the average energy of fission fragments have in average 0.9% relative difference, for a maximum discrepancy of 3.9% for ^{253}Es, with respect to JEFF-4.0. Due to the higher discrepancy with the average neutron number emitted, the neutron average energy has a larger discrepancy, in average of 11%.

b) Average energy from Q-value

When no experimental spectra is available, the convention for estimating average energy from available energy (Table 5.8) is applied. Yet, there are some concerns, that should be known.

When applying such convention, to ENDF/B-VIII.0 decay sub-library, on nuclides that do have information on secondary particle energy distributions, one observes significant discrepancies (Figure 5.7). For these nuclides, having at least one information on α or β

(a) Available decay energy

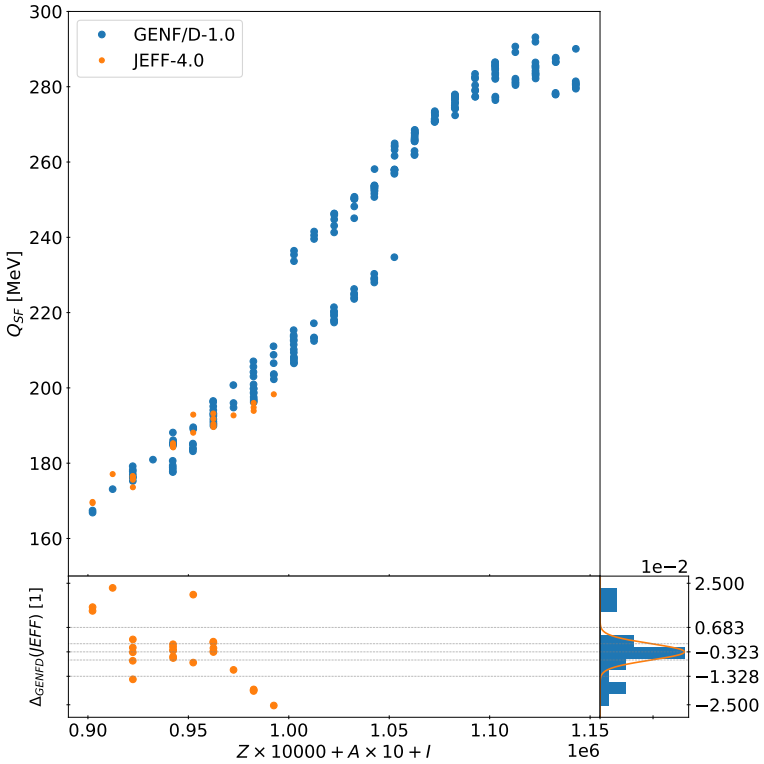

(b) Average neutron emission

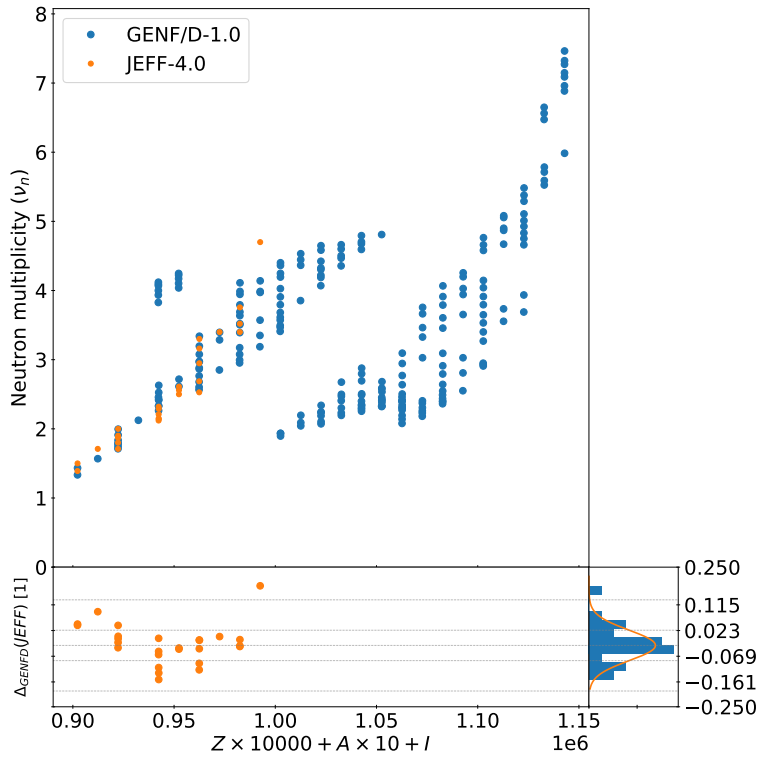

Figure 5.5.: Relative discrepancy between GENF/D and JEFF-4.0 for available decay energy and neutron multiplicity

(a) Original spectra of ^{238}U

(b) Rebinned spectra of ^{238}U

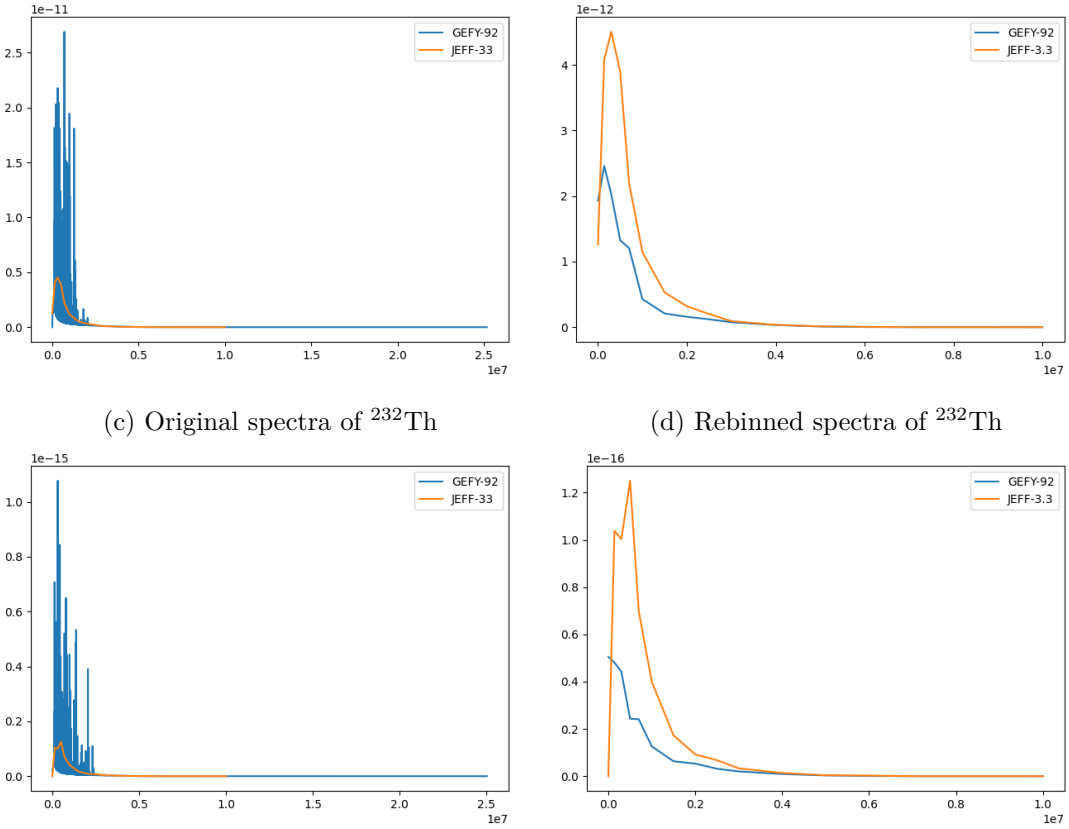

(c) Original spectra of ^{232}Th

(d) Rebinned spectra of ^{232}Th

Figure 5.6.: Comparison of the gamma relaxation spectra of the SF channel of GENF/D and JEFF-3.3.

secondaries in ENDF/B-VIII.0, the average total decay energy difference is $96.4 \pm 747\%$ (excluding deviations larger than 1000%).

The electromagnetic decay heat component is particularly affected, with an average discrepancy of about $10^6\%$ due to systematic overestimation. The heavy particle component is less affected, with an average discrepancy of 28%.

Since the JEFF and JENDL libraries use a comparable convention (showing discrepancies of $3.7 \pm 10.5\%$ and $0.04 \pm 0.8\%$, respectively), the agreement in Table 5.9 is not an independent validation of the convention's correctness but an indication of its consistent application.

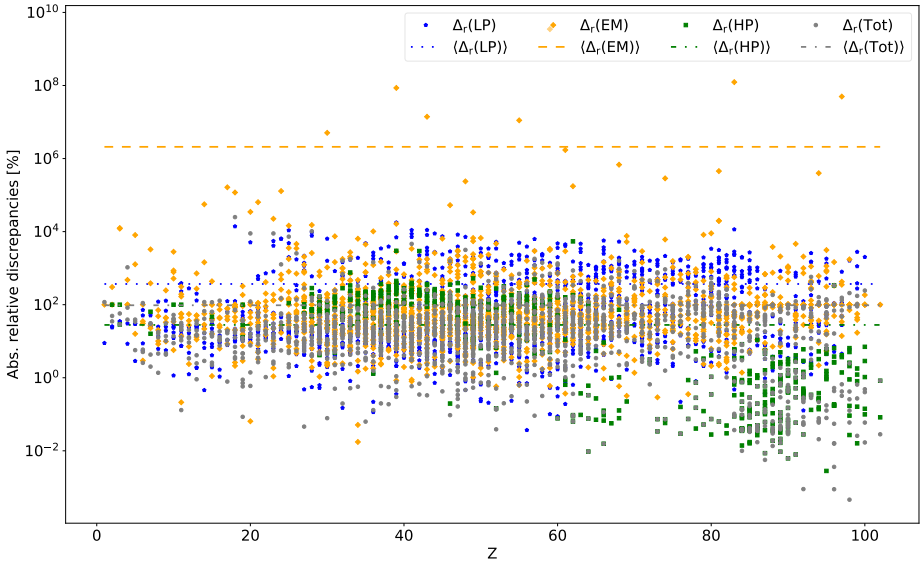

Figure 5.7.: Log-scaled relative difference between ENDF/B decay heat estimates (considering 10^{23} W total heat of each radionuclides) and the one recomputed based on Table 5.8 convention, considering only the nuclides with spectral information. The discrepancies for the total decay heat (blue hexagon), as well as light particle (yellow diamond), electromagnetic (green square) heavy particle (grey bullet) decay heats are represented, with their global average

The assumption that light particle decay heat equals one-third of the available energy is arguably arbitrary. This is shown in Figure 5.8, which plots the ratio of the average beta energy, calculated using BetaShape, to the corresponding Q-value from NUBASE2020. Empirical data suggest more accurate mean values of approximately 0.26 for β^+ emissions and 0.31 for β^- emissions. But finer models, accounting for spins, should bring better predictions, with the proposal of advanced phenomenological beta model using Gamow-Teller decay strength as [152][1].

[1] A. Letourneau et al. 'Origin of the Reactor Antineutrino Anomalies in Light of a New Summation Model with Parametrized beta- Transitions'. In: *Physical Review Letters* 130.2 (Jan. 2023), p. 021801. DOI: 10.1103/PhysRevLett.130.021801.

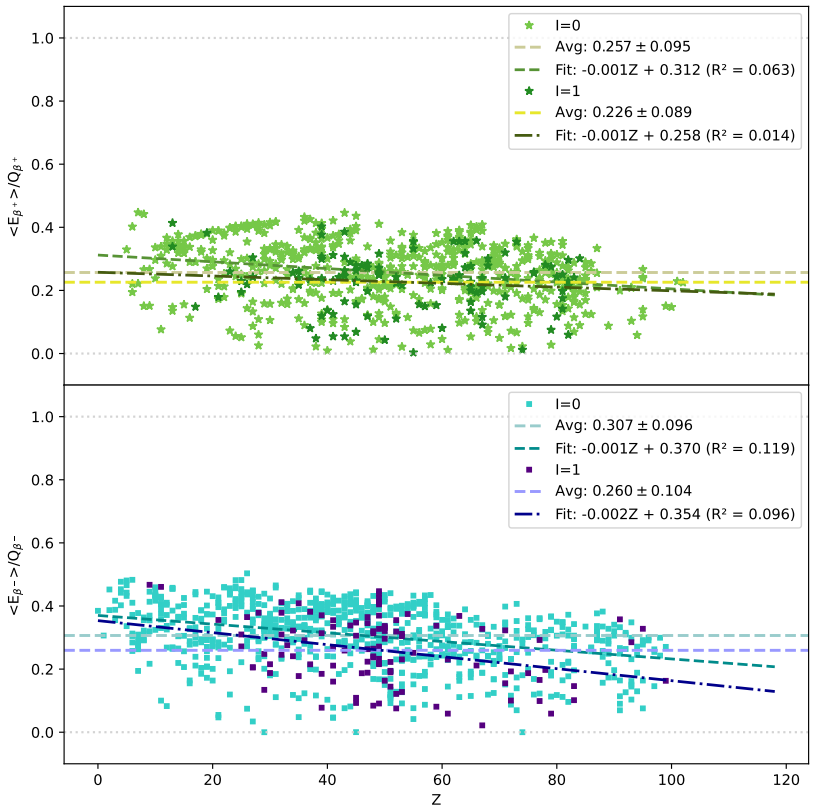

Figure 5.8.: Ratio of the average beta energy (from BetaShape) to the NUBASE2020 Q-value. The top panel shows results for β^+ emissions, and the bottom panel for β^- emissions. Data are shown for distinct isomeric states (I=1 corresponds to first isomeric states, in darker tones, and I=0 to ground states, in lighter tones), alongside the global average and a linear fit over atomic number Z

5.4. Validation against integral measurements

A critical aspect of the development of a decay database is its validity against heat benchmarks. There exists only an handful of them, due to the difficulty of such measurements.

Due to the heat estimation strategy, to avoid pandemonium effect and the questionable heat splitting, only total heat comparison in this section is considered.

It should be mentioned, that the pandemonium effect is not considered in GENF/D. Introducing the Total Absorption Gamma-ray Spectroscopy measurements, in order to access the higher energy beta transitions causing the pandemonium effect [115][1], and consequently reevaluate all derived transitions is beyond the scope of this first release. If such correction a correction is critical for end-user application, the use of the evaluated datasets provided by projects like JEFF [153][2] is recommended. Indeed, JEFF introduce partially such considerations, e.g. for ^{93}Rb, ^{96}Y, ^{96m}Y, ^{99}Y, ^{103}Tc, ^{108}Tc, ^{138}I or ^{142}Cs.

To produce the results of presented in this section, `FISPACT-II` has been used. This code follows the evolution of material irradiated by neutrons, alphas, gammas, protons, or deuterons, and provides a wide range of derived radiological output quantities to satisfy most needs for nuclear applications.

In Figure 5.9, two transuranic heat benchmarks are shown, the results of 10^{-6} seconds of thermal pulse (with a fluence of 10^{22} n/s) on pure ^{239}Pu, estimated by Dickens [113][3] and Tobias [114][4]. And the results of 2×10^4 seconds of irradiation of pure ^{235}U (with a fluence of 10^{13} n/s) by Yarnell [154][5].

Whereas the Figure 5.10 presents an irradiation of non fissible material, with an irradiation of alloy (Inconel 600) for 5 minutes with a fluence of 1.116×10^{10} n/s at the Fusion Neutron Source (FNS).

One should remember, that such benchmarks do not depend only on the decay database, but also heavily on the fission fragment estimates, in the case of fissile material, and on the neutron cross-sections for the FNS irradiation.

[1] J.C. Hardy et al. 'The essential decay of pandemonium: A demonstration of errors in complex beta-decay schemes'. en. In: *Physics Letters B* 71.2 (Nov. 1977), pp. 307–310. ISSN: 03702693. DOI: 10.1016/0370-2693(77)90223-4.

[2] Joint Evaluated Fission and Fusion Project. 'JEFF-4.0 Evaluated Data: spontaneous fission products yields'. en. In: *OECD Nuclear Energy Agency* (June 2025). DOI: 10.82555/tccek-e9s26.

[3] J. K. Dickens et al. 'Fission-Product Energy Release for Times Following Thermal-Neutron Fission of Plutonium-239 and Plutonium-241 Between 2 and 14 000 s'. In: *Nuclear Science and Engineering* 78.2 (June 1981). _eprint: https://doi.org/10.13182/NSE81-A20099, pp. 126–146. ISSN: 0029-5639. DOI: 10.13182/NSE81-A20099.

[4] A. Tobias. 'Decay heat'. In: *Progress in Nuclear Energy* 5.1 (Jan. 1980), pp. 1–93. ISSN: 0149-1970. DOI: 10.1016/0149-1970(80)90002-5.

[5] J. L. Yarnell and P. J. Bendt. *Calorimetric fission product decay heat measurements for 239Pu, 233U, and 235U*. English. Tech. rep. NUREG/CR-0349; LA-7452-MS. Los Alamos Scientific Lab., NM (USA), Aug. 1978. DOI: 10.2172/6577911.

The Figure 5.9 and the Figure 5.10 were generated using GEFY induced and spontaneous fragments. Due to the heavy link between GEF and GENF/D,the use of GEFY with GENF/D is recommended. But no correction (or evaluation) of the data was done to meet the experimental points, and create more links than already mentioned in subsection 5.2.4.

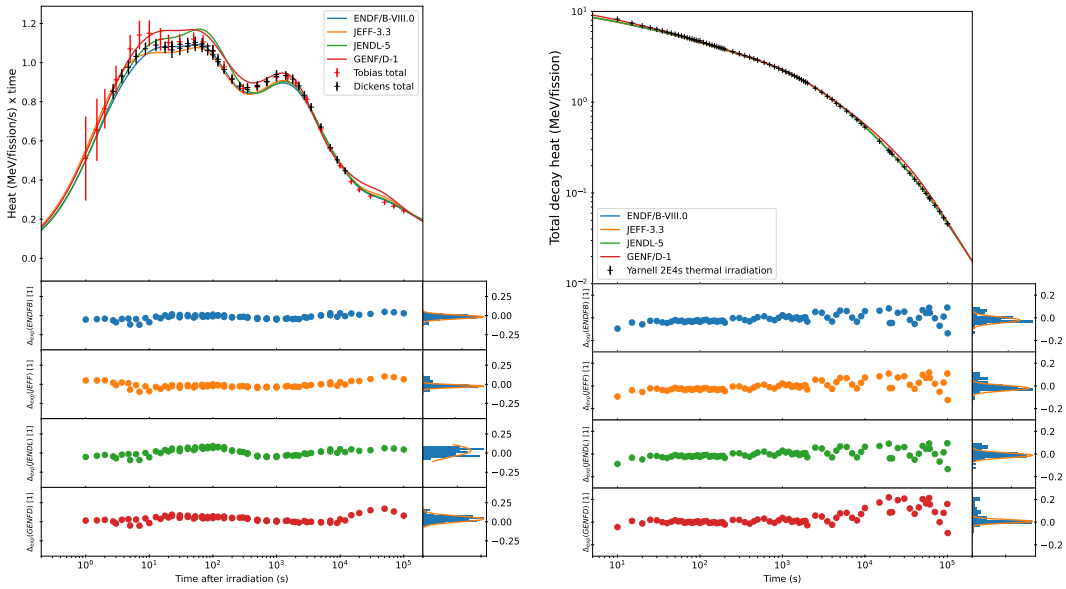

Figure 5.9.: Decay heat benchmark using ENDF/B-VIII.0 neutron cross-section for GENF/D against ENDF/B, JEFF and JENDL decay data (using their associated fission fragments). On the left, a long thermal irradiation on ^{235}U. On the right, a thermal pulse experiment on ^{239}Pu

5.4.1. Fission fragments difficulties

If the use of GEF is recommended, one should be aware of a certain limitation.

Conclusion

A novel decay database have been produced from NUBASE2020 and ENSDF2025 data in ENDF-6 format. It accounts for the new updated format rules, to discriminate neutrino spectra from their beta counterpart.

Summary of contributions The main objective of GENF/D was to produce a dataset extending far beyond the centre of the stability valley, including exotic and meta-stable nuclides. This was achieved by translating the NUBASE datasets into valid ENDF-6 format, thanks to the *endf_parserpy* utility, as well as IAEA LiveChart API.

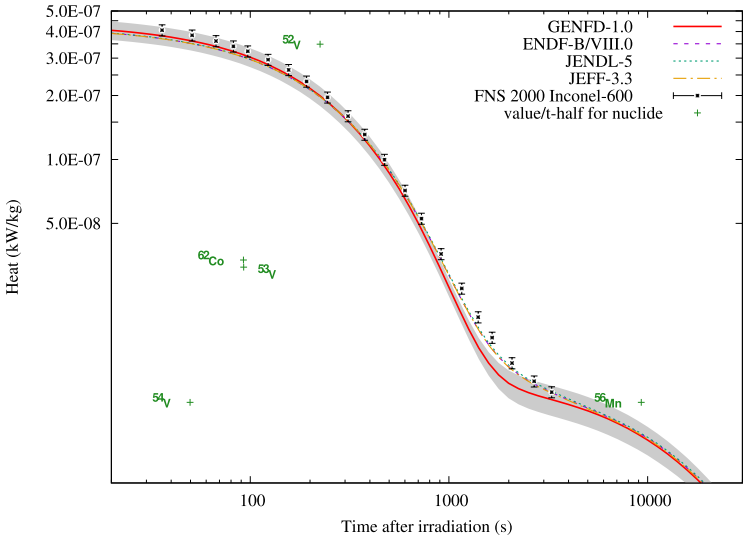

Figure 5.10.: Decay heat benchmark using TENDL-2017 neutron cross-section, GEFY fission fragments and GENF/D against ENDF/B, JEFF and JENDL decay data. Five minutes irradiation at FNS of ^{nat}Ni, ^{nat}Mn, ^{nat}Fe, ^{nat}Cr

The methodology and measurements have been confirmed over the common nuclides with the other evaluated database. Additional excited state data have been made available (from 797 excited states in JENDL-5, 768 in JEFF-3.3 or 738 in ENDF/B-VIII.0 to 1990 in GENF/D), enabling more comprehensive follow of inventory, especially in the case of induced and spontaneous fissions that both produces a large number of excited states.

This work also led to the production of a more complete GEFY fission fragment dataset. In addition, some errors have been highlighted in the other database (as missing rays, contribution to heat, ...), and transmitted to their maintainers.

The release of this new decay database marks a significant step forward, with several planned improvements on the horizon.

Future developments Taking advantage of the ongoing modernisation of the ENSDF format, additional delayed particle data – currently inaccessible via the IAEA API – will be incorporated, enhancing decay spectra completeness. To improve the accuracy and in-depth use of GENF/D, the uncertainty, and the error propagation, should be re-examined in the future. The first step would address the uncertainties on the Q-values, and its derived properties, in particular, to implement the mass covariance matrix provided by AME2020.

A major focus will be to revisit the heat computation, moving from the empirical $Q/3$ approximation for the beta decay average energy to more precise, isotope-dependent evaluations. The preliminary review of section b suggests revision of the estimation of E_β from Q, with the use of a more refined empirical factor or by accounting for some dependence on the atomic number. Recently, new estimations of energies for light particle heat have been studied, especially with the proposal of advanced phenomenological beta model using Gamow-Teller decay strength [152][1]. A larger review of such approaches should yield more accurate decay heat predictions in future updates of GENF/D, where experimental observation is lacking.

Applications GENF/D will become the backbone of `TMX_Bateman`. GENF/D will allow for better generation of clearance levels, raised by the radioprotection issues and during nuclear facility dismantling, and will also improve accuracy during fuel development.

[1] A. Letourneau et al. 'Origin of the Reactor Antineutrino Anomalies in Light of a New Summation Model with Parametrized beta- Transitions'. In: *Physical Review Letters* 130.2 (Jan. 2023), p. 021801. DOI: 10.1103/PhysRevLett.130.021801.

Chapter

Conclusions

Abattez la citadelle !

(Jean-Luc MÉLENCHON, *2023)*

The initial aim of this work was to propose a methodology applicable to high-energy particle accelerator facilities, in the context of the ADS prototype developed by TRANSMUTEX.

The use of Monte Carlo codes was explored for three main applications: modelling neutron activation around a simple benchmark of a radiotherapy linac head, modelling a thermalised AmBe source, and modelling a cyclotron facility for radioisotope production. This work has been partially published in [72, 73][1].

For these studies, models were constructed using the principal multiphysics codes: FlukaINFN, FlukaCERN, PHITS, and Geant4. For simpler models, the codes produced results in excellent agreement. However, for more complex models – particularly with FLUKA – discrepancies emerged. As the number of distinct physical processes increased, the differences between the codes became more pronounced. Consequently, for decommissioning planning, especially when a facility has not yet begun commissioning, a multi-code approach is advisable to explore potential biases introduced by the codes themselves.

Activation levels served as the primary observable for control in this work. This requires a precise understanding of the experimental or operational duration and the subsequent cooling time. The aforementioned codes do not necessarily incorporate the time variable; external modules are necessary to model the temporal evolution of material compositions. This task can be accomplished using Bateman solvers such as `FISPACT-II`, `DCHAIN-PHITS`, CINDER'90, or NUIT. These tools allow easy inclusion of time profiles and neutron fields obtained from Monte Carlo models to implement an irradiation profile, thereby enabling the determination of expected activity at any given time.

Nevertheless, these solvers present certain limitations, particularly in extracting decay spectra for comparison with experimental spectroscopy. To address this, the present work contributed to the development of a new Bateman solver, `TMX_Bateman`. This code

[1] Jonathan Collin et al. 'Validation of Monte Carlo simulations by experimental measurements of neutron-induced activation in cyclotrons'. en. In: *EPJ Web of Conferences*. Vol. 288. Italy: EDP Sciences, 2023, p. 04025. DOI: 10.1051/epjconf/202328804025, Abdel-Mjid Nourreddine et al. 'Assessment of photon and proton-induced activation in particles accelerators'. In: *Radiation Protection Dosimetry*. Vol. 200. 16-18. Japan, Nov. 2024, pp. 1507–1513. DOI: 10.1093/rpd/ncae146.

enables the tracking of any inventory through transmutation trajectory analysis and allows extraction of decay spectra with arbitrary binning for gamma, alpha, or neutron radiation. The code has been validated against `FISPACT-II` and `DCHAIN-PHITS`, and compared with reference decay heat benchmarks.

The development of this Bateman solver highlighted two further considerations. First, to track and manage nuclide interactions, evaluated nuclear data (cross-sections and decay properties) are necessary to avoid implementing interaction models –and thus an entire Monte Carlo engine– when considering processes beyond decay. Second, evaluated libraries released in ENDF-6 format permit flexible inclusion of any process with cross-sections for neutrons and charged particles. These files are also used for neutron transport in Monte Carlo codes, making them a cornerstone of nuclear process modelling, whether deterministic or stochastic.

This work led to the creation of tools for parsing and comparing such ENDF-6 files. In particular, a preliminary comparison of neutron cross-sections for a selected set of materials and reactions was performed against experimental data from EXFOR. The need for pre-comparison of cross-section data was highlighted in chapter 2, as the impact of both code variation and database variation was demonstrated. Refinement through database comparison is possible but can be time-consuming, especially for full-facility modelling. To guide such comparisons, particularly for codes such as MCNP or PHITS (which allow flexible per-nuclide database selection), an inter-code comparison and comparison against EXFOR experimental cross-sections was initiated for a few material–reaction pairs.

Subsequently, these cross-section data were formatted in friendly standard for deep learning applications and used in [155][1].

Finally, decommissioning requires precise estimation of nuclear inventory, including accurate gamma spectra. Up-to-date and extensive data are essential for constructing a robust Bateman solver. This work produced a novel evaluated decay database, more precisely a new compilation of evaluated data. The generation of the GENF/D database has been presented and accepted [156][2]. This database builds upon NUBASE2020, which includes reviews of multiple experiments from the literature, ENSDF, DDEP, and nuclear predictions based on trend properties. NUBASE was translated into ENDF-6 format and supplemented with improved spin estimates from RIPL-3, as well as decay spectra from ENSDF. The estimation of beta and neutrino spectra was refined using BetaShape, which provides more precise beta spectrum management and access to continuous spectral descriptions. Atomic data were included via RadiationReport to obtain discrete electrons (Auger and conversion electrons), X-rays, and internal bremsstrahlung. In the context

[1] Lévana Gesson et al. 'Enhancing nuclear cross-section predictions with deep learning: the DINo algorithm'. en. In: *The European Physical Journal Plus* 140.7 (July 2025), p. 645. ISSN: 2190-5444. DOI: 10.1140/epjp/s13360-025-06562-z.

[2] Jonathan Collin et al. 'Global Evaluated Nuclear File (GENF/D): a decay data sub-library for radionuclide inventory applications'. en. In: *EPJ Nuclear Sciences & Technologies* 11 (2025), p. 77. ISSN: 2491-9292. DOI: 10.1051/epjn/2025070.

of ADS, spontaneous fission was also implemented: estimates from the Monte Carlo code GEF were used to provide fission fragment lists, neutron and gamma spectra, and Q-value computations.

Perspectives

SSNTD for low-fluence areas As introduced, SSNTDs enable neutron detection using cost-effective detectors that can be readily deployed in a facility. Although preliminary implementation of this technique was conducted around the CYRCé facility and inside its casemate, the results were inconclusive. Improvements to the optical acquisition system are required, particularly for track identification and extraction of characteristics: radius, colour intensity, ... The SSNTD analysis must be enhanced, especially regarding proton–alpha discrimination, to obtain better estimates of fast and thermal components in neutron spectra. Machine learning algorithms, such as random forests, should be explored for this task. Such approaches require large datasets of images for training. Coupling Monte Carlo simulations with codes such as TRACK_P [157][1] (which estimates tracks resulting from protons) could generate synthetic data to complement experimental acquisitions. Further work could enable extraction of track incidence angles, providing access to neutron energy beyond proton–alpha discrimination. SSNTDs are proposed for acquiring neutron rates in low-fluence areas, serving as cumulative detectors with archivable tracks. This strategy must be accompanied of experimental campaign around controlled proton and alpha beams.

Multifoil activation The CYRCé facility offers a suitable use case for deploying such detectors. Although Monte Carlo models were constructed in this work, they do not fully validate the neutron spectra inside the accelerator casemate. The multifoil activation technique [158, 159][2] should be applied to obtain more precise experimental estimates of secondary neutron spectra. By using multiple foil materials with different energy-dependent nuclear reactions, and applying spectral deconvolution methods (analogous to Bonner sphere spectrometry), a significant refinement of the neutron energy distribution could be achieved. This methodology could be extended to higher-energy accelerator facilities, enabling exploration of the technique at elevated neutron energies and would provide additionnal benchmarks for inter-code Monte Carlo comparisons. Higher beam energies would broaden the range of physical processes under consideration, notably producing higher-energy photons via bremsstrahlung. These photons may exceed reaction thresholds, especially the giant dipole resonance, leading to photoneutron production.

[1] D. Nikezic, M. Ivanovic, and K. N. Yu. 'A computer program TRACK_P for studying proton tracks in PADC detectors'. In: *SoftwareX* 5 (Jan. 2016), pp. 74–79. ISSN: 2352-7110. DOI: 10.1016/j.softx.2016.04.006.

[2] Isao Murata et al. 'Neutron and gamma-ray source-term characterization of AmBe sources in Osaka University'. en. In: *Progress in Nuclear Science and Technology* 4 (2014), pp. 345–348. ISSN: 2185-4823. DOI: 10.15669/pnst.4.345, Davide Chiesa et al. 'Measurement of the neutron flux at spallation sources using multi-foil activation'. In: *Nuclear Instruments and Methods in Physics Research Section A: Accelerators, Spectrometers, Detectors and Associated Equipment* 902 (2018), pp. 14–24. ISSN: 0168-9002. DOI: https://doi.org/10.1016/j.nima.2018.06.016.

This additional neutron source would contribute substantially to the total activation inventory and must be accounted for in comprehensive models.

Determining the exact energy thresholds of these reactions remains a significant challenge for precise activation estimation in accelerator facilities. Correct threshold estimation is crucial for identifying components with activation levels sufficiently low for conventional waste classification, thereby facilitating recycling pathways and reducing long-term storage costs.

`TMX_Bateman` Future development of the `TMX_Bateman` solver should focus on several key enhancements to improve computational efficiency, physical comprehensiveness, and practical utility for decommissioning and radiological protection. A primary objective is implementing a numerical integration scheme based on Chebyshev approximations, which is anticipated to accelerate the resolution and reliability of Bateman equations under irradiation: a scenario where linearised decay channels can introduce loops that render Transmutation Trajectory Analysis less suitable. Improved versions of TTA have been proposed [101][1]. The solver's physical models should be expanded to integrate neutron interactions from decay processes such as spontaneous fission or (α,n) reactions. Currently, these neutronic contributions are not fully coupled back into the neutron spectra considered. Enabling this capability would create a more physically realistic simulation of the neutron field and its effects over time, particularly in environments with significant actinide inventories. To directly support decommissioning planning, automatic clearance level assessment functionality should be integrated, allowing users to define regulatory limits for specific radionuclides or material categories and to compute the time required for activated materials to decay below these thresholds –an essential feature for waste management and logistics planning. Finally, dose computation capabilities should be added. By leveraging the detailed decay spectra provided by the solver and incorporating appropriate dose conversion coefficients, `TMX_Bateman` could calculate effective dose rates from computed nuclide inventories, providing insights for assessing occupational exposure risks during operational and decommissioning phases, and enabling optimisation of shielding requirements and intervention planning.

GENF/D While the current version of GENF/D successfully translates NUBASE2020, several points for improvement remain, particularly regarding uncertainty treatment. Some uncertainties, especially those pertaining to branching ratios, are currently overestimated. Errors are propagated using a basic Taylor expansion method; implementing mass covariances from the Atomic Mass Evaluation (AME) would improve Q-value computation accuracy.

Furthermore, as delayed particle emission data are not available through the current Livechart API, alternative sources should be used: either the ENSDF-JSON format from the ongoing ENSDF modernisation project or predictions from dedicated nuclear

[1] Kai Huang et al. 'Improvements to the Transmutation Trajectory Analysis of depletion evaluation'. In: *Annals of Nuclear Energy* 87 (Jan. 2016), pp. 637–647. ISSN: 0306-4549. DOI: 10.1016/j.anucene.2015.10.013.

models, particularly for delayed neutrons.

The former could provide direct access to ENSDF in a Python-friendly format. Since the database is intended primarily for Bateman solvers rather than evaluators or metrological applications, improving the robustness of computed observables is a key consideration.

Although decay heat estimates are consistently provided, corresponding decay spectra sometimes lack complete information. Adding estimated spectra could improve internal consistency; for example, an isotope marked as α-decaying but without associated ray data should be assigned an alpha spectrum consistent with its heavy-particle heat contribution.

This enhancement would be particularly valuable for radiological dose evaluation codes. It should be noted that BetaShape is systematically called using the latest raw ENSDF.

BetaShape operates on the basis of registered spins; thus, spin inconsistencies may exist between what GENF/D ultimately considers and what BetaShape uses. Preprocessing ENSDF files could improve coherence, as was done for the GEF database used for fission fragment estimation.

Finally, the conventional approach used by evaluators for estimating average energies from Q-values is open to criticism. Since all data have been formatted into Python objects, multi-parameter fitting procedures could be performed incorporating variables such as atomic number, nucleon parity, decay modes, and distance from the valley of stability. Machine learning techniques could facilitate these complex fitting tasks efficiently.

Appendix A.

TMX_Bateman: advanced uses

A.1. Input

Listing A.1: Complete input file for `TMX_Bateman`

```
{
    "moles" : {
        "922350": 1,
        "922380": 1
    },
    "time_bins" : [
        0,
        1,
        100,
        200
    ],
    "json": true,
    "csv_per_meas": true,
    "csv_per_step": true,
    "hdf5_decay": "/path/to/decay_db_file.hdf5",
    "hdf5_sff": "/path/to/sff_db_file.hdf5",
    "hdf5_xs": "/path/to/xs_db_file.hdf5",
    "hdf5_nff": "/path/to/nff_db_file.hdf5"
}
```

A.1.1. Irradiation

Listing A.2 gives an example of irradiation during the two first steps, considering thermal neutrons. The flux value of `spec_flux` will be renormalised to 1 n/cm/s, only `int_flux` is relevant.

The temperature of the cross-sections can be controlled on the fly thanks to `temperature`.

Listing A.2: Irradiation section of input file for `TMX_Bateman`

```
{
     "int_flux": [
         0, 1e12, 1e6
     ],
     "spec_flux": {
         "bins": [
             2.5163772E-03, 3.000E-03
         ],
         "flux": [
```

```
                1.000E+01
            ]
        },
        "temperature": 0,
}
```

A.1.2. External yield

One can directly indicate reaction rate into the input in moles (or grams) per seconds: Listing A.3. The reaction rate is constant and activated only when the `int_flux` is different from 0. This rate is not impacted by `int_flux` except for this aspect.

Listing A.3: Yield section of input file for `TMX_Bateman`

```
{
    "rate_moles" : {
        "230520": 1.6605390671738466
    },
    "rate_grams" : {
        "230520": 1.3940505050505050e+06
    },
}
```

A.1.3. Secondary spectra

If the most relevant spectrum is the photon one, to estimate the missed threshold reaction from alpha, or their energy spread, each secondary described can be activated or not.

Listing A.4: Secondary spectra section of input file for `TMX_Bateman`

```
{
    "time_bins" : [
        0,
        1,
        100,
        200
    ],
}
```

a) Efficiency functions

One can directly indicate, reaction rate into the input in moles per seconds (or grams): Listing A.3.

Listing A.5: Polynomial efficiency functions for `TMX_Bateman`

```
{
    "intensity_efficiency" : {
        "linlin": [1],
        "linlog": [1],
        "loglog": [1],
```

```
        "loglin": [1]
    },
}
```

A.1.4. Threshold for outputs

One can control the ammount of information printed, only in the csv per measurements and the json outputs.

Listing A.6: Threshold section of input file for `TMX_Bateman`

```
{
    "time_bins" : [
        0,
        1,
        100,
        200
    ],
}
```

A.2. Supported decays and reactions

The different reactions supported are listed in Table A.1 and Table A.2.

A.3. Committed dose

A.4. Inputs for examples

This section lists the JSON for the different examples presented in chapter 3. Thanks to `FISPACT-II` API and some scripting, these inputs can be (and have been) automatically translated for `FISPACT-II` and `DCHAIN-PHITS`.

Listing A.7: UOx fuel input example for `TMX_Bateman`

```
{
    "moles": {
        "320720": 0.00017129163715315,
        "320730": 0.00041793561416804,
        "320740": 0.0012206500483907,
        "320760": 0.0099687425049887,
        "330750": 0.0026325147873326,
        "340760": 0.00012957093045061,
        "340770": 0.017412524829836,
        "340780": 0.056558692358199,
        "340790": 0.10630806763967,
        "340800": 0.28575380452038,
        "340820": 0.70005099489504,
        "350810": 0.42687980500967,
        "360820": 0.021203602498926,
```

Table A.1.: List of supported reactions.

MT code	reaction
5	(z,anything)
11	(z,2n+d)
16	(z,2n)
17	(z,3n)
18	(z,f)
28	(z,n+p)
29	(z,n+2a)
30	(z,2n+2a)
32	(z,n+d)
33	(z,n+t)
34	(z,n+he3)
35	(z,nd+2a)
36	(z,nt+2a)
37	(z,4n)
41	(z,2n+p)
42	(z,3n+p)
44	(z,n+2p)
45	(z,n+pa)
102	(z,g)
103	(z,p)
104	(z,d)
105	(z,t)
106	(z,he3)
107	(z,a)
108	(z,2a)
109	(z,3a)
111	(z,2p)
112	(z,p+a)
113	(z,t+2a)
114	(z,d+2a)
115	(z,p+d)
116	(z,p+t)
117	(z,d+a)
152-199	
200	
403	

Table A.2.: List of supported decays.

RTYP	decay
3	IT
3.4	IT+A
4	A
4.44	3A
5	N
5.5	2N
5.55	3N
7	P
7.7	2P
7.77	3P
2	B+
2.2	B++B+
2.2	B++EC
2.7	B++P
2.77	B++2P
2.777	B++3P
2.4	B++A
2.74	B++P+A
1	B-
1.1	B-+B-
1.5	B-+N
1.55	B-+2N
1.555	B-+3N
1.5555	B-+4N
1.54	B-+N+A
1.7	B-+P
1.77	B-+2P
1.777	B-+3P
1.4	B-+A
1.6	B-+SF
2	EC
2.2	EC+EC
2.7	EC+P
2.77	EC+2P
2.777	EC+3P
2.4	EC+A
2.74	EC+P+A
6	SF
2.6	EC+SF

```
        "360830": 0.72674257575841,
        "360840": 2.3709119242128,
        "360850": 0.34518804481507,
        "360860": 3.743254613572,
        "370850": 2.1779153793415,
        "370870": 4.8454707810852,
        "380860": 0.015167887288537,
        "380880": 6.7267514619892,
        "380890": 3.6205808230117995e-12,
        "380900": 8.6022359631824,
        "390890": 8.6019137398732,
        "390900": 0.0021854723201121,
        "390910": 1.7156376582252001e-10,
        "400900": 1.7794763996566,
        "400910": 11.128396052906,
        "400920": 12.15183649852,
        "400930": 13.506906289477,
        "400940": 14.198555943305,
        "400950": 1.8741119231781e-09,
        "400960": 14.737904039901,
        "410930": 8.507119710636e-06,
        "410931": 3.8748608914142e-05,
        "410950": 2.2580839344246e-09,
        "420950": 13.642742190223,
        "420960": 1.2162284821407,
        "420970": 14.56720657087,
        "420980": 15.09139366422,
        "421000": 16.735334677234,
        "430990": 13.522178532136,
        "441000": 2.5002248361909,
        "441010": 13.621113412717,
        "441020": 14.595948346312,
        "441030": 5.0818446060911e-15,
        "441040": 10.102632085187,
        "441060": 0.073237146096229,
        "451030": 7.1852500070091,
        "451031": 4.9885949879661e-18,
        "451060": 6.8248452895339e-08,
        "461040": 5.4066997915965,
        "461050": 7.3949113115351,
        "461060": 6.8041128145639,
        "461070": 4.1410309123312,
        "461080": 2.8280975310822,
        "461100": 0.99858388881854,
        "471070": 2.9875712390665e-06,
        "471081": 7.6599769755026e-06,
        "471090": 1.2899327871333,
        "471101": 0.00010168011844481,
        "481100": 0.91053003161165,
        "481110": 0.41659938453452,
        "481120": 0.19914309782105,
        "481130": 0.0010514913220594,
        "481131": 0.0012322008378434,
        "481140": 0.2235415572139,
```

```
        "481151": 1.0773193261495001e-16,
        "481160": 0.08832163958054,
        "491130": 0.00047313241768961,
        "491150": 0.021716786336439,
        "501150": 0.0037447403040125,
        "501160": 0.056071810006879,
        "501170": 0.077559580896194,
        "501180": 0.076062594530539,
        "501190": 0.077276132459355,
        "501191": 9.69474895808e-05,
        "501200": 0.074369416828298,
        "501210": 3.0235403186468e-07,
        "501211": 0.0069494146929998,
        "501220": 0.11010225334858,
        "501230": 1.5250226053575e-07,
        "501240": 0.19029265775263,
        "501260": 0.38590638993465,
        "511210": 0.072847192617497,
        "511230": 0.12263363862282,
        "511240": 7.1370953250518e-13,
        "511250": 0.034783729138652,
        "511260": 7.9748892321118e-09,
        "511261": 6.093201816672e-11,
        "511262": 3.9145711047867e-13,
        "521220": 0.007648238018647,
        "521230": 0.00010402589064816,
        "521231": 7.048981611453901e-10,
        "521240": 0.0088682833508078,
        "521250": 0.15484131668604,
        "521251": 0.00047021302157613,
        "521260": 0.059492092843843,
        "521270": 4.628306084277e-10,
        "521271": 1.3220359072498e-07,
        "521280": 1.3995454028186,
        "521291": 1.2490946028377e-18,
        "521300": 5.5557693374153,
        "531270": 0.64571933354395,
        "531290": 2.4089803135713,
        "541280": 0.058476397482235,
        "541300": 0.15941267652678,
        "541310": 4.8478470653493,
        "541320": 15.748257177702,
        "541340": 19.36823886139,
        "541360": 30.364504251048,
        "551330": 13.758317614995,
        "551340": 0.39500130240851,
        "551350": 5.4934699682,
        "551370": 13.923609747867,
        "561340": 3.0007668755086,
        "561350": 0.016249357310568,
        "561360": 0.38245817650441,
        "561370": 2.6086494173474,
        "561371": 2.1230147211515e-06,
        "561380": 16.836789181469,
```

```
        "571390": 15.757131669436,
        "581400": 15.760271818165,
        "581410": 4.6201674427503e-18,
        "581420": 14.386974283344,
        "581440": 0.03084354290399,
        "591410": 14.05128675762,
        "591420": 6.2760504900881e-19,
        "591440": 1.2987334771692e-06,
        "601420": 0.4013109762753,
        "601430": 8.2277945292184,
        "601440": 17.723730102869,
        "601450": 7.695171035162,
        "601460": 9.1488523874465,
        "601480": 4.505782663796,
        "601500": 2.1802198124666,
        "611470": 0.41376720478802,
        "611480": 3.4930428261261e-18,
        "611481": 4.6437715803428e-16,
        "621470": 2.0929583340008,
        "621480": 2.1687293673475,
        "621490": 0.024577636013694,
        "621500": 3.4394511727,
        "621510": 0.10059907574249,
        "621520": 1.0100950413495,
        "621540": 0.4660331399483,
        "631510": 0.0040572032236143,
        "631520": 6.3180861458422e-05,
        "631530": 1.3717039099904,
        "631540": 0.2146220900108,
        "631550": 0.048954298377524,
        "641540": 0.15026969636901,
        "641550": 0.053367415707082,
        "641560": 1.5126581176204,
        "641570": 0.0014847580430181,
        "641580": 0.30395434617356,
        "641600": 0.027698503762476,
        "651590": 0.043386150896971,
        "651600": 3.6660779380695004e-11,
        "661600": 0.0058602740379483,
        "661610": 0.010649870080869,
        "661620": 0.011939182713173,
        "661630": 0.009852994866321,
        "661640": 0.0029075436453227,
        "671650": 0.0064764618813627,
        "671661": 8.9872469733624e-05,
        "882240": 1.2549285645028e-09,
        "882260": 2.4329278112125e-11,
        "902280": 2.4139054202979e-07,
        "902290": 8.6517071427453e-09,
        "902300": 1.0617937401e-06,
        "902320": 6.2805871756019e-06,
        "912310": 2.6418758954523e-07,
        "912320": 1.2474608581529e-16,
        "912330": 1.2245696939524e-07,
```

```
        "922320": 1.259096873629e-05,
        "922330": 7.5735490085143e-06,
        "922340": 0.10696971103186,
        "922350": 24.274405852446,
        "922360": 26.500449358692,
        "922370": 1.9574930269189e-07,
        "922380": 3832.1900761346,
        "932360": 3.30422829454e-06,
        "932370": 3.5453209546322,
        "932380": 1.0791671955048e-09,
        "932390": 1.1632425588037e-06,
        "942360": 3.8932496616889e-06,
        "942370": 3.0493701571926003e-18,
        "942380": 2.1226151393189,
        "942390": 24.979467563392,
        "942400": 13.260487033621,
        "942410": 6.1622215921331,
        "942420": 4.9568844157452,
        "942430": 5.1035534173624e-15,
        "942440": 0.0005292787090352,
        "952410": 1.9467457979348,
        "952420": 7.3240585305225e-08,
        "952421": 0.0056699322195344,
        "952430": 1.3287135722217,
        "962420": 7.5261382359378e-05,
        "962430": 0.0040071218337861,
        "962440": 0.60624253666045,
        "962450": 0.051821730988723,
        "962460": 0.010060421059062,
        "962470": 0.00014443193840274,
        "962480": 1.3127762363209e-05,
        "972490": 3.3067734106134e-09,
        "982490": 1.9826905642876e-07,
        "982500": 9.9173622004726e-08,
        "982510": 3.2198235876246e-08,
        "982520": 7.2065621311062e-09
    },
    "time_bins": [
        0.0,
        31557600000000.0
    ],
    "ffmt": 454,
    "csv_per_step": false,
    "csv_per_meas": true,
    "json": true
}
```

Appendix

GENF/D: list of faulty isotopes

B.

Même si c'est faux, au moins c'est beau

(Ronan Viel*, 2025)*

Issue with half-life

^{12}Li, ^{23}C, ^{13}F, ^{17}Na, ^{41}Mg, ^{24}P, ^{32}K, ^{32m}K, ^{33}Ca, ^{35}Sc, ^{36}Sc, ^{37}Sc, ^{38m}Sc, ^{39}Sc, ^{37}Ti, ^{39}V, ^{40}V, ^{41}V, ^{44n}V, ^{41}Cr, ^{43}Mn, ^{47m}Fe, ^{47}Co, ^{48}Co, ^{52}Cu, ^{84}Cu, ^{86}Zn, ^{56}Ga, ^{57}Ga, ^{58}Ga, ^{58m}Ga, ^{61m}Ga, ^{88}Ga, ^{58}Ge, ^{60}As, ^{60m}As, ^{61}As, ^{62}As, ^{67}Br, ^{69m}Br, ^{69n}Br, ^{71}Rb, ^{71m}Rb, ^{71n}Rb, ^{72m}Rb, ^{73m}Rb, ^{79}Nb, ^{80}Nb, ^{83}Tc, ^{84}Tc, ^{133}Ag, ^{135}Cd, ^{102}Sb, ^{106}I, ^{159}Ce, ^{170}Eu, ^{145m}Tb, ^{182}Tm, ^{163}Ir, ^{168}Au, ^{178q}Au, ^{192p}Tl, ^{250p}Bk.

Issue with spin

^{10}Li, ^{12}Li, ^{20}B, ^{10}N, ^{35}Mg, ^{35}Al, ^{40}P, ^{45}Ar, ^{54m}Sc, ^{63}V, ^{64}V, ^{70}Mn, ^{72}Co, ^{72m}Co, ^{81}Zn, ^{85}Ge, ^{86}As, ^{87}As, ^{89}Br, ^{97m}Rb, ^{102m}Y, ^{104}Y, ^{86m}Nb, ^{104m}Nb, ^{106}Tc, ^{118m}Ag, ^{96n}Cd, ^{140m}Sb, ^{109}I, ^{126}Pr, ^{130}Pm, ^{158}Pm, ^{129}Sm, ^{142}Ho, ^{152}Lu, ^{160m}Ta, ^{164m}Re, ^{170}Re, ^{179p}Re, ^{168m}Ir, ^{172}Ir, ^{174}Ir, ^{174m}Ir, ^{185m}Ir, ^{196}Ir, ^{200}Ir, ^{172m}Au, ^{178}Au, ^{178m}Au, ^{178n}Au, ^{178p}Au, ^{176}Tl, ^{178}Tl, ^{210m}Tl, ^{194m}Bi, ^{216}Bi, ^{187}Po, ^{218}At, ^{242n}Am, ^{256}Lr, ^{262m}Rf.

Issue with negative Q-values

^{31}Ar, ^{55}Ti, ^{69}Fe, ^{78}Ni, ^{68}Kr, ^{85}Ru, ^{173}Dy, ^{179}Tm, ^{186}Lu, ^{219}Bi, ^{225}At, ^{260}Rf, ^{290}Fl

Issue with LIS-LISO links

^{130p}In, ^{143m}Gd, ^{145m}Gd, ^{150m}Tb, ^{151m}Tb, ^{156m}Tb, ^{176m}Au, ^{191m}Hg, ^{195m}Hg, ^{194m}Tl, ^{215m}Bi, ^{234m}Pa

Missing isotopes according to other evaluated databses

Hence 59 isotopes are taken from JENDL-5, 9 from JEFF-3.3 and 4 from EAF-2010. The 5 from ENDF/B-VII.0, 3 from JEFF-2.2 and one from JENDL-FPD-2000 were ignored, as they were not kept in their updated distributions.

Appendix

Inventory of ADS decay data needs

C.

I have a pen, I have an apple. Uh!
Apple pen

(Pikotaro, *"PPAP (Pen-Pineapple-Apple-Pen)" song – 2016)*

C.1. ADS test libraries 206
C.2. Status on decay data 207
C.2.1. Short Lived Isotopes 208
C.2.2. Delayed neutron emitters 211
C.3. Status on Fission Fragments 215
C.3.1. Spontaneous fission 215
C.3.2. Neutron-induced fission 219
C.4. Conclusion 221

Nuclear data are key for the modellisation of any physics system. Decay data are fundamental in order to define a coherent identity of the different isotopes (Z, A, but also excitation energy (ELIS), designated by an integer (LISO), as well as spin, parity, ...)

Several evaluations are available, from organisations that either do the experimental acquisition, or do deep review of any published data, or both. Each have their particularity, aiming for different application, be it focused on a only a few nuclides, or extended to any nuclides experimentally observed or even predicted.

The main database, with data covering most on the known nuclear chart, are ENDF/B

(VIII.1) [81][1], JENDL (5) [92][2], JEFF (4) [82][3], CENDL (3.2) [116][4]. These are "evaluated" database, released in a specific format: ENDF-6 [108][5]. This format is designed for computer parsing. Decay data is primarily released in ENSDF format, the 4 collaboration mentioned operate the translation and the additional evaluation.

The picture cannot be complete without mentioning NUBASE2020 [16][6]. Released along side the Atomic Mass Evaluation (AME) project, it contains the recommended values of the main nuclear physics properties for all nuclei in their ground and excited, isomeric ($T_{1/2} \geq 100$ ns) states. NUBASE encompasses all experimental data published in primary (journal articles) and secondary (mainly laboratory reports and conference proceedings) references, together with the corresponding bibliographical information. In cases where no experimental data were available for a particular nuclide, trends in the behaviour of specific properties in neighbouring nuclei were examined and estimated values are proposed.

Such situation, makes NUBASE2020 the most extensive database currently. As such, GENF/D (chapter 5) is an attempt to translate this database into ENDF-6 format. Secondary goal of GENF/D is to provide all the further estimates brought by Radiation-Report, but also BetaShape (a code adopted by IAEA NSDD Network for beta spectra re-computation) and GEF (a Monte Carlo code for Fission Fragments modelling).

C.1. ADS test libraries

These two "beta" libraries prepared by the IAEA are evaluated libraries, dedicated to ADS tests and current benchmarks. They do focus only on neutron cross-sections, as of now, but provides insight on nuclides of interest for the ADS field.

The ADS-2.0 proposes evaluated neutron cross-sections for 156 target nuclides, whereas the ADS-HE interest was to expand the energy range beyond the usual 20 MeV up to

[1] D. A. Brown et al. 'ENDF/B-VIII.0: The 8th Major Release of the Nuclear Reaction Data Library with CIELO-project Cross Sections, New Standards and Thermal Scattering Data'. In: *Nuclear Data Sheets*. Special Issue on Nuclear Reaction Data 148 (Feb. 2018), pp. 1–142. ISSN: 0090-3752. DOI: 10.1016/j.nds.2018.02.001.

[2] Osamu Iwamoto et al. 'Japanese evaluated nuclear data library version 5: JENDL-5'. In: *Journal of Nuclear Science and Technology* 60.1 (Jan. 2023). _eprint: https://doi.org/10.1080/00223131.2022.2141903, pp. 1–60. ISSN: 0022-3131. DOI: 10.1080/00223131.2022.2141903.

[3] A. J. M. Plompen et al. 'The joint evaluated fission and fusion nuclear data library, JEFF-3.3'. en. In: *The European Physical Journal A* 56.7 (July 2020), p. 181. ISSN: 1434-601X. DOI: 10.1140/epja/s10050-020-00141-9.

[4] Zhigang Ge et al. 'CENDL-3.2: The new version of Chinese general purpose evaluated nuclear data library'. en. In: *EPJ Web of Conferences* 239 (2020), p. 09001. ISSN: 2100-014X. DOI: 10.1051/epjconf/202023909001.

[5] David A. Brown. *ENDF-6 Formats Manual - Data Formats and Procedures for the Evaluated Nuclear Data Files ENDF/B-VI, ENDF/B-VII and ENDF/B-VIII*. English. Tech. rep. BNL-224854-2023-INRE. Brookhaven National Laboratory (BNL), Upton, NY (United States), Sept. 2023. DOI: 10.2172/2007538.

[6] F.G. Kondev et al. 'The NUBASE2020 evaluation of nuclear physics properties *'. en. In: *Chinese Physics C* 45.3 (Mar. 2021), p. 030001. ISSN: 1674-1137, 2058-6132. DOI: 10.1088/1674-1137/abddae.

1 GeV of such cross-sections with, for now, ^{202}Hg, ^{208}Pb, ^{209}Bi, ^{232}Th, ^{235}U, ^{238}U, ^{237}Np, ^{239}Pu, ^{242}Am and ^{245}Cm. From these incident neutron data, 743 isotopes can be produced, accounting for neither the decay by-products nor the fission fragments. They are represented in Figure C.1.

There is interest to pursuing this effort, by tackling first decay (and fission fragments) allowing to define the basic isotopes properties. And extend to proton and neutron cross-sections. The alpha-, but also the photon-incident cross-sections, should not be overseen as the energy considered with ADS put the by-products particles far higher than most reactions thresholds

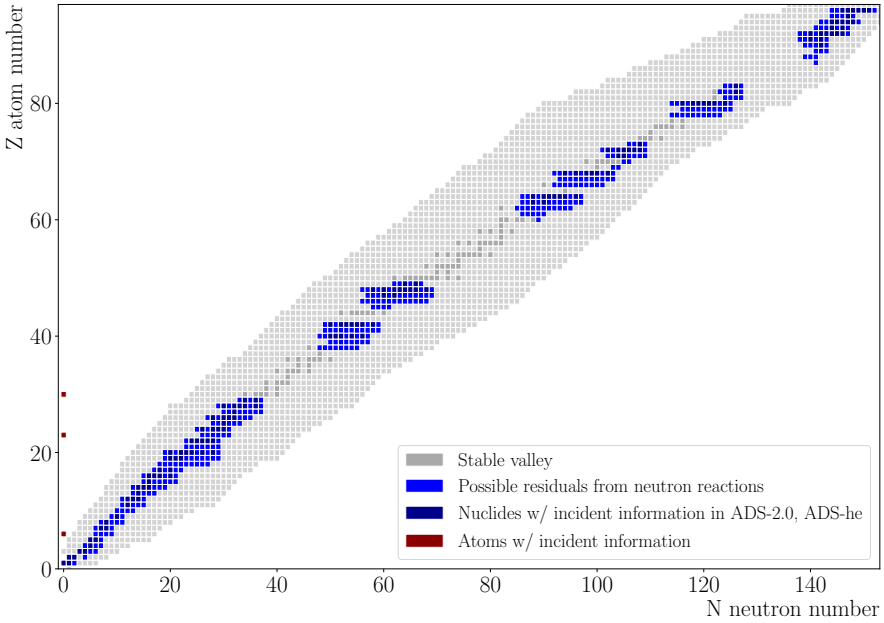

Figure C.1.: Distribution of nuclides present in current ADS libraries

C.2. Status on decay data

Let's start with some statistics :

- JEFF: 3084 ground states (768 excited states), with 4340 channels (4340 non-null)
- JENDL: 3274 ground states (797 excited states), with 4509 channels (4509 non-null)
- ENDF/B: 3083 ground states (738 excited states), with 4354 channels (4354 non-null)
- GENF/D: 3511 ground states (1990 excited states), with 5799 channels (4731 non-null)
- NUBASE: 3558 ground states (2007 excited states)

Comparing isomeric states is not easy, as the definition can differ between database. Indeed, Excitation Energy can be different (either due to the number of digits used, or from consideration of different metastable states). So from now on, except when specifically mentioned, only ground states are considered. There are 3556 nuclides registered in total (3281 without GENF/D). 3057 are present in all libraries. If we check the nuclides, that are missing from this total, we have :

- JEFF: 472 are missing (197 without GENF/D)
- JENDL: 282 are missing (7 without GENF/D)
- ENDF/B: 473 are missing (198 without GENF/D)
- GENF/D: 45 are missing (45 without GENF/D)
- NUBASE: 18 are missing (18 without GENF/D)

The Figure C.2 represent the location of the missing nuclides. If we compare them against NUBASE2020, the situation get worse. There are 3576 nuclides registered in total. 3075 are present in all four DB. Summing the missing nuclides:

- JEFF: 492 are missing
- JENDL: 302 are missing
- ENDF/B: 493 are missing
- NUBASE: 18 are missing

Of the 18, most of the isotopes missing from NUBASE are for $N > 160$, or on the exterior of the "standard" chart. The ground state nuclides missing from NUBASE, with respect to evaluated databases, are ^{89}Ga, ^{91}Ge, ^{93}As, ^{94}As, ^{95}As, ^{96}Se, ^{99}Br, ^{100}Br, ^{102}Kr, ^{105}Rb, ^{136}Cd, ^{138}In, ^{143}Sb, ^{148}I, ^{160}Ce, ^{162}Pr, ^{164}Nd, ^{166}Pm.

There is hence interest in translating NUBASE-2020, as GENF/D is about, especially to manage the excited states. More than a thousand additional nuclides can be tracked, compared to regular databases.

C.2.1. Short Lived Isotopes

Considering Ground States only, over the 4 libraries, 1732 nuclides have half-life below 10 seconds (1529 without GENF/D), of which 1286 are commonly below 10s (1307 without GENF/D). In this delta of 446 isotopes, 47 nuclides are present in every database (65 without GENF/D).

Considering the 1732 nuclides,

- JEFF: have 381 undefined half-lives
- JENDL: have 204 undefined half-lives
- ENDF/B: have 374 undefined half-lives
- GENF/D: have 55 undefined half-lives
- NUBASE: have 45 undefined half-lives

Taking as reference NUBASE, as it has the biggest coverage, and plotting this discrepancies (Figure C.3), we get a some very high discrepancies.

(a) JEFF-4

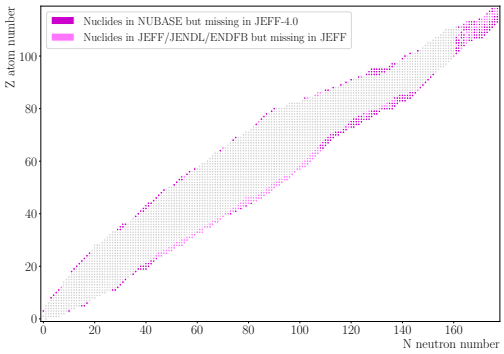

(b) JENDL-5

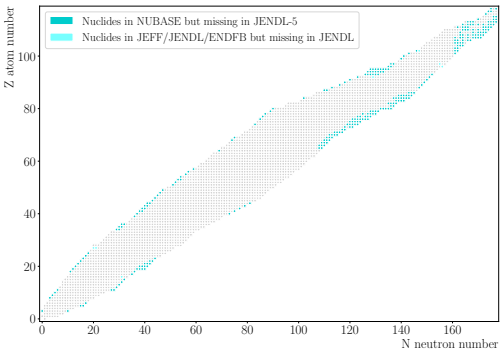

(c) ENDF/B-VIII.1

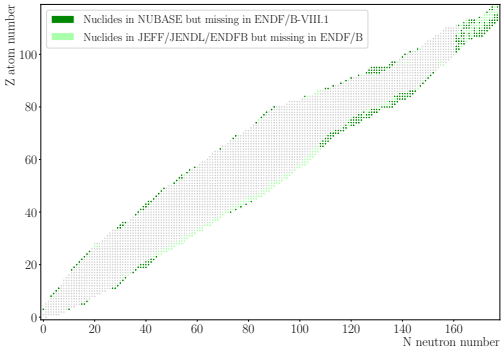

(d) GENF/D

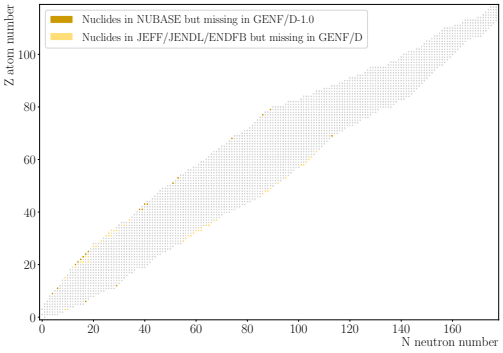

Figure C.2.: Distribution of missing ground states between evaluated databases and NUBASE20

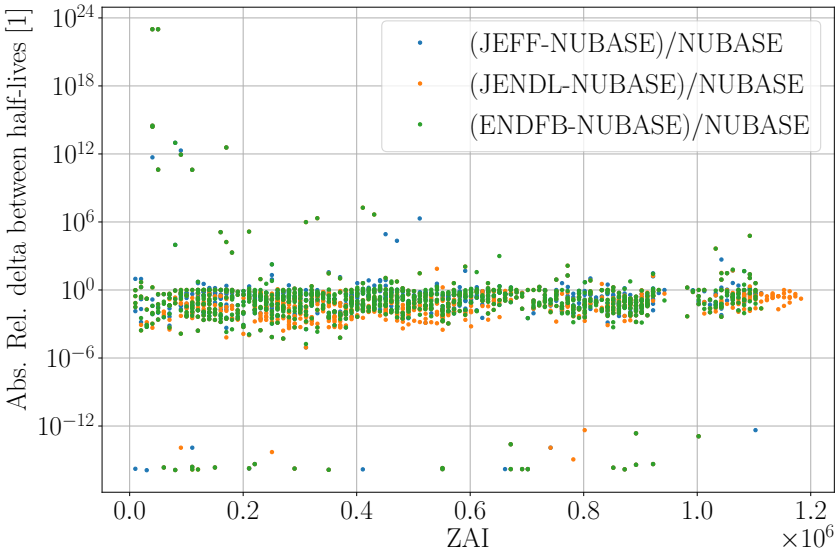

Figure C.3.: Discrepancies in short half-lives against NUBASE2020

As shown, some isotopes can consider very different half-lives, in absolute value of the relative difference with respect to NUBASE (Table C.1). Of course, there are virtually no difference expected between GENF/D and NUBASE, as they are the same database. When comparing to JENDL (Table C.2), discrepancies are "tighter" but there are still a few long half-lives with important differences, that should be investigated.

Table C.1.: Average and median half-lives of isotopes with ambiguous half-lives, with respect to NUBASE.

Database	Mean [s]	Median [s]
JEFF	1.509×10^{20}	3.148×10^{-2}
JENDL	1.353×10^{20}	5.909×10^{-3}
ENDF/B	1.504×10^{20}	3.325×10^{-2}
GENF/D	1.561×10^{-9}	0.00

If we list explicitly the isotopes with half-lives discrepancies larger than 100 %, there are 129 isotopes, using NUBASE as reference, and discarding ground states not present in it.

Among them, 18 have in at least one database an half-life larger than 10 seconds, and 38 larger than one second. In ADS lib, we find 16 of them (16 without GENFD), see Table C.4.

^{58}Mn is the isotope of concern in this list, has it has the largest discrepancy compared to the other database. the other candidates would be long-lived isotopes as ^{151}Eu, ^{46}Ca

Table C.2.: Average and median half-lives of isotopes with ambiguous half-lives, with respect to JENDL.

Database	Mean [s]	Median [s]
JEFF	7.537×10^{9}	1.449×10^{-2}
ENDF/B	5.866×10^{9}	0.000
GENF/D	1.429×10^{6}	5.944×10^{-3}
NUBASE	1.429×10^{6}	5.944×10^{-3}

or ^{160}Gd. But has their half-lives is extremely long, estimating their half-lives is not an easy task.

C.2.2. Delayed neutron emitters

There are some uncertainties on the existence of delayed neutrons, within evaluated databases. Some are considered as neutron emitters, whereas other may only consider the prompt beta emission. In this section, we will catalogue the nuclides, where discrepancies between databases are observed. We will consider as usual, JEFF-4.0, JENDL-5, ENDF/B-VIII.1, GENF/D-1.0 and NUBASE2020. All the decay channels available are: 'B-', '2B-', 'B-A', 'B-N', 'B-2N', 'B-3N', 'B-4N', 'B-SF', 'B-P', 'B-2P', 'B-3P', 'EC', '2EC', 'ECA', 'ECSF', 'ECP', 'ECPA', 'EC2P', 'EC3P', 'IT', 'A', '3A', 'N', '2N', '3N', 'SF', 'P', '2P', '3P', 'UKWN'. The one considered, and available, as delayed neutrons are 'B-N', 'B-2N', 'B-3N', 'B-4N', per database, we have (in parenthesis are presented without including GENF/D or NUBASE):

- JEFF: over the 520 (430) nuclides that does appear, 296 (206) are not registering delayed channels.
- JENDL: over the 653 (517) nuclides that does appear, 234 (98) are not registering delayed channels.
- ENDF/B: over the 520 (435) nuclides that does appear, 132 (47) are not registering delayed channels.
- GENF/D: over the 717 (492) nuclides that does appear, 13 (10) are not registering delayed channels.
- NUBASE: over the 726 (499) nuclides that does appear, 10 (10) are not registering delayed channels.

NUBASE indicates much more easily the possibility of delayed neutron emissions. The 10 "missing" nuclides are : ^{98m}Y, ^{159}Pm, ^{169}Eu, ^{128m}In, ^{76}Fe, ^{81}Ni, ^{73}Mn, ^{158}Nd, ^{82}Ni, ^{78}Co.

As shown in Figure C.4, JEFF is very conservative in the estimation of presence of delayed neutron channels. In ADS lib, we find 4 of them (2 without NUBASE/GENFD). Explicitly, they are ^{9}Li, ^{11}Be, ^{36}P and ^{48}K.

To better interpret, this situation, if we consider this nuclides in the light of neutron-induced yields. The NFY of JENDL-5 is used as they encompass the most nuclides, in

Table C.3.: Comprehensive list of isotopes with mean-lives discrepancies higher than 100 % (w.r.t. NUBASE), but half-lives greater than 1 s.

ZSYMAM	NUBASE	GENF/D	JEFF	JENDL	ENDF/B
^{265}Mt	0.002	0.002	0.002	120.0	120.0
^{251}Lr	0.0003	0.0003	0.000 15	1.341	1.341
^{60}Mn	0.28	0.28	51.0	0.28	51.0
^{121}Pr	0.012	0.012	0.6	1.4	1.4
^{266}Sg	0.39	0.39	21.0	21.0	25.0
^{273}Hs	1.06	1.06	50.0	0.76	50.0
^{140}Pm	9.2	9.2	9.2	9.2	357.0
^{255}Db	0.054	0.054	1.7	1.7	1.7
^{261}Rf	2.1	2.1	5.5	70.0	65.0
^{273}Mt	0.8	0.8	20.0	20.0	20.0
^{271}Mt	0.4	0.4	5.0	5.0	5.0
^{170}Re	1.0	1.0	9.2	9.2	9.2
^{262}Rf	0.25	0.25	2.3	2.3	2.3
^{186}Tl	3.5	3.5	40.0	27.5	27.5
^{209}Hg	6.3	6.3	37.0	6.0	36.5
^{104}Nb	0.98	0.98	4.9	4.9	4.9
^{170}Tb	0.96	0.96	3.0	0.96	3.0
^{144}Xe	0.388	0.388	0.388	0.388	1.15
^{188}Hf	7.0	7.0	20.0	20.0	20.0
^{175}Ho	1.88	1.88	5.0	2.888 95	5.0
^{237}Cf	0.8	0.8	2.1	2.1	2.1
^{138}Eu	5.0	5.0	12.1	12.1	12.1
^{97}Cd	1.16	1.16	2.8	2.8	2.8
^{174}Ho	3.7	3.7	8.0	3.2	8.0
^{160}Pm	0.725	0.725	2.0	0.725	1.561
^{136}Xe	6.88×10^{28}	6.88×10^{28}	3.16×10^{29}	5.21×10^{30}	0.00
^{184}Os	3.53×10^{20}	3.53×10^{20}	1.77×10^{21}	1.89×10^{20}	0.00
^{220}Po	10.0	10.0	40.0	3.0×10^{-7}	3.0×10^{-7}
^{270}Mt	0.8	0.8	2.0	0.48	0.006 05
^{265}Rf	96.0	96.0	46 800.0	1.0	1.0
^{258}Db	2.17	2.17	4.5	4.3	4.0
^{157}Nd	1.15	1.15	2.5	1.15	1.906
^{154}Ce	0.722	0.722	2.0	0.722	0.775
^{199}Ir	7.0	7.0	20.0	6.5	6.5
^{110}Rh	3.35	3.35	28.5	3.35	3.2
^{159}Pm	1.49	1.49	3.0	1.49	1.47
^{58}Mn	3.0	3.0	65.2	3.0	3.0
^{116}Ru	0.204	0.204	1.7	0.204	0.204

Table C.4.: Comprehensive list of isotopes with mean-lives discrepancies higher than 100 % (w.r.t. NUBASE), but half-lives greater than 1 s and present in ADS libraries.

ZSYMAM	NUBASE	GENF/D	JEFF	JENDL	ENDF/B
^{58}Mn	3.0	3.0	65.2	3.0	3.0
^{8}Be	8.19×10^{-17}	8.19×10^{-17}	7.0×10^{-17}	8.18×10^{-17}	8.18×10^{-17}
^{27}Si	4.117	4.117	4.16	4.16	4.16
^{30}Al	3.62	3.62	3.65	3.62	3.62
^{26}Na	1.071 28	1.071 28	1.08	1.071 28	1.077
^{48}K	6.83	6.83	6.8	6.83	6.8
^{6}He	0.806 92	0.806 92	0.8081	0.8067	0.8067
^{8}Li	0.84	0.8387	0.838	0.8399	0.838
^{39}Ca	0.8603	0.8603	0.8596	0.8603	0.8596
^{9}Li	0.1782	0.1782	0.1783	0.1782	0.1783
^{34}Cl	1.5267	1.5267	1.526	1.5266	1.5264
^{36}P	5.6	5.6	5.6	5.7	5.6
^{33}Si	6.18	6.18	6.18	6.11	6.11
^{31}S	2.5534	2.5534	2.5534	2.5534	2.572
^{151}Eu	1.45×10^{26}	1.45×10^{26}		2.21×10^{25}	0.0
^{46}Ca	stable				0.0
^{160}Gd	stable		4.10×10^{24}		0.0

(a) JEFF-4

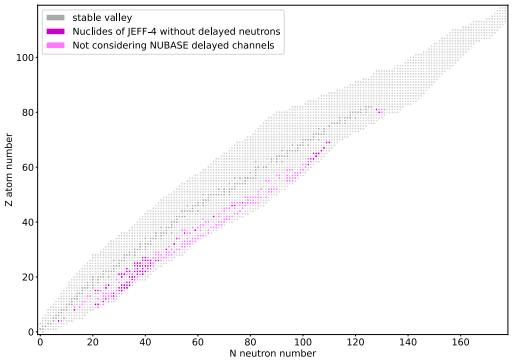

(b) JENDL-5

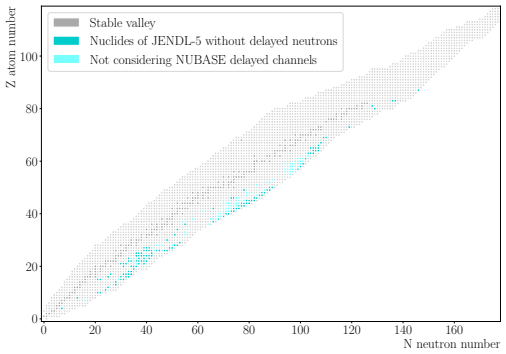

(c) ENDF/B-VIII.1

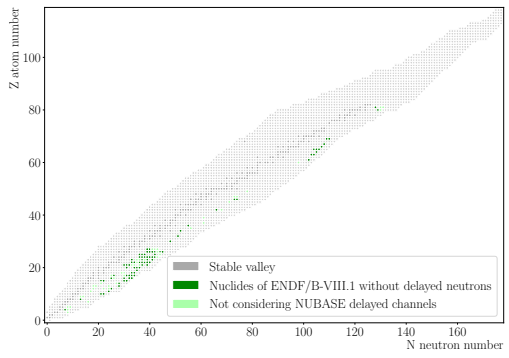

(d) GENF/D

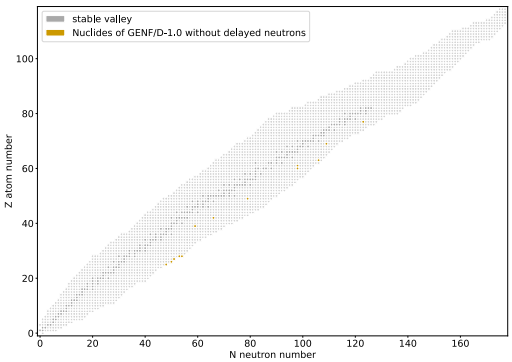

Figure C.4.: Distribution of missing delayed neutron channels between evaluated databases and NUBASE20

addition the YI values used correspond to the sum over all available NFY of JENDL-5 (so combining multiple targets).

If we list explicitly the nuclides overstepping the mean, we have :

- JEFF: ^{134}Sb, ^{104}Zr, ^{93}Kr, ^{147}Ba, ^{101}Y, ^{108}Mo, ^{91}Rb, ^{98}Sr, ^{92}Kr, ^{103}Zr, ^{92}Rb, ^{91}Kr, ^{148}La, ^{136}Te, ^{96}Sr, ^{147}La, ^{142}Cs, ^{103}Nb, ^{141}Cs;
- JENDL: ^{134}Sb, ^{108}Mo, ^{91}Rb, ^{91}Kr, ^{96}Sr, ^{103}Nb;
- ENDF/B: ^{108}Mo, ^{91}Kr;
- GENF/D: ^{108}Mo, ^{98m}Y;
- NUBASE: ^{98m}Y.

C.3. Status on Fission Fragments

The evaluated fission fragments (FF) are distributed for spontaneous decay, and neutron-induced fission. Both are provided, with independent yields (YI) and cumulative yields (YC), the latter take into account decay. In this report, we will only refer to independent yields.

C.3.1. Spontaneous fission

If we check the DD (Decay Database) content, and their mention of isotopes undergoing Spontaneous Fission (SF) :

- JEFF: 131 isotopes do SF, 119 gnds. Of which 131 are non-null, with $\langle \mathrm{BR} \rangle = 0.263$ (median = 0.030)
- JENDL: 98 isotopes do SF, 92 gnds. Of which 98 are non-null, with $\langle \mathrm{BR} \rangle = 0.340$ (median = 0.025)
- ENDF/B: 127 isotopes do SF, 117 gnds. Of which 127 are non-null, with $\langle \mathrm{BR} \rangle = 0.320$ (median = 0.078)
- GENF/D: 338 isotopes do SF, 279 gnds. Of which 275 are non-null, with $\langle \mathrm{BR} \rangle = 0.439$ (median = 0.500)

a) Nuclides with SFY lists

But if we check for Spontaneous Fission Yields (SFY), the lists provided are not as extensive: there are 401 target available in total (211 in GEF), and only 10 when not considering GEF/GENFD. Amongst them 2 target are available in all libraries (2 when not considering GEF/GENFD), which are ^{244}Cm, ^{252}Cf. Of this 401 targets, 52 are found in ADS test libraries (or 5 when not considering GEF/GENFD). The isotopes with SFY are represented in Figure C.5.

b) SFY lists content

Accounting for excited isomeric states, there are 3251 FF obtainable in total (1664 when not considering GEF or GENF/D). Amongst them 921 target are obtainable in all libraries (951 when not considering GEF or GENF/D). Considering gnds only:

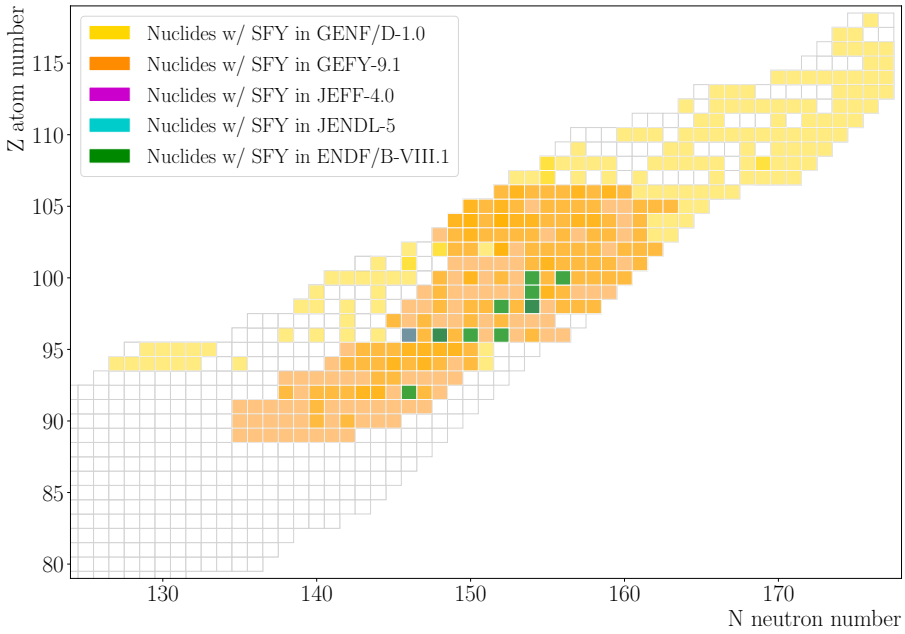

Figure C.5.: Nuclides with Fission Fragments lists for spontaneous fission

There are 1894 FF obtainable in total (1338 when not considering GEF or GENF/D). Amongst them 761 target are obtainable in all libraries (789 when not considering GEF or GENF/D). In ADS lib, we find 351 of them (247 without GEF/GENFD).

Only JEFF and JENDL account for the very rare ternary fission (three body emitted, in place of the 2 usual one, the third fragment is very light $Z < 4$). The Figure C.6 presents the sum of yield for all spontaneous decay nuclides, and the representation of such FF on the nuclear chart.

According to visual check of the distribution, JENDL merges datasets from ENDF/B and JEFF. With ENDF/B operating a cut at the two edges of the fission fragment distribution. As GEF, covers more targets, the general spread is slightly disfigured, and some low yields appear in the two high yields region, due to the finer description of excitation of fragments (here only FF in ground states are shown).

Example of a distribution But it is better, to check over a single fissioning nuclide, taking the example of Cm-244. The Figure C.7 represents the ground state nuclides, as above, but with the summation of yields of the isomers. As depicted in Figure C.8, the mass distribution are similar between databases, only the length of umbrella is different, except for the JEFF model that have higher discrepancies in the tails.

GEF model has the advantage, of enabling the estimation of Fragments for any nuclides, with a more detailed description of the intermediate states, as it uses NUBASE2020. The released version (GEFY-9.1) does not correspond with latest version of GEF, the FF of GENF/D are provided with model of version 2025.1.2, with higher primaries (GEF is

(a) JEFF-4

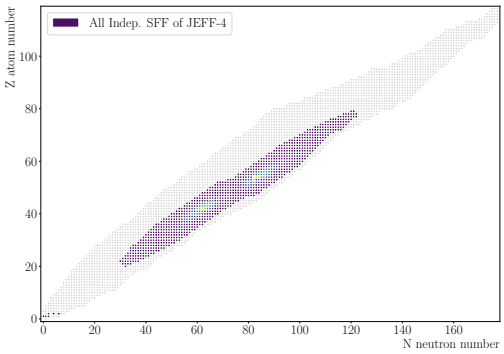

(b) JENDL-5

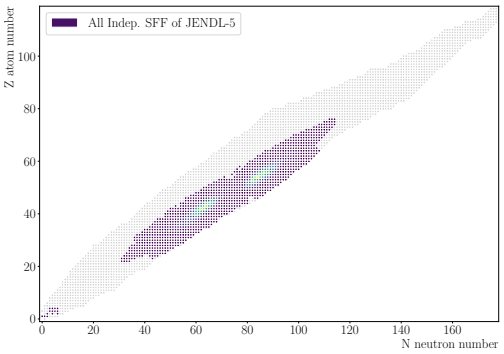

(c) ENDF/B-VIII.1

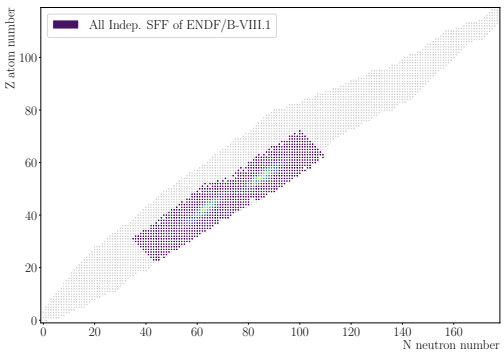

(d) GEFY-9.1

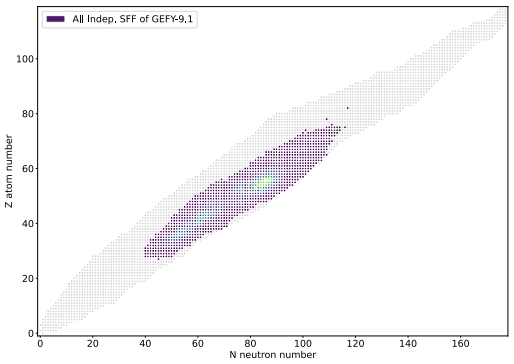

Figure C.6.: Distribution of all spontaneous fission yields per evaluated databases

(a) JEFF-4

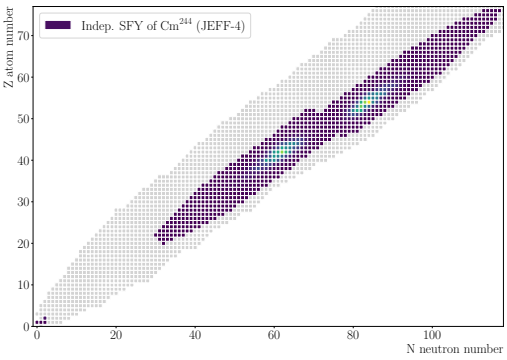

(b) JENDL-5

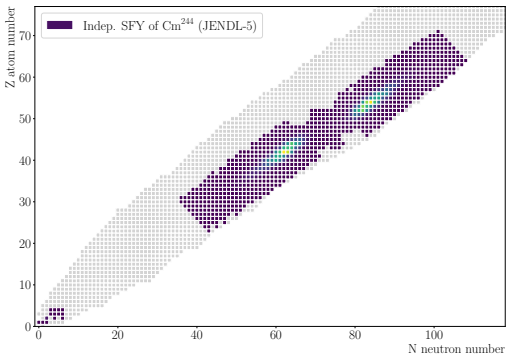

(c) ENDF/B-VIII.1

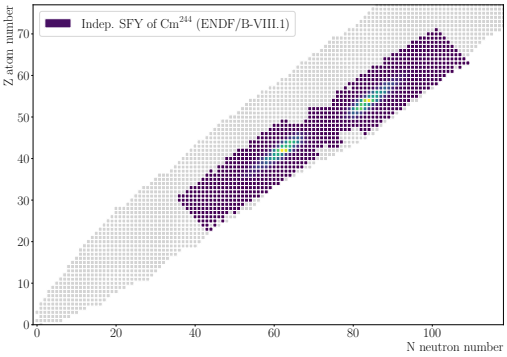

(d) GEFY-9.1

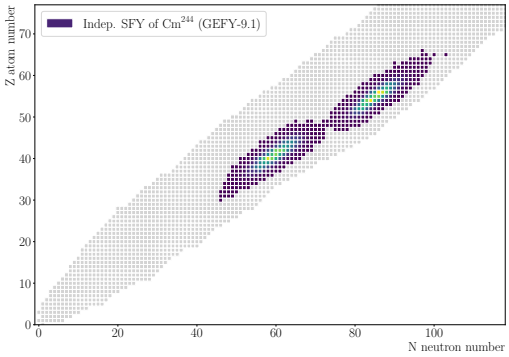

(e) GENF/D

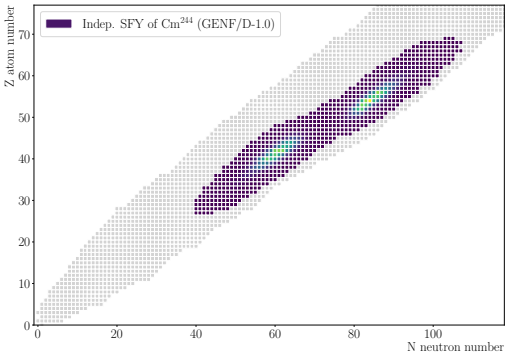

Figure C.7.: Distribution of spontaneous fission yields for ^{244}Cm per evaluated databases

(a) ENDF/B-VIII.1 (b) GEFY-9.1

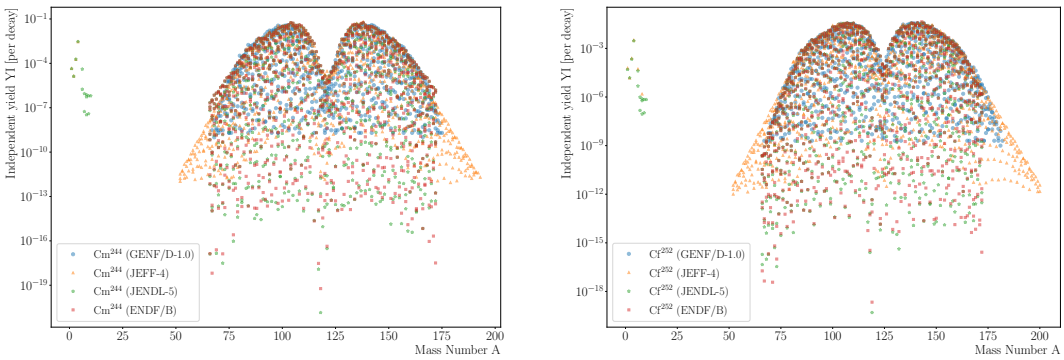

Figure C.8.: Mass distribution of spontaneous fission yields for ^{244}Cm and ^{252}Cf

a MonteCarlo code, GENF/D was ran with 1×10^9 primaries, against 1×10^5 for GEFY). The advantage of GEF is that it directly generate ENDF-6 files, and the database can be easily changed. It is mandatory to change the fission fragment list, and that they corresponds to their own reference.

C.3.2. Neutron-induced fission

There will be no mention of GENF/D NFY library, as the library has not yet been prepared, consequently the list of targets addressed here, will help list the nuclides that needs potential NFY list.

a) Fission cross-sections

If we give a little overview, there are 963 nuclides that can do fission (MT=18,19, 20,21,38 present in MF=3), this number corresponds to the databases listed below (in addition to INDEN, IRDFF, ROSFOND, IAEA-Standard, WIND, and the previous version of all mentioned libraries)

- ADS-2.0: 23 nuclides
- ADS-he: 8 nuclides
- BROND-3.1: 39 nuclides
- CENDL-3.2: 30 nuclides
- EAF-2010: 95 nuclides
- ENDFB-VIII.1: 99 nuclides
- FENDL-3.2c: 8 nuclides
- JEFF-3.3: 115 nuclides
- JEFF-4.0: 933 nuclides
- JENDL-5: 92 nuclides
- TENDL-2023: 927 nuclides

JEFF-4.0 has significantly more nuclides that can potentially fission, as they incorporate the TENDL (including TENDL-2025 beta) results, where they have not their own evaluations.

Considering only ENDFB-VIII.1, JEFF-4.0, JENDL-5, TENDL-2023, there are 951 targets, with 83 appearing in all libraries (Figure C.9).

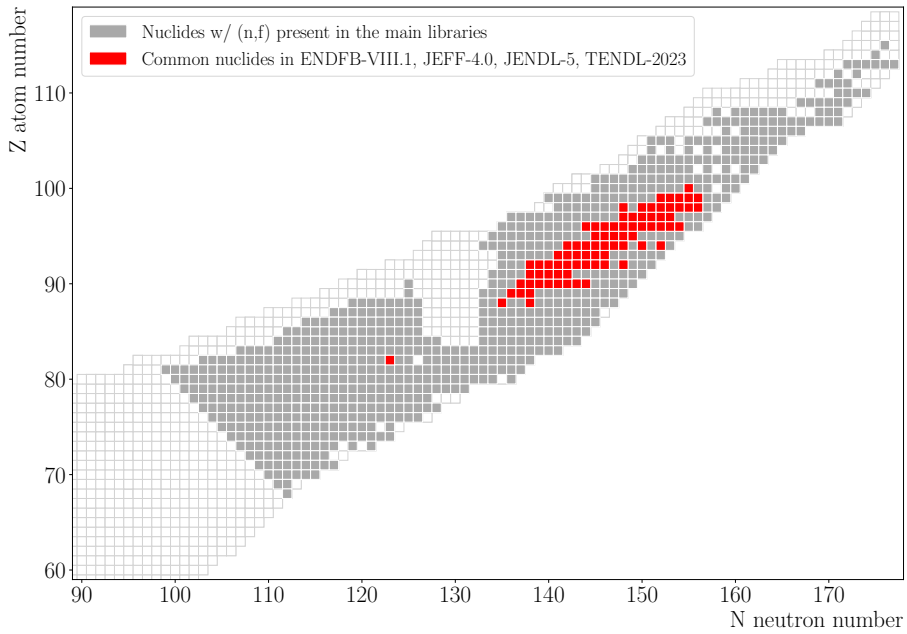

Figure C.9.: Distribution of nuclides with Neutron Induced Cross-sections

This accounting is based only on the presence of (n,f) reaction in the File 3 of the database. But if one wants to do a actual inventory list, the cross-section is not sufficient. The File 8 presents the list of fragments. In ADS lib, we find 108 of them (47 in the selection).

b) Nuclides with NFY lists

Considering ENDF/B-VIII.1, JEFF-4.0, JENDL-5 and GEFY-9.1, there are 164 target available in total (159 in GEF), and only 36 when not considering GEF. Amongst them 2 target are available in all libraries (2 when not considering GEF), as shown in Figure C.10. In ADS lib, we find 55 of them (26 without GEF).

Hence to have a complete inventory of a reactor, the current status of datasets is limited. GEF code offer the possibility to access all of the missing nuclides.

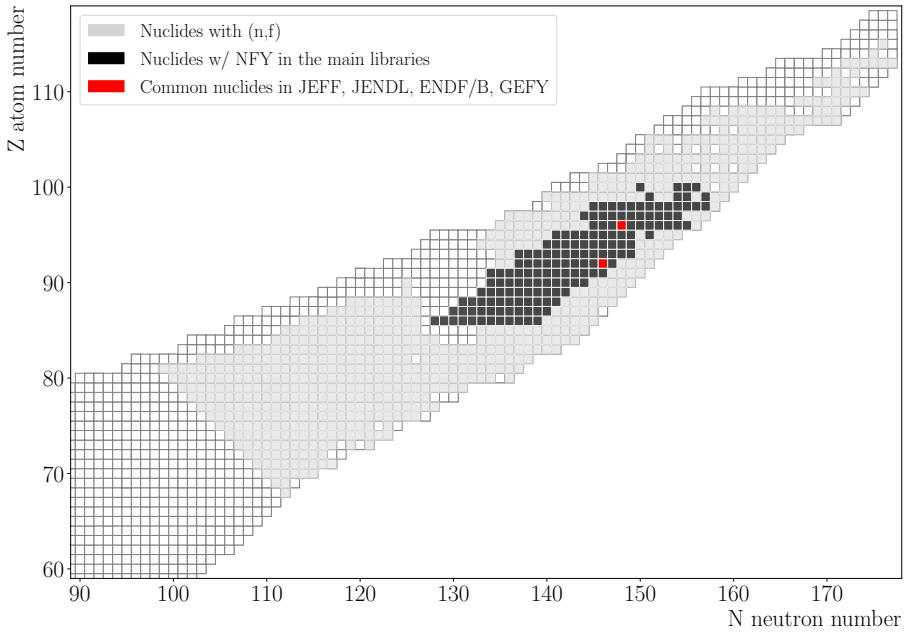

Figure C.10.: Distribution of nuclides with Neutron Induced Fission Yields

c) NFY lists content

There are 1817 FF obtainable in total (1729 when not considering GEF). Amongst them 987 target are obtainable in all libraries (991 when not considering GEF). Considering gnds only: there are 1447 FF obtainable in total (1387 when not considering GEF). Amongst them 824 target are obtainable in all libraries (843 when not considering GEF). In ADS lib, we find 285 of them (272 without GEF). The Fission Fragments spread on the Segrè Map (Figure C.11) is similar to the SFY (Figure C.6).

C.4. Conclusion

The fission fragments list are very lacking, be it for spontaneous fission and for neutron-induced fission. As highlighted in this review, there is interest in generating a more complete list of fission fragments. There are several tools able to estimate this fragments, this review focused on GEF, but the model is not complete (does not include ternary fission) and should be compared to the other similar codes (FREYA, FIFRELIN, ...). The most important concern is the validation of this fragments, there are only an handfull of complete fission fragment list. In addition, they are measured in thermal reactor, where the spectrum is considered as only thermal. This simplification is understandable as the fragments does not vary much below . But creates a biais. A deeper bibliography review is necessary to find novel points of confirmation of the validity of the model, in order to choose between the different one available.

(a) JEFF-4

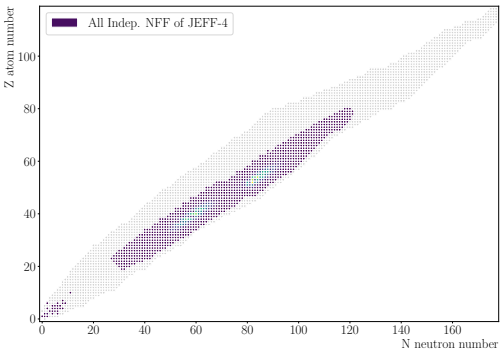

(b) JENDL-5

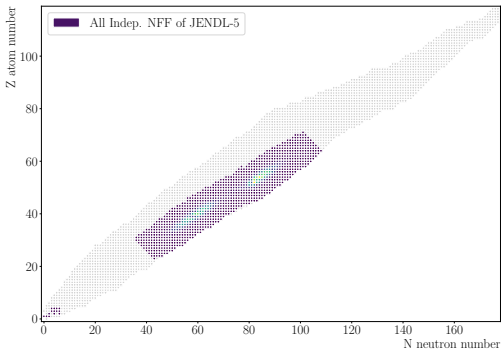

(c) ENDF/B-VIII.1

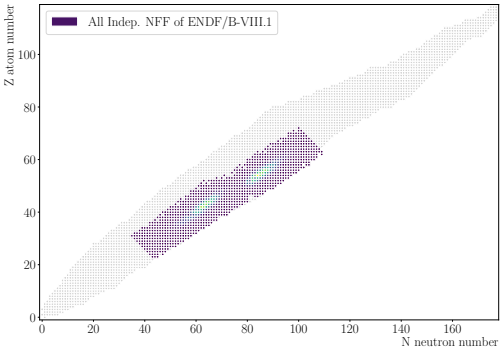

(d) GEFY-9.1

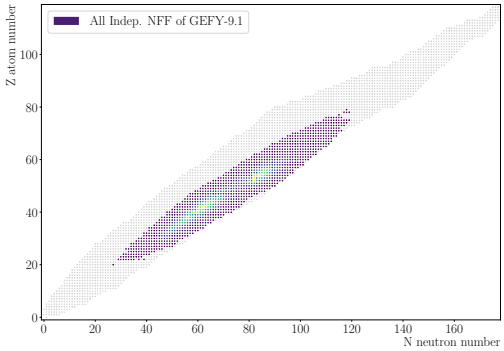

Figure C.11.: Distribution of all neutron-induced fission yields per evaluated databases

Another challenge highlighted in this document, is the prediction of delayed neutrons emission for neutron rich nuclides, in the lower belly of the FF lists. General contextualisation has been done, but review in the light of predicted content of ADS reactor (as the fuel) should be operated, to predict the impact of that. GENF/D offer a way to introduce this contribution, as NUBASE has a broader prediction of such channel and is the base for GENF/D. Comparison between JEFF and GENF/D should be conducted using either ADS benchmark, or regular reactor models. This study would ease the interpretation of the data, by introducing radiotoxicity and other observable, allowing to conclude on the effect of their presence or not. The estimation on their energy distribution is also a key factor, when considering radionuclides inventory consideration (propension to capture) but also for criticality computations. To conduct such review, especially compared to short-lived isotopes, would necessitate far greater time than can be allowed within a month. But this time would be well invested.

Short lived isotopes in one database can be considered as long-lived nuclides in another. Candidates have been highlighted in the prism of the ADS library. The available experimental data in ENSDF should be reviewed to focus and understand the large discrepancies in half-life that can be found between evaluated databases.

To end this complete picture, the experimental database reports should be reviewed for the isotopes highlighted within this report. But the discussion should also be transported in the cross-sections, to take into account production feasibility. There would be value, especially in fission models, to conduct fission experiments in heavy nuclides, has well has on the lower region, to validate the presence or not of predicted fission channel either spontaneous predicted by NUBASE, but also neutron-induced predicted by TENDL/TALYS.

Appendix

Condensé de thèse

Pas mal non ? C'est français.

(Orson Welles, *La classe américaine – 1993)*

D.0. Introduction . . . 226
D.1. Consideration générales . . . 231
D.1.1. Taxonomie nucléaire . . . 231
D.1.2. Radionucléides . . . 232
D.1.3. Activité et filiation radioactive . . . 232
D.1.4. Caractérisation des rayonnements ionisants . . . 233
D.1.5. Conclusion . . . 234
D.2. Activité induite auprès d'accélérateurs . . . 234
D.2.1. Généralités sur les Méthodes de Monte Carlo . . . 234
D.2.2. Méthodes expérimentales . . . 234
D.2.3. Études de cas pour l'évaluation de l'activation induite . . . 235
D.2.4. Conclusion et perspectives . . . 236
D.3. Synthèse : Résolution des équations de Bateman et développement du solveur `TMX_Bateman` . . . 236
D.3.1. Contexte et motivations . . . 237
D.3.2. Résolution des équations de Bateman . . . 237
D.3.3. Le solveur `TMX_Bateman` . . . 238
D.3.4. Validation et comparaison . . . 239
D.3.5. Applications supplémentaires . . . 239
D.3.6. Conclusion et perspectives . . . 240
D.4. GENF/D . . . 240
D.4.1. Contexte et nécessité d'une nouvelle base de données . . . 241
D.4.2. État des lieux des bases de données de désintégration . . . 241
D.4.3. Génération de la base GENF/D . . . 242
D.4.4. Comparaison avec les bases évaluées existantes . . . 243
D.4.5. Validation sur des mesures intégrales . . . 244
D.4.6. Conclusion et perspectives . . . 245
D.5. Conclusions . . . 246
D.6. Besoins en données nucléaires pour les ADS . . . 252
D.6.1. Comparaison des couvertures isotopiques . . . 252
D.6.2. Désaccords sur les périodes radioactives . . . 252
D.6.3. Émission neutronique retardée . . . 252
D.6.4. Fragments de fission . . . 252
D.6.5. Conclusion et perspectives . . . 253

D.0. Introduction

Depuis les travaux pionniers de G. Ising en 1924 et le brevet du cyclotron d'E. Lawrence en 1934, les accélérateurs de particules sont devenus une pierre angulaire de la science

moderne. Cette avancée a permis d'avoir des faisceaux de particules chargées contrôlés, et d'aboutir à des découvertes majeures et au développement d'une famille diversifiée d'accélérateurs (des LINAC aux synchrotrons). Au fil des décennies, leur utilisation s'est étendue au-delà de la recherche fondamentale vers des domaines critiques tels que la médecine (radiothérapie, production d'isotopes médicaux), l'industrie (traitement des matériaux, stérilisation), les sciences environnementales (analyse des polluants), et même l'art (datation et restauration d'oeuvres patrimoniales).

Cette évolution a conduit à une flotte vaste et croissante d'accélérateurs dans le monde. Le rapport EuCARD-2 estime qu'il y a plus de 30 000 accélérateurs en fonctionnement aujourd'hui dans le monde, dont seulement environ 1% sont utilisés pour la recherche "fondamentale". L'expansion des installations cliniques, comme le montre Figure 1, et la large gamme d'énergies des cyclotrons en utilisation (Figure 2), illustrent la croissance dynamique de la flotte mondiale. Cette flotte en expansion introduit une préoccupation grandissante à mesure que le parc vieilli : le démantèlement systématique et la gestion des déchets radioactifs de ces installations.

Quelques mots sur les ADS

Ce paysage devrait connaître une évolution significative avec l'émergence des ADS, une technologie nucléaire avancée conçue pour relever le double défi de la production d'énergie et de la gestion des déchets radioactifs à vie longue.

Un ADS comprend trois éléments clefs : un accélérateur de particules de haute puissance, une cible de spallation et un réacteur nucléaire sous-critique. Un tel concept a gagné en importance après la proposition de Carlo Rubbia en 1995. Le système fonctionnera en dirigeant un faisceau de protons de haute intensité (typiquement de l'ordre du mA) provenant de l'accélérateur vers une cible de spallation en métal lourd (par exemple, LBE).

Le coeur du réacteur est maintenu dans un état sous-critique (c'est-à-dire un facteur de multiplication neutronique effectif $k_{eff} < 1$), ce qui signifie qu'il ne peut pas entretenir une réaction en chaîne par lui-même. Il dépend entièrement de la source de neutrons externe fournie par l'accélérateur (et sa cible de spallation), ce qui améliore intrinsèquement la sécurité opérationnelle : le processus de fission s'arrête immédiatement si le faisceau de l'accélérateur est interrompu.

La motivation principale pour le développement des ADS est de pouvoir mettre en oeuvre une stratégie de Partition et Transmutation (P&T) pour les déchets nucléaires. Cette stratégie, illustrée dans Figure 3, implique :

- *Partition* : la séparation chimique des isotopes radioactifs à vie longue, en particulier les actinides mineurs comme le Neptunium, l'Américium ou le Curium, du combustible nucléaire usé.
- *Transmutation* : l'irradiation ultérieure de ces Minor Actinides (MA) séparés dans le réacteur ADS. Le flux neutronique intense les convertit en isotopes à vie plus courte ou stables par fission.

Il en résulte une forte réduction de la radiotoxicité et du temps d'isolement requis

des déchets finaux, passant de centaines de milliers d'années à une échelle plus gérable de plusieurs siècles, avec des volumes réduits, allégeant ainsi la charge pesant sur les installations de stockage géologique profond.

Comme résumé dans Table 1, de nombreux projets ADS ont été lancés dans le monde. La société genevoise Transmutex propose également sa propre conception, avec son prototype appelé START. Ce réacteur permettrait la transmutation des déchets nucléaires actuels et futurs en utilisant du combustible à base de Thorium tout en produisant de l'énergie décarbonée en toute sécurité. Transmutex vise à construire un prototype pré-industriel d'ici 2032.

Alors que la plupart des conceptions, comme MYRRHA et JAEA-ADS, utilisent des LINAC supraconducteurs, certaines propositions, telles que SKKU-ADS et TRANSMUTEX-START, explorent les cyclotrons de haute puissance.

Cependant, bien que les ADS offrent une solution au problème de déchets nucléaires, ils représentent eux-mêmes une nouvelle classe complexe d'installation d'accélérateur de haute puissance qui nécessitera éventuellement un démantèlement. Les faisceaux de haute énergie et de haute intensité impliqués devraient générer une activation significative des composants comme les arrêts de faisceau, les blindages et les aimants — dépassant de loin les niveaux d'activation typiquement rencontrés dans les accélérateurs cliniques ou industriels. Cela rend la caractérisation radiologique avancée et la planification du démantèlement une exigence critique pour la durabilité de ces projets.

Le défi du démantèlement : de la caractérisation à la gestion des déchets

Le fonctionnement des accélérateurs de particules, au-delà de certains seuils d'énergie, induit de la radioactivité dans leurs matériaux et composants par le biais de réactions nucléaires. Les niveaux d'activation dans la plupart des accélérateurs médicaux et industriels sont historiquement considérés comme faibles. Cette perception relative a conduit à ce que le démantèlement des installations accélérateurs de particules soit une préoccupation secondaire. Cela a été entretenu par le fait que l'application généralisée de ces machines est relativement récente, de nombreuses premières installations étant gérées par des instituts de recherche qui ont développé des conceptions uniques et ponctuelles, entravant l'établissement de protocoles de démantèlement standardisés.

Cependant, compte tenu de la taille immense de la flotte mondiale actuelle, le démantèlement de ces installations est désormais un défi urgent et croissant. Cette urgence est motivée par les exploitants, les entités de gestion des déchets (comme ANDRA en France) et les autorités de sûreté, tous confrontés à une vague d'installations arrivant en fin de vie. Le défi est encore amplifié par le développement d'accélérateurs de haute puissance, tels que les ADS, où les niveaux d'activation devraient être significativement plus élevés.

Reconnaissant cela, l'IAEA recommande d'établir des plans de démantèlement avant la mise en service de toute nouvelle installation, élevant ainsi le niveau des installations accélérateurs de particules vers celui des installations nucléaires. Une première étape critique, et le défi central que cette thèse aborde, est la caractérisation radiologique : la prédiction et la mesure précises de l'inventaire des radionucléides produits pendant

le fonctionnement. L'IAEA souligne une "approche graduée", où la complexité de la planification est directement liée à la classe, c'est-à-dire l'énergie et le type de particules de l'accélérateur.

Les principaux déchets issu du démantèlement des accélérateurs sont les matériaux solide activé (par exemple, aimants, béton de blindage, arrêts de faisceau, collimateurs, câbles), la contamination étant rare mais importante à considérer. Un exemple typique est l'activation du béton, où des contaminants induisent la présence d'Europium. Voici une liste non exhaustive des isotopes provenant des matériaux les plus activés autour d'un accélérateur de particules : ^{3}H, ^{7}Be, ^{11}C, ^{22}Na, ^{24}Na, ^{32}P, ^{42}K, ^{45}Ca, ^{44}Sc, ^{44m}Sc, ^{46}Sc, ^{47}Sc, ^{48}Sc, ^{48}V, ^{51}Cr, ^{52}Mn, ^{52m}Mn, ^{54}Mn, ^{55}Fe, ^{56}Mn, ^{57}Co, ^{57}Ni, ^{58}Co , ^{59}Fe, ^{60}Co, ^{61}Cu, ^{63}Ni, ^{63}Zn, ^{64}Cu, ^{65}Ni, ^{65}Zn, ^{152}Eu, ...

Les principes clés pour la gestion de ces déchets sont :

- Minimisation des déchets : réalisée par des choix de conception (par exemple, sélection des matériaux, blindage modulaire) et des pratiques opérationnelles qui minimisent la perte de faisceau.
- Libération et recyclage : une fraction significative des matériaux peut être admissible au recyclage (ou l'élimination) conventionnel. Cependant, l'absence de dispositions claires en matière de libération dans certains pays complique ce processus.
- Caractérisation précise : essentielle pour déterminer la voie d'élimination appropriée, mais elle est notoirement difficile en raison du mélange complexe de radionucléides produits.

Le cœur du problème de caractérisation réside dans les limites des méthodes de mesure actuelles. Généralement, la pratique courante lors du démantèlement repose sur des contrôles simples in situ, sensibles uniquement au rayonnement gamma. Cette méthode échoue complètement si les radionucléides dominants sont des *émetteurs bêta purs* (par exemple, ^{3}H, ^{32}P, ^{63}Ni, c'est-à-dire des noyaux n'émettant que des β sans relaxation γ), conduisant à une grave sous-estimation de l'activité totale et potentiellement à une mauvaise classification des déchets.

Par conséquent, la modélisation computationnelle, en particulier avec des codes de Monte Carlo (par exemple, MCNP, FLUKA, Geant4) couplés à des solveurs d'activation (par exemple, `FISPACT-II`), est identifiée comme indispensable pour la caractérisation préventive. Cela est particulièrement vrai pour les nouvelles installations pour lesquelles aucune donnée expérimentale n'existe. Ces outils sont la seule méthode capable de fournir une image complète du vecteur radiologique, y compris les émetteurs bêta purs difficiles à détecter, constituant ainsi une base fiable pour la planification des filières de déchets, l'estimation des coûts et la garantie de la sécurité des travailleurs.

En fin de compte, le démantèlement des accélérateurs de particules est un processus gérable s'il est planifié et exécuté systématiquement dès les premières phases de conception. Le succès repose sur une planification précoce et continue, une stratégie de caractérisation radiologique robuste intégrant une modélisation avancée, et l'application d'une approche réglementaire graduée proportionnelle aux risques.

Ce travail vise à contribuer à la résolution de ce défi en développant une approche, et

des outils, pour améliorer la précision de ces simulations prédictives.

Une stratégie pour relever ce défi de démantèlement

Cette thèse s'inscrit dans le cadre d'une collaboration entre le CNRS/Université de Strasbourg et la start-up TRANSMUTEX SA.

Elle propose une méthodologie pour aborder la planification prédictive du démantèlement. Ce travail s'organise autour de la feuille de route illustrée dans Figure 4.

Bien que les codes de Monte Carlo couplés à des solveurs d'activation soient reconnus comme des outils essentiels, leurs prédictions peuvent varier considérablement. Ce travail propose une comparaison entre ces codes, pour mieux se familiariser avec les défis de la modélisation.

Cette variance provient non seulement des différences dans leurs modèles physiques, mais aussi des bibliothèques de données nucléaires sous-jacentes sur lesquelles ils reposent.

En effet, les données nucléaires sont fondamentales pour de nombreuses applications. Des évaluations ont été réalisées sur les propriétés nucléaires, afin de fournir la capacité de modéliser avec précision les interactions entre les particules, en particulier les neutrons de basse énergie, et intègrent les propriétés des noyaux atomiques, au-delà des modèles théoriques. Ces bases de données permettent la modélisation, la conception et l'optimisation de systèmes complexes.

Les bases de données évaluées les plus courantes sont ENDF/B, JEFF, JENDL, TENDL ou TENDL. Elles fournissent des données de sections efficaces (des neutrons aux alphas), mais aussi des données de désintégration et des données de fission.

Ce travail propose une comparaison de ces bases de données, car elles peuvent avoir un impact significatif sur les installations accélérateurs de particules. Il présente un cadre pour simuler et analyser les inventaires radiologiques dans les accélérateurs de particules. Le cadre utilise des outils informatiques avancés et des données nucléaires enrichies pour éclairer les stratégies de démantèlement. Le manuscrit est organisé en cinq chapitres interdépendants.

Chapitre 1 pose les bases théoriques essentielles pour comprendre le comportement du rayonnement ionisant et son interaction avec la matière. Il présente une classification des radionucléides, détaille les mécanismes des interactions photoniques et neutroniques, et introduit les principes physiques régissant le transport du rayonnement. Ces éléments fondamentaux sous-tendent les modèles computationnels et les protocoles expérimentaux développés dans les chapitres suivants.

Chapitre 2 est consacré à l'étude des phénomènes d'activation. Il décrit une série de mesures expérimentales et de simulations Monte Carlo employées pour évaluer la radioactivité induite dans divers contextes, y compris à proximité d'une source de neutrons AmBe, les composants activés d'un accélérateur médical démantelé, et les zones autour d'un cyclotron. Le chapitre mettra en évidence la nature complexe des processus

d'activation et soulignera la nécessité d'une modélisation précise pour garantir la sûreté opérationnelle et guider les stratégies de démantèlement.

Chapitre 3 présente `TMX_Bateman`, un solveur dédié aux équations de Bateman, conçu pour simuler l'évolution temporelle des chaînes de désintégration des radionucléides. Le solveur est comparé à des outils computationnels établis tels que `FISPACT-II` et `DCHAIN-PHITS`, des analyses comparatives démontrant sa précision, sa robustesse et son efficacité computationnelle dans une série de scénarios représentatifs.

Chapitre 4 aborde la question critique du choix des données nucléaires en proposant une stratégie systématique pour sélectionner les sections efficaces évaluées. Cette méthodologie est soutenue par le développement d'un outil python, qui facilite l'exploration, la comparaison et la validation des bibliothèques de données nucléaires. Le chapitre examine l'influence du choix des sections efficaces sur la fidélité des simulations et offre une approche structurée pour compiler des ensembles de données adaptés à des applications spécifiques.

Chapitre 5 présente GENF/D, une base de données complète et cohérente de données de désintégration nucléaire évaluées, qui a été générée par cette thèse. Il détaille la méthodologie de compilation, les procédures de validation et les comparaisons de performances par rapport à d'autres bibliothèques de référence. Le chapitre souligne la pertinence de la base de données pour les calculs de chaleur de désintégration et la caractérisation des déchets radioactifs, positionnant GENF/D comme une ressource précieuse tant pour la recherche que pour la prise de décision opérationnelle.

D.1. Consideration générales

D.1.1. Taxonomie nucléaire

Les atomes sont constitués d'un noyau (protons et neutrons) et d'un nuage électronique organisé en couches. Le nombre de protons Z et de neutrons N, ou leur somme A, déterminent le comportement du noyau. Les noyaux sont classés en isobares (même A), isotones (même N) ou isotopes (même Z). La carte des noyaux présentée sur Figure 1.1 recense 3821 isotopes et isomères, dont seulement 289 existent naturellement.

Les orbitales électroniques sont discrètes et organisées en couches (K, L, M selon la notation de Siegbahn). Les transitions électroniques produisent des rayons X caractéristiques. De même, le noyau possède une structure quantique discrète décrite par le modèle en couches, avec des niveaux d'excitation bien définis. Les états métastables, comme ^{99m}Tc dont le schéma est donné en Figure 1.4, sont notés identifiés par un suffixe supplémentaire (m, n, m2, ...).

D.1.2. Radionucléides

La radioactivité, phénomène découvert par Henri Becquerel en 1896 et compris par Marie Curie, est la capacité de certains noyaux à se transformer spontanément en émettant des particules (α, β^+, β^-) souvent accompagnées de rayonnements γ.

Vallée de stabilité

Sur les 254 noyaux stables connus, la stabilité est maximale au fond d'un puits de potentiel défini par l'excès de masse, formant la "vallée de stabilité" illustrée en Figure 1.5. Les limites de stabilité sont les drip lines (proton et neutron), dont la position exacte reste incertaine pour les éléments lourds.

Désintégration radioactive

Les modes principaux sont α, β^-, β^+ et la capture électronique. L'énergie disponible Q est calculée par différence de masse-énergie entre père et fils. Les désintégrations β sont des processus à trois corps donnant des spectres continus, tandis que les désintégrations α (deux corps) produisent des raies discrètes. La capture électronique est dominante lorsque $Q < 1,022$ MeV, seuil nécessaire pour l'émission β^+.

D'autres modes existent : transition isomérique (IT), fission spontanée (SF), émission de neutrons, protons, voire de clusters plus lourds (carbone, néon, magnésium, silicium). La double désintégration β a été observée pour 10 isotopes naturels.

Émissions associées

Outre les particules déjà mentionnées, on observe des rayons X (réarrangement électronique), des électrons Auger, un rayonnement de freinage interne (bremsstrahlung), des photons d'annihilation à 511 keV (pour β^+), et des électrons de conversion interne (transfert direct d'énergie à un électron orbital).

D.1.3. Activité et filiation radioactive

L'activité $A = \lambda N$ s'exprime en becquerels. La loi de décroissance est $A(t) = A_0 e^{-\lambda t}$, avec $\lambda = \ln 2 / T_{1/2}$. L'activité massique vaut $A_0/m = N_A \ln 2/(M T_{1/2})$.

Pour une chaîne de désintégration, les équations de Bateman décrivent l'évolution temporelle de chaque nucléide. Le Figure 1.13 illustre la filiation complète du ^{232}Th.

Production de radionucléides

Les réactions $X(a,b)Y$ (activation neutronique ou interactions particules chargées) produisent des radioisotopes. Sous flux constant ϕ, l'activité produite est $A_Y(t_{irr}) \approx N_X \sigma \phi (1 - e^{-\lambda_Y t_{irr}})$, avec saturation après environ 10τ. Les équations de Bateman généralisées intègrent à la fois la décroissance et la transmutation sous flux.

D.1.4. Caractérisation des rayonnements ionisants

Les rayonnements ionisants sont classés en directement ionisants (particules chargées) et indirectement ionisants (neutrons, photons).

Particules chargées

Le pouvoir d'arrêt $S = -dE/dx$ (électronique + nucléaire) décrit la perte d'énergie. Le parcours CSDA est obtenu par intégration de $1/S$. La Figure 1.15 montre ces grandeurs pour protons et alphas dans le polycarbonate.

Photons et neutrons

L'atténuation suit $I(x) = I_0 e^{-\mu x} = I_0 e^{-N\sigma x}$. Pour les photons, $\mu_{tot} = \mu_{pe} + \mu_c + \mu_{pp}$ (effets photoélectrique, Compton, matérialisation). Le Figure 1.16 présente ces coefficients pour le germanium.

Interaction photons-matière

- **Effet photoélectrique** : prédominant sous 100 keV, section efficace $\sigma_{pe} \propto Z^n/E_\gamma^m$ ($n \approx 4-5$, $m \approx 1-3,5$).
- **Effet Compton** : diffusion incohérente, $\sigma_{Compton} \propto Z/E_\gamma$, avec formule de Klein-Nishina pour la section efficace différentielle.
- **Création de paire** : seuil à $2m_e c^2$, $\sigma_{pp} \propto Z^2$, prédominante aux hautes énergies.

Interaction neutrons-matière

Les neutrons, découverts en 1932 par Chadwick, sont classés par énergie (de froids à rapides, voir Table 1.3). Le Figure 1.17 présente la classification des sections efficaces, et Figure 1.18 donne l'exemple du ^{232}Th.

- **Diffusion élastique** : thermalisation, maximale pour l'hydrogène (formule semi-empirique de Gammel, comparée à ENDF/B en Figure 1.19).
- **Diffusion inélastique** : réaction seuil avec émission d'un neutron désexcité.
- **Capture radiative** : (n, γ), section efficace en $1/v$ pour les neutrons thermiques.
- **Transmutation** : réactions (n, p), (n, α) (ex: $^{10}B(n, \alpha)$), utiles pour la détection.
- **Fission** : pour les noyaux lourds, produisant fragments radioactifs (voir Figure 1.20).

Les résonances (domaine résolu et non résolu) peuvent être décrites par la formule de Breit-Wigner. La Figure 1.21 illustre l'influence du nombre de masse sur les résonances.

Sources de neutrons

- Fission réacteur
- Radioactivité : sources (α, n) (AmBe, réactions listées dans Table 1.4), photoneutrons (γ, n)

– Spallation par accélérateur (processus en deux étapes : cascade intra-nucléaire puis évaporation)

D.1.5. Conclusion

Ce chapitre a posé les bases nécessaires à la compréhension des phénomènes d'activation : classification des nucléides, modes de désintégration, lois d'atténuation, interactions particules-matière, et équations de Bateman. Ces principes seront utilisés dans les chapitres suivants pour la modélisation de l'activation et la caractérisation radiologique.

D.2. Estimation d'activité induite auprès d'accélérateurs de particules: approches expérimentale et modélisation

Dans le domaine de la physique nucléaire et des accélérateurs de particules, la compréhension et la gestion des phénomènes d'activation induite sont essentielles pour assurer la sécurité des installations et du personnel. Les méthodes de Monte Carlo jouent un rôle clé dans la modélisation de ces phénomènes, permettant de simuler les interactions complexes entre les particules et la matière. Ce document explore les principes des méthodes de Monte Carlo, leur application dans l'évaluation de l'activation induite, ainsi que les méthodes expérimentales complémentaires. Ces outils sont indispensables pour optimiser la conception des installations et minimiser les risques associés aux rayonnements ionisants.

D.2.1. Généralités sur les Méthodes de Monte Carlo

Les méthodes de Monte Carlo reposent sur l'utilisation de nombres aléatoires pour simuler des phénomènes complexes. Elles permettent d'estimer des grandeurs difficiles à calculer analytiquement, comme les distributions de dose ou les taux de réaction dans les matériaux exposés à des rayonnements.

Principe de base Le transport d'une particule est simulé depuis son émission jusqu'à sa disparition, en échantillonnant aléatoirement chaque interaction à partir de lois de probabilité physiques (comme les sections efficaces), voir Figure 2.1.

La méthode de Monte Carlo sert d'outil de référence dans des domaines tels que la physique des réacteurs, la radioprotection ou la physique médicale. Plusieurs codes spécialisés existent, chacun avec ses domaines d'application. Dans ce document, on mentionnera plus particulièrement MCNP (EUA), Geant4 (UE), FLUKA (UE) et PHITS (JP).

D.2.2. Méthodes expérimentales

Deux types de détecteurs ont été principalement utilisés.

Spectroscopie gamma Technique non destructive d'identification et de quantification des radionucléides par l'énergie des rayons gamma émis. Les détecteurs au germanium hyperpur (HPGe) offrent une excellente résolution énergétique. La calibration en énergie et en efficacité, réalisée à l'aide de sources étalons, est essentielle. L'activité spécifique d'un échantillon est calculée à partir du taux de comptage net d'un pic gamma, en tenant compte de nombreux facteurs de correction (efficacité, intensité de raie, coïncidences, auto-absorption, décroissance).

Détecteurs solides de traces nucléaires (DSTN) Ces détecteurs passifs enregistrent les traces de particules chargées (protons, alphas, fragments de fission). Le mécanisme repose sur la formation d'un trail de dommages (trace latente) le long du parcours de la particule, révélé par une attaque chimique différentielle. Le détecteur CR-39, associé à des convertisseurs (polyéthylène pour les protons de recul, bore pour les alphas), permet la dosimétrie neutronique en distinguant les composantes thermiques et rapides du champ neutronique.

D.2.3. Études de cas pour l'évaluation de l'activation induite

Trois études de cas illustrent l'approche combinant modélisation et expérimentation.

a) Activation autour d'un accélérateur médical (LINAC)

L'objectif était d'estimer l'activité gamma et bêta dans les composants d'un LINAC médical, en particulier les émetteurs bêta purs, par calcul.

Une géométrie simplifiée (cible en cuivre, bloc d'acier) a été utilisée dans MCNP, PHITS et FLUKA. La production de photoneutrons par réaction (γ, n) sur les noyaux de la tête de traitement a été simulée pour un faisceau d'électrons de 18,8 MeV. Les spectres neutroniques obtenus sont en bon accord entre PHITS et MCNP, avec une légère déviation pour FLUKA.

Des mesures par spectrométrie gamma sur un Beam Flattening Filter démantelé ont été réalisées. Les incertitudes majeures proviennent du manque de connaissance précise du profil et du temps d'utilisation de l'accélérateur.

b) Activation autour d'une source AmBe

Une comparaison systématique des codes MCNP, FLUKA, PHITS et Geant4 a été réalisée pour le calcul de l'activation par capture neutronique, validée par des mesures expérimentales.

Des échantillons d'or et de vanadium ont été irradiés auprès d'une source ^{241}AmBe placée au centre d'un baril de paraffine. Les activités induites ont été mesurées par spectrométrie gamma. Les simulations ont utilisé différentes bibliothèques de données nucléaires (ENDF, JEFF, JENDL, TENDL) et listes physiques. Les spectres neutroniques calculés sur les échantillons sont en bon accord entre tous les codes, à l'exception de Geant4 avec la liste `ShieldingLEND`, qui présente une thermalisation différente (écart de 43% à l'énergie thermique par rapport à MCNP).

c) Activation autour du cyclotron CYRCé

Cette étude visait à caractériser le champ neutronique généré lors de la production de ^{18}F dans un cyclotron, par activation d'échantillons et par détecteurs SSNTD.

Des échantillons (Au, Sc, Tb, Ta) ont été placés à quatre emplacements dans la casemate du cyclotron. Leurs activités induites ont été mesurées par spectrométrie gamma et comparées aux prédictions des codes FLUKA, Geant4 et PHITS couplés à `FISPACT-II`.

PHITS reproduit le mieux la production de ^{18}F (erreur de 5 %), contrairement à FLUKA qui la surestime (250 %), probablement à cause du modèle physique utilisé. Pour les activités induites calculées avec la bibliothèque ENDF/B, PHITS donne le meilleur rapport calcul/mesure $1,45 \pm 0,7$. Les SSNTD ont permis de distinguer la composante thermique et rapide. La comparaison montre que les simulations ont tendance à surestimer la composante thermique par rapport aux mesures. Cette technique passive reste adaptée pour des mesures à faible fluence et pour une cartographie relative du champ neutronique.

D.2.4. Conclusion et perspectives

Ce travail fournit une base méthodologique pour les utilisateurs de LINACs médicaux et de cyclotrons, et introduit la nécessité d'un outil analytique supplémentaire. La comparaison des codes MCNP, FLUKA, PHITS et Geant4, souvent couplés à des codes d'inventaire comme `FISPACT-II`, montre un accord global satisfaisant avec les mesures par spectrométrie gamma, bien que des disparités persistent selon les modèles physiques et les bibliothèques utilisées. Les SSNTDs constituent un complément utile pour la cartographie des champs neutroniques.

Les perspectives incluent l'estimation des émetteurs bêta purs à partir des émetteurs gamma facilement mesurables, la validation sur des jeux de données EXFOR pour les systèmes pilotés par accélérateur (ADS), et le développement d'un outil déterministe `TMX_Bateman`

D.3. Synthèse : Résolution des équations de Bateman et développement du solveur `TMX_Bateman`

L'analyse de l'inventaire des radionucléides est essentielle pour de nombreuses applications nucléaires. Elle repose sur la résolution des équations de Bateman, un système d'équations différentielles décrivant l'évolution temporelle d'une population de nucléides sous l'effet de la désintégration et des interactions avec un flux de particules. Bien que de nombreux codes existent, ils présentent des limitations en termes de flexibilité et d'exhaustivité spectrale. Ce chapitre présente le développement d'un nouveau solveur, `TMX_Bateman`, conçu pour pallier ces lacunes, notamment pour l'extraction complète des spectres de particules secondaires.

D.3.1. Contexte et motivations

Le calcul d'inventaire peut être abordé de manière déterministe ou par Monte Carlo. Des codes historiques comme ORIGEN (au sein de la suite SCALE) ou plus récents comme FISPACT-II, DCHAIN ou NUIT sont couramment utilisés. Les principaux outils Monte Carlo (FLUKA, MCNP, PHITS, TRIPOLI-4) intègrent également des modules de calcul d'évolution.

Cependant, ces outils présentent des limites :

- Les outils Monte Carlo nécessitent parfois de relancer l'intégralité de la simulation en cas de modification du profil d'irradiation.
- Les codes dédiés, bien que plus flexibles sur les profils d'irradiation, n'exploitent pas toujours l'intégralité des données de désintégration disponibles.
- L'extraction de spectres de particules secondaires (alpha, neutrons, gammas) est souvent restreinte ou peu flexible.

L'objectif est donc de développer un module capable d'extraire tout spectre de particules secondaires, de décomposer les différentes contributions à la puissance thermique et d'améliorer la précision des estimations.

D.3.2. Résolution des équations de Bateman

L'équation de Bateman généralisée (Equation 3.1) décrit l'évolution du nombre N_j de noyaux de l'isotope j. Plusieurs stratégies de résolution existent.

a) Méthodes de résolution

LSODE (Livermore Solver for Ordinary Differential Equations) Cette méthode réduit le système à un problème de Cauchy. En raison de la raideur (stiffness) du système, due à la grande différence d'ordre de grandeur des valeurs propres de la matrice d'évolution, les méthodes explicites sont inefficaces. Des méthodes implicites, comme les formules de différenciation rétrograde (Gear), sont préférées. FISPACT-II utilise cette approche.

CRAM (Chebyshev Rational Approximation Method) La solution de l'équation matricielle $\frac{d\mathbf{n}(t)}{dt} = \mathbf{A}\mathbf{n}(t)$ s'écrit $\mathbf{n}(t) = \mathbf{n_0}e^{\mathbf{A}t}$. L'approximation de Chebyshev permet de calculer efficacement l'exponentielle de matrice. C'est une méthode rapide, utilisée par SERPENT et NUIT, mais elle peut échouer pour les nucléides présents en très faibles quantités.

TTA (Transmutation Trajectory Analysis) Cette méthode consiste à linéariser les chaînes de désintégration et de transmutation. Elle fournit une solution analytique exacte en l'absence de cycles (désintégration pure). En présence de cycles (transmutation), un critère d'arrêt est nécessaire. Elle est précise mais peut être coûteuse en temps de calcul. C'est la méthode retenue pour `TMX_Bateman`, car adaptée à l'analyse des cycles du combustible où la désintégration est prédominante.

D.3.3. Le solveur `TMX_Bateman`

Le code `TMX_Bateman`, développé initialement par Transmutex et enrichi durant ce travail, intègre l'analyse des données de désintégration au format ENDF-6, l'export des spectres de particules secondaires et la physique des interactions neutroniques.

a) Principe de résolution

Le code implémente une stratégie de résolution basée sur la TTA, car ce code est principalement dédié à des calculs de décroissances. L'inventaire initial est traité en deux parties :

- Un terme de désintégration, résolu par linéarisation exacte des chaînes.
- Un terme de source (transmutation), où l'on suppose que le flux est constant sur le pas de temps et que les produits de réaction n'interagissent pas. La production maximale est calculée, puis désintégrée sur la durée du pas.

L'équation résolue pour la désintégration est Equation 3.10.

b) Gestion des données nucléaires

La robustesse du code repose sur ses bases de données évaluées, principalement issues du format ENDF-6. Pour optimiser l'accès et la cohérence, les données sont réorganisées en quatre fichiers HDF5 :

- Désintégration (constantes, modes, spectres).
- Fission spontanée (fragments).
- Sections efficaces (notamment les réactions MT=5 et MT=18).
- Fragments de fission induite.

Cette structure permet de surmonter certaines limitations d'outils comme FISPACT-II, qui ne peut suivre des éléments que s'ils ont des données complètes (de décroissance et de sections efficaces).

c) Observables et grandeurs calculées

À partir de la composition isotopique ($N_i(t)$), `TMX_Bateman` calcule de nombreuses grandeurs :

- **Composition :** nombre d'atomes, masse.
- **Activités :** activité totale, émissions α, β, γ, neutrons, transitions isomériques.
- **Puissance thermique :** contributions des particules lourdes (α, fragments de fission), légères (β, protons, neutrons) et des rayonnements électromagnétiques (γ, X), ainsi que la puissance maximale disponible.
- **Doses engagées :** ingestion et inhalation (coefficients ICRP).
- **Spectres de désintégration :** extraction possible de tout spectre de particules secondaires (photons, électrons, alphas, etc.) avec un binning personnalisable.

D.3.4. Validation et comparaison

Le code a été comparé à `FISPACT-II` et `DCHAIN-PHITS` dans plusieurs scénarios.

a) Validation des données

La comparaison des propriétés initiales (activité, masses) pour un matériau contenant tous les isotopes de NUBASE2020 montre un accord quasi-parfait avec FISPACT-II (écart $< 1\times10^{-5}$ %) et un écart acceptable avec DCHAIN (1×10^{-3} %), attribuable à la précision numérique des sorties. Des divergences spécifiques ont été identifiées et expliquées, comme un bogue dans FISPACT-II pour les désintégrations $\beta+\alpha$ et la distinction β^+/CE.

b) Validation du suivi temporel

Pour des chaînes de désintégration simples (^{48}V) et plus complexes (^{211}Tl), les écarts relatifs avec FISPACT-II et DCHAIN restent très faibles (inférieurs à 10^{-3}%). Pour la décroissance d'un combustible UOX, incluant la fission spontanée, les écarts sont généralement inférieurs à 10^{-5}, à l'exception de quelques isotopes stables (écart de 8% avec DCHAIN). Le choix de la sous-bibliothèque pour les fragments de fission est crucial pour la précision de l'inventaire.

c) Validation de la transmutation

Lors de l'irradiation simple du ^{51}V, une légère déviation de `TMX_Bateman` par rapport aux autres codes est observée aux temps courts, due à la non-prise en compte de l'interaction des résidus. Ceci peut être corrigé en subdivisant le profil d'irradiation. La comparaison avec l'expérience de Maekawa sur la chaleur de décroissance après irradiation par neutrons de 14 MeV montre un excellent accord entre `TMX_Bateman` et FISPACT-II, ainsi qu'un bon accord avec les valeurs expérimentales. Enfin, le benchmark sur la fission impulsionnelle du plutonium-239 met en évidence des écarts avec l'expérience (jusqu'à 10%), soulignant les limites des données de désintégration (effet pandémonium) plutôt qu'une défaillance du solveur.

D.3.5. Applications supplémentaires

Extraction des spectres gamma Contrairement à FISPACT-II et DCHAIN, `TMX_Bateman` peut fournir des spectres gamma avec un binnage variable, incluant les rayons X. La comparaison des spectres montre un bon accord, mais révèle que les codes alternatifs ne peuvent pas toujours prendre en compte les spectres continus et que leur méthode de reconversion du spectre pondéré en énergie peut introduire des erreurs. Une application directe est la comparaison avec des spectres gamma expérimentaux (exemple du tantale, Figure 3.12), permettant de renormaliser ou de valider les simulations.

Extraction des spectres alpha `TMX_Bateman` peut également fournir des spectres alpha, mais cette capacité est limitée par la rareté des données évaluées (seulement 256

isotopes sur 820 émetteurs alpha potentiels dans ENDF/B). Une réévaluation des bases de données est nécessaire pour exploiter pleinement cette fonctionnalité.

Identification des émetteurs bêta purs Le code identifie les émetteurs bêta purs selon un critère strict (présence d'un spectre bêta documenté et absence de spectre gamma). Soixante-deux nucléides de ce type sont identifiés dans ENDF/B-VIII.1. Ceci permet d'attirer l'attention de l'utilisateur sur les difficultés liées à la détection de ces émetteurs, essentiels pour le démantèlement. Mais ce critère a ses limites, car très centré sur les expériences (et donc le seuil de détection des gammas, definissant la "pûreté effective".

D.3.6. Conclusion et perspectives

Ce chapitre présente un outil de suivi d'inventaire nucléaire qui améliore la modélisation des chaînes de désintégration et la complétude des spectres de rayonnement pour la radioprotection. Le solveur `TMX_Bateman` offre des capacités clefs : estimation des taux d'émission et de la chaleur de décroissance, extraction de tous les spectres de particules secondaires, et interfaces d'entrée flexibles. Deux innovations majeures sont introduites : la traçabilité complète des branches de transmutation (même avec des données incomplètes) via un atome "fantoche", et l'accès unifié à toutes les émissions secondaires avec un binnage personnalisable.

Les performances du solveur restent tributaires des bibliothèques de données choisies. L'utilisation de la base de données présentée dans un autre chapitre est recommandée pour combler les lacunes (bremsstrahlung interne, spectres bêta).

Les perspectives d'amélioration incluent :

- **Intégration des incertitudes** : Prendre en compte les incertitudes sur les observables, ainsi que sur les périodes radioactives et les rapports d'embranchement ;
- **Optimisation du solveur** : Implémenter les récentes avancées sur les équations de Bateman, telles que les méthodes TTA ou les techniques de résolvante de Chebyshev pour les profils d'irradiation complexes ;
- **Analyse de dose** : Développer une fonctionnalité dédiée aux défis posés par le démantèlement des accélérateurs, en particulier pour la sécurité des travailleurs.

D.4. GENF/D, une base de données de désintégration pour des inventaires radionucléidiques étendus

Ce chapitre présente le développement d'une nouvelle base de données de désintégration, nommée GENF/D (Global Evaluated Nuclear File, Decay sub-library). Conçue pour pallier les limitations des bibliothèques évaluées existantes, elle vise à fournir un jeu de données plus complet et cohérent, intégrant des isotopes exotiques et des états isomériques souvent oubliés, tout en corrigeant certaines incohérences de formatage. Cette base est destinée à alimenter des solveurs d'équations de Bateman comme `TMX_Bateman`.

D.4.1. Contexte et nécessité d'une nouvelle base de données

Les bases de données de désintégration conventionnelles, bien qu'essentielles, présentent des lacunes qui limitent la précision des calculs d'inventaire.

a) Limitations des bases existantes

- **Incomplétion :** Des isotopes et de nombreux états isomériques, pourtant documentés dans des bases comme NUBASE ou ENSDF, sont absents des sous-bibliothèques de désintégration au format ENDF-6. Leur suivi est donc impossible par les codes d'inventaire.
- **Incohérences :** Pour accéder à plus d'isotopes, une des approches est celle d'une hybridation de différentes sources par certains codes (`FISPACT-II`, DCHAIN) qui peut engendrer des incohérences internes (rayons gamma non associés au bon isotope, méthodologie pour l'estimations des chaleurs moyennes différentes).
- **Obsolescence :** Les cycles de révision des grandes bibliothèques (JEFF, ENDF/B, JENDL) sont longs (7 à 11 ans), alors que des mises à jour expérimentales sont plus fréquentes via des projets comme ENSDF.
- **Défauts de formatage :** La dernière version de la norme ENDF6 n'est pas toujours rigoureusement suivie. Par exemple, les neutrinos sont systématiquement classés comme des particules β, ce qui masque la nature réelle de certaines désintégrations (e.g., capture électronique pure).

b) Objectifs de GENF/D

Pour répondre à ces défis, GENF/D est conçue pour :

- Être aussi exhaustive que possible, en incluant un maximum d'isotopes et d'isomères.
- Se baser sur les données les plus récentes (NUBASE-2020, ENSDF2025) et les compléter par des modèles théoriques reconnus (BetaShape, GEF).
- Respecter strictement le format ENDF-6 dans sa version la plus récente (2018), en distinguant notamment les spectres de neutrinos.
- Fournir des estimations pour les données manquantes (spectres β, électrons de conversion, rayonnement de freinage interne, fission spontanée).

D.4.2. État des lieux des bases de données de désintégration

a) Principales sources de données

- **ENSDF :** La source de données évaluées la plus complète, contenant des informations détaillées sur les niveaux nucléaires et les rayonnements. Elle est accessible via l'API LiveChart de l'AIEA. Environ 220 noyaux y sont entièrement réévalués chaque année.
- **NUBASE :** Stocke les masses nucléaires, les modes de désintégration, les périodes et les énergies de désintégration totales (Q). NUBASE-2020 répertorie 5565

isotopes (dont 3558 états fondamentaux). C'est la source privilégiée pour l'exhaustivité.
- **Bibliothèques ENDF-6 (MF=8) :** Les formats de distribution standard pour les codes d'inventaire (JEFF, ENDF/B, JENDL). Une analyse comparative montre qu'elles couvrent 4219 isotopes (3337 états fondamentaux) mais avec des disparités dans la couverture des isomères et des modes de désintégration.
- **RIPL :** Fournit des estimations de spins et de parités pour compléter les données manquantes.

b) Incohérences identifiées

La comparaison de ces sources révèle des problèmes :

- **Classification des neutrinos :** Dans les fichiers ENDF-6, les neutrinos sont systématiquement associés au type spectral `STYP=1/2` (désintégration β), même pour les cas de capture électronique pure.
- **Données de fission spontanée incomplètes :** ENDF/B-VIII.1 ne documente la fission spontanée que pour 128 isotopes, contre 338 dans NUBASE-2020. Seuls 28 ont des données d'énergie complètes.

D.4.3. Génération de la base GENF/D

La construction de GENF/D s'effectue en trois étapes principales, orchestrées par une chaîne de traitement en Python. Cette chaîne utilise des outils comme `endf_parserpy` pour le format ENDF-6, et des codes externes pour les calculs théoriques.

a) Étape 1 : Création d'une base ENDF-6 minimale depuis NUBASE

Cette étape traduit les données de NUBASE-2020 dans un squelette de fichier ENDF-6.

- **Traitement des états isomériques :** Seuls les états fondamentaux et les isomères sont conservés. Les énergies d'excitation négatives sont corrigées par la méthode RIPL.
- **Gestion des modes de désintégration :** Les modes de NUBASE sont convertis en codes `RTYP` ENDF-6. Les désintégrations de clusters (émission de ^{14}C, ^{18}O, etc.) sont ignorées (excepté ^{12}C), leur intensité étant négligeable. Les rapports d'embranchement sont systématiquement renormalisés à 100%.
- **Calcul des Q-values :** Les valeurs Q pour l'ensemble des canaux de désintégration sont calculées à partir des masses atomiques de AME-2020, avec des corrections pour les états excités lorsque l'information est disponible.

Cette première version permet un suivi d'inventaire de base.

b) Étape 2 : Insertion des spectres de désintégration

Cette étape enrichit la base avec les spectres détaillés des rayonnements émis, en puisant dans ENSDF via l'API LiveChart (données de mai 2025) et en les complétant par des

calculs théoriques.

Association des états isomériques Une correspondance est établie entre les niveaux d'excitation de NUBASE et ceux de ENSDF en utilisant l'énergie et la période. Une correspondance exacte est obtenue pour 93,6% des cas. Pour les 12 isotopes restants, où plusieurs niveaux ENSDF correspondent à un seul niveau NUBASE, les spectres sont additionnés.

Données spectrales intégrées

- **Spectres γ, X, et électrons discrets :** Extraits directement de l'API LiveChart.
- **Coefficients de conversion interne :** Recalculés avec le code BrIcc pour garantir l'homogénéité et la précision.
- **Spectres β et ν continus :** Recalculés avec la version 2.4 de BetaShape (qui inclut des effets atomiques avancés) pour 783 isotopes (β^-) et 612 isotopes (β^+). Ces spectres remplacent les estimations plus anciennes (LogFT).
- **Rayonnement de freinage interne :** Calculé avec le code RadiationReport pour 1826 isotopes, fournissant un spectre gamma continu.
- **Neutrons retardés :** Les spectres expérimentaux compilés par l'AIEA pour 44 isotopes sont intégrés.
- **Séparation β/ν :** Conformément à la norme ENDF-6 de 2018, les spectres de neutrinos sont séparés dans leurs propres sections (`STYP=10/11`), une première pour une base de données de ce type.

c) Étape 3 : Ajout des propriétés de fission spontanée

Cette étape comble une lacune majeure des bibliothèques évaluées en calculant systématiquement les données de fission spontanée.

- Le code Gef (version 2025.1.2) est utilisé pour simuler la fission de 338 isotopes (dont 279 états fondamentaux).
- Les listes de fragments, les spectres de neutrons et de photons de fission, ainsi que l'énergie cinétique totale des fragments sont générés.
- La multiplicité neutronique moyenne est ajoutée dans la section MF=1/MT=452.

d) Estimation des énergies moyennes

Lorsque les spectres sont disponibles, les énergies moyennes pour les composantes de chaleur (particules légères, rayonnements EM, particules lourdes) sont calculées directement via Equation 5.6. Lorsqu'ils sont absents, une convention empirique (Table 5.8) est appliquée pour les estimer à partir de la valeur Q.

D.4.4. Comparaison avec les bases évaluées existantes

a) Exhaustivité

GENF/D se distingue par sa couverture étendue :

- Elle inclut 1990 états isomériques, contre 797 dans JENDL-5, 768 dans JEFF-3.3 et 738 dans ENDF/B-VIII.0.
- Sur les 5583 isotopes répertoriés dans l'ensemble des bibliothèques publiques, GENF/D en manque 82 (49 états fondamentaux, 33 isomères), principalement ceux dont la période est inférieure à 100 ns (limite de NUBASE-2020) ou non référencés dans ENSDF. L'intégration de données de bibliothèques plus anciennes a été délibérément évitée pour préserver la cohérence méthodologique.

b) Comparaison des propriétés nucléaires

Pour les isotopes communs (périodes > 1 s), l'accord entre GENF/D et les bases de référence est globalement bon :

- L'accord sur les périodes et les valeurs Q est supérieur à 90% (différence relative $< 5\%$).
- L'accord sur les composantes de la chaleur de désintégration est plus variable, particulièrement pour la chaleur des particules lourdes dans JENDL-5 (62,4% d'accord). Ceci est attribué à des erreurs de calcul dans JENDL-5 pour certains canaux (e.g., neutrons retardés).

c) Évaluation des données de fission spontanée

La comparaison avec JEFF-4.0 valide l'approche GEF :

- L'accord sur l'énergie Q disponible pour 27 isotopes communs est excellent (différence $< 2\%$).
- La multiplicité neutronique moyenne présente un écart moyen de 7%, avec un maximum de 21%, ce qui reste acceptable.
- Les écarts sur les spectres de photons (jusqu'à 14% pour ^{232}Th) sont principalement dus à des différences de représentation (spectre lissé dans JEFF vs. histogramme avec binning fin dans GEF).

d) Critique de l'estimation des énergies moyennes

La convention empirique de partage de la valeur Q, bien qu'utilisée par toutes les bibliothèques, est discutable. Une analyse avec BETASHAPE montre que le rapport $< E_\beta > /Q$ n'est pas constant (0,31 pour β^-, 0,26 pour β^+) et varie avec le numéro atomique Z. De plus, l'application de cette convention aux nucléides de ENDF/B pour lesquels des spectres existent génère d'importantes erreurs, en particulier sur la composante électromagnétique (erreur moyenne de $\sim 10^6\%$), ce qui souligne la nécessité de modèles plus raffinés.

D.4.5. Validation sur des mesures intégrales

La base GENF/D, couplée au solveur `FISPACT-II` et aux données de fission de GEF (GEF-based Fission Yield library (GEFY)), est confrontée à des benchmarks expérimentaux de puissance résiduelle.

- **Benchmarks sur matières fissiles :** Pour des irradiations pulsées de ^{239}Pu (Dickens) et des irradiations longues de ^{235}U (Yarnell), les résultats obtenus avec GENF/D sont en bon accord avec les mesures et cohérents avec ceux obtenus avec les bibliothèques JEFF, ENDF/B et JENDL.
- **Benchmark sur matière non fissile :** L'irradiation d'un alliage Inconel 600 auprès d'une source de neutrons de fusion (FNS) montre que GENF/D reproduit correctement l'évolution de la puissance résiduelle.

On notera une surestimation de la chaleur dûe à l'utilisation de la règle empirique et non des données expérimentales. Ce choix a été fait, en l'abscence des données exhaustive des spectres de neutrons.

Pour conclure, ces tests confirment que la méthodologie employée pour GENF/D produit des résultats fiables et comparables aux bibliothèques établies, avec l'avantage d'une couverture isotopique accrue.

D.4.6. Conclusion et perspectives

a) Bilan

La base de données GENF/D constitue une avancée significative pour la modélisation des inventaires nucléaires. Ses atouts principaux sont :

- **Exhaustivité :** Couverture sans précédent des isotopes et des états isomériques, permettant de suivre des chaînes de désintégration complexes jusqu'à leurs extrémités.
- **Cohérence :** Construction unifiée à partir de sources de référence (NUBASE, ENSDF) et de modèles théoriques homogènes (BetaShape, BrIcc, Gef).
- **Conformité :** Respect strict de la norme ENDF-6 la plus récente, avec la séparation des spectres de neutrinos.
- **Complétude spectrale :** Intégration de spectres continus pour les β, les photons de Bremsstrhalung interne, et les émissions issues de la fission spontanée.

Cette base est destinée à devenir le coeur de données pour le solveur `TMX_Bateman`, et des autres applications de ce type, grâce à sa génération dans un format standard.

b) Perspectives d'amélioration

Plusieurs développements sont envisagés pour enrichir encore GENF/D :

- **Incertitudes :** Intégrer les matrices de covariance des masses de AME-2020 pour une propagation rigoureuse des incertitudes.
- **Données retardées :** Incorporer les spectres de particules retardées (protons, alphas) qui ne sont pas encore accessibles via l'API LiveChart.
- **Modèle β amélioré :** Remplacer la convention empirique $Q/3$ par un modèle phénoménologique plus précis pour estimer l'énergie moyenne des β en fonction du numéro atomique et de la structure nucléaire.

– **Effet pandémonium :** Intégrer des données de spectroscopie gamma par absorption totale (TAGS) pour corriger les effets de ”pandémonium” dans les chaînes de fission.

Ces améliorations permettront d'accroître la précision des calculs de chaleur résiduelle et d'élargir le champ d'application de la base, notamment pour le démantèlement et la gestion des déchets nucléaires.

D.5. Conclusions

L'objectif initial de ce travail était de proposer une méthodologie pour les installations de particules de haute énergie, dans le contexte du prototype d'ADS développé par TRANSMUTEX.

L'utilisation de codes Monte Carlo a été explorée, en particulier pour la modélisation de l'activation neutronique autour d'un benchmark simple d'une tête d'accélérateur médical de radiothérapie, la modélisation d'une source AmBe thermalisée, et la modélisation d'une installation de cyclotron pour la production de radioisotopes. Ce travail a déjà été partiellement publié dans [72, 73][1].

Pour ces études, des modèles ont été construits en utilisant les principaux codes multiphysiques : FlukaINFN, FlukaCERN, PHITS et Geant4. Alors que pour les modèles simples, les codes produisaient un excellent accord, ce n'était pas le cas pour les modèles plus complexes. Avec l'augmentation du nombre de processus physiques différents, les disparités entre les codes sont devenues plus apparentes, notamment avec FLUKA.

Par conséquent, pour la planification du démantèlement – surtout lorsqu'une installation n'a pas commencé sa phase de mise en service – une implémentation multi-codes est nécessaire, permettant d'explorer le biais pouvant être introduit par les codes eux-mêmes.

Les niveaux d'activation étaient le principal observable utilisé pour le contrôle dans ce travail. Ceci implique de maîtriser parfaitement la durée de l'expérience ou de l'opération, ainsi que le temps de refroidissement subséquent. Les codes mentionnés n'incluent pas directement la variable temporelle. Pour ce faire, il est nécessaire d'utiliser des modules externes pour modéliser l'évolution temporelle des compositions du matériau.

[1] Jonathan Collin et al. 'Validation of Monte Carlo simulations by experimental measurements of neutron-induced activation in cyclotrons'. en. In: *EPJ Web of Conferences*. Vol. 288. Italy: EDP Sciences, 2023, p. 04025. DOI: 10.1051/epjconf/202328804025, Abdel-Mjid Nourreddine et al. 'Assessment of photon and proton-induced activation in particles accelerators'. In: *Radiation Protection Dosimetry*. Vol. 200. 16-18. Japan, Nov. 2024, pp. 1507–1513. DOI: 10.1093/rpd/ncae146.

Cette tâche peut être accomplie via des solveurs de Bateman tels que `FISPACT-II`, `DCHAIN-PHITS`, ou NUIT. Ces outils permettent d'inclure le profil temporel, ainsi que le champ neutronique obtenu à partir des modèles Monte Carlo mentionnés ci-dessus, afin d'implémenter un profil d'irradiation. Ceci permet de déterminer l'activité attendue à tout moment.

Cependant, ces codes souffrent de certaines limitations, notamment dans l'extraction des spectres de désintégration pour une comparaison avec la spectroscopie expérimentale. À cette fin, ce travail a conduit à une contribution au développement d'un nouveau solveur de Bateman, `TMX_Bateman`.

Ce code permet de suivre n'importe quel inventaire, grâce à une analyse de trajectoire de transmutation, et d'extraire ses spectres de désintégration avec n'importe quel binning, que ce soit pour le rayonnement gamma, alpha ou neutronique. Le code a été validé par rapport à `FISPACT-II` et `DCHAIN-PHITS`, ainsi que comparé à des références de chaleur de désintégration.

La production de ce solveur de Bateman a mis en évidence deux problèmes supplémentaires. Pour suivre et gérer les interactions des nucléides, des données nucléaires évaluées (sections efficaces et propriétés de désintégration) sont nécessaires afin d'éviter d'implémenter des modèles d'interaction, et donc essentiellement tout un moteur Monte Carlo, lorsqu'on considère non seulement les processus de désintégration.

Les bibliothèques évaluées, publiées au format ENDF-6, permettent l'inclusion flexible de tout processus avec des sections efficaces pour les neutrons et les particules chargées. Cette interface entre les modèles nucléaires, les données expérimentales et l'examen critique des évaluateurs équivaut à simplifier les considérations de modélisation.

Ces fichiers sont également utilisés pour le traitement des neutrons dans les codes Monte Carlo ; ils sont donc une pierre angulaire de la modélisation, qu'elle soit déterministe ou stochastique, des processus nucléaires.

Ce travail a conduit à la création d'outils pour analyser et comparer de tels fichiers ENDF-6. En particulier, une comparaison préliminaire des sections efficaces neutroniques pour une sélection de matériaux et de réactions a été effectuée par rapport aux données expérimentales d'EXFOR.

La nécessité d'une pré-comparaison des données de sections efficaces a été soulignée dans le chapitre sur le Monte Carlo, car l'impact non seulement de la variation du code mais aussi de la variation de la base de données a été démontré. Un affinement peut être obtenu en effectuant une comparaison des bases de données, mais cela peut être très chronophage, en particulier lors de la modélisation d'installations entières.

Pour guider une telle comparaison, particulièrement pour les codes comme MCNP ou PHITS qui permettent un choix très flexible de la base de données (par radionucléide plutôt que seulement globalement), la comparaison des modèles en amont, via une comparaison inter-codes et par rapport aux sections efficaces expérimentales stockées dans EXFOR, a été initiée sur quelques sélections de matériaux et de réactions. Par la suite, ce travail a conduit au formatage de ces données de sections efficaces dans un format adapté aux applications de Deep Learning, et a été utilisé dans les travaux [155][1].

Enfin, le démantèlement exige une estimation très précise de l'inventaire nucléaire ; l'estimation de l'activité signifie également connaître précisément les spectres gamma. Disposer de données à jour est primordial, et des données étendues sont nécessaires pour construire un solveur de Bateman robuste.

Ce travail a donné lieu à la génération d'une nouvelle base de données de désintégration évaluée, ou plus précisément, une nouvelle compilation de données évaluées. La génération de la base de données GENF/D a fait l'objet d'une publication [156][2]. Cette base de données a été construite à partir de la vaste base de données de propriétés de désintégration NUBASE-2020. NUBASE a été traduite au format ENDF-6 et complétée par de meilleures estimations du spin provenant de RIPL-3, et par l'inclusion des spectres de désintégration d'ENSDF. L'estimation des spectres bêta et neutrino a été améliorée en utilisant BetaShape, qui devient le successeur de LogFT pour une gestion plus précise du spectre bêta et donne accès à sa description en spectre continu. De plus, des données atomiques ont été incluses en faisant appel à RadiationReport pour obtenir les électrons discrets (Auger et conversion), ainsi que les rayons X et le rayonnement de Bremmstrahlung interne.

Cette base de données de désintégration ayant été construite pour offrir des informations ENDF-6 très complètes et cohérentes. Étant dans le contexte de l'ADS, la fission spontanée a également été implémentée : les estimations du code Monte Carlo GEF ont été utilisées pour fournir des listes de fragments de fission, des spectres de neutrons et gamma, et des calculs de valeurs Q.

Perspectives

SSNTD pour les zones à faible fluence Comme présenté, les SSNTD permettent de détecter les neutrons avec des détecteurs économiques, pouvant être facilement déployés dans l'installation. Bien qu'une mise en oeuvre préliminaire de cette technique ait été réalisée, autour de l'installation CYRCé et à l'intérieur de son casemate, les résultats n'ont pas été concluants, mais restent encourageants.

[1] Lévana Gesson et al. 'Enhancing nuclear cross-section predictions with deep learning: the DINo algorithm'. en. In: *The European Physical Journal Plus* 140.7 (July 2025), p. 645. ISSN: 2190-5444. DOI: 10.1140/epjp/s13360-025-06562-z.

[2] Jonathan Collin et al. 'Global Evaluated Nuclear File (GENF/D): a decay data sub-library for radionuclide inventory applications'. en. In: *EPJ Nuclear Sciences & Technologies* 11 (2025), p. 77. ISSN: 2491-9292. DOI: 10.1051/epjn/2025070.

Les SSNTD permettent la détection des neutrons à l'aide de détecteurs assez simple pouvant être facilement déployés dans une installation. Bien qu'une première mise en oeuvre de cette technique ait été réalisée autour du cyclotron CYRCé et à l'intérieur de sa casemate, les résultats se sont révélés peu concluants.

Des améliorations du système d'acquisition optique sont nécessaires, en particulier pour l'identification des traces et l'extraction de leurs caractéristiques : rayon, intensité de couleur, etc. L'analyse des SSNTD doit être renforcée, notamment en ce qui concerne la discrimination proton–alpha, afin d'obtenir de meilleures estimations des composantes rapide et thermique des spectres neutroniques. Des algorithmes d'apprentissage automatique, tels que les random forests, devraient être explorés pour cette tâche. De telles approches nécessitent de grands ensembles d'images pour l'entraînement. Le couplage de simulations Monte Carlo avec des codes tels que TRACK_P (qui estime les traces résultant des protons) pourrait générer des données synthétiques pour compléter les acquisitions expérimentales. Des travaux ultérieurs pourraient permettre l'extraction des angles d'incidence des traces, donnant ainsi accès à l'énergie des neutrons au-delà de la simple discrimination proton–alpha. Les SSNTD sont proposés pour l'acquisition des taux de neutrons dans les zones de faible fluence, en tant que détecteurs cumulatifs dont les traces peuvent être archivées. Cette stratégie doit être accompagnée d'une campagne expérimentale autour de faisceaux contrôlés de protons et de particules alpha.

Ce travail pourrait être poursuivi pour obtenir l'angle d'incidence de la trace et permettre un accès à l'énergie du neutron au-delà de la simple discrimination entre l'identification du proton et de l'alpha. La technique SSNTD est proposée pour acquérir le taux de neutrons dans les zones où un faible fluence est attendue, en disposant d'un détecteur cumulatif, dont les traces sont conservées et peuvent être archivées.

Activation multi-feuillets L'installation CYRCé constitue un cas d'usage adapté au déploiement d'une telle technique. Bien que des modèles Monte Carlo aient été construits dans le cadre de ce travail, ils ne valident pas pleinement les spectres neutroniques à l'intérieur du casemate de l'accélérateur.

La technique d'activation par multi-feuillets devrait être appliquée pour obtenir des estimations expérimentales plus précises des spectres neutroniques secondaires. En utilisant plusieurs matériaux en feuillets présentant des réactions nucléaires dépendant différemment de l'énergie, et en appliquant des méthodes de déconvolution spectrale (analogues à la spectrométrie par sphères de Bonner), un affinement significatif de la distribution en énergie des neutrons pourrait être atteint.

Cette méthodologie devrait être étendue à des installations d'accélération à plus haute énergie, permettant d'explorer la technique à des énergies neutroniques élevées et fournissant des benchmarks supplémentaires pour les comparaisons inter-codes Monte Carlo.

Des énergies de faisceau plus élevées élargiraient la gamme des processus physiques pris en compte, produisant notamment des photons de plus haute énergie par rayonnement de freinage. Ces photons peuvent dépasser les seuils de réaction, en particulier

la résonance dipolaire géante, conduisant à une production de photoneutrons. Cette source neutronique supplémentaire contribuerait substantiellement à l'inventaire d'activation total et doit être prise en compte dans les modèles complets. La détermination précise des seuils énergétiques de ces réactions reste un défi majeur pour une estimation précise de l'activation dans les installations accélératrices. Une estimation correcte des seuils est cruciale pour identifier les composants dont les niveaux d'activation sont suffisamment bas pour une classification conventionnelle des déchets, facilitant ainsi les voies de recyclage et réduisant les coûts de stockage à long terme.

`TMX_Bateman` Le développement futur du solveur `TMX_Bateman` devrait se concentrer sur plusieurs améliorations clés pour accroître son efficacité de calcul, son exhaustivité physique et son utilité pratique pour les applications de démantèlement et de radioprotection.

Un objectif principal est l'implémentation d'un schéma d'intégration numérique basé sur des approximations de Chebyshev. Cette approche devrait accélérer de manière significative la résolution et la fiabilité des équations de Bateman, lors de la prise en compte de l'irradiation. En effet, comme mentionné, un tel cas peut introduire des boucles dans les canaux de désintégration linéarisés, pour lesquels l'analyse par trajectoire de transmutation n'est pas recommandée. À ce sujet, il existe des propositions de versions améliorées de TTA, qui peuvent réduire le temps de résolution [101][1].

Les modèles physiques du solveur doivent être étendus pour intégrer la simulation des interactions neutroniques provenant des processus de désintégration, tels que la fission spontanée ou les réactions (α,n). Actuellement, ces contributions neutroniques ne sont pas entièrement recouplées dans les spectres neutroniques considérés. Permettre cette capacité créera une simulation physiquement plus réaliste du champ neutronique et de ses effets dans le temps, en particulier dans les environnements présentant des inventaires d'actinides significatifs.

Pour soutenir directement la planification du démantèlement, une fonctionnalité d'évaluation automatique des niveaux d'exemption devrait être intégrée. Cela permettra à l'utilisateur de définir des limites réglementaires pour des radionucléides ou des catégories de matériaux spécifiques, permettant au code de calculer et de rapporter le temps nécessaire pour que les matériaux activés se désintègrent en dessous de ces seuils d'exemption stipulés. Cette fonctionnalité est essentielle pour la gestion pratique des déchets et la planification logistique.

Enfin, la feuille de route de développement inclut l'intégration de capacités de calcul de dose. En exploitant les spectres de désintégration détaillés fournis par le solveur et en incorporant des coefficients de conversion de dose appropriés, `TMX_Bateman` sera capable de calculer les débits de dose efficaces à partir des inventaires de nucléides calculés. Cela fournira des informations précieuses pour évaluer les risques d'exposition professionnelle

[1] Kai Huang et al. 'Improvements to the Transmutation Trajectory Analysis of depletion evaluation'. In: *Annals of Nuclear Energy* 87 (Jan. 2016), pp. 637–647. ISSN: 0306-4549. DOI: 10.1016/j.anucene.2015.10.013.

pendant les phases opérationnelles et de démantèlement, permettant l'optimisation des exigences de blindage et la planification des interventions.

GENF/D Bien que la version actuelle de GENF/D traduise avec succès NUBASE2020, plusieurs points d'amélioration subsistent, notamment concernant le traitement des incertitudes. Certaines incertitudes, en particulier celles relatives aux rapports d'embranchement, sont actuellement surestimées.

Actuellement, les erreurs sont propagées en utilisant seulement une méthode de base de développement de Taylor. L'implémentation des covariances des masse issues de l'AME améliorerait la précision des calculs de valeurs Q, entre autres paramètres.

De plus, comme les données sur les émissions de particules retardées ne sont pas disponibles via l'API Livechart actuellement utilisée, elles devraient être implémentées en utilisant des sources alternatives. Celles-ci pourraient inclure le format ENSDF-JSON issu du projet de modernisation d'ENSDF en cours, ou des prédictions de modèles nucléaires dédiés, en particulier pour les neutrons retardés. La première option pourrait être un moyen de contourner l'API Livechart, en accédant directement à ENSDF dans un format plus adapté à Python.

Étant donné que la base de données est principalement destinée à être utilisée dans des solveurs de Bateman plutôt que pour des applications d'évaluation ou métrologiques, l'amélioration de la robustesse des observables calculés est une considération clé. Bien que les estimations de chaleur de désintégration soient toujours fournies, les spectres de désintégration correspondants peuvent parfois manquer d'informations complètes. L'ajout de spectres estimés pourrait aider à maintenir la cohérence interne ; par exemple, un isotope marqué comme étant à désintégration α mais sans données de rayon associées pourrait tout de même se voir attribuer un spectre de rayons alpha cohérent avec sa contribution thermique due aux particules lourdes. Cette amélioration serait particulièrement précieuse pour les codes qui évaluent les doses radiologiques.

À ce sujet, il convient de noter que BetaShape est systématiquement appelé, en utilisant les données brutes les plus récentes d'ENSDF. BetaShape opère en se basant sur les spins enregistrés ; cela implique une possible incohérence de spin entre ce qui est finalement considéré par GENF/D et ce qui est utilisé par BetaShape. Le prétraitement des fichiers ENSDF pourrait améliorer la cohérence, comme cela a été fait pour la base de données GEF utilisée pour les estimations de fragments de fission.

Enfin, comme indiqué précédemment, l'approche conventionnelle utilisée par les évaluateurs pour estimer les énergies moyennes à partir des valeurs Q est discutable. Toutes les données ayant été formatées en objets Python, des procédures d'ajustement multiparamétriques pourraient être réalisées, incorporant des variables telles que le numéro atomique, la parité des nucléons, les modes de désintégration et la distance à la vallée de

stabilité. Des techniques d'apprentissage automatique pourraient être employées pour faciliter ces tâches d'ajustement complexes de manière efficace.

D.6. Besoins en données nucléaires pour les ADS

Les données nucléaires, en particulier les données de désintégration, sont essentielles pour la modélisation des systèmes physiques, notamment pour les réacteurs pilotés par accélérateur (ADS). Ce chapitre compare les principales bases de données évaluées (JEFF-4.0, JENDL-5, ENDF/B-VIII.1) avec la base étendue NUBASE2020 et sa traduction en format ENDF-6, GENF/D.

D.6.1. Comparaison des couvertures isotopiques

- **NUBASE2020** est la base la plus complète, recensant 3558 noyaux dans l'état fondamental et 2007 états excités.
- **GENF/D** traduit NUBASE2020 en format ENDF-6 et l'enrichit avec des données de spectres (BetaShape, RadiationReport) et de fission (GEF). Elle couvre 3511 états fondamentaux et 1990 états excités.
- Les bases évaluées classiques (JEFF, JENDL, ENDF/B) présentent des lacunes significatives en nombre de noyaux, notamment pour les états excités (plus de 1000 noyaux supplémentaires dans GENF/D).

D.6.2. Désaccords sur les périodes radioactives

- Pour les noyaux à vie courte ($T_{1/2} < 10$ s), des écarts importants existent entre les bases.
- 129 isotopes présentent des différences de période supérieures à 100% par rapport à NUBASE.
- Parmi ceux-ci, 18 ont une période > 10 s et 38 une période > 1 s.
- Dans le contexte ADS, l'isotope ^{58}Mn montre la plus grande divergence (3,0 s dans NUBASE contre 65,2 s dans JEFF).

D.6.3. Émission neutronique retardée

- NUBASE/GENF/D indique beaucoup plus de canaux d'émission neutronique retardée que les autres bases.
- JEFF est très conservatrice dans l'attribution de ces canaux.
- 4 émetteurs retardés d'intérêt pour les ADS sont identifiés : ^{9}Li, ^{11}Be, ^{36}P, ^{48}K.

D.6.4. Fragments de fission

Fission spontanée

- Les listes de rendements de fission spontanée (SFY) sont très limitées : seulement 10 cibles disponibles hors GEF/GENF/D.

- GENF/D (avec GEF) étend considérablement cette couverture à 401 cibles.
- La distribution des fragments est globalement cohérente entre bases, mais GEF permet une modélisation plus fine des états excités.

Fission induite par neutrons

- De nombreuses sections efficaces de fission (n,f) existent (jusqu'à 933 cibles dans JEFF-4.0).
- Cependant, les listes de rendements de fission induite (NFY) sont très incomplètes : seulement 36 cibles hors GEF.
- GEF permet de générer des listes NFY pour un grand nombre de noyaux manquants.

D.6.5. Conclusion et perspectives

- Les listes de fragments de fission (spontanée et induite) sont très lacunaires dans les bases classiques. GEF/GENF/D comble partiellement ce manque.
- Une validation expérimentale accrue des modèles de fission (GEF, FREYA, FIFRELIN) est nécessaire, notamment pour les noyaux lourds et les spectres non thermiques.
- L'impact des désaccords sur les périodes courtes et les neutrons retardés doit être évalué dans le contexte spécifique des ADS (radiotoxicité, criticité).
- La revue des données expérimentales (ENSDF, EXFOR) pour les isotopes à forts écarts est recommandée.
- La base GENF/D, par son étendue et son formatage ENDF-6, constitue un outil précieux pour les études d'inventaire et de démantèlement des installations ADS.

Appendix

Acronyms

ACSI Advanced Cyclotron System Inc.

ADS Accelerator Driven System.

AME Atomic Mass Evaluation.

ANDRA Agence Nationale des Dechets Radioactifs.

ASAP Adjoint Sensitivity Analysis Procedure.

ASCII American Standard Code for Information Interchange.

BNL Brookhaven National Laboratory.

BROND Library of Russian Evaluated Neutron Data.

CERN European Organization for Nuclear Research.

CG Combinatorial Geometry.

CGMF Cascading Gamma-ray Multiplicity and Fission.

CRAM Chebyshev Rational Approximation Method.

CSV Comma-Separated Values.

CYRCé Cyclotron pour la ReCherche et l'Enseignement.

DCHAIN Decay Chain Analysis code.

DPA Displacement Per Atom.

DPM Dual Parton Model.

EAF European Activation File.

EGS Electron Gamma Shower.

ENDF-6 Evaluated Nuclear Data File 6.

ENDF/B Evaluated Nuclear Data File B.

ENSDF Evaluated Nuclear Structure Data File.

EuCARD European Coordination for Accelerator Research and Development.

EXFOR EXperimental FORmat.

FENDL Fusion Evaluated Nuclear Data Library.

FF Fission Fragments.

FISPACT Fusion-Induced Spallation and Activation Code Tool.

FLUKA FLUktuierende KAskade.

FREYA Fission Reaction Event Yield Algorithm.

Geant4 GEometry ANd Tracking.

GEFY GEF-based Fission Yield library.

GEM Generalied Evaporation Model.

GENF/D Global Evaluated Nuclear File, Decay Data.

HDF5 Hierarchical Data Format 5.

HEP High-Energy Physics.

HP High Precision.

IAEA International Atomic Energy Agency.

IBA Ion Beam Applications.

INDEN International Nuclear Data Evaluation Network.

INFN Istituto Nazionale di Fisica Nucleare.

IRDFF International Reactor Dosimetry and Fusion File.

JAEA-ADS Japanese Atomic Energy Agency - ADS.

JEFF Joint Evaluated Fission and Fusion File.

JENDL Japansese Evaluated Nuclear Data Library.

JQMD Jaeri Quantum Molecular Dynamics.

JSON JavaScript Object Notation.

KORIGEN KIT-ORIGEN.

LANL Los Alamos National Laboratory.

LBE Lead-Bismuth Eutectic.

LEND Low Energy Nuclear Data.

LHC Large Hadron Collider.

LINAC LINear ACcelerator.

LLNL Lawrence Livermore National Laboratory.

LNHB National Laboratory Henri Becquerel.

LSODE Livermore Solver for Ordinary Differential Equations.

MA Minor Actinides.

MCNP Monte Carlo N-Particle.

MIT Massachusetts Institute of Technology.

MYRRHA Multi-purpose hYbrid Research Reactor for High-tech Applications.

NIEL Non-Ionizing Energy Loss.

NUBASE Nuclear DataBase.

NUIT Nuclear Inventory Uncertainty Tool.

ORIGEN Oak Ridge Isotope Generation and Depletion Code.

PEANUT PreEquilibrium Approach to Nuclear Thermalization).

PHITS Particle and Heavy Ion Transport code System.

PTCOG Particle Therapy Co-Operative Group.

QRAM Quadrature-based Rational Approximation Method.

RIPL Reference Input Parameter Library.

RRR Resolved Resonance Region.

SCALE Standardized Computer Analyses for Licensing Evaluation.

SKKU-ADS Sungkyunkwan University - ADS.

SSNTD Solid-State Nuclear Track Detector.

START Subcritical Transmutation Accelerated Reactor Technology.

TENDL Chinese Evaluated Nuclear Data Library.

TENDL Talys Evaluated Nuclear Data Library.

TTA Transmutation Trajectory Analysis.

UKHEDD United Kingdom Heavy Decay Data.

UKPADD United Kingdom Product Decay Data.

URR Unresolved Resonance Region.

WIND Waste Incineration Nuclear Data.

WNP Wide range NeutonPit.

XMuDat X-ray Mass attenuation and energy absorption DATa.

Appendix

References

[1] G Ising. 'Prinzip einer Methode zur Herstellung von Kanalstrahlen hoher Voltzahl'. In: *Ark. Mat. Astron. Fys.* 18.30 (1924), pp. 1–4 (cit. on p. 1).

[2] Ernest O. Lawrence. 'Method and apparatus for the acceleration of ions'. US1948384A. Feb. 1934 (cit. on p. 1).

[3] M. Menu et al. 'The dedicated accelerator-based IBA facility AGLAE at the Louvre'. In: *Nuclear Instruments and Methods in Physics Research Section B: Beam Interactions with Materials and Atoms* 45.1 (Jan. 1990), pp. 610–614. ISSN: 0168-583X. DOI: 10.1016/0168-583X(90)90910-M (cit. on p. 1).

[4] The EuCARD-2 Collaboration. *Applications of Particle Accelerators in Europe*. en. 2020. DOI: 10.17181/CERN.HA4I.UT3N (cit. on p. 1).

[5] Carlo Rubbia et al. *Conceptual design of a fast neutron operated high power energy amplifier*. Tech. rep. Geneva: CERN, 1995 (cit. on p. 3).

[6] Bruce Yee-Rendón. 'Overview of ADS Projects in the World'. en. In: *Proceedings of the 31st International Linear Accelerator Conference* LINAC2022 (2022). Ed. by McIntosh Peter (Ed.) et al., 4 pages, 2.664 MB. ISSN: 2226-0366. DOI: 10.18429/JACOW-LINAC2022-TU2AA01 (cit. on pp. 3, 5).

[7] Xunchao Zhang et al. 'Strategies of eliminating nuclear waste using accelerator-driven system in the transition stage for sustainable and clean nuclear energy in China'. In: *Annals of Nuclear Energy* 185 (June 2023), p. 109713. ISSN: 0306-4549. DOI: 10.1016/j.anucene.2023.109713 (cit. on p. 3).

[8] Ogugua P. Unokiwedi et al. 'Deep geological repositories — A review of design concepts, near-field evolution, and their implications for nuclear waste containment'. In: *Journal of Environmental Radioactivity* 289 (Oct. 2025), p. 107750. ISSN: 0265-931X. DOI: 10.1016/j.jenvrad.2025.107750 (cit. on p. 3).

[9] H. Oigawa. 'JAEA's R&D Activities on Transmutation Technology for Long-lived Nuclear Wastes'. In: *ImPACT International Symposium on New Horizons of Partitioning and Transmutation Technologies with Accelerator System*. Tokyo, Japan, Dec. 2018 (cit. on p. 4).

[10] International Atomic Energy Agency. *Decommissioning of Particle Accelerators*. en. Text. International Atomic Energy Agency, 2020, pp. 1–160 (cit. on pp. 5, 6).

[11] P. Carbonez et al. 'Residual radioactivity at the CERN 600MeV synchro-cyclotron'. en. In: *Nuclear Instruments and Methods in Physics Research Section A: Accelerators, Spectrometers, Detectors and Associated Equipment* 694 (Dec. 2012), pp. 234–245. ISSN: 01689002. DOI: 10.1016/j.nima.2012.08.011 (cit. on p. 5).

[12] N. Soppera, M. Bossant, and E. Dupont. 'JANIS 4: An Improved Version of the NEA Java-based Nuclear Data Information System'. In: *Nuclear Data Sheets* 120 (June 2014), pp. 294–296. ISSN: 0090-3752. DOI: 10.1016/j.nds.2014.07.071 (cit. on pp. 10, 140).

[13] Rolf Woldseth. *X-ray energy spectrometry*. en. First. Kevex Corporation, 1973 (cit. on p. 11).

[14] Walter D. Loveland, David J. Morrissey, and Glenn T. Seaborg. 'Nuclear Structure'. en. In: *Modern Nuclear Chemistry*. John Wiley & Sons, Ltd, 2017, pp. 125–165. ISBN: 978-1-119-34845-0. DOI: 10.1002/9781119348450.ch6 (cit. on p. 11).

[15] Laboratoire National Henri Becquerel. *Nucléide – Lara Application – Laboratoire National Henri Becquerel*. en-GB (cit. on pp. 12, 15, 16, 18, 22, 86).

[16] F.G. Kondev et al. 'The NUBASE2020 evaluation of nuclear physics properties *'. en. In: *Chinese Physics C* 45.3 (Mar. 2021), p. 030001. ISSN: 1674-1137, 2058-6132. DOI: 10.1088/1674-1137/abddae (cit. on pp. 13, 17, 117, 206).

[17] W.J. Huang et al. 'The AME 2020 atomic mass evaluation (I). Evaluation of input data, and adjustment procedures*'. en. In: *Chinese Physics C* 45.3 (Mar. 2021), p. 030002. ISSN: 1674-1137, 2058-6132. DOI: 10.1088/1674-1137/abddb0 (cit. on pp. 13, 14, 167).

[18] H. M. Devaraja et al. 'Systematic studies to produce heavy above-target nuclides in multinucleon transfer reactions'. In: *Physics Letters B* 862 (Mar. 2025), p. 139353. ISSN: 0370-2693. DOI: 10.1016/j.physletb.2025.139353 (cit. on p. 13).

[19] H. L. Crawford et al. 'Crossing $N=28$ Toward the Neutron Drip Line: First Measurement of Half-Lives at FRIB'. In: *Physical Review Letters* 129.21 (Nov. 2022), p. 212501. DOI: 10.1103/PhysRevLett.129.212501 (cit. on p. 14).

[20] S. Navas et al. 'Review of Particle Physics'. In: *Phys. Rev. D* 110.3 (Aug. 2024), p. 030001. DOI: 10.1103/PhysRevD.110.030001 (cit. on p. 15).

[21] M.-M. Bé et al. *Table of Radionuclides*. Vol. 1. Monographie BIPM-5. Pavillon de Breteuil, F-92310 Sèvres, France: Bureau International des Poids et Mesures, 2004. ISBN: 92-822-2206-3 (cit. on pp. 19, 78).

[22] Xavier Mougeot. 'Atomic exchange correction in forbidden unique beta transitions'. In: *Applied Radiation and Isotopes* 201 (Nov. 2023), p. 111018. ISSN: 0969-8043. DOI: 10.1016/j.apradiso.2023.111018 (cit. on pp. 20, 110, 159, 171).

[23] Jun Chen. *IAEA-NSDDNetwork/RadiationReport*. Apr. 2025 (cit. on pp. 21, 151, 168).

[24] G. M. Volkoff. 'The Atomic Nucleus. Robley D. Evans. McGraw-Hill, New York, 1955. xv+ 972 pp. Illus. $14.50.' In: *Science* 123.3197 (Apr. 1956), pp. 592–593. DOI: 10.1126/science.123.3197.592.b (cit. on p. 23).

[25] Youbba Ould Salem. 'Etude expérimentale et modélisation Monte Carlo des grandeurs opérationnelles en métrologie des rayonnements ionisants: application à la dosimétrie neutrons par radiophotoluminescence'. français. Thèse de doctorat. Institut pluridisciplinaire Hubert Curien: Université de Strasbourg, 2014 (cit. on p. 29).

[26] V.G. Pronyaev and Vienna (Austria) International Atomic Energy Agency Nuclear Data Section. *XMuDat: Photon attenuation data on PC. Version 1.0.1 of August 1998. Summary documentation.* Jan. 2025 (cit. on p. 31).

[27] Henri Métivier. *Radioprotection et ingénierie nucléaire.* EDP Sciences, 2006 (cit. on p. 31).

[28] Kai Siegbahn. *Alpha-, Beta- and gamma-ray spectroscopy.* en. Vol. 1. North-Holland publishing company, 1965 (cit. on p. 32).

[29] Samir Dziri. 'Etudes expérimentales et simulations Monte Carlo en spectrométrie gamma: Correction des effets de cascade et de matrice pour des mesures environnementales'. fr. PhD thesis. Université de Strasbourg, May 2013 (cit. on p. 33).

[30] H. Bethe and W. Heitler. 'On the stopping of fast particles and on the creation of positive electrons'. In: *Proceedings of the Royal Society of London. Series A, Containing Papers of a Mathematical and Physical Character* 146.856 (Aug. 1934), pp. 83–112. ISSN: 0950-1207. DOI: 10.1098/rspa.1934.0140 (cit. on p. 33).

[31] Raymond Pannetier. *Vade-mecum du technicien.* fr. First. Vol. 1. Vade-mecum du technicien nucléaire : contrôle des rayonnements ionisants, mise en oeuvre des techniques de protection. 1966 (cit. on p. 35).

[32] Jerry B. Marion and J. L. Fowler. *Fast neutron physics.* eng. Vol. 2. Interscience monographs and texts in physics and astronomy. New York: Interscience Publishers, 1960 (cit. on p. 36).

[33] Gordon R. Gilmore. 'Radioactive Decay and the Origin of Gamma and X-Radiation'. en. In: *Practical Gamma-Ray Spectrometry.* John Wiley & Sons, Ltd, 2008, pp. 1–24. ISBN: 978-0-470-86198-1 (cit. on p. 39).

[34] Nicholas Metropolis and S. Ulam. 'The Monte Carlo Method'. In: *Journal of the American Statistical Association* 44.247 (1949), pp. 335–341. DOI: 10.1080/01621459.1949.10483310 (cit. on p. 44).

[35] Abdellatif Nachab. 'Etudes expérimentales et modélisations Monte Carlo de l'autoabsorption gamma et de la dosimétrie active par capteurs CMOS'. fr. PhD thesis. Université Louis Pasteur - Strasbourg I, Dec. 2003 (cit. on p. 45).

[36] Christopher John Werner et al. *MCNP User's Manual Code Version 6.2.* Tech. rep. LA-UR-17-29981. Los Alamos, NM, USA: Los Alamos National Laboratory, Oct. 2017 (cit. on pp. 46, 74).

[37] Pavel Obložinský, Michal Herman, and Said F. Mughabghab. 'Evaluated Nuclear Data'. en. In: *Handbook of Nuclear Engineering*. Ed. by Dan Gabriel Cacuci. Boston, MA: Springer US, 2010, pp. 83–187. ISBN: 978-0-387-98149-9. DOI: 10.1007/978-0-387-98149-9_2 (cit. on p. 47).

[38] Dan Gabriel Cacuci and Mihaela Ionescu-Bujor. 'Sensitivity and Uncertainty Analysis, Data Assimilation, and Predictive Best-Estimate Model Calibration'. en. In: *Handbook of Nuclear Engineering*. Ed. by Dan Gabriel Cacuci. Boston, MA: Springer US, 2010, pp. 1913–2051. ISBN: 978-0-387-98149-9. DOI: 10.1007/978-0-387-98149-9_17 (cit. on p. 47).

[39] L. Fiorito et al. 'Nuclear data uncertainty propagation to integral responses using SANDY'. In: *Annals of Nuclear Energy* 101 (Mar. 2017), pp. 359–366. ISSN: 0306-4549. DOI: 10.1016/j.anucene.2016.11.026 (cit. on p. 47).

[40] W. Zwermann et al. 'NUCLEAR DATA UNCERTAINTY AND SENSITIVITY ANALYSIS WITH XSUSA FOR FUEL ASSEMBLY DEPLETION CALCULATIONS'. In: *Nuclear Engineering and Technology* 46.3 (June 2014), pp. 343–352. ISSN: 1738-5733. DOI: 10.5516/NET.01.2014.711 (cit. on p. 47).

[41] Dan G. Cacuci. *Sensitivity & Uncertainty Analysis, Volume 1: Theory*. New York: Chapman and Hall/CRC, May 2003. ISBN: 978-0-429-21009-9. DOI: 10.1201/9780203498798 (cit. on p. 47).

[42] D. G. Cacuci, Mihaela Ionescu-Bujor, and Ionel Michael Navon. *Sensitivity and uncertainty analysis, Volume 2: Application to Large Scale Systems*. en. Boca Raton: Chapman & Hall/CRC Press, 2003. ISBN: 978-1-58488-115-5 978-1-58488-116-2 (cit. on p. 47).

[43] J. Allison et al. 'Recent developments in Geant4'. In: *Nuclear Instruments and Methods in Physics Research Section A: Accelerators, Spectrometers, Detectors and Associated Equipment* 835 (2016), pp. 186–225. ISSN: 0168-9002. DOI: https://doi.org/10.1016/j.nima.2016.06.125 (cit. on pp. 48, 85).

[44] J. Allison et al. 'Geant4 developments and applications'. In: *IEEE Transactions on Nuclear Science* 53.1 (Feb. 2006), pp. 270–278. ISSN: 1558-1578. DOI: 10.1109/TNS.2006.869826 (cit. on p. 48).

[45] S. Agostinelli et al. 'Geant4—a simulation toolkit'. In: *Nuclear Instruments and Methods in Physics Research Section A: Accelerators, Spectrometers, Detectors and Associated Equipment* 506.3 (July 2003), pp. 250–303. ISSN: 0168-9002. DOI: 10.1016/S0168-9002(03)01368-8 (cit. on p. 48).

[46] Geant4 Collaboration. *Introduction to Geant4*. en. Tech. rep. Release 11.3 - Rev9.2. June 2025, p. 17 (cit. on p. 49).

[47] A. Ferrari et al. *FLUKA: A Multi-Particle Transport Code*. English. Tech. rep. SLAC-R-773. SLAC National Accelerator Lab., Menlo Park, CA (United States), Dec. 2005. DOI: 10.2172/877507 (cit. on pp. 51, 76, 85, 97).

[48] G. Battistoni et al. 'The FLUKA code: description and benchmarking'. In: *AIP Conference Proceedings* 896.1 (Mar. 2007), pp. 31–49. ISSN: 0094-243X. DOI: 10.1063/1.2720455 (cit. on p. 51).

[49] T. T. Böhlen et al. 'The FLUKA Code: Developments and Challenges for High Energy and Medical Applications'. In: *Nuclear Data Sheets* 120 (2014), pp. 211–214. ISSN: 0090-3752. DOI: https://doi.org/10.1016/j.nds.2014.07.049 (cit. on p. 51).

[50] Tatsuhiko Sato et al. 'Recent improvements of the particle and heavy ion transport code system – PHITS version 3.33'. In: *Journal of Nuclear Science and Technology* 0.0 (2023), pp. 1–9. ISSN: 0022-3131. DOI: 10.1080/00223131.2023.2275736 (cit. on pp. 54, 97).

[51] D. V. Freck and J. Wakefield. 'Gamma-Ray Spectrum obtained with a Lithium-drifted p–i–n Junction in Germanium'. en. In: *Nature* 193.4816 (Feb. 1962), pp. 669–669. ISSN: 1476-4687. DOI: 10.1038/193669a0 (cit. on p. 57).

[52] Gordon R. Gilmore. 'Interactions of Gamma Radiation with Matter'. en. In: *Practical Gamma-Ray Spectrometry*. John Wiley & Sons, Ltd, 2008, pp. 25–38. ISBN: 978-0-470-86198-1 (cit. on pp. 58, 59).

[53] Gordon R. Gilmore. 'Semiconductor Detectors for Gamma-Ray Spectrometry'. en. In: *Practical Gamma-Ray Spectrometry*. John Wiley & Sons, Ltd, 2008, pp. 39–60. ISBN: 978-0-470-86198-1 (cit. on p. 60).

[54] Gordon R. Gilmore. 'Resolution: Origins and Control'. en. In: *Practical Gamma-Ray Spectrometry*. John Wiley & Sons, Ltd, 2008, pp. 131–141. ISBN: 978-0-470-86198-1 (cit. on p. 61).

[55] Ramkumar Venkataraman. 'Chapter 4 - Semiconductor detectors'. In: *Handbook of Radioactivity Analysis (Fourth Edition)*. Ed. by Michael F. L'Annunziata. Fourth Edition. Academic Press, 2020, pp. 409–491. ISBN: 978-0-12-814397-1. DOI: https://doi.org/10.1016/B978-0-12-814397-1.00004-2 (cit. on p. 61).

[56] Glenn F. KNOLL. *Radiation Detection and Measurements*. Fourth. Wiley, 2010. ISBN: 978-0-470-13148-0 (cit. on p. 61).

[57] K. Debertin and R.G. Helmer. *Gamma- and X-ray spectrometry with semiconductor detectors*. North-Holland., Jan. 2025 (cit. on p. 63).

[58] International Organization for Standardization (ISO). *Measurement of radioactivity in the environment — Soil — Part 3: Test method of gamma-emitting radionuclides using gamma-ray*. Geneva, Switzerland, July 2023 (cit. on p. 63).

[59] D. A. Young. 'Etching of Radiation Damage in Lithium Fluoride'. en. In: *Nature* 182.4632 (Aug. 1958), pp. 375–377. ISSN: 1476-4687. DOI: 10.1038/182375a0 (cit. on p. 64).

[60] P. B. Price and R. M. Walker. 'A new track detector for heavy particle studies'. In: *Physics Letters* 3.3 (1962), pp. 113–115. ISSN: 0031-9163. DOI: https://doi.org/10.1016/0031-9163(62)90051-3 (cit. on p. 64).

[61] C. Baccou et al. 'CR-39 track detector calibration for H, He, and C ions from 0.1-0.5 MeV up to 5 MeV for laser-induced nuclear fusion product identification'. In: *Review of Scientific Instruments* 86.8 (Aug. 2015), p. 083307. ISSN: 0034-6748. DOI: 10.1063/1.4927684 (cit. on p. 64).

[62] Mukhtar Ahmed Rana. 'Summary of a comprehensive data bank for nuclear track research using CR-39 detectors'. In: *Nuclear Instruments and Methods in Physics Research Section A: Accelerators, Spectrometers, Detectors and Associated Equipment* 944 (2019), p. 162590. ISSN: 0168-9002. DOI: https://doi.org/10.1016/j.nima.2019.162590 (cit. on p. 64).

[63] F. Castillo et al. 'Fast neutron dosimetry using CR-39 track detectors with polyethylene as radiator'. In: *Radiation Measurements*. 25th ICNTS 50 (Mar. 2013), pp. 71–73. ISSN: 1350-4487. DOI: 10.1016/j.radmeas.2012.09.007 (cit. on p. 65).

[64] Shi-Lun Guo, Bao-Liu Chen, and S. A. Durrani. 'Chapter 3 - Solid-state nuclear track detectors'. In: *Handbook of Radioactivity Analysis (Fourth Edition)*. Ed. by Michael F. L'Annunziata. Fourth Edition. Academic Press, 2020, pp. 307–407. ISBN: 978-0-12-814397-1. DOI: https://doi.org/10.1016/B978-0-12-814397-1.00003-0 (cit. on p. 66).

[65] Paul Henderson. '(R. L.) Fleischer, (P. B.) Price, and (R. M.) Walker. Nuclear Tracks in Solids: Principles and Applications. Berkeley and London (Univ. California Press), 1975. xxii+605 pp., 205 figs., I pl. Price'. In: *Mineralogical Magazine* 42.322 (1978), pp. 306–307. DOI: 10.1180/minmag.1978.042.322.40 (cit. on p. 67).

[66] D. Nikezic and K.N. Yu. 'Formation and growth of tracks in nuclear track materials'. In: *Materials Science and Engineering: R: Reports* 46.3 (Dec. 2004), pp. 51–123. ISSN: 0927-796X. DOI: 10.1016/j.mser.2004.07.003 (cit. on p. 67).

[67] M. Bolzonella et al. 'Neutron personal dosimetry using polyallyl diglycol carbonate (PADC): Current status, best practices and proposed research'. In: *Physics Open* 12 (2022), p. 100114. ISSN: 2666-0326. DOI: https://doi.org/10.1016/j.physo.2022.100114 (cit. on p. 67).

[68] Chiyoda Technologies. *Solid-state Track Detector – TechnoTrak 2*. en (cit. on p. 68).

[69] H. Ohguchi et al. 'New pre-soaking technique for PADC and application to wide-range personal neutron dosimeter'. In: *Radiation Measurements*. Proceedings of the 23rd International Conference on Nuclear Tracks in Solids 43 (Aug. 2008), S500–S503. ISSN: 1350-4487. DOI: 10.1016/j.radmeas.2008.03.015 (cit. on p. 68).

[70] Takuya Hashizume et al. 'Development of a high-speed and precise automatic reading system of CR-39 plastic nuclear track detector for neutron dose measurements'. en. In: *Radiation Measurements* 191 (Feb. 2026), p. 107572. ISSN: 13504487. DOI: 10.1016/j.radmeas.2025.107572 (cit. on p. 69).

[71] Youbba Ould Salem et al. 'RPL Neutron Dosimetry in n- Fields in Comparison with Polymer Detectors Type CR-39'. In: *Polymers* 14.9 (2022). ISSN: 2073-4360. DOI: 10.3390/polym14091801 (cit. on p. 69).

[72] Jonathan Collin et al. 'Validation of Monte Carlo simulations by experimental measurements of neutron-induced activation in cyclotrons'. en. In: *EPJ Web of Conferences*. Vol. 288. Italy: EDP Sciences, 2023, p. 04025. DOI: 10.1051/epjconf/202328804025 (cit. on pp. 69, 85, 87, 187, 246).

[73] Abdel-Mjid Nourreddine et al. 'Assessment of photon and proton-induced activation in particles accelerators'. In: *Radiation Protection Dosimetry*. Vol. 200. 16-18. Japan, Nov. 2024, pp. 1507–1513. DOI: 10.1093/rpd/ncae146 (cit. on pp. 69, 70, 78, 187, 246).

[74] Douglas A. Fynan. 'Photoneutron reaction kinematics and error of commonly used approximations'. In: *Nuclear Instruments and Methods in Physics Research Section A: Accelerators, Spectrometers, Detectors and Associated Equipment* 977 (Oct. 2020), p. 164271. ISSN: 0168-9002. DOI: 10.1016/j.nima.2020.164271 (cit. on p. 73).

[75] D. J. S. Findlay. 'Applications of photonuclear reactions'. In: *Nuclear Instruments and Methods in Physics Research Section B: Beam Interactions with Materials and Atoms* 50.1 (Apr. 1990), pp. 314–320. ISSN: 0168-583X. DOI: 10.1016/0168-583X(90)90374-4 (cit. on p. 73).

[76] B. J. Patil et al. 'Estimation of neutron production from accelerator head assembly of 15 MV medical LINAC using FLUKA simulations'. In: *Nuclear Instruments and Methods in Physics Research Section B: Beam Interactions with Materials and Atoms*. Proceedings of the 10th European Conference on Accelerators in Applied Research and Technology (ECAART10) 269.24 (Dec. 2011), pp. 3261–3265. ISSN: 0168-583X. DOI: 10.1016/j.nimb.2011.04.013 (cit. on p. 74).

[77] Francois Begin, Addil Sellam, and Abdel-Mjid Nourreddine. 'Monte Carlo simulations of photoneutron activation in a medical LINAC'. en. In: *2015 4th International Conference on Advancements in Nuclear Instrumentation Measurement Methods and their Applications (ANIMMA)*. Lisbon, Portugal: IEEE, Apr. 2015, pp. 1–4. ISBN: 978-1-4799-9918-7. DOI: 10.1109/ANIMMA.2015.7465550 (cit. on p. 74).

[78] M. Fassbender et al. 'Proton beam simulation with MCNPX: Gallium metal activation estimates below 30 MeV relevant to the bulk production of 68Ge and 65Zn'. In: *Nuclear Instruments and Methods in Physics Research Section B: Beam Interactions with Materials and Atoms*. The Application of Accelerators in Research and Industry 261.1 (Aug. 2007), pp. 742–746. ISSN: 0168-583X. DOI: 10.1016/j.nimb.2007.03.099 (cit. on p. 76).

[79] A. Esposito et al. 'Determination of the neutron spectra around an 18 MV medical LINAC with a passive Bonner sphere spectrometer based on gold foils and TLD pairs'. In: *Radiation Measurements*. Proceedings of the 15th Solid State Dosimetry (SSD15) 43.2 (Feb. 2008), pp. 1038–1043. ISSN: 1350-4487. DOI: 10.1016/j.radmeas.2007.10.035 (cit. on p. 76).

[80] K. Amgarou et al. 'Characterization of the neutron field from the 241Am-Be isotopic source of the IPHC irradiator'. en. In: *Radiation Measurements*. 25th ICNTS 50 (Mar. 2013), pp. 61–66. ISSN: 1350-4487. DOI: 10.1016/j.radmeas.2012.11.015 (cit. on p. 79).

[81] D. A. Brown et al. 'ENDF/B-VIII.0: The 8th Major Release of the Nuclear Reaction Data Library with CIELO-project Cross Sections, New Standards and Thermal Scattering Data'. In: *Nuclear Data Sheets*. Special Issue on Nuclear Reaction Data 148 (Feb. 2018), pp. 1–142. ISSN: 0090-3752. DOI: 10.1016/j.nds.2018.02.001 (cit. on pp. 79, 86, 137, 153, 206).

[82] A. J. M. Plompen et al. 'The joint evaluated fission and fusion nuclear data library, JEFF-3.3'. en. In: *The European Physical Journal A* 56.7 (July 2020), p. 181. ISSN: 1434-601X. DOI: 10.1140/epja/s10050-020-00141-9 (cit. on pp. 79, 86, 137, 153, 206).

[83] Geant4 Collaboration. *Shielding — PhysicsListGuide 11.4 documentation* (cit. on p. 79).

[84] Geant4 Collaboration. *QGSP_BIC — PhysicsListGuide 11.4 documentation* (cit. on p. 79).

[85] Keiichi SHIBATA et al. 'JENDL-4.0: A New Library for Nuclear Science and Engineering'. In: *Journal of Nuclear Science and Technology* 48.1 (Jan. 2011), pp. 1–30. ISSN: 0022-3131. DOI: 10.1080/18811248.2011.9711675 (cit. on p. 79).

[86] M. B. Chadwick et al. 'ENDF/B-VII.1 Nuclear Data for Science and Technology: Cross Sections, Covariances, Fission Product Yields and Decay Data'. In: *Nuclear Data Sheets*. Special Issue on ENDF/B-VII.1 Library 112.12 (Dec. 2011), pp. 2887–2996. ISSN: 0090-3752. DOI: 10.1016/j.nds.2011.11.002 (cit. on pp. 79, 150).

[87] A. J. Koning et al. 'TENDL: Complete Nuclear Data Library for Innovative Nuclear Science and Technology'. In: *Nuclear Data Sheets*. Special Issue on Nuclear Reaction Data 155 (Jan. 2019), pp. 1–55. ISSN: 0090-3752. DOI: 10.1016/j.nds.2019.01.002 (cit. on pp. 80, 86, 137).

[88] International Organization for Standardization (ISO). *Part 1: Characteristics and methods of production*. Standard ISO 8529-1:2021. Geneva, CH, Nov. 2021, p. 30 (cit. on p. 80).

[89] C. Ahdida et al. 'New Capabilities of the FLUKA Multi-Purpose Code'. In: *Frontiers in Physics* 9 (2022). ISSN: 2296-424X (cit. on p. 85).

[90] Tatsuhiko Sato et al. 'Features of Particle and Heavy Ion Transport code System (PHITS) version 3.02'. In: *Journal of Nuclear Science and Technology* 55.6 (June 2018), pp. 684–690. ISSN: 0022-3131. DOI: 10.1080/00223131.2017.1419890 (cit. on p. 85).

[91] J. -Ch. Sublet et al. 'FISPACT-II: An Advanced Simulation System for Activation, Transmutation and Material Modelling'. In: *Nuclear Data Sheets*. Special Issue on Nuclear Reaction Data 139 (Jan. 2017), pp. 77–137. ISSN: 0090-3752. DOI: 10.1016/j.nds.2017.01.002 (cit. on pp. 85, 96).

[92] Osamu Iwamoto et al. 'Japanese evaluated nuclear data library version 5: JENDL-5'. In: *Journal of Nuclear Science and Technology* 60.1 (Jan. 2023), pp. 1–60. ISSN: 0022-3131. DOI: 10.1080/00223131.2022.2141903 (cit. on pp. 86, 137, 153, 206).

[93] Caroline A. Schneider, Wayne S. Rasband, and Kevin W. Eliceiri. 'NIH Image to ImageJ: 25 years of image analysis'. en. In: *Nature Methods* 9.7 (July 2012), pp. 671–675. ISSN: 1548-7105. DOI: 10.1038/nmeth.2089 (cit. on p. 89).

[94] Halima Elazhar. 'Dosimétrie neutron en radiothérapie: étude expérimentale et développement d'un outil personnalisé de calcul de dose Monte Carlo'. français. Thèse de doctorat. Université de Strasbourg, 2018 (cit. on p. 89).

[95] C V Parks and P O Box. *Overview of ORIGEN2 and ORIGEN-S: capabilities and limitations*. en. Tech. rep. (cit. on p. 96).

[96] U. Fischer and H. W. Wiese. 'Verbesserte konsistente Berechnung des nuklearen Inventars abgebrannter DWR-Brennstoffe auf der Basis von Zell-Abbrand-Verfahren mit KORIGEN'. de. In: *Karlsruher Institut für Technologie*. Institut für Neutronenphysik und Reaktortechnik (INR) (1983). DOI: 10.5445/IR/270018961 (cit. on p. 96).

[97] W. A. Wieselquist and R. A. Lefebvre. *SCALE 6.3.1 User Manual*. en. Tech. rep. Oak Ridge National Laboratory, 2023 (cit. on p. 96).

[98] Hunter N. Ratliff et al. 'Modernization of the DCHAIN-PHITS activation code with new features and updated data libraries'. In: *Nuclear Instruments and Methods in Physics Research Section B: Beam Interactions with Materials and Atoms* 484 (Dec. 2020), pp. 29–41. ISSN: 0168-583X. DOI: 10.1016/j.nimb.2020.10.005 (cit. on pp. 96, 109).

[99] Jian Li et al. 'The NUIT code for nuclide inventory calculations'. In: *Annals of Nuclear Energy* 148 (Dec. 2020), p. 107690. ISSN: 0306-4549. DOI: 10.1016/j.anucene.2020.107690 (cit. on p. 96).

[100] Maria Pusa and Jaakko Leppänen. 'Computing the Matrix Exponential in Burnup Calculations'. In: *Nuclear Science and Engineering* 164.2 (Feb. 2010), pp. 140–150. ISSN: 0029-5639. DOI: 10.13182/NSE09-14 (cit. on p. 96).

[101] Kai Huang et al. 'Improvements to the Transmutation Trajectory Analysis of depletion evaluation'. In: *Annals of Nuclear Energy* 87 (Jan. 2016), pp. 637–647. ISSN: 0306-4549. DOI: 10.1016/j.anucene.2015.10.013 (cit. on pp. 96, 100, 101, 103, 133, 190, 250).

[102] Joel Aaron Kulesza et al. *MCNP\textsuperscript® Code Version 6.3.0 Theory & User Manual*. Tech. rep. LA-UR-22-30006, Rev. 1. Los Alamos, NM, USA: Los Alamos National Laboratory, Sept. 2022. DOI: 10.2172/1889957 (cit. on p. 97).

[103] François-Xavier Hugot et al. 'Overview of the TRIPOLI-4 Monte Carlo code, version 12'. en. In: *EPJ Nuclear Sciences & Technologies* 10 (2024), p. 17. ISSN: 2491-9292. DOI: 10.1051/epjn/2024018 (cit. on p. 97).

[104] Krishnan Radhakrishnan. 'Description and Use of LSODE, the Livermore Solver for Ordinary Differential Equations'. en. In: () (cit. on p. 98).

[105] Jaakko Leppänen et al. 'The Serpent Monte Carlo code: Status, development and applications in 2013'. In: *Annals of Nuclear Energy*. Joint International Conference on Supercomputing in Nuclear Applications and Monte Carlo 2013, SNA + MC 2013. Pluri- and Trans-disciplinarity, Towards New Modeling and Numerical Simulation Paradigms 82 (Aug. 2015), pp. 142–150. ISSN: 0306-4549. DOI: 10.1016/j.anucene.2014.08.024 (cit. on p. 100).

[106] Pertti A Aarnio. *Decay and Transmutation of Nuclides*. 1999 (cit. on pp. 103, 104).

[107] Kanji Tasaka. 'DCHAIN2 : A COMPUTER CODE FOR CALCULATION OF TRANSMUTATION OF NUCLIDES'. en. In: (1980), p. 171. DOI: 10.11484/jaeri-m-8727 (cit. on p. 103).

[108] David A. Brown. *ENDF-6 Formats Manual - Data Formats and Procedures for the Evaluated Nuclear Data Files ENDF/B-VI, ENDF/B-VII and ENDF/B-VIII*. English. Tech. rep. BNL-224854-2023-INRE. Brookhaven National Laboratory (BNL), Upton, NY (United States), Sept. 2023. DOI: 10.2172/2007538 (cit. on pp. 106, 164, 206).

[109] 'ICRP Publication 72: Age-dependent Doses to Members of the Public from Intake of Radionuclides - Part 5 Compilation of Ingestion and Inhalation Coefficients'. en. In: *Annals of the ICRP* 26.1 (Jan. 1996), pp. 1–91. ISSN: 0146-6453. DOI: 10.1016/S0146-6453(00)89192-7 (cit. on p. 106).

[110] *ICRP Publication 151: Occupational Intakes of Radionuclides: Part 5* (cit. on pp. 106, 116).

[111] N. B. Gove and M. J. Martin. 'Log-*f* tables for beta decay'. In: *Atomic Data and Nuclear Data Tables* 10.3 (Nov. 1971), pp. 205–219. ISSN: 0092-640X. DOI: 10.1016/S0092-640X(71)80026-8 (cit. on p. 110).

[112] Fujio Maekawa et al. *Decay heat experiment and validation of calculation code systems for fusion reactor*. Oct. 1999 (cit. on p. 124).

[113] J. K. Dickens et al. 'Fission-Product Energy Release for Times Following Thermal-Neutron Fission of Plutonium-239 and Plutonium-241 Between 2 and 14 000 s'. In: *Nuclear Science and Engineering* 78.2 (June 1981), pp. 126–146. ISSN: 0029-5639. DOI: 10.13182/NSE81-A20099 (cit. on pp. 127, 183).

[114] A. Tobias. 'Decay heat'. In: *Progress in Nuclear Energy* 5.1 (Jan. 1980), pp. 1–93. ISSN: 0149-1970. DOI: 10.1016/0149-1970(80)90002-5 (cit. on pp. 127, 183).

[115] J.C. Hardy et al. 'The essential decay of pandemonium: A demonstration of errors in complex beta-decay schemes'. en. In: *Physics Letters B* 71.2 (Nov. 1977), pp. 307–310. ISSN: 03702693. DOI: 10.1016/0370-2693(77)90223-4 (cit. on pp. 127, 183).

[116] Zhigang Ge et al. 'CENDL-3.2: The new version of Chinese general purpose evaluated nuclear data library'. en. In: *EPJ Web of Conferences* 239 (2020), p. 09001. ISSN: 2100-014X. DOI: 10.1051/epjconf/202023909001 (cit. on pp. 137, 206).

[117] Russia Blokhin et al. 'NEW VERSION OF NEUTRON EVALUATED DATA LIBRARY BROND-3.1 (in Russian), published in Voprosy At. Nauki i Tekniki, ser Yadernye Konstanty, issue 2, p. 92 (2016)'. In: *Voprosy atomnoj nauki i techniki = Pytannja atomnoï nauky i techniky = Problems of atomic science and technology* 2016 (Aug. 2016), p. 92 (cit. on p. 137).

[118] G. Schnabel et al. 'FENDL: A library for fusion research and applications'. In: *Nuclear Data Sheets*. Special Issue on Nuclear Reaction Data 193 (Feb. 2024), pp. 1–78. ISSN: 0090-3752. DOI: 10.1016/j.nds.2024.01.001 (cit. on pp. 137, 153).

[119] Daniel Lopez Aldama. *ADS-HE: Evaluated Nuclear Data Library up to 1 GeV for 202Hg, 208Pb, 209Bi, 232Th, 235U, 238U, 237Np, 239Pu, 242Am and 245Cm*. en. Tech. rep. IAEA-Nuclear Data Section, Dec. 2013. DOI: 10.61092/iaea.r81b-0sjz (cit. on p. 137).

[120] *Index of /public/download-endf/IAEA-Medical* (cit. on p. 137).

[121] *IRPhEP Handbook Online - OECD Nuclear Energy Agency* (cit. on p. 137).

[122] *Nuclear Energy Agency* (cit. on p. 137).

[123] Ivan A. Kodeli and Enrico Sartori. 'SINBAD – Radiation shielding benchmark experiments'. In: *Annals of Nuclear Energy* 159 (Sept. 2021), p. 108254. ISSN: 0306-4549. DOI: 10.1016/j.anucene.2021.108254 (cit. on p. 137).

[124] Georg Schnabel, Daniel Lopez Aldama, and Roberto Capote. *How to explain ENDF-6 to computers: A formal ENDF format description language*. Dec. 2023 (cit. on pp. 140, 157).

[125] Viktor Zerkin. *X4Pro – universal, fully relational EXFOR database*. English. 2023 (cit. on p. 140).

[126] NNDC. *IAEA-NSDDNetwork/LOGFT*. National Nuclear Data Center, May 2025 (cit. on p. 150).

[127] X. Mougeot. 'Erratum: Reliability of usual assumptions in the calculation of beta and nu spectra'. In: *Physical Review C* 92.5 (Nov. 2015), p. 059902. DOI: 10.1103/PhysRevC.92.059902 (cit. on p. 150).

[128] Greg Baily et al. *FISPACT-II User Manual*. en. Manual UKAEA-CCFE-RE(21)02. United Kingdom Atomic Energy Authority, May 2023 (cit. on p. 150).

[129] *Evaluated Nuclear Structure Data File (ENSDF)*. en. 2022. DOI: 10.18139/NNDC.ENSDF/1845010 (cit. on p. 150).

[130] R. Capote et al. 'RIPL – Reference Input Parameter Library for Calculation of Nuclear Reactions and Nuclear Data Evaluations'. In: *Nuclear Data Sheets*. Special Issue on Nuclear Reaction Data 110.12 (Dec. 2009), pp. 3107–3214. ISSN: 0090-3752. DOI: 10.1016/j.nds.2009.10.004 (cit. on p. 150).

[131] K. -H. Schmidt et al. 'General Description of Fission Observables: GEF Model Code'. In: *Nuclear Data Sheets*. Special Issue on Nuclear Reaction Data 131 (Jan. 2016), pp. 107–221. ISSN: 0090-3752. DOI: 10.1016/j.nds.2015.12.009 (cit. on p. 151).

[132] T. Kibédi et al. 'Evaluation of theoretical conversion coefficients using *BrIcc*'. In: *Nuclear Instruments and Methods in Physics Research Section A: Accelerators, Spectrometers, Detectors and Associated Equipment* 589.2 (May 2008), pp. 202–229. ISSN: 0168-9002. DOI: 10.1016/j.nima.2008.02.051 (cit. on pp. 151, 159, 160).

[133] L W Packer and J-Ch Sublet. *The European Activation File: EAF-2010 biological, clearance and transport libraries*. en. Tech. rep. CCFE-R (10)04. Culham Science Centre: Culham Centre for Fusion Energy, 2010, p. 46 (cit. on p. 153).

[134] A. Trkov et al. 'IRDFF-II: A New Neutron Metrology Library'. In: *Nuclear Data Sheets* 163 (Jan. 2020), pp. 1–108. ISSN: 0090-3752. DOI: 10.1016/j.nds.2019.12.001 (cit. on p. 153).

[135] R. J. Perry, C. J. Dean, and A. L. Nichols. 'Actinide, Activation Product and Fission Product Decay Data for Reactor-based Applications'. In: *Nuclear Data Sheets* 120 (June 2014), pp. 261–263. ISSN: 0090-3752. DOI: 10.1016/j.nds.2014.07.062 (cit. on p. 153).

[136] Enrico Sartori. 'Nuclear data for radioactive waste management'. In: *Annals of Nuclear Energy* 62 (Dec. 2013), pp. 579–589. ISSN: 0306-4549. DOI: 10.1016/j.anucene.2013.02.003 (cit. on p. 153).

[137] G. Audi. 'The History of Nuclidic Masses and of their Evaluation'. en. In: *International Journal of Mass Spectrometry* 251.2-3 (Apr. 2006), pp. 85–94. ISSN: 13873806. DOI: 10.1016/j.ijms.2006.01.048 (cit. on p. 156).

[138] The pandas development team. *pandas-dev/pandas: Pandas*. Aug. 2025. DOI: 10.5281/zenodo.16918803 (cit. on p. 157).

[139] Hernan E. Grecco et al. *Pint: a Python units library*. 2015 (cit. on p. 157).

[140] J. Liang et al. 'Compilation and Evaluation of Beta-Delayed Neutron Emission Probabilities and Half-Lives for Z > 28 Precursors'. In: *Nuclear Data Sheets* 168 (Sept. 2020), pp. 1–116. ISSN: 0090-3752. DOI: 10.1016/j.nds.2020.09.001 (cit. on pp. 158, 169, 172).

[141] M. Birch et al. 'Evaluation of Beta-Delayed Neutron Emission Probabilities and Half-Lives for Z = 2–28'. In: *Nuclear Data Sheets* 128 (Sept. 2015), pp. 131–184. ISSN: 0090-3752. DOI: 10.1016/j.nds.2015.08.002 (cit. on pp. 158, 169, 172).

[142] T. Kibédi et al. 'Internal conversion coefficients - How good are they now?' en. In: *ND2007*. Nice, France: EDP Sciences, 2007, p. 017. DOI: 10.1051/ndata:07771 (cit. on p. 159).

[143] E. Schönfeld and H. Janßen. 'Calculation of emission probabilities of X-rays and Auger electrons emitted in radioactive disintegration processes'. In: *Applied Radiation and Isotopes* 52.3 (Mar. 2000), pp. 595–600. ISSN: 0969-8043. DOI: 10.1016/S0969-8043(99)00216-X (cit. on pp. 160, 168).

[144] D.E. Cullen. *EPICS2023: August 2023 Status Report*. en. Tech. rep. Vienna: IAEA Nuclear Data Section, Aug. 2023. DOI: 10.61092/iaea.cfw1-fws6 (cit. on p. 160).

[145] J. M. Verbeke, J. Randrup, and R. Vogt. 'Fission Reaction Event Yield Algorithm FREYA 2.0.2'. In: *Computer Physics Communications* 222 (Jan. 2018), pp. 263–266. ISSN: 0010-4655. DOI: 10.1016/j.cpc.2017.09.006 (cit. on p. 161).

[146] Olivier Litaize, Olivier Serot, and Léonie Berge. 'Fission modelling with FIFRELIN'. en. In: *The European Physical Journal A* 51.12 (Dec. 2015), p. 177. ISSN: 1434-601X. DOI: 10.1140/epja/i2015-15177-9 (cit. on p. 161).

[147] M. H. Brennan. 'jj Coupling Model in Odd-Odd Nuclei'. In: *Physical Review* 120.3 (1960), pp. 927–933. DOI: 10.1103/PhysRev.120.927 (cit. on p. 162).

[148] Torleif Ericson. 'The statistical model and nuclear level densities'. EN. In: *Advances in Physics* (Oct. 1960), p. 425. DOI: 10.1080/00018736000101239 (cit. on p. 162).

[149] A. Gilbert and A. G. W. Cameron. 'A Composite Nuclear-level density formula with shell corrections'. en. In: *Canadian Journal of Physics* 43 (Aug. 1965). DOI: 10.1139/p65-139 (cit. on p. 162).

[150] M. Herman. *ENDF-6 Formats Manual Data Formats and Procedures for the Evaluated Nuclear Data File ENDF/B-VI and ENDF/B-VII*. English. Tech. rep. BNL–90365-2009. Brookhaven National Laboratory (BNL) National Nuclear Data Center, June 2009. DOI: 10.2172/981813 (cit. on p. 172).

[151] Andre Trkov and David A. Brown. *ENDF-6 Formats Manual: Data Formats and Procedures for the Evaluated Nuclear Data Files*. English. Tech. rep. BNL-203218-2018-INRE. Brookhaven National Laboratory (BNL), Upton, NY (United States), Jan. 2018. DOI: 10.2172/1425114 (cit. on p. 172).

[152] A. Letourneau et al. 'Origin of the Reactor Antineutrino Anomalies in Light of a New Summation Model with Parametrized beta- Transitions'. In: *Physical Review Letters* 130.2 (Jan. 2023), p. 021801. DOI: 10.1103/PhysRevLett.130.021801 (cit. on pp. 181, 186).

[153] Joint Evaluated Fission and Fusion Project. 'JEFF-4.0 Evaluated Data: spontaneous fission products yields'. en. In: *OECD Nuclear Energy Agency* (June 2025). DOI: 10.82555/tccek-e9s26 (cit. on p. 183).

[154] J. L. Yarnell and P. J. Bendt. *Calorimetric fission product decay heat measurements for 239Pu, 233U, and 235U*. English. Tech. rep. NUREG/CR-0349; LA-7452-MS. Los Alamos Scientific Lab., NM (USA), Aug. 1978. DOI: 10.2172/6577911 (cit. on p. 183).

[155] Lévana Gesson et al. 'Enhancing nuclear cross-section predictions with deep learning: the DINo algorithm'. en. In: *The European Physical Journal Plus* 140.7 (July 2025), p. 645. ISSN: 2190-5444. DOI: 10.1140/epjp/s13360-025-06562-z (cit. on pp. 188, 248).

[156] Jonathan Collin et al. 'Global Evaluated Nuclear File (GENF/D): a decay data sub-library for radionuclide inventory applications'. en. In: *EPJ Nuclear Sciences & Technologies* 11 (2025), p. 77. ISSN: 2491-9292. DOI: 10.1051/epjn/2025070 (cit. on pp. 188, 248).

[157] D. Nikezic, M. Ivanovic, and K. N. Yu. 'A computer program TRACK_P for studying proton tracks in PADC detectors'. In: *SoftwareX* 5 (Jan. 2016), pp. 74–79. ISSN: 2352-7110. DOI: 10.1016/j.softx.2016.04.006 (cit. on p. 189).

[158] Isao Murata et al. 'Neutron and gamma-ray source-term characterization of AmBe sources in Osaka University'. en. In: *Progress in Nuclear Science and Technology* 4 (2014), pp. 345–348. ISSN: 2185-4823. DOI: 10.15669/pnst.4.345 (cit. on p. 189).

[159] Davide Chiesa et al. 'Measurement of the neutron flux at spallation sources using multi-foil activation'. In: *Nuclear Instruments and Methods in Physics Research Section A: Accelerators, Spectrometers, Detectors and Associated Equipment* 902 (2018), pp. 14–24. ISSN: 0168-9002. DOI: https://doi.org/10.1016/j.nima.2018.06.016 (cit. on p. 189).

Université de Strasbourg

IPHC Institut Pluridisciplinaire Hubert CURIEN STRASBOURG

TRANSMUTEX

Jonathan Collin

Estimation de l'activité induite par neutrons et inventaire radiologique autour d'accélérateurs de hautes puissances

Résumé

L'utilisation croissante des accélérateurs de particules, notamment pour les Accelerator Driven Systems, génère des déchets radioactifs dont la caractérisation est cruciale pour leur démantèlement et leur gestion. Ce travail de thèse, mené dans le cadre d'un partenariat avec la start-up suisse Transmutex, propose une méthodologie et des outils pour l'estimation de l'inventaire radiologique, nécessaire au démantèlement de telles installations. Une campagne expérimentale de spectrométrie gamma (et l'utilisation de détecteur solides de traces nucléaire) a été réalisée autour d'une source neutronique AmBe et du cyclotron CYRCé et comparée à des modélisations Monte Carlo utilisant les codes Geant4, PHITS, et FLUKA couplés aux outils `FISPACT-II`, `DCHAIN-PHITS` et `TMX_Bateman`. La thèse a également contribué à l'amélioration du code `TMX_Bateman` et à la création de la base de données GENF/D, intégrant NUBASE2020 et ENDSF, afin d'optimiser les simulations de décroissance et d'activation.

Mots-clés: Données nucléaires; ENDF-6; Activation neutronique; Inventaire Radionucléide; Estimation de chaleur de décroissance; Simulation Monte Carlo

Summary

The growing use of particle accelerators, particularly for Accelerator Driven Systems, generates radioactive waste whose characterisation is crucial for their dismantling and management. This thesis, conducted in partnership with the Swiss start-up Transmutex, proposes a methodology and tools for estimating the radiological inventory required for the decommissioning of such facilities. An experimental gamma spectrometry campaign (using solid nuclear trace detectors) was carried out around an AmBe neutron source and the CYRCé cyclotron and compared with Monte Carlo modelling using the Geant4, PHITS, and FLUKA codes coupled with the `FISPACT-II`, `DCHAIN-PHITS`, and `TMX_Bateman` tools. The thesis also contributed to the improvement of the `TMX_Bateman` code and the creation of the GENF/D database, integrating NUBASE2020 and ENDSF, in order to optimise decay and activation simulations.

Keywords: Nuclear Decay data; ENDF-6 Sub-Library; Neutron Activation; Radionuclide Inventory; Decay heat computation; Monte Carlo simulation